DOE/BC/14862-10
(DE95000163)

PRODUCTIVITY AND INJECTIVITY OF HORIZONTAL WELLS

Annual Report for the Period
March 10, 1994 to March 9, 1995

By
F. J. Fayers

July 1995

Performed Under Contract No. DE-FG22-93BC14862

Stanford University
Stanford, California

Bartlesville Project Office
U. S. DEPARTMENT OF ENERGY
Bartlesville, Oklahoma

DOE/BC/14862-10
Distribution Category UC-122

Productivity and Injectivity of Horizontal Wells

Annual Report for the Period
March 10, 1994 to March 9, 1995

By
F. J. Fayers

July 1995

Work Performed Under Contract No. DE-FG22-93BC14862

Prepared for
U.S. Department of Energy
Assistant Secretary for Fossil Energy

Thomas Reid, Project Manager
Bartlesville Project Office
P.O. Box 1398
Bartlesville, OK 74005

Prepared by
Stanford University
Dept. of Petroleum Engineering
Stanford, CA 94305-2220

Contents

Management Summary

1. DOE Approval

The DOE approval for the annual renewal of the research grant to the Stanford Project on the *Productivity and Injectivity of Horizontal Wells* was received in early March 1994. The Project formally commenced on March 10, 1993. Mr. Thomas Reid is the DOE Project Manager in Bartlesville and Mr. John Augustine is the DOE Contracts Officer in Pittsburgh.

2. Industrial Affiliates Program

The DOE Project operates in association with an Industrial Affiliates program on horizontal wells, for which oil company membership has also continued during 1994. The membership during this year comprised the following organizations:

Amoco (USA)
AGIP (Italy)
ARTEP/IFP (France)
BP Exploration (USA)
Chevron (USA)
INTEVEP (Venezuela)
Marathon (USA)
Norsk Hydro (Norway)
Petrobras America (Brazil)
Texaco (USA)
Union Pacific Resources (USA)

3. Project Goals

The Project has eight principal goals to be studied and developed over a five year period. These goals are as follows:

TASK 1: Advanced Modeling of Horizontal Wells - Develop special gridding techniques and associated averaging algorithms for accurate simulation of HW-performance.

TASK 2: Investigate and Incorporate the Effects of Reservoir Heterogeneities - Study impacts of various types of heterogeneity and develop methods for incorporating their effects in both fine grid and coarse grid models.

TASK 3: Develop Improved Methods for Calculating Multi-Phase Pressure Drops within the Wellbore - Plan, execute, and interpret two-phase flow experiments at an oil company research facility, and use results to analyze/validate a new two-phase model.

TASK 4: Pseudo-Functions - Define improved methods for computing two-phase pseudo-functions for effective relative permeabilities for coarse grid blocks near an HW - determine sensitivities to heterogeneities, flow conditions, skin factors, etc.

TASK 5: Develop Multi-Well Models - Develop numerical techniques and software in a parallel computing architecture capable of interactively coupling multiple detailed HW-models to a large scale reservoir simulator.

TASK 6: Test HW-Models with Field Examples - Work with affiliate's member companies to establish HW-modeling capabilities from field measurements, particularly for pathological problem cases.

TASK 7: EOR Applications - Provide and implement practical HW aspects into modeling of EOR processes - miscible gas, steam displacement, in-situ combustion.

TASK 8: Application Studies and Their Optimization - Seek field opportunities for HW's and study their best implementation in various reservoir scenarios e.g., multiple laterals, hydraulic fracture variants, etc.

Tasks 1, 2, 3, 4, and 8 were the primary focus of activities scheduled for 1994, and the annual report is therefore written around these five tasks, which are also ongoing in 1995. Some of our principal achievements are summarized below.

4. Large-Scale Flow Loop Experiments

The funding from the Industrial Affiliates Project is mainly expended on a series of large scale experiments in an outdoor flow loop being conducted at the Marathon Research Center in Littleton, Colorado. Contractual arrangements have continued with Marathon to undertake these experiments, for which a substantial part of the costs ($\sim$ 50%) is born by Marathon. The arrangements to allow air or nitrogen injection through the manifolds for the perforations have been successfully completed, and also to allow two-phase core flows along the 100 ft acrylic wellbore model. New Rosemount DP-gauges have been installed and have given results with good accuracy and reliability. A range of two-phase flow experiments with both air/water and nitrogen/oil combinations have been completed. Results over the central section of the acrylic wellbore appear to be good, but there are indications of end effects associated with having pipe diameter changes from 4 to 6 inches at inlet and outlet to the 6 inch diameter test section. Some further end effects are also caused by the use of a mixing T-junction for core two-phase flow which is not too far removed from the inlet. The rig is undergoing further modifications to improve these features. Another major modification currently being made is to the offtake pipework and separator designs to allow use of a higher capacity compressor for gas flows. Preliminary design work has also been undertaken to set up experiments with a slotted liner within the wellbore, using a porous packing to create dispersed radial flow to the slots of the liner.

5. Improved Theoretical Modeling of Two-Phase Flow within the Wellbore

Analysis of the Marathon measurement using two of the industry preferred two-phase flow correlations, namely the Beggs and Brill method, and the Dukler, Wicks and Cleveland method, have been made. The measured pressure drops are larger under two-phase conditions than the theoretical predictions, due to the fact that the inflow from the perforations disturbs the boundary layer and flow patterns. The predicted two-phase pressure drops can be artificially matched by increasing the effective roughness of the smooth acrylic wellbore.

The development of a new "analytic" two-phase pipeflow model has continued under Professor Aziz at Stanford. Most of the major features in this model have been programmed and various aspects of its dealing with six possible two-phase flow regimes are now being tested. A large two-phase flow data bank with international information is being assembled for parameter assessments and accuracy checking. The problems of dealing with two-phase cross flow entry from perforations will be a difficult future challenge to add to this new analytically based development.

6. Generalized Gridding Methods

The work on developing a 3D-generalized Voronoi gridding code has progressed well. Methods have been programmed which allow a tessellation, or Delaunay triangulation, to be produced for assignments of node points, picked in any user desired manner to describe the primary geological features of a reservoir, and its deviated wells. The triangulation in 3D is based on tetrahedra, for which perpendicular bisectors of the edges then lead to the definition of Voronoi blocks. Thus variably sized blocks with polyhedral shapes result, whose spacing and size allow close definition of flows near wells with arbitrary contours, and the effects of tilted faults, primary stratigraphic layerings, etc. to be properly represented. Two different forms of algebraic approximations (one finite-element type with face centered points and the other block centered finite-difference type) are being tested, with promising initial results.

7. Coning and Cresting Methods

The work commenced in 1993 on investigating semi-analytical methods for predicting the critical cresting rates of horizontal wells has progressed further. We have developed a new semi-analytical theory for calculating critical cresting rates. The new method has been shown to be accurate by extensive simulation studies using the Eclipse code. Six previous analytical methods developed over a period of some 30 years are shown to have various limitations, with the most recent method being in error by a factor of about 23 in the critical rate. We have further confirmed that time to breakthrough for a horizontal well flowing at super critical rates is an important attribute of its cresting characteristics. For the breakthrough time, a simple adaptation of the analytical results by Papatzacos, et al. for wells with infinite spacing, gives acceptable agreement with simulation results for wells with finite spacing. This work is being published in a paper to an international symposium.

8. Effects of Heterogeneities on Flow Performance

Studies have continued on the effects of severe heterogeneities (e.g. discontinuous shale distributions) on flow distributions in 2D reservoir problems with horizontal wells. The main intent of this work is to find techniques for successfully upscaling fine grid solutions of the heterogeneous problem to coarser grid sizes which are typically used in field models. The normal industry techniques led to significant difficulties, with negative effective transmissivities apparently being required, which are unacceptable to reservoir simulators. Ad hoc fix-up procedures to avoid the negative values resulted in predicted pressure and flow distributions from the coarse grid solution with serious errors. A new upscaling procedure has been devised based on calculating the streamlines for the fine grid flows. The results are

used to give a positive dissipation procedure for determining fluxes, and consequently effective transmissivities, for modified coarse grid boundaries. This new upscaling procedure avoids the occurrence of negative values and yields accurate results at the coarse scale.

The above developments for single phase flow have been extended to two-phase flow. Knowledge of the streamlines is used to infer the two-phase fluxes at the modified coarse grid boundaries. The use of Buckley-Leverett solutions scaled along the streamlines gives estimates of pseudo-relative permeabilities and average saturations within each coarse grid block. The adaptability of these techniques is now being tested for problems in which well flow rates change and/or new well positions come into operation.

9. Calculation of Contributions to Total Skin Factor

Variations in skin factors for horizontal wells can be an important feature affecting the inflow distribution along the well. As a first step in understanding the primary contributions to skin factor, a computer code has been written which follows the semi-analytical/empirical equations and rules set out in a review paper by Thomas, et al. for calculating skin factor contributions to well performance. The features dealt with include perforation geometry, mud invasion, crushed zone, partial penetration, and well deviation. Gravel packing and non-Darcy flow effects can also be predicted. For an example case, the damaged region, crushed zone, and partial penetration significantly dominated the other contributions. This work is being viewed with regard to possible extension to look at more detailed modeling methods for joining the two-phase flow in the wellbore to the main grid blocks of a reservoir simulator. The HOSIM code obtained from Norsk Hydro has been set up and may be developed further for these purposes.

10. Factors Influencing Gas/Oil Ratio History in a Field Application

Studies have been undertaken by a visiting scholar from Norsk Hydro on sensitivity of the oil and gas production history to various aspects of the modeling assumptions. A 3D-model was set up for a reservoir with a horizontal well placed slightly above a water/oil contact, with a gas/oil contact at a higher level. The slightly simplified reservoir description was taken to be representative of a real field application. The water breaks through quickly because of the adjacent contact near the well, but gas breakthrough is delayed by characteristics of the cresting behavior. The primary sensitivity investigated was that due to wellbore two/three-phase wellbore pressure drop. Based on the homogeneous pipeflow model in the Eclipse code, inclusion of the wellbore pressure drop caused the gas breakthrough position to move from the center to the heel of the well. However, the subsequent changes in producing gas/oil ratios were rather small. For this application, the main significance of the results could be in designing completion, or recompletion policies.

11. Affiliates Progress Review Meeting

An annual review meeting for member companies in the Stanford Horizontal Well Project was held at Stanford on September 22-23, 1994. This meeting was well attended and member companies made presentations on their horizontal well interests and activities on the second day. The next meeting is scheduled for October 19 and 20, 1995, to be adjacent to the SPE Fall Meeting, for the benefit of travel arrangements for overseas members.

12. Presentations at Conferences, etc.

A review paper was written by invitation and presented at the Canadian SPE/CIM/CANMET international meeting on horizontal wells, March 20-24, 1994. A presentation entitled "Three Dimensional Voronoi Grids in Reservoir Simulation" was made at the Third Geosciences Conference organized by the Society of Industrial and Applied Mathematics, February 8-10, 1995, San Antonio, Texas. A paper entitled "Comparative Aspects of Coning Behavior in Horizontal and Vertical Wells" has been prepared for presentation at the European IOR Conference in Vienna, May 15-17, 1995.

1. Detailed Well Model for Reservoir Simulation (Task 1)

Research work by Ph.D. student Santosh Verma
Advisors: Profs. Khalid Aziz and John Fayers

1.1 Objective

The objective of this Task is to develop a three–dimensional reservoir simulator based on generalized Voronoi grids which honor horizontal/deviated wells, local flow geometry, faults, major heterogeneities, anisotropy, etc. There are difficult geometrical/logical problems associated with automatic generation and visualization of the gridding geometry in 3D, which forms a significant aspect of this Task. The mathematical formulation for the flow simulation should take into account such a complex gridding scheme. Pressure and flow calculations in a wellbore (obtained from a wellbore simulator) will be coupled with similar reservoir variables.

1.2 Introduction

One of earliest methods used in reservoir simulation to obtain flexibility in gridding was local Cartesian grid refinement (LCGR). Figure 1.1 shows the use of fine grids inside a coarse grid. LCGR can thus be used in regions which require finer resolution. A sharp saturation front, a region of widely varying petrophysical properties, flow geometry near a wellbore, etc., are cases where LCGR can be used. Some disadvantages of this method are

- Lines connecting grid points in the coarse region to those in the refined are not always orthogonal to the boundary between them.
- Potential gradients at the coarse-fine block boundaries become dependent on potentials of a few more blocks than is the case for a regular grid, thus increasing the bandwidth of the Jacobian matrix.
- The error reduction and time saving from LGGR is not always as attractive as might have been expected, in comparison with the complete fine grid solution.

To obtain radial flow geometry near a well, hybrid local grid refinement [1] is quite popular. Figure 1.2 shows such a grid. These grids provide an accurate flow description very near the well. They also result in a very simple well model. Orthogonal curvilinear grids are used in the well region and Cartesian grids are used in the reservoir region. Some disadvantages of this method are

- Irregularly shaped blocks (pseudoblocks) are used at the boundary of the well and reservoir regions. These pseudoblocks give rise to the use of two different grid points to compute flow between the pseudoblock and curvilinear grid and that between pseudoblock and Cartesian grid.

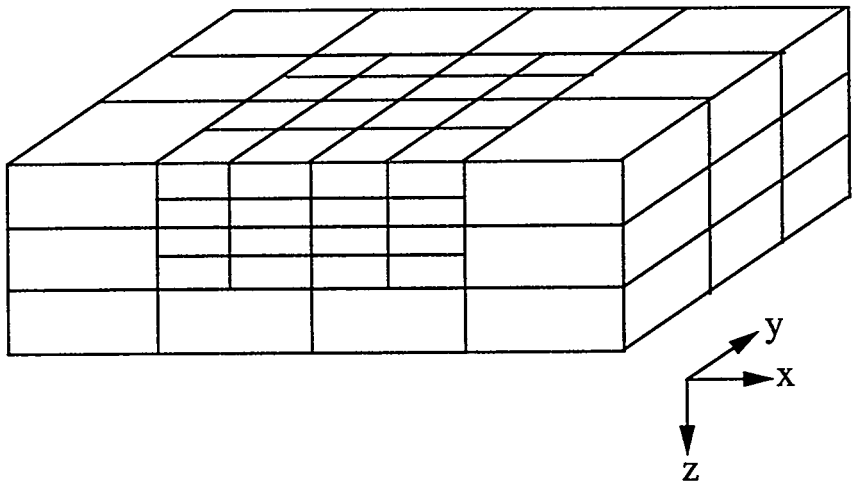

Figure 1.1: Cartesian Local Grid Refinement

- Some approximation is needed to handle transmissibility at the interface.

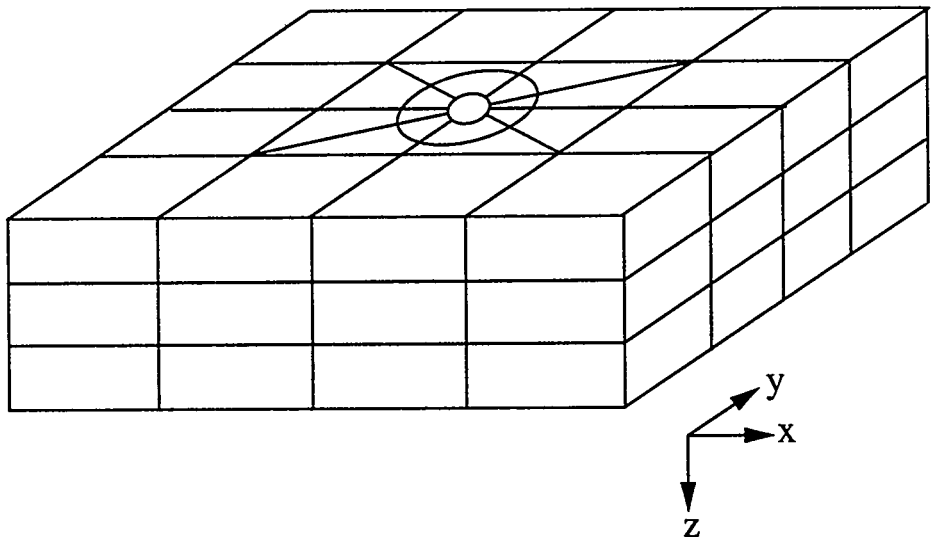

Figure 1.2: Hybrid Local Grid Refinement

Both the Cartesian and hybrid LGR require a base grid which is Cartesian. Hence it becomes difficult to align the grid to conform to varying facies, horizontal wellbores, etc., even in the horizontal plane. Use of Voronoi grids has been proposed to tackle this problem by Palagi [2].

Use of Voronoi grids facilitates the specification of grid points anywhere inside the domain. Grids are locally orthogonal, hence enabling a reasonably accurate computation of interblock transmissibility for heterogeneous but isotropic permeabilities (this may not be a clear advantage in an anisotropic permeability field).

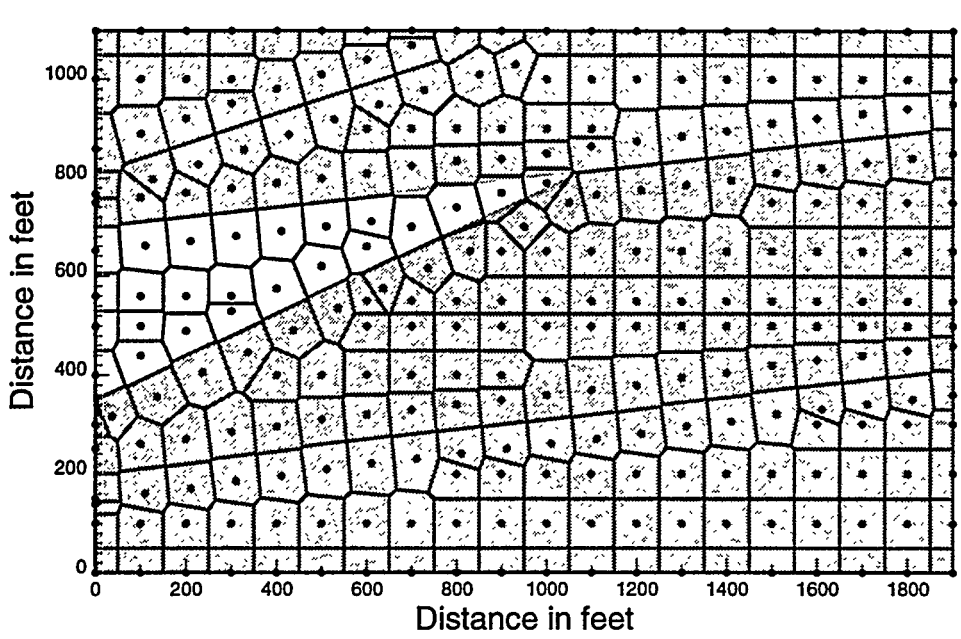

Figure 1.3: Voronoi Block Boundaries Aligned Along Bed Boundaries

A practical and easy way was proposed to generate the grids in the horizontal (bedding) plane by Palagi. The location of grid points is determined using modules. Voronoi blocks which conform to this distribution of grid points are then constructed. The Voronoi grid methods implemented previously have several limitations. These methods have been developed for heterogeneous but isotropic reservoirs and used only for the horizontal (bedding) plane. Variations in properties in the vertical (dip normal) direction are handled by dividing the reservoir into layers with the same horizontal grids used in all the layers. The algebraic approximation of flow equations for schemes using Voronoi grids, as used today, lack 3-D flexibility in modeling horizontal/inclined wells which may pass through layers of strongly varying properties. Heterogeneities, faults, local flow geometry, etc., which are not normally of two-dimensional nature cannot be modeled with the existing numerical schemes. The complex geology in Figure 1.3 (only a cross-section is shown) is an example where the existing numerical schemes are unsuccessful, but Voronoi grids are shown to represent very well the geological features in the figure.

One of the major factors which can't be ignored when dealing with vertical flow is the permeability anisotropy. Given a fine scale geostatistical realization of reservoir properties, the upscaling process to obtain coarse homogeneous grids may result in anisotropic and asymmetric permeability tensors which vary from block to block. The numerical approximation presented in this report is able to deal with this problem.

1.3 Mathematical Model for Voronoi Grids

Eq. 1.1 represents the application of the conservation law to an arbitrary component c in a control volume V with an external area A:

$$-\oint_A \sum_{p=1}^{N_p} \omega_{cp} \vec{v}_p \cdot \vec{n}\ dA = \frac{\partial}{\partial t} \int_V \sum_{p=1}^{N_p} \omega_{cp} S_p \phi\ dV \tag{1.1}$$

where

$$\vec{v}_p = -\bar{\bar{K}} \vec{\nabla} \Phi \tag{1.2}$$

$\bar{\bar{K}}$ is the permeability tensor. For a symmetric tensor the following relationship is true:

$$\bar{\bar{K}} \vec{\nabla}\, \Phi \cdot \vec{n} = \bar{\bar{K}} \vec{n} \cdot \vec{\nabla}\, \Phi \tag{1.3}$$

Our first method is based on a node centered finite difference approximation of the Eq. 1.1 which results in Eq. 1.4

$$\sum_{j=1}^{N_n} \sum_{p=1}^{N_p} (T \omega_{cp} \lambda_p)_{ij} (\Phi_{p,j} - \Phi_{p,i}) = \frac{V_{b,i}}{\Delta t} \sum_{p=1}^{N_p} [(\omega_{cp} S_p \phi)^{n+1} - (\omega_{cp} S_p \phi)^n]_i + \sum_{p=1}^{N_p} (\omega_{cp} q_p)_i^{n+1} \tag{1.4}$$

In the above equation N_n is number of neighbors of block i, N_p is number of phases in the system, T is transmissibility, ω_{cp} is product of mass fraction of component c (i.e. x_{cp}) in phase p and density of the phase, λ_p is mobility of phase p, $\Phi_{p,j}$ is potential in phase p at node j, $V_{b,i}$ is volume of block i, S_p is saturation of phase p, ϕ is porosity at node i and q_p is the source/sink term for node i. For simplicity, we will assume that x_{cp} is 1 and perform volume balance at standard conditions; the conservation equation Eq. 1.4 can then be written as (dropping the phase subscript p)

$$\sum_{j=1}^{N_n} (T\lambda)_{ij} (\Phi_j - \Phi_i) = \frac{V_{b,i}}{\Delta t} [(\frac{S\phi}{B})^{n+1} - (\frac{S\phi}{B})^n]_i + q_i^{n+1} \tag{1.5}$$

The LHS of Eq. 1.5 can also be put in the form

$$\sum_{j=1}^{N_n} \left(\lambda_{ij} \sum_{k=1}^{N_{nd}} (T_{jk}\, \Phi_k) \right) \tag{1.6}$$

where N_{nd} is the number of nodes whose potentials affect flow along connection j. For isotropic permeability and orthogonal grids a unique transmissibility term can be defined for each surface (of control volume V) which when multiplied with $(\Phi_j - \Phi_i)$ gives the flux across surface ij. The expression for T in such a case is given by:

$$T_{ij} = \left(\frac{A\, k}{D} \right)_{ij} \tag{1.7}$$

where A is the area open to flow, D is the distance between grid nodes and k_{ij} is the permeability between the i and j blocks. Methods for finding k_{ij} for an isotropic system are described by Palagi [2].

When permeability is an anisotropic tensor and/or grids are nonorthogonal then the potential difference $(\Phi_j - \Phi_i)$ also affects flow between some of the other surfaces. However, if the tensor is symmetric, i.e. Eq. 1.3 is true, then control volume surfaces can be oriented in a

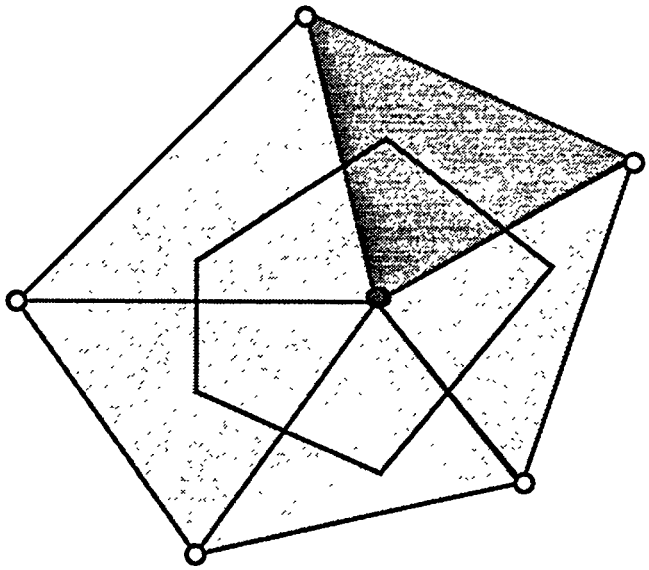

Figure 1.4: Generalized Pebi Grid Example

manner that a unique transmissibility can again be found so that potential difference between nodes across surface ij again determines flow only across that surface [4]. Heinemann [4] describes how to generate control volumes and expressions for T by using Eq. 1.3. The grids used in this method are popularly called generalized perpendicular bisector (GPEBI) grids. Figure 1.4 shows such a grid. Upstream weighting of mobilities can be easily used in such a scheme. However, the application becomes cumbersome when the principal axes of the permeability tensor change from block to block.

To construct GPEBI grids the region is first triangulated. Each triangle (Tetrahedra in 3D) is assumed to possess homogeneous properties. For small anisotropy this scheme may work quite well. However when the permeability becomes highly anisotropic, it may not be possible to define a control volume using the GPEBI approach. This is quite evident from the sequence of grids shown in Figure 1.5. As the value of k_z/k_x reduces it is observed that the circumcenters move towards the boundary of triangular element and when it crosses the boundary, the control volume boundaries can no longer be uniquely defined and they criss-cross each other. In our example, this occurs at $k_z/k_x = 0.2$, which can readily be appropriate to a real reservoir.

Other schemes (CVFE [5], see Figure 1.6) which maintain the flexibility of grids and do not run into the problem faced by GPEBI grids have been proposed, but it has been difficult to formulate them to use upstream weighting of phase mobilities.

Another fundamental disadvantage of both GPEBI and CVFE methods is in the estimation of block average saturations. Such block averaging may lead to numerically incorrect results when the triangles surrounding the grid node have strongly varying permeability values.

To overcome the above-mentioned problems, Voronoi grids are used in a new approach in the current study. It is assumed that properties inside each grid cell are homogeneous but may be anisotropic. The flow at a surface is constrained so that the velocity normal to the surface (i.e. in the direction of the connections) is the same on both sides of the

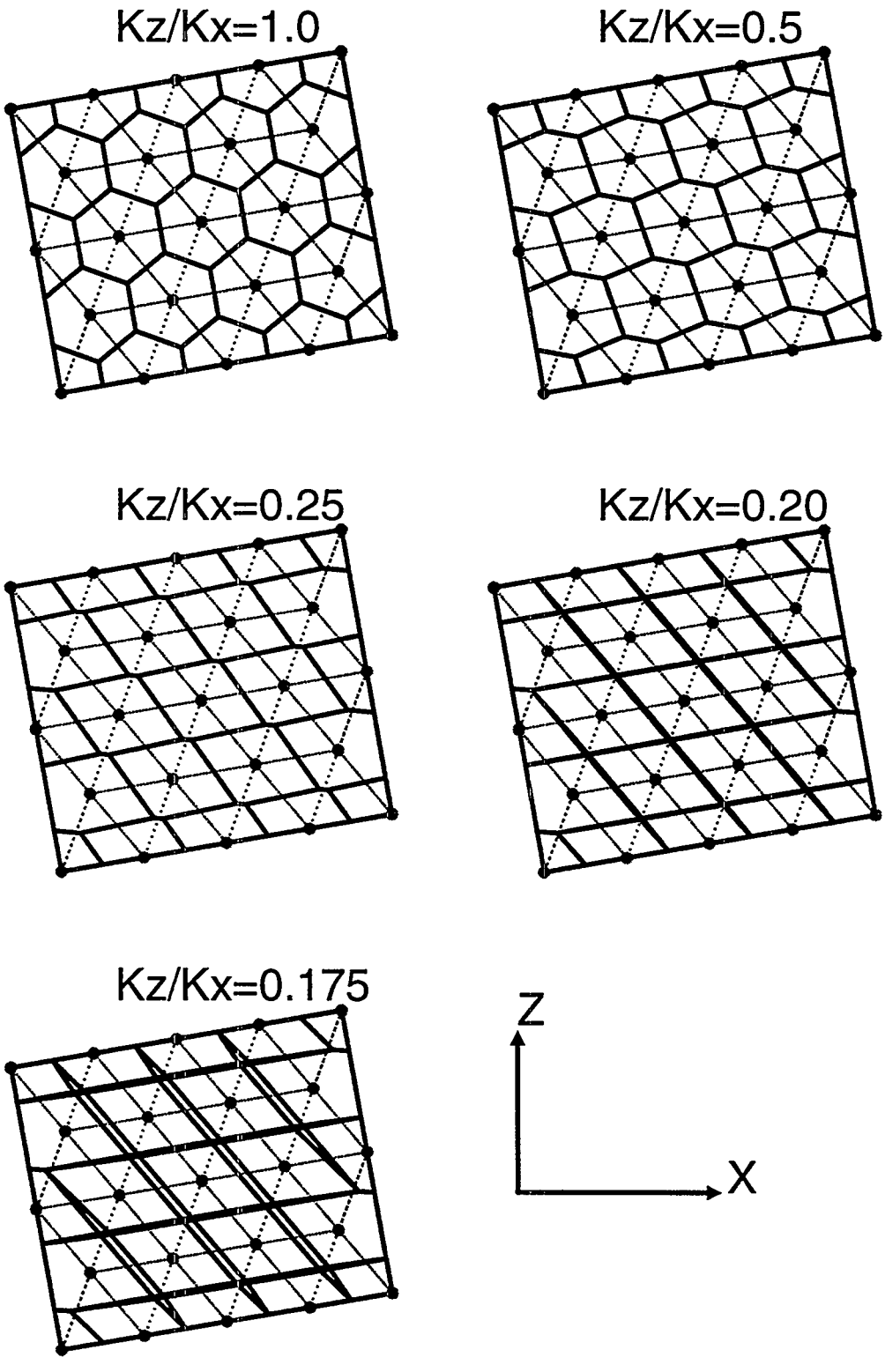

Figure 1.5: Generalized Pebi Grids

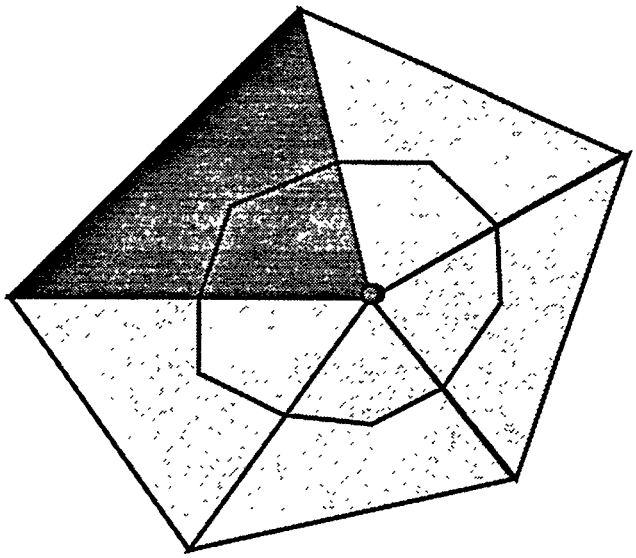

Figure 1.6: CVFE Grid

surface. Figure 1.7 shows 6 nodes and Voronoi blocks around those nodes. It is assumed that flow in $\triangle_{123}$ is dependent on the pressures at the nodes 1, 2 and 3 only. The $\triangle$ has three different permeability regions. A generalized harmonic averaging approach is used to compute internode transmissibility in the $\triangle$, subject to the above mentioned velocity constraints. The constraints give the following equation:

$$\begin{bmatrix} P_a \\ P_b \\ P_c \end{bmatrix} = \begin{bmatrix} R_{11} & R_{12} & R_{13} \\ R_{21} & R_{22} & R_{23} \\ R_{31} & R_{32} & R_{33} \end{bmatrix} \begin{bmatrix} P_1 \\ P_2 \\ P_3 \end{bmatrix} \tag{1.8}$$

After solving for pressures P_a, P_b and P_c and putting them into the flux equations one obtains the equation:

$$\begin{bmatrix} Q_a \\ Q_b \\ Q_c \end{bmatrix} = \begin{bmatrix} T_{a1} & T_{a2} & T_{a3} \\ T_{b1} & T_{b2} & T_{b3} \\ T_{c1} & T_{c2} & T_{c3} \end{bmatrix} \begin{bmatrix} P_1 \\ P_2 \\ P_3 \end{bmatrix} \tag{1.9}$$

Using the above equation the conservation equation for block i can be put in the form

$$\sum_{j=1}^{N_c} \left(\lambda_j \sum_{k=1}^{N_n} (T_{jk} P_k) \right)_i = \text{Accumulation} \tag{1.10}$$

Details of the derivation are given in the Appendix. The LHS of Eq. 1.10 corresponds to flow along all the connections associated with a grid node. Figure 1.8 shows a very simple example of nodes and the connections associated with the nodes. Advantage is taken of special features of this equation to simplify its computation in the C++ program which has been developed.

As is evident from Eq. 1.10 , in our formulation (as in the case of CVFE) flow at each connection does not depend only on fluid potentials at adjacent points. Because of this, it will take more time (as compared to a generalized PEBI grid [4]) to assemble the Jacobian matrix. But the structure of the Jacobian matrix is identical. Since, most of the

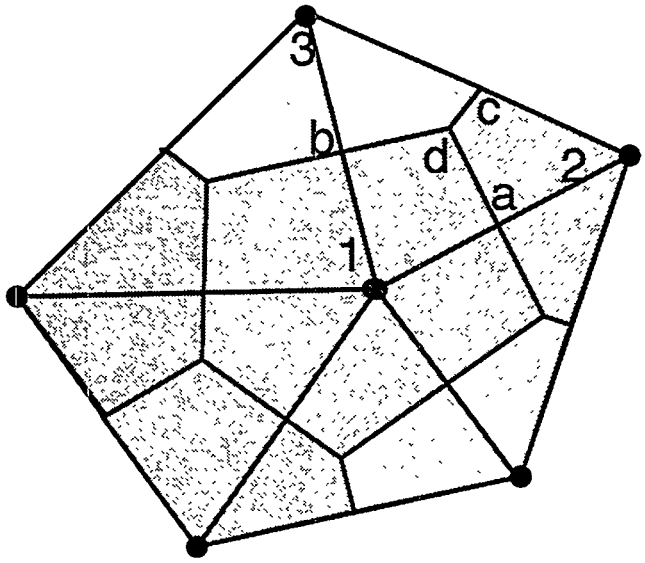

Figure 1.7: Voronoi Grid

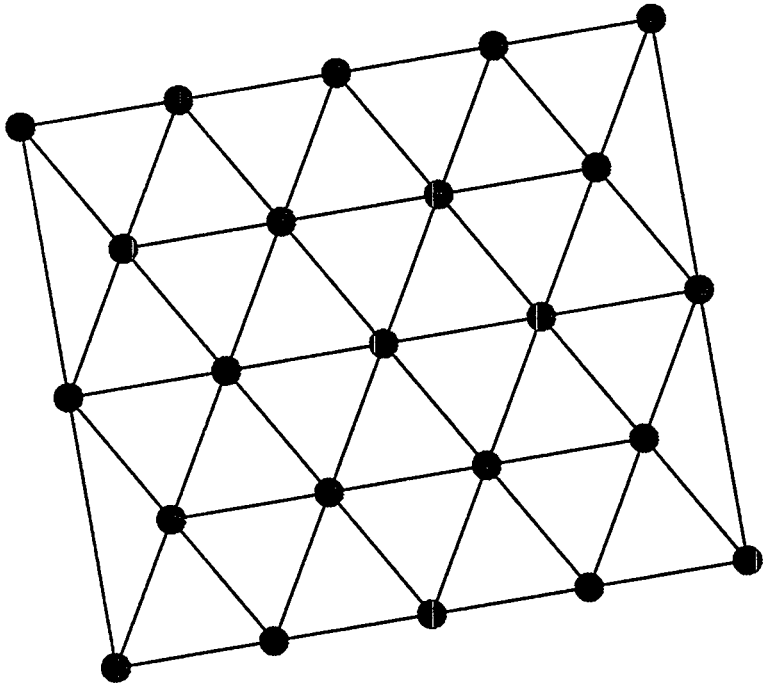

Figure 1.8: Connections Network

time (normally 80-90 %) in any simulation is taken by the iterative solver, the computer time of the current scheme will not increase significantly. Upstream evaluation of the mobility at any surface is based on the sign of the flux function

$$F = \sum_{k=1}^{N_n} T_{jk} P_k \tag{1.11}$$

a function which is a linear combination of the potentials affecting flow across that surface. As is evident from the detailed derivations shown in Appendix this scheme can be used for asymmetric permeability tensors as well. It also has no restriction on the angles of the tetrahedra generated by a triangulation code, other than the requirement that the triangulation be Delaunay.

1.4 Generation of Voronoi Grids

Palagi [4] presented a Voronoi grid generation scheme on a plane. The scheme used to generate the grids in three-dimension is presented in this section. The C++ code which implements this scheme is now complete and is being optimized.

For a set $S = \{p_1, p_2, ..., p_n\}$ of n points in Euclidean 3-space, R^3, the associated Voronoi diagram is a sequence $V(p_1)$, $V(p_2)$, ..., $V(p_n)$ of convex polyhedra covering 3-space, where $V(p_i)$ consists of all points of 3-space having p_i as the nearest point in the set S (see Avis and Bhattacharya [6]). Thus

$$V(p_i) = \{x \in R^d : d(x, p_i) \leq d(x, p_j), \qquad j = 1, 2, ..., n\} \tag{1.12}$$

where $d(x, p_i)$ denotes the Euclidean distance between the points x and p_i.

As a starting point, the Delaunay triangulation of a set of points is constructed using a special code **qhull** [7]. The set of tetrahedra thus obtained is used to generate sets of tetra–faces, tetra–edges and tetra–nodes. These objects contain all the connectivity information, e.g., a tetra–edge object contains the number and id's of tetrahedra it is connected to, the number and id's of tetra–faces it is connected to and the id of the two nodes at the end of the tetra–edge.

One Voronoi block is associated with each node. The faces of the block lie on the perpendicular bisector (PEBI) planes of each of the edges connected to the node. The intersections of the PEBI plane of an edge, with the PEBI planes of the other edges connected to the node, completely describe the geometry of the face on that edge. In the interior of the domain these intersections are the circumcenters of the tetrahedra connected to the edge. However, when any of these circumcenters, as well as the centers of the tetra–faces associated with the edge lie outside the boundary of the reservoir, then the Voronoi block faces formed have to be adjusted. This is done by finding the intersection of the PEBI planes with the boundary tetra faces and the boundary tetra edges. Figure 1.9 shows the generation of Voronoi Blocks in 3-D. The problem starts with allocation of 9 points in both the top and bottom planes. The figure shows the triangulation, Voronoi grid edges and faces from three viewpoints. A simple case of Voronoi grids in 3D is shown in Figure 1.10. The figure shows grids around 6 nodes. All the edges of the resulting grids are shown in the left figure. The Voronoi block surfaces are shown in the figure on the right. Voronoi blocks around a

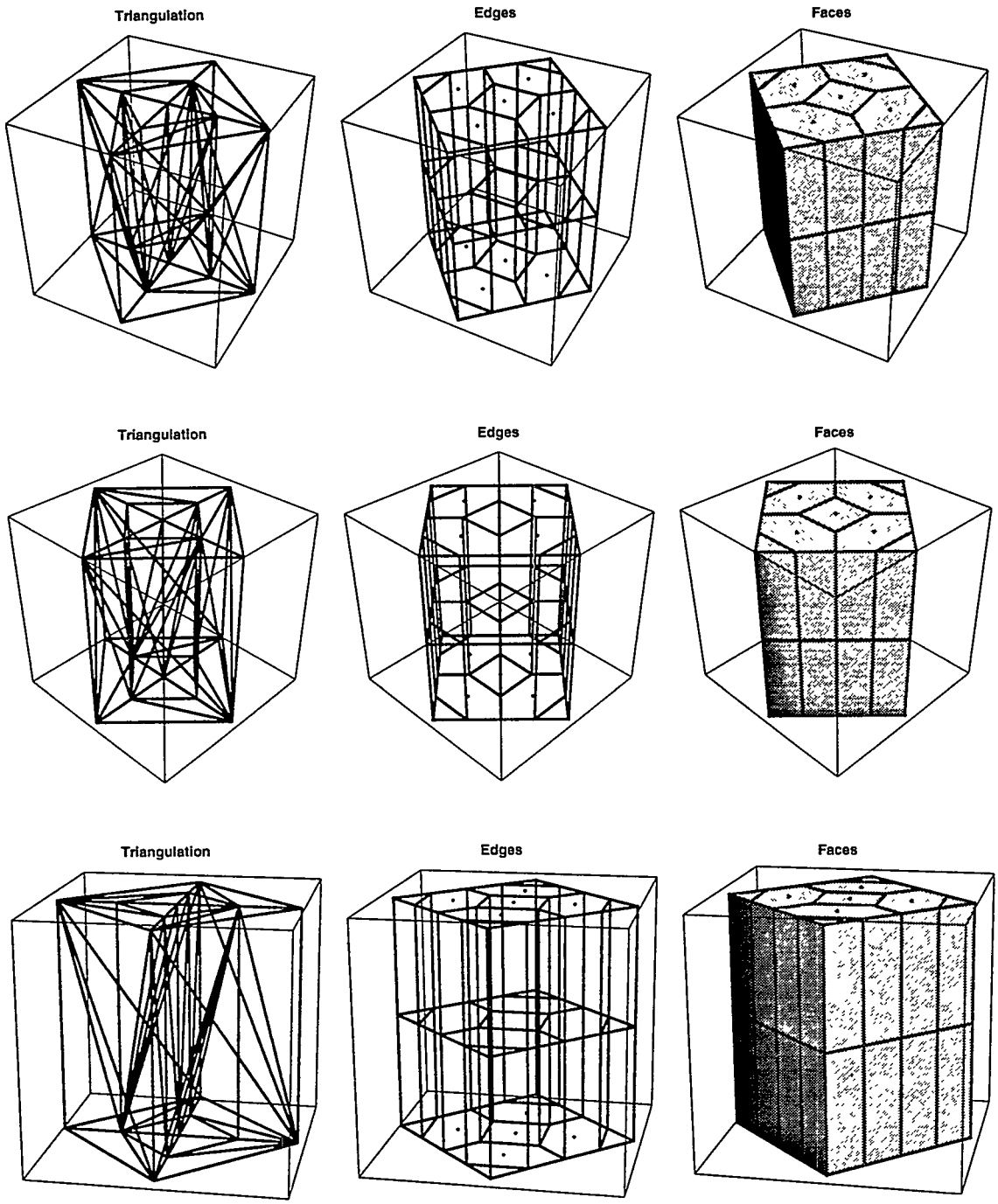

Figure 1.9: Triangulation, Voronoi Grid Edges and Faces in 3-D from Three Viewpoints

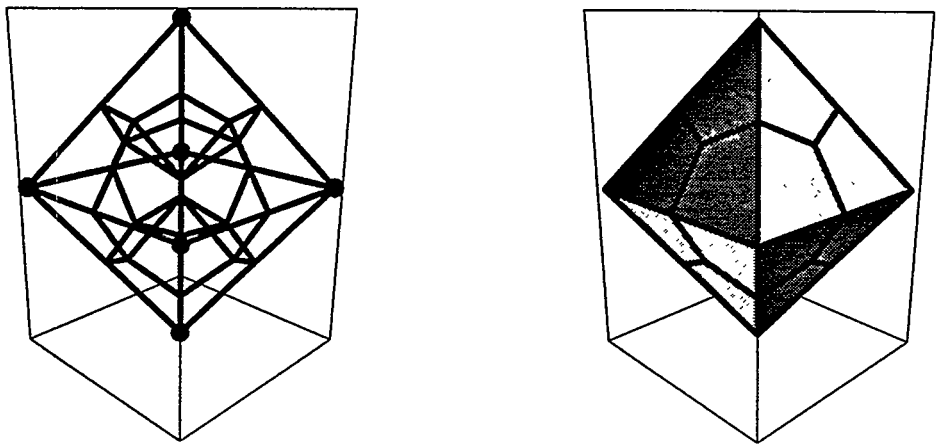

Figure 1.10: Example of 3D Voronoi Grids

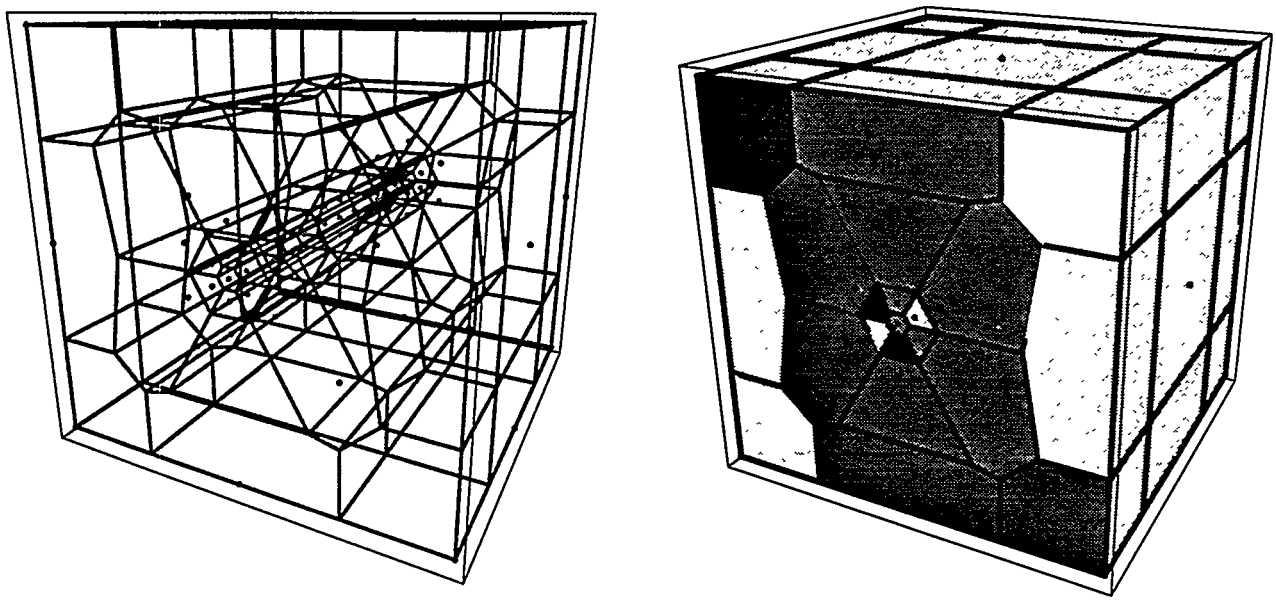

Figure 1.11: Voronoi Grids Around Horizontal Well

horizontal well are shown in Figure 1.11. The grids in the near-wellbore region allow radial flow. The surface appearance of the grids is also shown in the figure.

A challenge in this work is to align the Voronoi polyhedra along layers, faults, horizontal wells, etc. Figures 1.12 and 1.13 show in 2D the alignment of Voronoi Blocks along major reservoir features, such as layers, faults and horizontal/deviated wells. The actual grid in 3D can have polygonal shapes around the well axis which approximate cylindrical flows, e.g., hexagons. Such grids are shown around the deviated well. Figure 1.13 shows how the gridding can be efficiently done for dual-lateral wells drilled to drain from two different layers. The base Delaunay triangulation of the nodes in Figure 1.12 are given in Figure 1.14. To generate the Voronoi polygons in Figures 1.12 and 1.13, the nodes were placed in a direction normal to the layer and fault boundaries on both sides and equidistant from the boundaries. Thus it was possible to achieve the objective of aligning Block boundaries along layer boundaries. This results in better estimates of homogeneous properties inside a block.

1.5 Algebraic Approximation Scheme

A second algebraic scheme [8] which uses tetrahedra in 3D or triangles in 2-D as control volumes is described below. Figure 1.15 shows two such triangles for the 2D-case with a common interface *bc*.

In this face-centered scheme flux continuity is honored across each face. Flux across bc is

$$Q_{bc_p} = -h_{bc} \int_b^c \vec{v}_p \cdot \vec{n}\, dL = -A\,(\vec{v}_p \cdot \vec{n}) \tag{1.13}$$

Where velocity is given by

$$\vec{v}_p = -\lambda_{bc_p}\,[\bar{\bar{k}}\,\vec{\nabla}\Phi] \tag{1.14}$$

$$\vec{v}_p = -\lambda_{bc_p} \begin{pmatrix} k_{xx}\,\Phi_x + & k_{xy}\,\Phi_y \\ k_{yx}\,\Phi_x + & k_{yy}\,\Phi_y \end{pmatrix} \tag{1.15}$$

Φ inside $\triangle$ is obtained from a linear interpolation of face pressures. Hence gradients are given by:

$$\Phi_x = A_{11}(\Phi_1 - \Phi_3) + A_{12}(\Phi_2 - \Phi_3) \tag{1.16}$$

$$\Phi_y = A_{21}(\Phi_1 - \Phi_3) + A_{22}(\Phi_2 - \Phi_3) \tag{1.17}$$

Putting the expression for gradients in Eq. 1.15 and the resulting expression for velocity in Eq. 1.13, flux across *bc* in $\triangle_1$ is given by

$$Q^1_{bc_p} = \lambda_{bc_p}\,[T_{13}(\Phi_1 - \Phi_3) + T_{23}(\Phi_2 - \Phi_3)] \tag{1.18}$$

and flux across *bc* in $\triangle_2$ is given by

$$Q^2_{bc_p} = \lambda_{bc_p}\,[T_{34}(\Phi_3 - \Phi_4) + T_{35}(\Phi_3 - \Phi_5)] \tag{1.19}$$

The T terms in the Eq. 1.18 and 1.19 are

$$\begin{aligned} T_{13} \;&= n_x(k_{xx_1}A_{11} + k_{xy_1}A_{21}) + \\ &\quad\; n_y(k_{yx_1}A_{11} + k_{yy_1}A_{21}) \end{aligned} \tag{1.20}$$

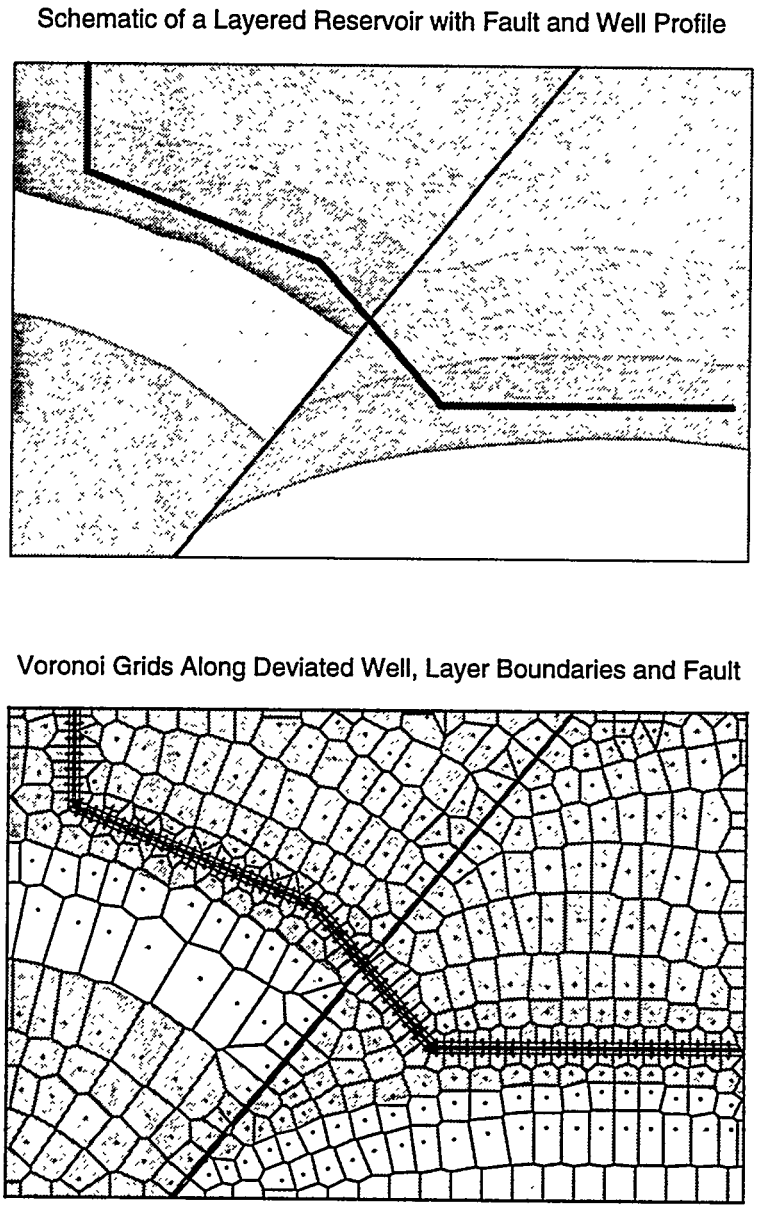

Figure 1.12: Voronoi Grids for Layered Reservoir with Fault and Horizontal Well

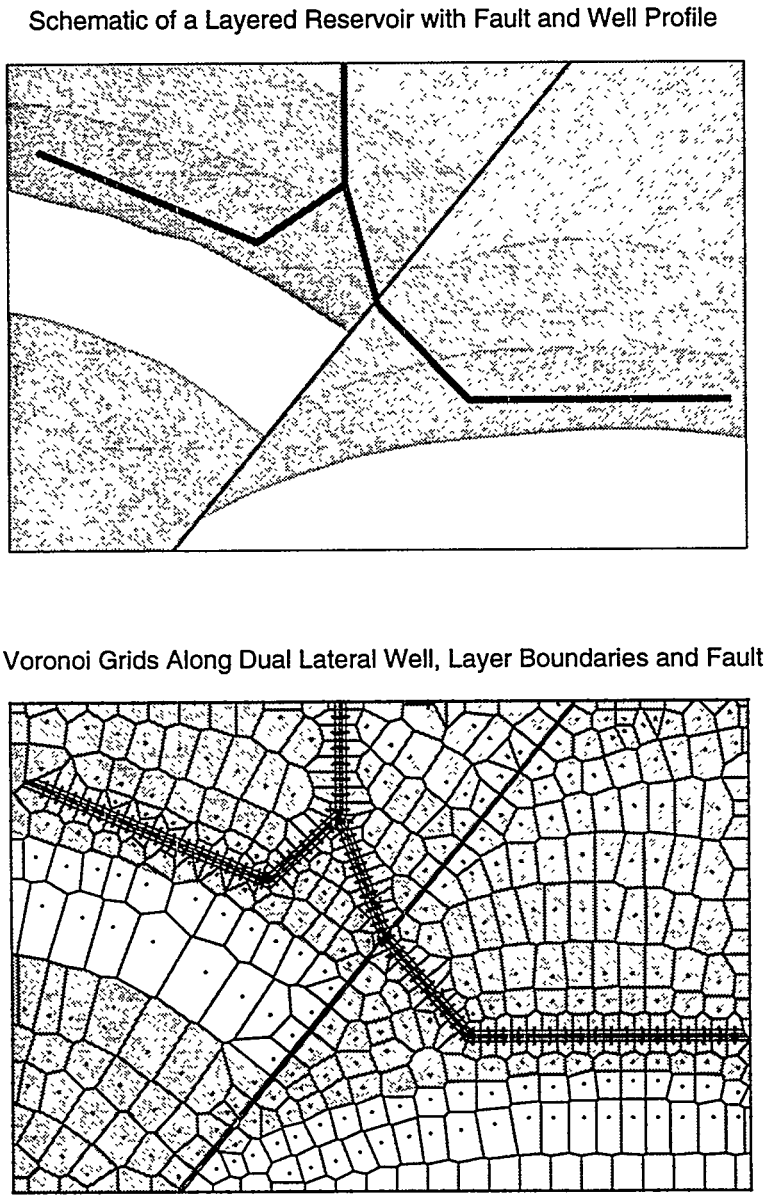

Figure 1.13: Voronoi Grids for Layered Reservoir with Fault and a Dual Lateral Horizontal Well

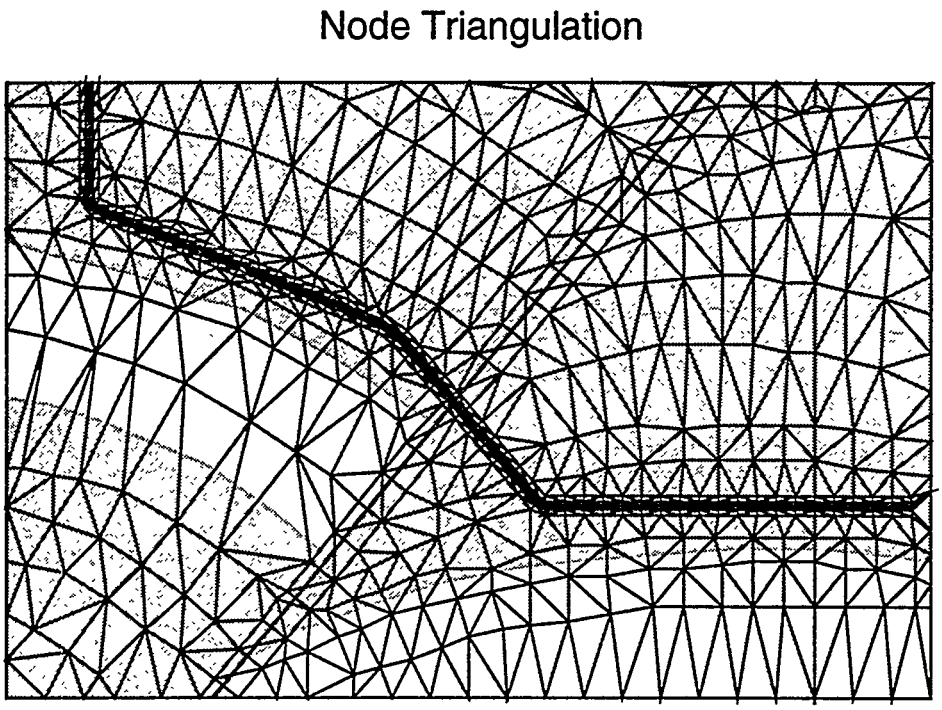

Figure 1.14: Delaunay Triangulation for Figure 1.12

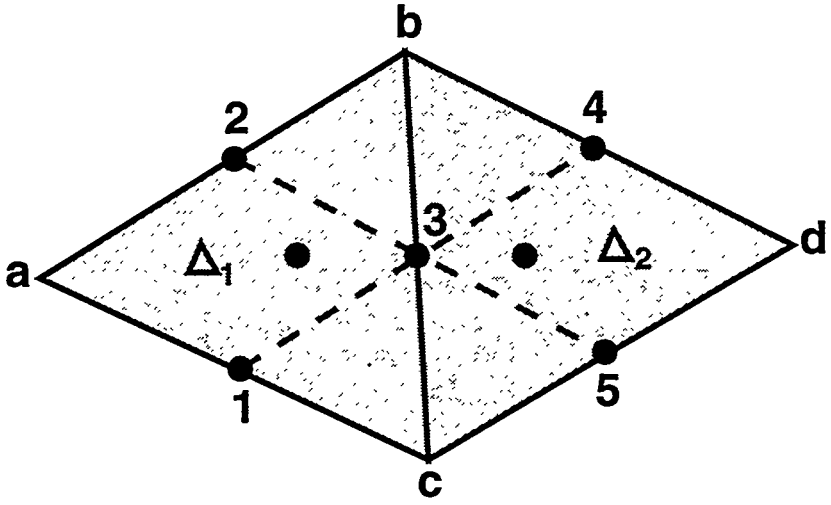

Figure 1.15: Description of Algebraic Approximation Formulation

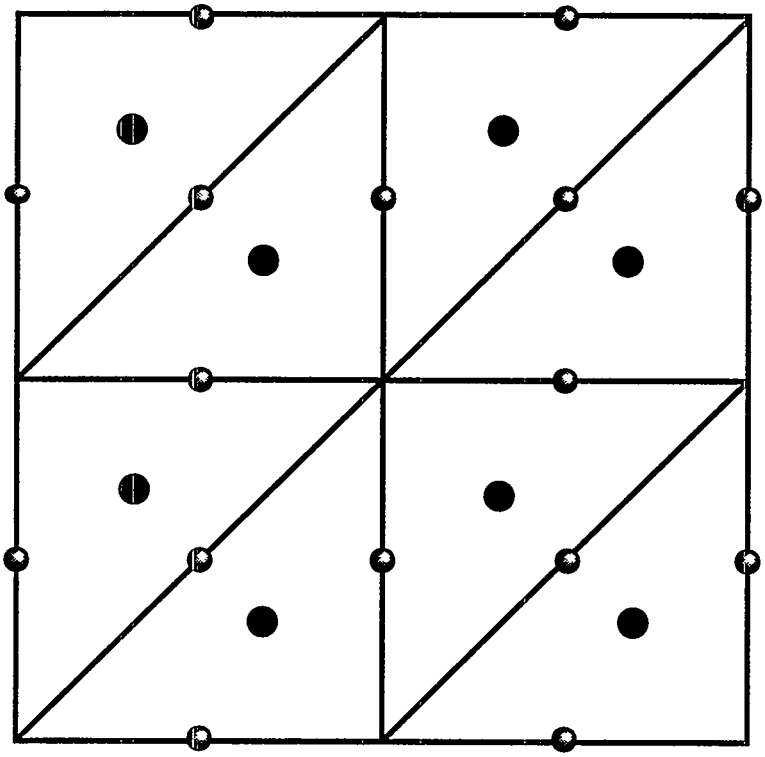

Figure 1.16: Algebraic Approximation: An Example

$$\begin{aligned} T_{23} &= n_x(k_{xx_1}A_{12} + k_{xy_1}A_{22}) + \\ &\quad n_y(k_{yx_1}A_{12} + k_{yy_1}A_{22}) \end{aligned} \tag{1.21}$$

Equating the fluxes in the two triangles gives rise to a flux continuity equation:

$$\sum_{p=1}^{N_p} Q^1_{bc_p} + \sum_{p=1}^{N_p} Q^2_{bc_p} = 0 \tag{1.22}$$

which leads to a 5 point algebraic approximation for potentials involving $\Phi_1, \ldots, \Phi_5$. The Material Balance Equation for each $\triangle$ in two–phase flow is given by

$$\sum_{i=1}^{3} Q^{n+1}_{p_{i,j}} = \frac{V_j}{\Delta t}\left[\left(\frac{\phi S_p}{B_p}\right)^{n+1} - \left(\frac{\phi S_p}{B_p}\right)^{n}\right]_j \tag{1.23}$$

where ϕ, S_p, and B_p are at the barycenter.

Figure 1.16 shows an example of such a grid. There are 8 triangles and 16 faces. The unknowns in the system are 16 pressures and 8 saturations (2 phase problem). There are 16 flux continuity equations and 8 material balance equations. The flux continuity equations are 5 point in 2-D and 7-point in 3-D. The material balance equations are 9 point in 2-D and 16 point in 3-D. This scheme also handles a full and asymmetric permeability tensor. Compared to this scheme, a regular Cartesian grid will have 9 points in 2-D and 27 points in 3-D. The Cartesian scheme is conceptually much simpler, but it has poor ability to accurately deal with spatially complex reservoir properties and varying well trajectories. The location of the pressure nodes for the Voronoi grid scheme and the triangle scheme are shown in Figure 1.17. The circles denote Voronoi pressure nodes while the triangles denote the triangular control volume pressure nodes.

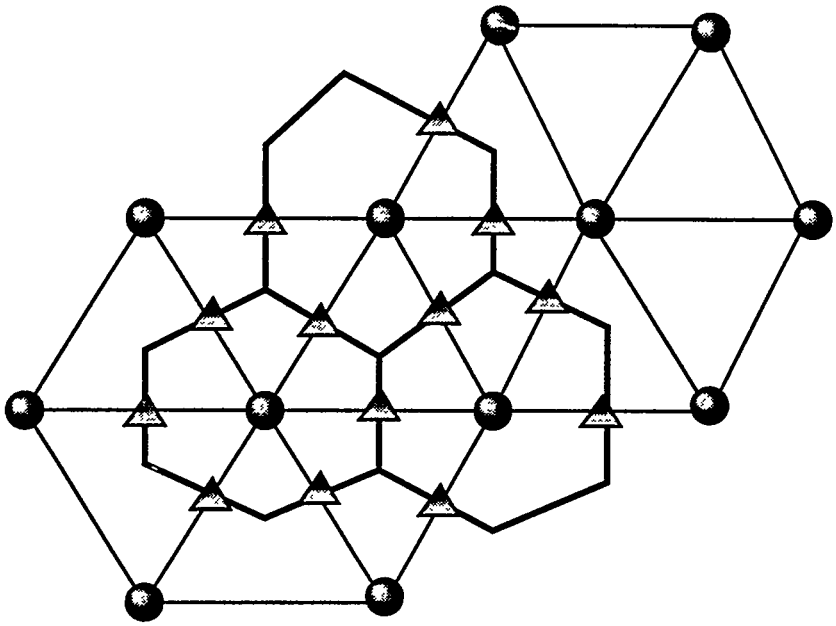

Figure 1.17: Pressure Nodes for Voronoi and FCD Schemes

1.6 Status of Fluid Flow Simulation Code

C++ code to simulate 2D flow in Voronoi grids is complete. Number of test cases have been run to debug the code. Test runs with Cartesian grids (which can be handled by Eclipse and Imex) give results identical to Eclipse and Imex. Cases with full and anisotropic tensors have also been tested. Code to simulate 3-D flow in Voronoi grids is now being written and is expected to be complete in three more months. The numerical stability of triangular/tetrahedral control volume scheme is still to be tested.

References

1. Pedrosa, O.A.: Use of Hybrid Grid in Reservoir simulation, Ph.D. Dissertation, Stanford University, December 1984.

2. Palagi, C.L.: Generation and Application of Voronoi Grids to Model flow in Heterogeneous Reservoirs, Ph.D. Dissertation, Stanford University, May 1992.

3. Bird, R.B., Stewart, W.E. and Lightfoot, E.N.: *Transport Phenomena*, John Wiley & Sons, New York (1960).

4. Heinemann, Z.E.: Advances in Gridding Techniques, Fifth International Forum on Reservoir Simulation, Dec 10-14, 1994,Muscat, Oman.

5. Fung, L.S, Hiebert, A.D and Nghiem, Long: Reservoir Simulation with a Control-Volume Finite-Element Method, Paper SPE 21224 presented at 11th SPE Symposium

on Reservoir Simulation, Anaheim, California, February 17-20, 1991.

6. Avis D. and Bhattacharya, B.K: Algorithms for computing d-dimensional Voronoi diagrams and their duals, in: F.P. Preprate ed., Advances in Computing Research (1983), 1, JAI Press,159-180.

7. **qhull** (1993), The Geometry Center, University of Minnesota.

8. Michael J. King, BP International, Ltd., Sunbury-On-Thames, UK: Personal Communication (1994).

Appendix: Derivation of Interblock Transmissibility for Voronoi Grids

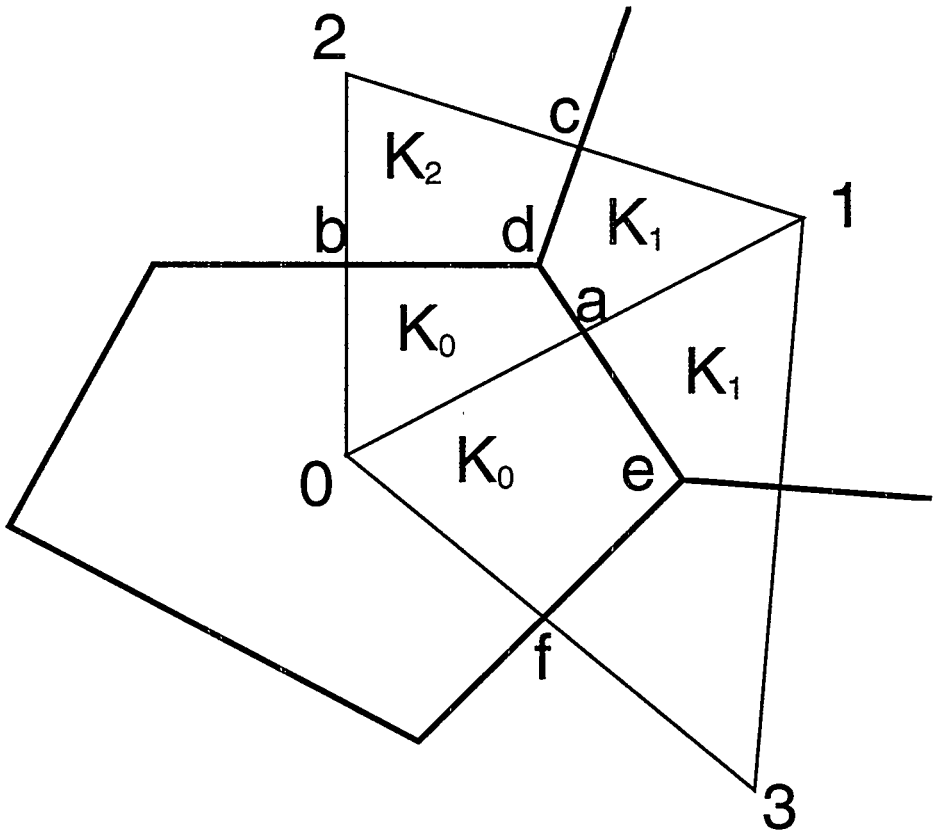

Figure 1.18: Derivation of Generalized Harmonic Averaging

Refer to Figure 1.18 for the derivation of interblock transmissibility for Voronoi grids. Flow rate across connection a–d is

$$\begin{aligned} Q_{0a} &= -\int_{ad} \vec{V}_0 \cdot \vec{n}_{ad}\, dL = -A_{ad}\vec{V}_0 \cdot \vec{n}_{ad} \\ &= A_{ad}\left[V_{0x}n_{x_{ad}} + V_{0y}n_{y_{ad}}\right] \end{aligned} \tag{1.24}$$

A positive value of Q signifies flow into the block while a negative value signifies flow out of the block.
Single phase velocity in region 0 is estimated by:

$$\begin{aligned} \vec{V}_0 &= -[\bar{\bar{k}}_0 \vec{\nabla} P_0] \\ &= -\begin{bmatrix} k_{xx_0} P_{x_0} + k_{xy_0} P_{y_0} \\ k_{yx_0} P_{x_0} + k_{yy_0} P_{y_0} \end{bmatrix} \end{aligned} \tag{1.25}$$

To estimate the pressure gradients in the above equation we assume that pressure varies linearly in region 0. Hence we have the equations

$$\begin{aligned} P_a &= P_0 + (x_a - x_0) P_{x_0} + (y_a - y_0) P_{y_0} \\ P_b &= P_0 + (x_b - x_0) P_{x_0} + (y_b - y_0) P_{y_0} \end{aligned} \tag{1.26}$$

Which gives

$$\begin{aligned} \begin{bmatrix} P_{x_0} \\ P_{y_0} \end{bmatrix} &= \begin{bmatrix} (x_a - x_0) & (y_a - y_0) \\ (x_b - x_0) & (y_b - y_0) \end{bmatrix}^{-1} \begin{bmatrix} P_a - P_0 \\ P_b - P_0 \end{bmatrix} \\ &= \frac{1}{D_0} \begin{bmatrix} (y_b - y_0) & (y_0 - y_a) \\ (x_0 - x_b) & (x_a - x_0) \end{bmatrix} \begin{bmatrix} P_a - P_0 \\ P_b - P_0 \end{bmatrix} \end{aligned} \tag{1.27}$$

where

$$D_0 = x_0(y_a - y_b) + x_a(y_b - y_0) + x_b(y_0 - y_a) \tag{1.28}$$

Hence we can write Eq. 1.27 as

$$\begin{bmatrix} P_{x_0} \\ P_{y_0} \end{bmatrix} = \begin{bmatrix} A_{00} & A_{01} \\ A_{10} & A_{11} \end{bmatrix} \begin{bmatrix} P_a - P_0 \\ P_b - P_0 \end{bmatrix} \tag{1.29}$$

In a similar manner we get expressions for regions 1 and 2. **For region 1**

$$\begin{aligned} \vec{V}_1 &= -[\bar{\bar{k}}_1 \vec{\nabla} P_1] \\ &= -\begin{bmatrix} k_{xx_1} P_{x_1} + k_{xy_1} P_{y_1} \\ k_{yx_1} P_{x_1} + k_{yy_1} P_{y_1} \end{bmatrix} \end{aligned} \tag{1.30}$$

$$\begin{aligned} P_a &= P_1 + (x_a - x_1) P_{x_1} + (y_a - y_1) P_{y_1} \\ P_c &= P_1 + (x_c - x_1) P_{x_1} + (y_c - y_1) P_{y_1} \end{aligned} \tag{1.31}$$

Hence

$$\begin{aligned} \begin{bmatrix} P_{x_1} \\ P_{y_1} \end{bmatrix} &= \begin{bmatrix} (x_a - x_1) & (y_a - y_1) \\ (x_c - x_1) & (y_c - y_1) \end{bmatrix}^{-1} \begin{bmatrix} P_a - P_1 \\ P_c - P_1 \end{bmatrix} \\ &= \frac{1}{D_1} \begin{bmatrix} (y_c - y_1) & (y_1 - y_a) \\ (x_1 - x_c) & (x_a - x_1) \end{bmatrix} \begin{bmatrix} P_a - P_1 \\ P_c - P_1 \end{bmatrix} \end{aligned} \tag{1.32}$$

where

$$D_1 = x_1(y_a - y_c) + x_a(y_c - y_1) + x_c(y_1 - y_a) \tag{1.33}$$

Hence we can write Eq. 1.32 as

$$\begin{bmatrix} P_{x_1} \\ P_{y_1} \end{bmatrix} = \begin{bmatrix} B_{00} & B_{01} \\ B_{10} & B_{11} \end{bmatrix} \begin{bmatrix} P_a - P_1 \\ P_c - P_1 \end{bmatrix} \tag{1.34}$$

For region 2 the equations are:

$$\begin{aligned} \vec{V}_2 &= -[\bar{\bar{k}}_2 \vec{\nabla} P_2] \\ &= -\begin{bmatrix} k_{xx_2} P_{x_2} + k_{xy_2} P_{y_2} \\ k_{yx_2} P_{x_2} + k_{yy_2} P_{y_2} \end{bmatrix} \end{aligned} \tag{1.35}$$

$$\begin{aligned} P_b &= P_2 + (x_b - x_2)P_{x_2} + (y_b - y_2)P_{y_2} \\ P_c &= P_2 + (x_c - x_2)P_{x_2} + (y_c - y_2)P_{y_2} \end{aligned} \tag{1.36}$$

Hence

$$\begin{aligned} \begin{bmatrix} P_{x_2} \\ P_{y_2} \end{bmatrix} &= \begin{bmatrix} (x_b - x_2) & (y_b - y_2) \\ (x_c - x_2) & (y_c - y_2) \end{bmatrix}^{-1} \begin{bmatrix} P_b - P_2 \\ P_c - P_2 \end{bmatrix} \\ &= \frac{1}{D_2} \begin{bmatrix} (y_c - y_2) & (y_2 - y_b) \\ (x_2 - x_c) & (x_b - x_2) \end{bmatrix} \begin{bmatrix} P_b - P_2 \\ P_c - P_2 \end{bmatrix} \end{aligned} \tag{1.37}$$

where

$$D_2 = x_2(y_b - y_c) + x_b(y_c - y_2) + x_c(y_2 - y_b) \tag{1.38}$$

Hence we can write Eq. 1.36 as

$$\begin{bmatrix} P_{x_2} \\ P_{y_2} \end{bmatrix} = \begin{bmatrix} C_{00} & C_{01} \\ C_{10} & C_{11} \end{bmatrix} \begin{bmatrix} P_b - P_2 \\ P_c - P_2 \end{bmatrix} \tag{1.39}$$

We thus have the following equations for the gradient:

$$\begin{aligned} P_{x_0} &= A_{00}(P_a - P_0) + A_{01}(P_b - P_0) \\ P_{y_0} &= A_{10}(P_a - P_0) + A_{11}(P_b - P_0) \\ P_{x_1} &= B_{00}(P_a - P_1) + B_{01}(P_c - P_1) \\ P_{y_1} &= B_{10}(P_a - P_1) + B_{11}(P_c - P_1) \\ P_{x_2} &= C_{00}(P_b - P_2) + C_{01}(P_c - P_2) \\ P_{y_2} &= C_{10}(P_b - P_2) + C_{11}(P_c - P_2) \end{aligned} \tag{1.40}$$

We want velocities normal to the interfaces to match at the points a, b and c. Hence we form three constraint equations:

At a:

$$\vec{V_0} \cdot \vec{n}_{ad} = \vec{V_1} \cdot \vec{n}_{ad} \tag{1.41}$$

where $\vec{n}_{ad}$ is outward normal with respect to point 0 on the face *ad*. Expanding the above equation we get:

$$(V_{x_0} - V_{x_1}) n_{x_{ad}} + (V_{y_0} - V_{y_1}) n_{y_{ad}} = 0 \tag{1.42}$$

and putting in the terms for the velocities we get

$$\begin{aligned}
n_{x_{ad}} [k_{xx_0} \, (A_{00} \, (P_a - P_0) + A_{01} \, (P_b - P_0)) + \\
k_{xy_0} \, (A_{10} \, (P_a - P_0) + A_{11} \, (P_b - P_0)) - \\
k_{xx_1} \, (B_{00} \, (P_a - P_1) + B_{01} \, (P_c - P_1)) - \\
k_{xy_1} \, (B_{10} \, (P_a - P_1) + B_{11} \, (P_c - P_1))] + \\
n_{y_{ad}} [k_{yx_0} \, (A_{00} \, (P_a - P_0) + A_{01} \, (P_b - P_0)) + \\
k_{yy_0} \, (A_{10} \, (P_a - P_0) + A_{11} \, (P_b - P_0)) - \\
k_{yx_1} \, (B_{00} \, (P_a - P_1) + B_{01} \, (P_c - P_1)) - \\
k_{yy_1} \, (B_{10} \, (P_a - P_1) + B_{11} \, (P_c - P_1))] = 0
\end{aligned} \tag{1.43}$$

We now arrange the above expression in terms of the coefficients of P_a, P_b, P_c, P_0 and P_1. Coefficient of P_a is:

$$\begin{aligned}
M_{0a} = n_{x_{ad}} (A_{00} \, k_{xx_0} - B_{00} \, k_{xx_1} + A_{10} \, k_{xy_0} - B_{10} \, k_{xy_1}) + \\
n_{y_{ad}} (A_{00} \, k_{yx_0} - B_{00} \, k_{yx_1} + A_{10} \, k_{yy_0} - B_{10} \, k_{yy_1})
\end{aligned} \tag{1.44}$$

Coefficient of P_b is:

$$M_{0b} = (A_{01} \, k_{xx_0} \, n_{x_{ad}} + A_{11} \, k_{xy_0} \, n_{x_{ad}} + A_{01} \, k_{yx_0} \, n_{y_{ad}} + A_{11} \, k_{yy_0} \, n_{y_{ad}}) \tag{1.45}$$

Coefficient of P_c is:

$$M_{0c} = -B_{01} \, k_{xx_1} \, n_{x_{ad}} - B_{11} \, k_{xy_1} \, n_{x_{ad}} - B_{01} \, k_{yx_1} \, n_{y_{ad}} - B_{11} \, k_{yy_1} \, n_{y_{ad}} \tag{1.46}$$

Coefficient ofP_0 is:

$$\begin{aligned}
M_{00} = n_{x_{ad}} (-A_{00} \, k_{xx_0} - A_{01} \, k_{xx_0} - A_{10} \, k_{xy_0} - A_{11} \, k_{xy_0}) \\
+ n_{y_{ad}} (-A_{00} \, k_{yx_0} - A_{01} \, k_{yx_0} - A_{10} \, k_{yy_0} - A_{11} \, k_{yy_0})
\end{aligned} \tag{1.47}$$

Coefficient of P_1 is:

$$\begin{aligned}
M_{01} = n_{x_{ad}} (B_{00} \, k_{xx_1} + B_{01} \, k_{xx_1} + B_{10} \, k_{xy_1} + B_{11} \, k_{xy_1}) \\
+ n_{y_{ad}} (+B_{00} \, k_{yx_1} + B_{01} \, k_{yx_1} + B_{10} \, k_{yy_1} + B_{11} \, k_{yy_1})
\end{aligned} \tag{1.48}$$

Coefficient of P_2 is $M_{02} = 0.0$:

At b:

$$\vec{V_0} \cdot \vec{n}_{bd} = \vec{V_2} \cdot \vec{n}_{bd} \tag{1.49}$$

where $\vec{n}_{bd}$ is outward normal with respect point 0 on the face *bd*. Expanding the above equation we get:

$$(V_{x_0} - V_{x_2}) n_{x_{bd}} + (V_{y_0} - V_{y_2}) n_{y_{bd}} = 0 \tag{1.50}$$

and putting the terms for the velocities we get

$$\begin{aligned} & n_{x_{bd}}(k_{xx_0}(A_{00}(P_a-P_0)+A_{01}(P_b-P_0))+k_{xy_0}(A_{10}(P_a-P_0)+A_{11}(P_b-P_0))- \\ & \quad k_{xx_2}(C_{00}(P_b-P_2)+C_{01}(P_c-P_2))-k_{xy_2}(C_{10}(P_b-P_2)+C_{11}(P_c-P_2)))+ \\ & n_{y_{bd}}(k_{yx_0}(A_{00}(P_a-P_0)+A_{01}(P_b-P_0))+k_{yy_0}(A_{10}(P_a-P_0)+A_{11}(P_b-P_0))- \\ & \quad k_{yx_2}(C_{00}(P_b-P_2)+C_{01}(P_c-P_2))-k_{yy_2}(C_{10}(P_b-P_2)+C_{11}(P_c-P_2)))=0 \end{aligned} \quad (1.51)$$

We now arrange the above expression in terms of the coefficients of P_a, P_b, P_c, P_0 and P_1.
Coefficient of P_a is:

$$M_{1a} = n_{x_{bd}}(A_{00}\,k_{xx_0} + A_{10}\,k_{xy_0}) + n_{y_{bd}}(A_{00}\,k_{yx_0} + A_{10}\,k_{yy_0}) \quad (1.52)$$

Coefficient of P_b is:

$$\begin{aligned} M_{1b} = {} & n_{x_{bd}}(A_{01}\,k_{xx_0} - C_{00}\,k_{xx_2} + A_{11}\,k_{xy_0} - C_{10}\,k_{xy_2}) + \\ & n_{y_{bd}}(A_{01}\,k_{yx_0} - C_{00}\,k_{yx_2} + A_{11}\,k_{yy_0} - C_{10}\,k_{yy_2}) \end{aligned} \quad (1.53)$$

Coefficient of P_c is:

$$M_{1c} = -C_{01}\,k_{xx_2}\,n_{x_{bd}} - C_{11}\,k_{xy_2}\,n_{x_{bd}} - C_{01}\,k_{yx_2}\,n_{y_{bd}} - C_{11}\,k_{yy_2}\,n_{y_{bd}} \quad (1.54)$$

Coefficient ofP_0 is:

$$\begin{aligned} M_{10} = {} & n_{x_{bd}}(-A_{00}\,k_{xx_0} - A_{01}\,k_{xx_0} - A_{10}\,k_{xy_0} - A_{11}\,k_{xy_0}) + \\ & n_{y_{bd}}(-A_{00}\,k_{yx_0} - A_{01}\,k_{yx_0} - A_{10}\,k_{yy_0} - A_{11}\,k_{yy_0}) \end{aligned} \quad (1.55)$$

Coefficient of P_1 is $M_{11} = 0.0$;
Coefficient of P_2 is:

$$\begin{aligned} M_{12} = {} & n_{x_{bd}}(C_{00}\,k_{xx_2} + C_{01}\,k_{xx_2} + C_{10}\,k_{xy_2} + C_{11}\,k_{xy_2}) + \\ & n_{y_{bd}}(C_{00}\,k_{yx_2} + C_{01}\,k_{yx_2} + C_{10}\,k_{yy_2} + C_{11}\,k_{yy_2}) \end{aligned} \quad (1.56)$$

At c:

$$\vec{V}_1 \cdot \vec{n}_{cd} = \vec{V}_2 \cdot \vec{n}_{cd} \quad (1.57)$$

where $\vec{n}_{cd}$ is outward normal with respect point 1 on the face *cd*. Expanding the above equation we get:

$$(V_{x_1} - V_{x_2})n_{x_{cd}} + (V_{y_1} - V_{y_2})n_{y_{cd}} = 0 \quad (1.58)$$

and putting the terms for the velocities we get

$$\begin{aligned} & n_{x_{cd}}(k_{xx_1}(B_{00}(P_a-P_1)+B_{01}(P_c-P_1))+k_{xy_1}(B_{10}(P_a-P_1)+B_{11}(P_c-P_1))- \\ & \quad k_{xx_2}(C_{00}(P_b-P_2)+C_{01}(P_c-P_2))-k_{xy_2}(C_{10}(P_b-P_2)+C_{11}(P_c-P_2)))+ \\ & n_{y_{cd}}(k_{yx_1}(B_{00}(P_a-P_1)+B_{01}(P_c-P_1))+k_{yy_1}(B_{10}(P_a-P_1)+B_{11}(P_c-P_1))- \\ & \quad k_{yx_2}(C_{00}(P_b-P_2)+C_{01}(P_c-P_2))-k_{yy_2}(C_{10}(P_b-P_2)+C_{11}(P_c-P_2)))=0 \end{aligned} \quad (1.59)$$

Coefficient of P_a is:

$$M_{2a} = n_{x_{cd}}(B_{00}k_{xx_1} + B_{10}k_{xy_1}) + n_{y_{cd}}(B_{00}k_{yx_1} + B_{10}k_{yy_1}) \tag{1.60}$$

Coefficient of P_b is:

$$M_{2b} = n_{x_{cd}}(-C_{00}k_{xx_2} - C_{10}k_{xy_2}) + n_{y_{cd}}(-C_{00}k_{yx_2} - C_{10}k_{yy_2}) \tag{1.61}$$

Coefficient of P_c is:

$$\begin{aligned} M_{2c} = n_{x_{cd}}(B_{01}k_{xx_1} - C_{01}k_{xx_2} + B_{11}k_{xy_1} - C_{11}k_{xy_2}) + \\ n_{y_{cd}}(B_{01}k_{yx_1} - C_{01}k_{yx_2} + B_{11}k_{yy_1} - C_{11}k_{yy_2}) \end{aligned} \tag{1.62}$$

Coefficient of P_0 is $M_{20} = 0.0$.
Coefficient of P_1 is:

$$\begin{aligned} M_{21} = n_{x_{cd}}(-B_{00}k_{xx_1} - B_{01}k_{xx_1} - B_{10}k_{xy_1} - B_{11}k_{xy_1}) + \\ n_{y_{cd}}(-B_{00}k_{yx_1} - B_{01}k_{yx_1} - B_{10}k_{yy_1} - B_{11}k_{yy_1}) \end{aligned} \tag{1.63}$$

Coefficient of P_2 is:

$$\begin{aligned} M_{22} = n_{x_{cd}}(C_{00}k_{xx_2} + C_{01}k_{xx_2} + C_{10}k_{xy_2} + C_{11}k_{xy_2}) \\ n_{y_{cd}}(C_{00}k_{yx_2} + C_{01}k_{yx_2} + C_{10}k_{yy_2} + C_{11}k_{yy_2}) \end{aligned} \tag{1.64}$$

The three velocity constraint equations can thus be put as follows:

$$\begin{bmatrix} M_{0a} & M_{0b} & M_{0c} \\ M_{1a} & M_{1b} & M_{1c} \\ M_{2a} & M_{2b} & M_{2c} \end{bmatrix} \begin{bmatrix} P_a \\ P_b \\ P_c \end{bmatrix} = - \begin{bmatrix} M_{00} & M_{01} & M_{02} \\ M_{10} & M_{11} & M_{12} \\ M_{20} & M_{11} & M_{22} \end{bmatrix} \begin{bmatrix} P_0 \\ P_1 \\ P_2 \end{bmatrix} \tag{1.65}$$

$$\begin{bmatrix} P_a \\ P_b \\ P_c \end{bmatrix} = - \begin{bmatrix} M_{0a} & M_{0b} & M_{0c} \\ M_{1a} & M_{1b} & M_{1c} \\ M_{2a} & M_{2b} & M_{2c} \end{bmatrix}^{-1} \begin{bmatrix} M_{00} & M_{01} & M_{02} \\ M_{10} & M_{11} & M_{12} \\ M_{20} & M_{11} & M_{22} \end{bmatrix} \begin{bmatrix} P_0 \\ P_1 \\ P_2 \end{bmatrix} \tag{1.66}$$

Simplifying the above equation we get (the R matrix is obtained numerically):

$$\begin{bmatrix} P_a \\ P_b \\ P_c \end{bmatrix} = \begin{bmatrix} R_{00} & R_{01} & R_{02} \\ R_{10} & R_{11} & R_{12} \\ R_{20} & R_{21} & R_{22} \end{bmatrix} \begin{bmatrix} P_0 \\ P_1 \\ P_2 \end{bmatrix} \tag{1.67}$$

We have thus obtained P_a, P_b and P_c in terms of P_0, P_1 and P_2. We will use this information to derive expressions for single phase flow across each interface in the triangle. From Eq. 1.24 and 1.25 we get

$$Q_{0a} = A_{ad}\left[\left(k_{xx_0}P_{x0} + k_{xy_0}P_{y0}\right)n_{x_{ad}} + \left(k_{yx_0}P_{x0} + k_{yy_0}P_{y0}\right)n_{y_{ad}}\right] \tag{1.68}$$

In a similar manner we also get the following expressions:

$$\begin{aligned} Q_{0b} &= A_{bd}\left[\left(k_{xx_0}P_{x0} + k_{xy_0}P_{y0}\right)n_{x_{bd}} + \left(k_{yx_0}P_{x0} + k_{yy_0}P_{y0}\right)n_{y_{bd}}\right] \\ Q_{1a} &= A_{ad}\left[-\left(k_{xx_1}P_{x1} + k_{xy_1}P_{y1}\right)n_{x_{ad}} - \left(k_{yx_1}P_{x1} + k_{yy_1}P_{y1}\right)n_{y_{ad}}\right] \\ Q_{1c} &= A_{cd}\left[\left(k_{xx_1}P_{x1} + k_{xy_1}P_{y1}\right)n_{x_{cd}} + \left(k_{yx_1}P_{x1} + k_{yy_1}P_{y1}\right)n_{y_{cd}}\right] \\ Q_{2b} &= A_{ad}\left[-\left(k_{xx_2}P_{x2} + k_{xy_2}P_{y2}\right)n_{x_{bd}} - \left(k_{yx_2}P_{x2} + k_{yy_2}P_{y2}\right)n_{y_{bd}}\right] \\ Q_{2c} &= A_{ad}\left[-\left(k_{xx_2}P_{x2} + k_{xy_2}P_{y2}\right)n_{x_{cd}} - \left(k_{yx_2}P_{x2} + k_{yy_2}P_{y2}\right)n_{y_{cd}}\right] \end{aligned} \tag{1.69}$$

Putting the expressions for the pressure gradient from Eq. 1.29 in Eq. 1.68 gives us

$$Q_{0a} = T_{0a0}P_0 + T_{0a1}P_1 + T_{0a2}P_2 \tag{1.70}$$

where

$$\begin{aligned} T_{0a0} = A_{ad}\,[\;& A_{00}(k_{xx_0}n_{x_{ad}} + k_{yx_0}n_{y_{ad}})(-1 + R_{00}) + \\ & A_{01}(k_{xx_0}n_{x_{ad}} + k_{yx_0}n_{y_{ad}})(-1 + R_{10}) + \\ & A_{10}(k_{xy_0}n_{x_{ad}} + k_{yy_0}n_{y_{ad}})(-1 + R_{00}) + \\ & A_{11}(k_{xy_0}n_{x_{ad}} + k_{yy_0}n_{y_{ad}})(-1 + R_{10})\;] \end{aligned} \tag{1.71}$$

$$\begin{aligned} T_{0a1} = A_{ad}\,[\;& A_{00}(k_{xx_0}n_{x_{ad}} + k_{yx_0}n_{y_{ad}})R_{01} + \\ & A_{01}(k_{xx_0}n_{x_{ad}} + k_{yx_0}n_{y_{ad}})R_{11} + \\ & A_{10}(k_{xy_0}n_{x_{ad}} + k_{yy_0}n_{y_{ad}})R_{01} + \\ & A_{11}(k_{xy_0}n_{x_{ad}} + k_{yy_0}n_{y_{ad}})R_{11}\;] \end{aligned} \tag{1.72}$$

$$\begin{aligned} T_{0a2} = A_{ad}\,[\;& A_{00}(k_{xx_0}n_{x_{ad}} + k_{yx_0}n_{y_{ad}})R_{02} + \\ & A_{01}(k_{xx_0}n_{x_{ad}} + k_{yx_0}n_{y_{ad}})R_{12} + \\ & A_{10}(k_{xy_0}n_{x_{ad}} + k_{yy_0}n_{y_{ad}})R_{02} + \\ & A_{11}(k_{xy_0}n_{x_{ad}} + k_{yy_0}n_{y_{ad}})R_{12}\;] \end{aligned} \tag{1.73}$$

In a similar manner we can get all the flow terms in Eq. 1.69. They are

$$\begin{aligned} Q_{0b} &= T_{0b0}P_0 + T_{0b1}P_1 + T_{0b2}P_2 \\ Q_{1a} &= T_{1a0}P_0 + T_{1a1}P_1 + T_{1a2}P_2 \\ Q_{1c} &= T_{1c0}P_0 + T_{1c1}P_1 + T_{1c2}P_2 \\ Q_{2b} &= T_{2b0}P_0 + T_{2b1}P_1 + T_{2b2}P_2 \\ Q_{2c} &= T_{2c0}P_0 + T_{2c1}P_1 + T_{2c2}P_2 \end{aligned} \tag{1.74}$$

The transmissibility terms in Eq. 1.74 are as below:

$$\begin{aligned} T_{0b0} = A_{bd}\,[\;& A_{00}(k_{xx0}n_{x_{bd}} + k_{yx0}n_{y_{bd}})(-1 + R_{00}) + \\ & A_{01}(k_{xx0}n_{x_{bd}} + k_{yx0}n_{y_{bd}})(-1 + R_{10}) + \\ & A_{10}(k_{xy0}n_{x_{bd}} + k_{yy0}n_{y_{bd}})(-1 + R_{00}) + \\ & A_{11}(k_{xy0}n_{x_{bd}} + k_{yy0}n_{y_{bd}})(-1 + R_{10})\;] \end{aligned} \tag{1.75}$$

$$\begin{aligned} T_{0b1} = A_{bd}\,[\;& A_{00}(k_{xx0}n_{x_{bd}} + k_{yx0}n_{y_{bd}})R_{01} + \\ & A_{01}(k_{xx0}n_{x_{bd}} + k_{yx0}n_{y_{bd}})R_{11} + \\ & A_{10}(k_{xy0}n_{x_{bd}} + k_{yy0}n_{y_{bd}})R_{01} + \\ & A_{11}(k_{xy0}n_{x_{bd}} + k_{yy0}n_{y_{bd}})R_{11}\;] \end{aligned} \tag{1.76}$$

$$\begin{aligned} T_{0b2} = A_{bd}\,[\;& A_{00}(k_{xx0}n_{x_{bd}} + k_{yx0}n_{y_{bd}})R_{02} + \\ & A_{01}(k_{xx0}n_{x_{bd}} + k_{yx0}n_{y_{bd}})R_{12} + \\ & A_{10}(k_{xy0}n_{x_{bd}} + k_{yy0}n_{y_{bd}})R_{02} + \\ & A_{11}(k_{xy0}n_{x_{bd}} + k_{yy0}n_{y_{bd}})R_{12}\;] \end{aligned} \tag{1.77}$$

$$\begin{aligned} T_{1a0} = A_{ad}\,[\;& -B_{00}(k_{xx1}n_{x_{ad}} + k_{yx1}n_{y_{ad}})R_{00} \\ & -B_{01}(k_{xx1}n_{x_{ad}} + k_{yx1}n_{y_{ad}})R_{20} \\ & -B_{10}(k_{xy1}n_{x_{ad}} + k_{yy1}n_{y_{ad}})R_{00} \\ & -B_{11}(k_{xy1}n_{x_{ad}} + k_{yy1}n_{y_{ad}})R_{20}\;] \end{aligned} \tag{1.78}$$

$$
\begin{aligned}
T_{1a1} = A_{ad}\,[\;& B_{00}(k_{xx1}n_{x_{ad}} + k_{yx1}n_{y_{ad}})(1 - R_{01}) + \\
& B_{01}(k_{xx1}n_{x_{ad}} + k_{yx1}n_{y_{ad}})(1 - R_{21}) + \\
& B_{10}(k_{xy1}n_{x_{ad}} + k_{yy1}n_{y_{ad}})(1 - R_{01}) + \\
& B_{11}(k_{xy1}n_{x_{ad}} + k_{yy1}n_{y_{ad}})(1 - R_{21})\;]
\end{aligned} \tag{1.79}
$$

$$
\begin{aligned}
T_{1a2} = A_{ad}\,[\;& -B_{00}(k_{xx1}n_{x_{ad}} + k_{yx1}n_{y_{ad}})R_{02} \\
& -B_{01}(k_{xx1}n_{x_{ad}} + k_{yx1}n_{y_{ad}})R_{22} \\
& -B_{10}(k_{xy1}n_{x_{ad}} + k_{yy1}n_{y_{ad}})R_{02} \\
& -B_{11}(k_{xy1}n_{x_{ad}} + k_{yy1}n_{y_{ad}})R_{22}\;]
\end{aligned} \tag{1.80}
$$

$$
\begin{aligned}
T_{1c0} = A_{cd}\,[\;& B_{00}(k_{xx1}n_{x_{cd}} + k_{yx1}n_{y_{cd}})R_{00} + \\
& B_{01}(k_{xx1}n_{x_{cd}} + k_{yx1}n_{y_{cd}})R_{20} + \\
& B_{10}(k_{xy1}n_{x_{cd}} + k_{yy1}n_{y_{cd}})R_{00} + \\
& B_{11}(k_{xy1}n_{x_{cd}} + k_{yy1}n_{y_{cd}})R_{20}\;]
\end{aligned} \tag{1.81}
$$

$$
\begin{aligned}
T_{1c1} = A_{cd}\,[\;& B_{00}(k_{xx1}n_{x_{cd}} + k_{yx1}n_{y_{cd}})(-1 + R_{01}) + \\
& B_{01}(k_{xx1}n_{x_{cd}} + k_{yx1}n_{y_{cd}})(-1 + R_{21}) + \\
& B_{10}(k_{xy1}n_{x_{cd}} + k_{yy1}n_{y_{cd}})(-1 + R_{01}) + \\
& B_{11}(k_{xy1}n_{x_{cd}} + k_{yy1}n_{y_{cd}})(-1 + R_{21})\;]
\end{aligned} \tag{1.82}
$$

$$
\begin{aligned}
T_{1c2} = A_{cd}\,[\;& B_{00}(k_{xx1}n_{x_{cd}} + k_{yx1}n_{y_{cd}})R_{02} + \\
& B_{01}(k_{xx1}n_{x_{cd}} + k_{yx1}n_{y_{cd}})R_{22} + \\
& B_{10}(k_{xy1}n_{x_{cd}} + k_{yy1}n_{y_{cd}})R_{02} + \\
& B_{11}(k_{xy1}n_{x_{cd}} + k_{yy1}n_{y_{cd}})R_{22}\;]
\end{aligned} \tag{1.83}
$$

$$
\begin{aligned}
T_{2b0} = A_{bd}\,[\;& -C_{00}(k_{xx2}n_{x_{bd}} + k_{yx2}n_{y_{bd}})R_{10} \\
& -C_{01}(k_{xx2}n_{x_{bd}} + k_{yx2}n_{y_{bd}})R_{20} \\
& -C_{10}(k_{xy2}n_{x_{bd}} + k_{yy2}n_{y_{bd}})R_{10} \\
& -C_{11}(k_{xy2}n_{x_{bd}} + k_{yy2}n_{y_{bd}})R_{20}\;]
\end{aligned} \tag{1.84}
$$

$$
\begin{aligned}
T_{2b1} = A_{bd}\,[\;& -C_{00}(k_{xx2}n_{x_{bd}} + k_{yx2}n_{y_{bd}})R_{11} \\
& -C_{01}(k_{xx2}n_{x_{bd}} + k_{yx2}n_{y_{bd}})R_{21} \\
& -C_{10}(k_{xy2}n_{x_{bd}} + k_{yy2}n_{y_{bd}})R_{11} \\
& -C_{11}(k_{xy2}n_{x_{bd}} + k_{yy2}n_{y_{bd}})R_{21}\;]
\end{aligned} \tag{1.85}
$$

$$
\begin{aligned}
T_{2b2} = A_{bd}\,[\;& C_{00}(k_{xx2}n_{x_{bd}} + k_{yx2}n_{y_{bd}})(1 - R_{12}) + \\
& C_{01}(k_{xx2}n_{x_{bd}} + k_{yx2}n_{y_{bd}})(1 - R_{22}) + \\
& C_{10}(k_{xy2}n_{x_{bd}} + k_{yy2}n_{y_{bd}})(1 - R_{12}) + \\
& C_{11}(k_{xy2}n_{x_{bd}} + k_{yy2}n_{y_{bd}})(1 - R_{22})\;]
\end{aligned} \tag{1.86}
$$

$$
\begin{aligned}
T_{2c0} = A_{cd}\,[\;& -C_{00}(k_{xx2}n_{x_{cd}} + k_{yx2}n_{y_{cd}})R_{10} \\
& -C_{01}(k_{xx2}n_{x_{cd}} + k_{yx2}n_{y_{cd}})R_{20} \\
& -C_{10}(k_{xy2}n_{x_{cd}} + k_{yy2}n_{y_{cd}})R_{10} \\
& -C_{11}(k_{xy2}n_{x_{cd}} + k_{yy2}n_{y_{cd}})R_{20}\;]
\end{aligned} \tag{1.87}
$$

$$
\begin{aligned}
T_{2c1} = A_{cd}\,[\;& -C_{00}(k_{xx2}n_{x_{cd}} + k_{yx2}n_{y_{cd}})R_{11} \\
& -C_{01}(k_{xx2}n_{x_{cd}} + k_{yx2}n_{y_{cd}})R_{21} \\
& -C_{10}(k_{xy2}n_{x_{cd}} + k_{yy2}n_{y_{cd}})R_{11} \\
& -C_{11}(k_{xy2}n_{x_{cd}} + k_{yy2}n_{y_{cd}})R_{21}\;]
\end{aligned} \tag{1.88}
$$

$$
\begin{aligned}
T_{2c2} \;=\; A_{cd}\,[\;\; & C_{00}(k_{xx2}n_{x_{cd}} + k_{yx2}n_{y_{cd}})(1 - R_{12}) + \\
& C_{01}(k_{xx2}n_{x_{cd}} + k_{yx2}n_{y_{cd}})(1 - R_{22}) + \\
& C_{10}(k_{xy2}n_{x_{cd}} + k_{yy2}n_{y_{cd}})(1 - R_{12}) + \\
& C_{11}(k_{xy2}n_{x_{cd}} + k_{yy2}n_{y_{cd}})(1 - R_{22})\;]
\end{aligned}
\tag{1.89}
$$

Since $Q_{0a} = Q_{1a}$, $Q_{0b} = Q_{2b}$ and $Q_{1c} = Q_{2c}$ we need to use only three of the six equations in Eq. 1.74. Thus Eq. 1.74 can be written in the following simple form

$$
\begin{bmatrix} Q_a \\ Q_b \\ Q_c \end{bmatrix} = \begin{bmatrix} T_{a0} & T_{a1} & T_{a2} \\ T_{b0} & T_{b1} & T_{b2} \\ T_{c0} & T_{c1} & T_{c2} \end{bmatrix} \begin{bmatrix} P_0 \\ P_1 \\ P_2 \end{bmatrix} \tag{1.90}
$$

2. Comparative Aspects of Coning Behavior in Vertical and Horizontal Wells (Task 1)

Reserach undertaken by Dr. Sepehr Arbabi and Professor John Fayers.

2.1 Introduction

Horizontal wells offer many attractions [1] compared to vertical wells, where the primary consideration is usually the relative productivities under single phase flow conditions [2, 3]. It is only when reservoirs have many non-communicating layers or have low vertical permeabilities that the vertical well may be more attractive. For cases where the reservoir has a moderate number of isolated layers, there may still be preferable opportunities for horizontal wells, by using stepped, or multi lateral configurations, or by creating hydraulic fractures. A secondary consideration for choosing horizontal wells (HWs) is in circumstances where vertical coning (or "cresting" describes better the shape of the fluid interface) may offer advantages in the critical rate at which a well can be operated to avoid breakthrough of gas from a gas cap, or water from a bottom aquifer, or both [4]. For example, operation of a field may have caused a gravity gas tongue to develop below a major shale in a reservoir zone, for which a horizontal lateral is to be drilled whose length, depth and flow rate should be designed to limit the timing and magnitude of gas breakthrough.

In this paper we examine a plethora of semi-analytical methods for calculating critical cresting rates, which yield a very large range of uncertainty for HWs. We show by using numerical simulation that none of these methods gives very reliable results. For vertical wells (VWs), the critical coning behavior is physically a better resolved problem and the available correlations span a narrower range of uncertainty. However, along with other authors [5], we find in comparison with simulations that it is only the elegant, but more complicated Wheatley's method [6] that gives reliable results for VWs. We use a strategy similar to Wheatley's ideas to obtain a new analytical theory for critical cresting rates in HWs, which is shown to give excellent agreement with our simulations.

The HW critical cresting rates calculated by the new method tend to give results towards the lower limit of the range of the previous methods, and these rates are apparently not particularly attractive in comparison with equivalent VW critical coning rates. For example, for HWs with infinite spacing Papatzacos *et al.* [7] have shown that a finite critical rate does not exist. A more important measure of cresting performance is found to be the time to breakthrough at supercritical flow rates. Here, the simulation results show very considerable advantage to HWs compared with VWs. We show that the Papatzacos *et al.* dynamic analysis for HWs with infinite spacing can be made to match closely our simulation results for a moderate spacing by a simple *ad hoc* correction to their formulae.

Table 2.1: Data for horizontal well gas cresting example (based on Example 8-7 of Joshi [13])

Well length, L	500 m
Well location, h_w	22 m below GOC
Oil column, h	22.1 m
Reservoir length, $2x_e$	804.6 m
Oil viscosity, μ_o	0.42×10^{-3} $Pa-s$
Oil FVF, b_o	1.1 $res\ m^3/m^3$
Density difference, $\triangle\rho$	0.48 gm/cm^3
Well radius, r_w	0.1 m
Permeability, k_h	0.069 μm^2
Permeability, k_v	0.069 and 0.0069 μm^2

2.2 Summary of Existing Methods for Calculation of Critical Cresting Rates

An important factor in determining the economics of horizontal wells is the assessment of the breakthrough time and subsequent two-phase production behavior. Because the breakthrough will tend to be induced towards the heel of the well, due to the effects of wellbore pressure drop, we might expect the post breakthrough behavior of GOR or WOR, to increase more dramatically for HWs than for VWs. The first step in this respect is to evaluate the potential cresting attributes of HWs under the assumptions that the anisotropic reservoir is uniform, and that simplified boundary conditions can be applied to a 2D-model problem for a well of infinite length. The intention is to understand how in uniform conditions the critical rate might vary as a function of spacing and depth location of the well.

There have been a number of approximate equations developed for evaluating critical cresting rates over an interval of 30 years which include methods due to Efros [8], Giger [9], Giger [10] and Karcher *et al.* [11], Joshi [12, 13], Chaperon [14] and Guo and Lee [15]. These methods have been recently summarized by Fayers *et al.* [1]. We have taken the gas cresting example (8-7) from Joshi's book for which the principal data are given in Table 2.1.

The results shown in Table 2.2 indicate large discrepancies between the methods, with the Guo and Lee result being nearly 23 times larger than the most pessimistic result due to Efros and Giger. These conclusions all assume a well placed at the bottom of the reservoir, although in principle, the Joshi and Guo and Lee methods can deal with situations where the well is not at the boundary.

In order to investigate which of the above methods might be the most accurate, we set up detailed 2D-simulation models using the Eclipse Simulator. Care has to be exercised in choosing the gridding arrangements, with finer grids in both directions near the well, and relative permeabilities should be chosen whose shapes will help to promote self sharpening of the gas saturation profiles at the fluid contact. A grid of 61×37 was suitable for most

Table 2.2: Estimates of critical oil rates in m^3/day for a single horizontal well from different methods and simulation

Method	Isotropic	Anisotropic*
Efros[8] and Giger[9]	18.4	-
Giger[10]	73.8	-
Joshi[12, 13]	62.2	-
Chaperon[14]	181.3	158.7
Guo and Lee[15]	441.7	139.6
Simulation	19.2	19.5

* $k_v/k_h = 0.1$

problems, although for cases with wider spacing's (say $x_e > 800$ meters) this grid had to be refined to 245 × 37 to preserve adequately small spacing near the well. The constant potential outer boundary conditions, in the simulator are obtained by using "point" well injectors with appropriate fixed potentials to allow the necessary oil inflows in the reservoir zone, and small gas inflows in the gas cap. Many of the transient behaviors are extremely slowly varying, so that a time step multiplying procedure must be used to determine whether the transients have achieved a final steady state. For example, transients can last for over 1000 years before reaching a steady state. At steady state, the position of the GOC becomes stationary, and the well rates on the gas injectors become negligibly small. The critical rates are determined by studying problems with successively larger rates until the critical rate is achieved. The simulation result in Table 2.2 indicates that the pessimistic Efros method is essentially correct for this example with the well at the bottom of the reservoir.

2.3 Summary of Methods for Critical Coning Rates for Vertical Wells

There is also a range of methods for estimating coning in vertical wells which date from the classical potential theory solution originally given by Muskat [16], to solutions due to Meyer and Garder [17], Chaperon [14], Wheatley [6] and Guo and Lee [18]. The geometry we consider for the vertical well cases is for a fractional well completion length Y_d in a reservoir with oil zone thickness 22.1 meter (the same as for the horizontal well), with a square drainage region with $2x_e = 804.6$ meters. This gives an effective outer radius of $r_e = 454$ meters in r-z geometry. The results of the critical coning rate comparisons for vertical wells are shown as a function of fractional completion length in Figure 2.1.

Simulations of the vertical well coning problems were made using a 1/4-area 3D-model with grids of 13 × 13 × 34. Grid spacing is again refined near the partially completed well. The solution behavior for coning in VWs is physically better determined so that the simulation transients are much shorter than those for HWs. It is much easier to find a proper steady state and the corresponding critical production rate for a vertical well, in contrast to

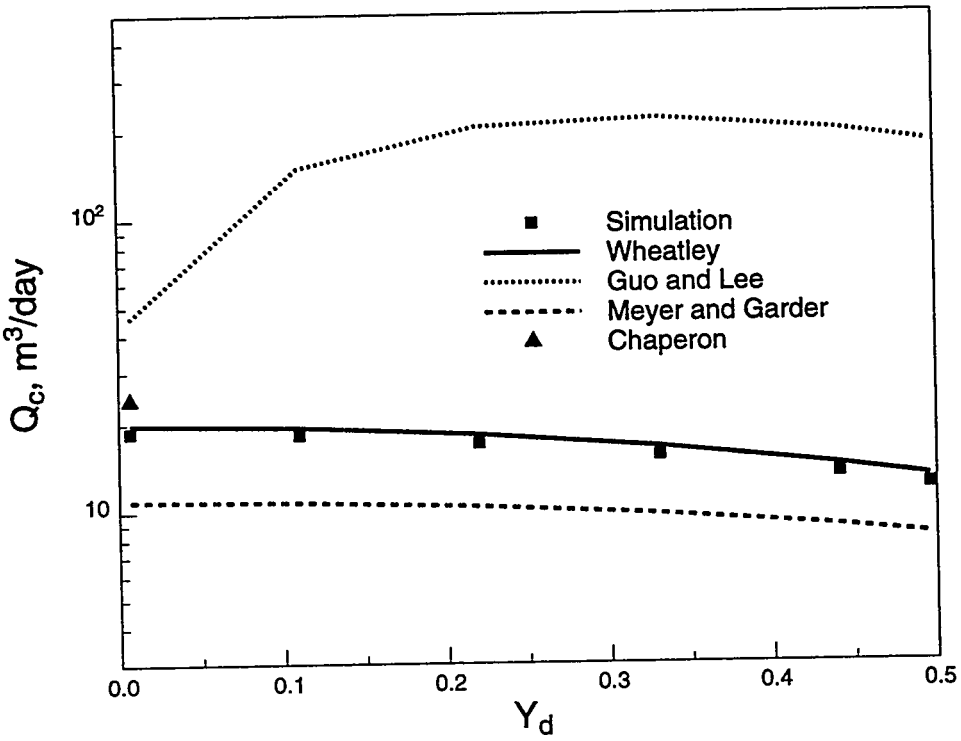

Figure 2.1: Comparison of critical rates between simulation and analytical solutions for a vertical well at various completion penetration fractions

a horizontal well.

The comparisons in Figure 2.1 also indicate a smaller range of uncertainty between methods than for HWs, which is probably associated with this being a better determined problem. The Guo and Lee method significantly overpredicts, but their errors are not as large as for HWs. We find that the Wheatley analysis is the only VW coning prediction method with good accuracy for vertical wells. This analysis has also been generalized successfully by Piper and Gonzales [19] to deal with dual interface problems associated with the presence of both a gas cap above, and an aquifer beneath a vertical well, which is partially completed with stand-off from both interfaces.

2.4 A New Semi-Analytic Solution for Critical Cresting Rates for Horizontal Wells

The accuracy achieved by Wheatley's method for VWs has suggested that a similar style of analysis could be successful for HWs, which we now describe. The key idea is to construct an approximate potential function which will lead to two conditions being fulfilled to acceptable accuracy on the steady state interface associated with a sub-critical flow rate. The geometry of our problem is shown in Figure 2.2 for a water cresting application, and by symmetry, gas cresting is dealt with by labelling the ordinate -y. The approximate potential function is created by introducing an extra sink of strength aq at depth s_1, and an extra source of strength bq at depth s_2, with $s_2 > s_1$. The major details of the derivation are given

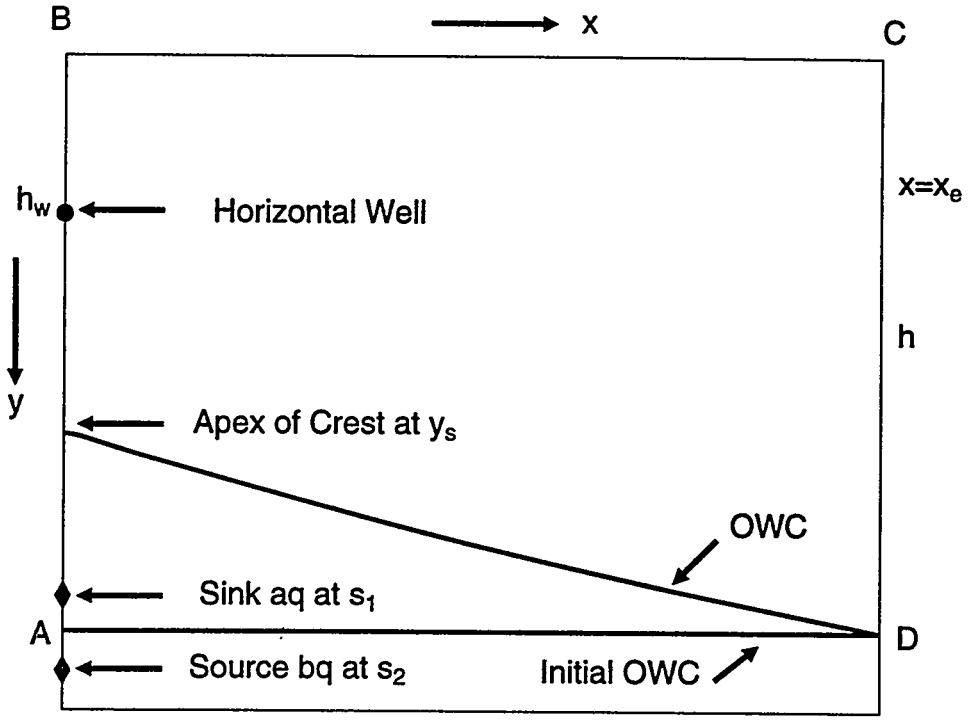

Figure 2.2: Schematic of the HW water cresting problem

in the Appendix, for which we describe some of the essential features here.

The conditions to be fulfilled on the contact are the following:

(i) The contact is the streamline $\Psi = -q/2$, where q is the HW flowrate, which must cross the outer boundary $x = x_e$ at the oil zone depth h, and cross the inner boundary $x = 0$, at the stagnation depth y_s.

(ii) The potential variation on the contact must ensure that the difference in gravity heads between the oil and water phases will cause the interface to remain stationery, i.e.,

$$\Phi(x_c, y_c) = -\triangle\rho \; g(h - y_c) \tag{2.1}$$

with $\Phi(x_c, y_c) = 0$ when $x_c = x_e$ and $y_c = h$.

A fundamental solution element in the problem is derived for the HW at depth h_w in a semi-infinite medium with constant potentials along the outer boundaries at $x = \pm x_e$, and with no flow along the upper boundary $y = 0$. In complex variable theory this element solution is given by

$$\gamma(z) = \frac{q}{2\pi} \ln \left[\cot\left(\frac{\pi(z - ih_w)}{4x_e}\right) + \cot\left(\frac{\pi(z + ih_w)}{4x_e}\right) \right] \tag{2.2}$$

Potential and stream functions are then obtained by taking real and imaginary parts. A stream function solution for Eq. (2.2) is illustrated in Figure 2.3, where we see a strong crowding of flow lines being driven into the well from the no-flow upper boundary. The streamline $\Psi = -q/2$ enters from infinity below the well along the $x = 0$ axis.

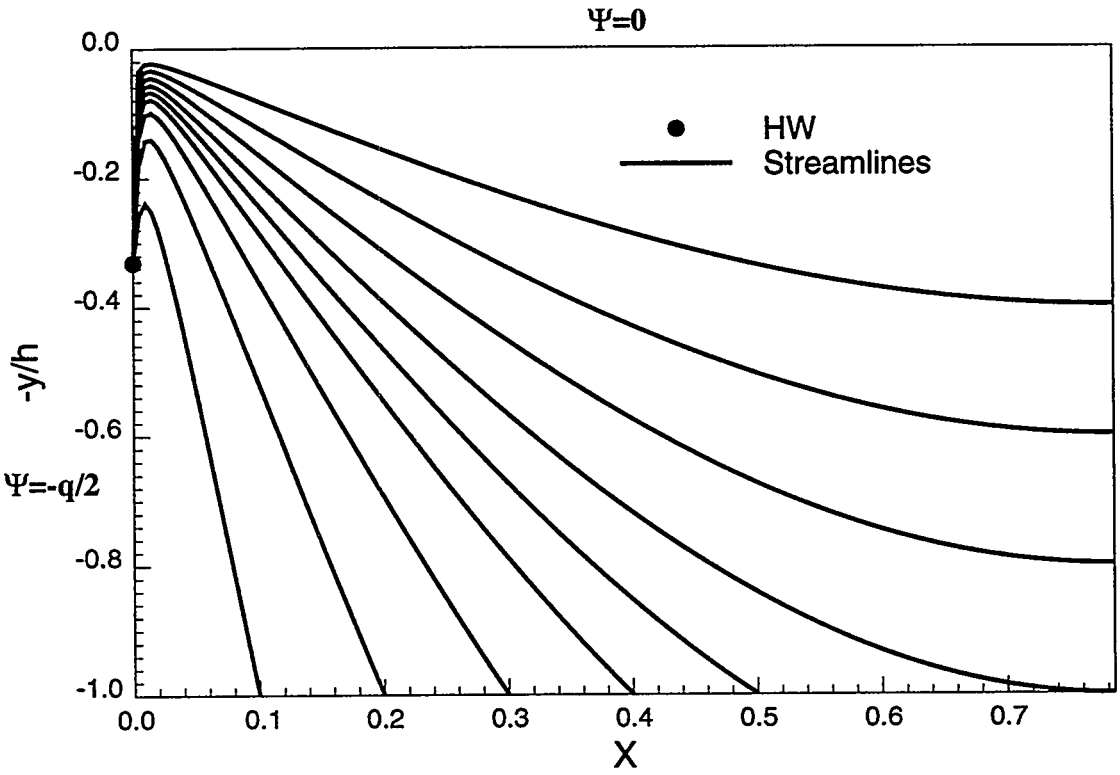

Figure 2.3: A stream function solution based on Eq. (2.2) for a HW in a semi-infinite medium

Inclusion of a single extra sink of strength aq at depth s_1 can be chosen to cause the interface conditions (i) and (ii) to be satisfied at the two ends, $x = x_e$ and $x = 0$, but the agreement elsewhere along the interface is poor. Figure 2.4 shows for a difficult case the possible divergence between the streamline, $\Psi = -q/2$ and the interface potential variation determined from Eq. (2.1). There is a substantial error in the slope and curvature of the stream function at positions close to the well. To correct this behavior, the source term bq is introduced at s_2. Extra conditions are then posed to force better agreement between the stream and potential functions for the interface, where equality in both the values and slopes of these functions is required at a position $x = x_m$. The resulting shapes of the two functions are now in much closer agreement as shown in Figure 2.5. The critical rate is then found by increasing q though an iterative process. Thus our procedure can be summarized as finding by iteration the best values of parameters a, b, s_1, and s_2 to give the closest match to the necessary conditions on the interface. The iterative procedure described in the Appendix converges quite reliably and we find that a problem is solved in a few seconds on a PC-computer.

The choice of $x_m = 0.1 \times 4x_e/\pi$ ($X_m = 0.1$) for the crossover is somewhat arbitrary, but we found this position was a useful fixing point for all the cases subsequently run. We find that varying the x_m position within a reasonable range close to the well gives some modest changes to the stream function shape, but almost no change to the potential function for the interface, and its all important stagnation position y_s on the $x = 0$ axis. Table 2.3 summarizes the comparisons with simulation with $h_w/h = 0.33$.

We also show in Figure 2.5, the equivalent crest shape and tip position obtained from

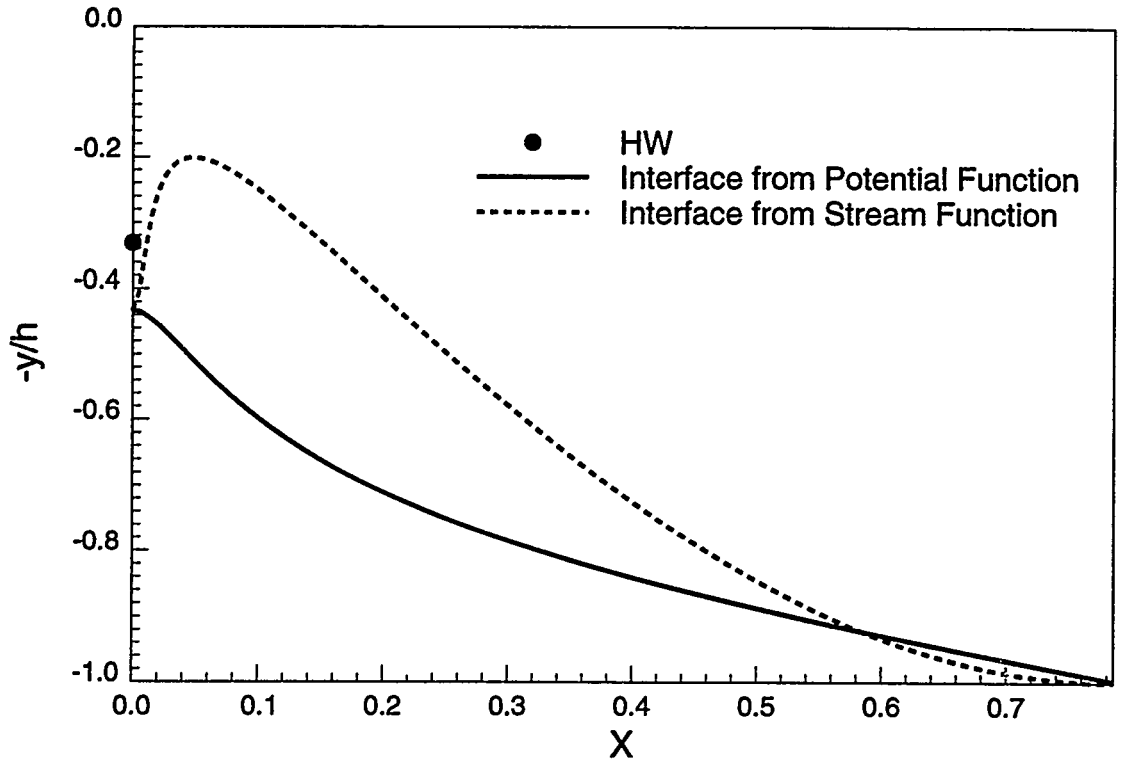

Figure 2.4: Interface shape from potential and stream functions at the critical rate with $s_1/h = 1.24$, $a = 17.33$, and $b = 0$

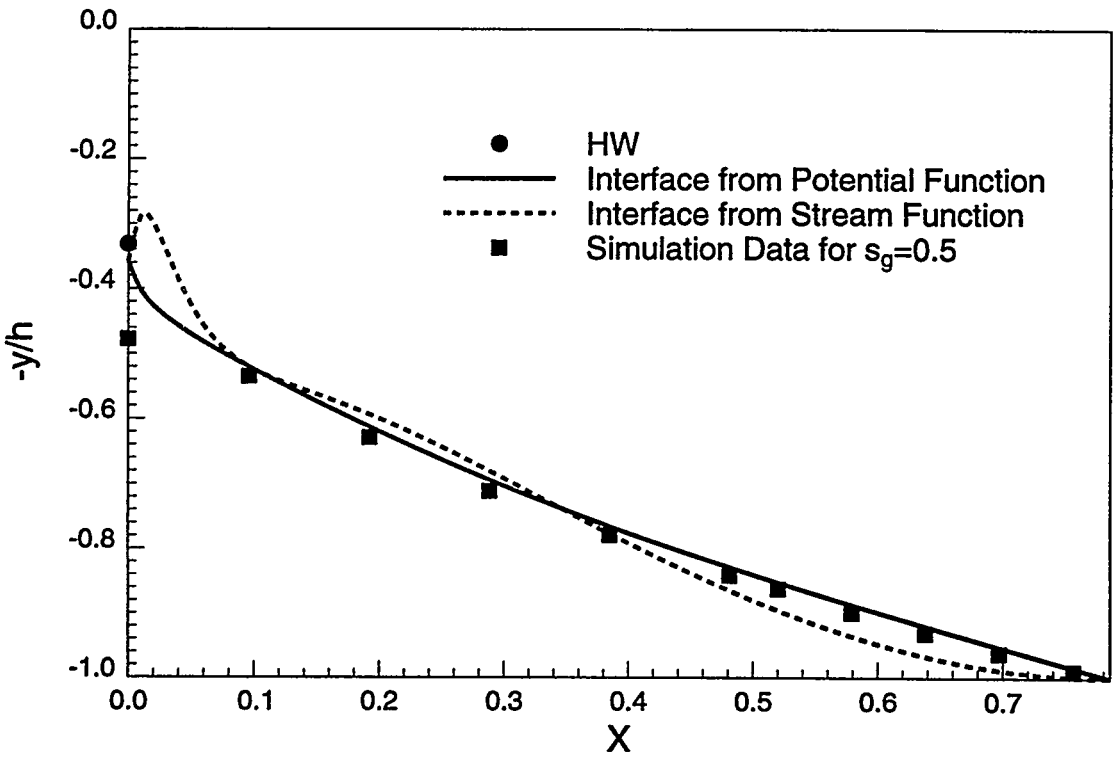

Figure 2.5: Interface shape from potential and stream functions at the critical rate with $s_1/h = 0.42$, $a = 2.79$, $s_2/h = 4.59$, and $b = 15.58$

Table 2.3: Sensitivity of y_s and Q_c to X_m and comparison with the simulation result with $h_w/h = 0.33$

X_m	y_s, m	Q_c, m^3/day
0.075	7.86	15.53
0.10	7.96	15.58
0.15	8.10	15.49
0.20	8.12	15.45
simulation	10.55	16.16

the direct simulation based on the Eclipse calculations described in Section 2. We use the contour $S_g = 0.5$ to assign an interface position to the modest region of the distributed saturations in the simulation solution. The agreement is reasonable. We would anticipate that the effect of a finite grid and smearing the sharp front in the simulation model, will be to make the cusp of the crest less sharp, and to cause the system to be slightly more stable.

Figure 2.6 displays a similar comparison between our method and direct simulation data for the case where the well is at the bottom and $q = 0.7 \times q_c$. The critical rates for this case, which corresponds to the parameters in Table 2.1, are estimated to be 18.5 for the isotropic and 18.8 m^3/day for the anisotropic case from the analytical method. These values are in close agreement with the simulation results shown in Table 2.2. Figure 2.7 shows critical rates from our method in excellent accord with the simulation results for gas/oil cresting as a function of x_e, with $h_w/h = 0.33$ (see Table 2.1 for principal parameters). The popular Joshi's method has errors by a factor of more than 3 at wide spacings. Critical rates are very small for wide well spacings with HWs, and only start to increase rapidly when the HW-spacing x_e becomes relatively small. From the analytical results, we find that the dependence of the critical rate on k_v/k_h is somewhat surprisingly, very weak for HWs, with an increase of only $1.02\,q_c$ when $k_v/k_h = 0.1$ and $x_e = 1000$ meters. This is also confirmed from the simulations (see Table 2.2).

In Figure 2.8 results are given comparing critical coning and cresting rates for vertical and horizontal wells, using respectively Wheatley's method for VWs and our new method for HWs. The vertical well has a partial completion over the bottom 10 meters of the reservoir of thickness 30 meters and the horizontal well of length 1000 meters is placed at the 10 meter position. The x-axis of the plot is the half spacing x_e for the horizontal well, and the drainage radius r_e for the vertical well. The relative performance of the HW critical cresting rates in comparison with critical coning for the VWs are not very impressive, except at close well spacings.

Figure 2.9 displays the relative shapes of the critical cones for a HW and a VW with $x_e = r_e = 850$ meters (based on the data in Fig. 2.8), which have the same critical rate of $27\,m^3/day$. The crest shape for the HW has a much less pronounced cusp in comparison with the VW.

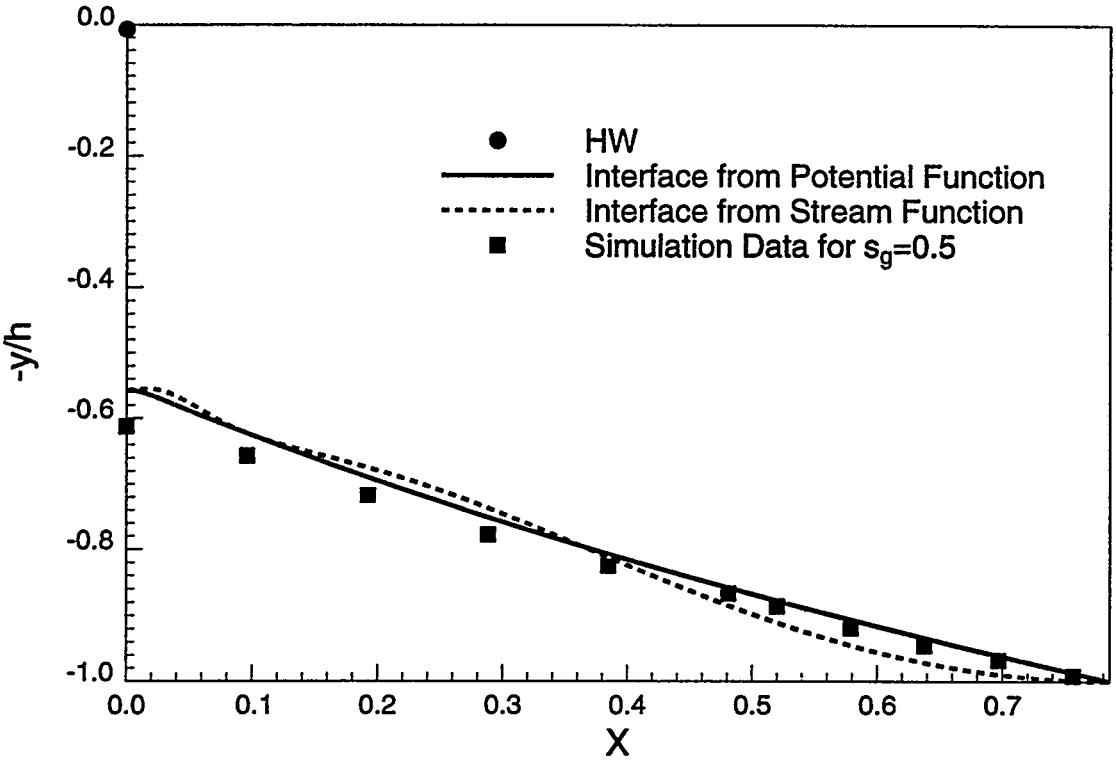

Figure 2.6: Comparison of crest shape from potential and stream functions with the simulation data for a sub-critical case with $q = 0.7 \times q_c$

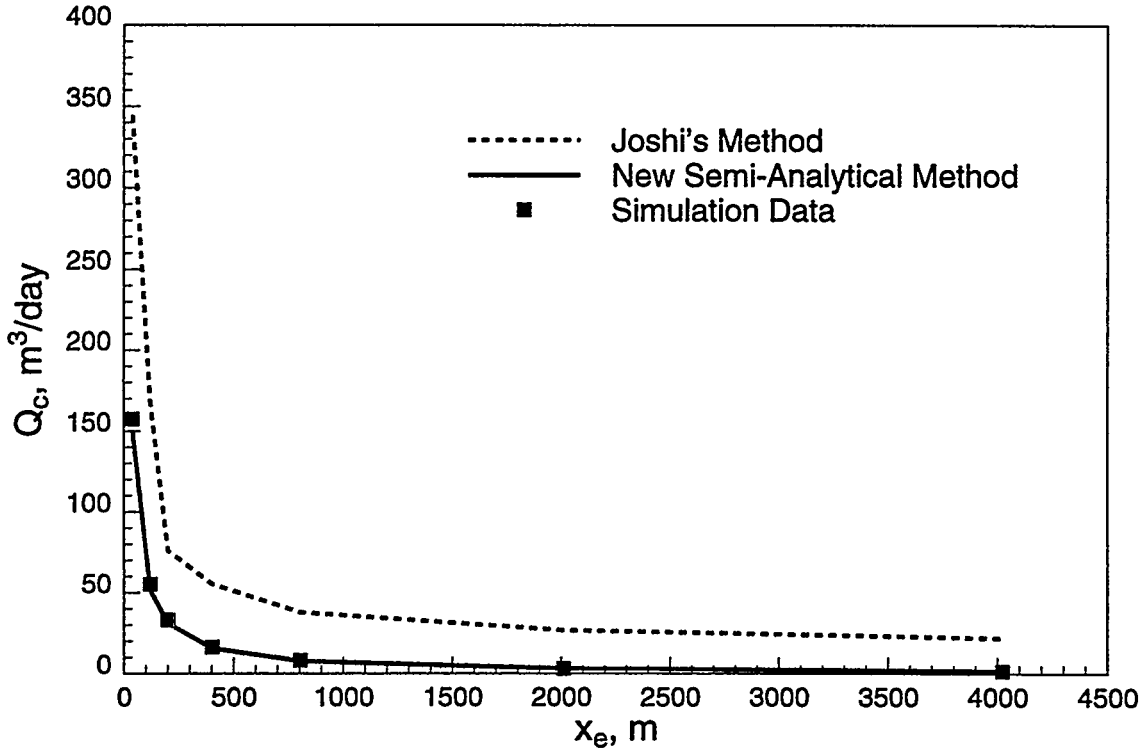

Figure 2.7: Variations of the critical rate with the horizontal dimension of the reservoir

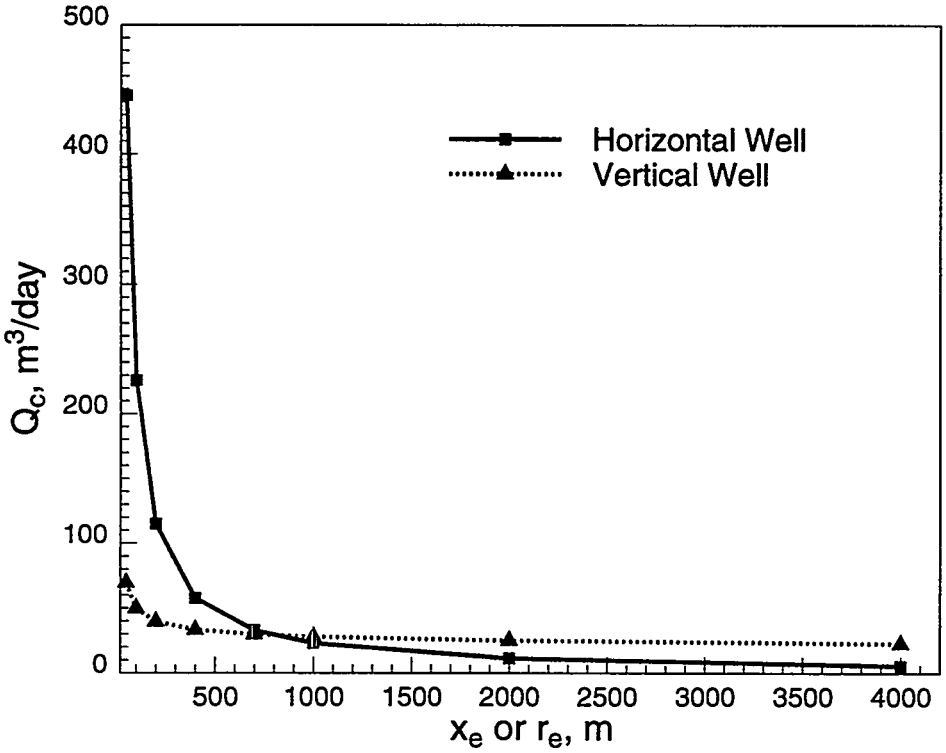

Figure 2.8: Critical rates based on Wheatley's method for a vertical well and the semi-analytical method for a horizontal well

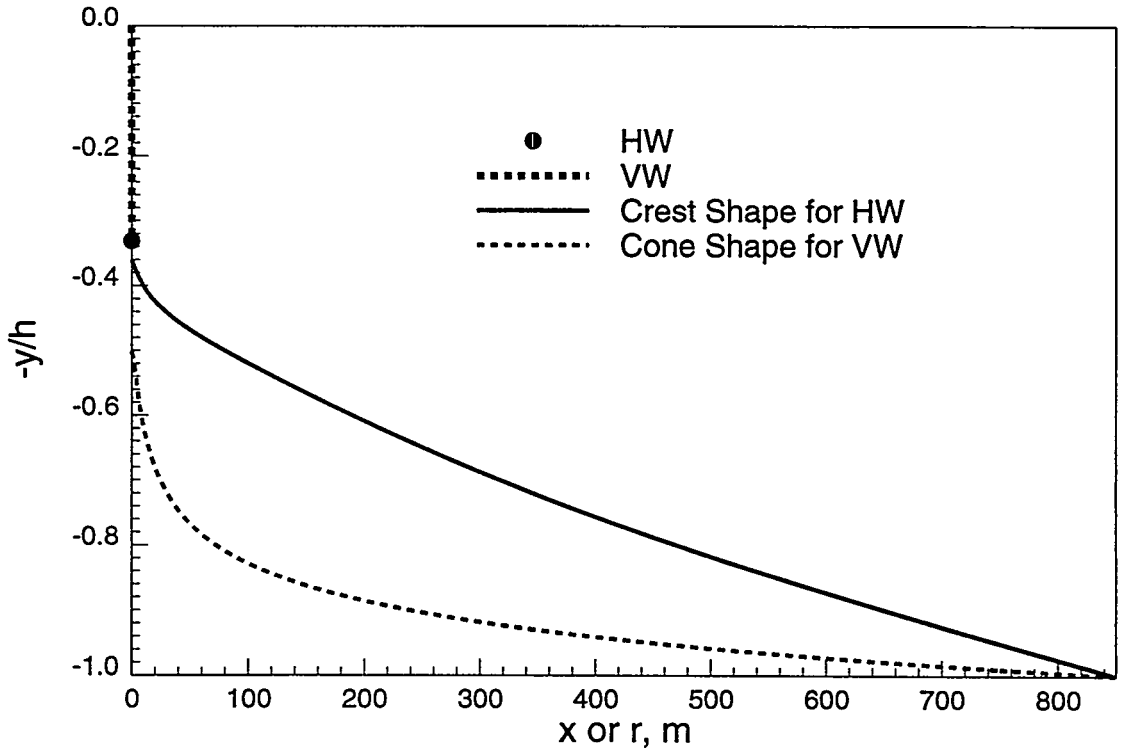

Figure 2.9: Shape of critical cones based on Wheatley's method for a vertical well and the semi-analytical method for a horizontal well

2.5 Transient Breakthrough Times for Horizontal Wells

The behavior of the simulation studies indicated marked differences between the transient characteristics of HWs and VWs. The expectation that HWs can have long breakthrough times was intimated by the analytical results obtained by Papatzacos *et al.*[7] for HWs with infinite spacing. They showed that for the infinite spacing case there is no finite critical cresting rate, and obtained results for the dynamic interface shapes using a moving boundary method and utilizing the Fast Fourier Transform (FFT) algorithm. The key results for time to breakthrough given by Papatzacos *et al.* are summarized by three expressions, as follows:

Ppt1

$$\begin{aligned} t_{BtD} &= 1/6q_D \\ \text{where} \quad q_D &= \frac{\mu_o b_o}{2\pi\sqrt{k_v k_h} h \triangle\rho\, g} q \\ \text{and} \quad t_{BtD} &= \frac{\triangle\rho\, g k_v}{h\phi\mu_o} t \end{aligned} \tag{2.3}$$

Ppt2

$$t_{BtD} = 1 - (3q_D - 1) ln[3q_D/(3q_D - 1)] \tag{2.4}$$

Ppt3

$$\begin{aligned} \ln(t_{BtD}) &= -1.7179 - 1.1633\, U + \\ &\quad 0.16308\, U^2 - 0.046508\, U^3 \\ \text{where} \quad U &= \ln(q_D) \end{aligned} \tag{2.5}$$

Ppt1 corresponds to the assumption of constant pressure on the interface and is expected to give an adequate approximation when $q_D > 0.5$. Ppt2 is a closed form solution assuming vertical equilibrium in the crest which should apply when $q_D > 0.33$. Ppt3 is a quadratic fit to the FFT-solution, which should be accurate for all values of q_D. In Figure 2.10 we compare results from the Papatzacos *et al.* theory for HWs with infinite spacing, to simulation results using the gridding scheme described in Section 2, where the half well spacing is $x_e = 402.3$ meters.

The critical cresting rate for this HW corresponds to $q_D = 0.028$. Thus the rates on the abscissa of Figure 2.10 are for very high values. All the methods agree quite well when $q_D > 0.5$, but there is divergence when $q_D \ll 0.5$. Some of this must be attributable to the differences in the spacing effects. The simulation solution is approximated quite accurately by the simple result

$$t_{BtDa} = \frac{1}{2}(t_{BtD1} + t_{BtD3}) \tag{2.6}$$

where t_{BtD1} and t_{BtD3} are obtained from Ppt1 and Ppt3 above. This approximation was tested again for a series of simulations with reduced well spacing for the faster transient

region with $x_e = 80.5$ meters, where Eq. (2.6) was again satisfactory. In terms of the real quantities t_{Bt} and q, the effects of varying k_v/k_h on the solution shapes are confirmed by simulation to be small for q_D values in the range $0.1 < q_D < 0.3$. At higher rates, the dimensionless times to breakthrough were unaffected by k_v/k_h, which implies that the real time increases proportionally to $\sqrt{k_h/k_v}$.

Our final results compares times to breakthrough for HWs with those for VWs. We have to rely on simulation for the latter since there are no satisfactory analytical techniques. Figure 2.11 gives the comparison, where the HW data are given in Table 2.1, and the VW case refers to a short well at the bottom of the reservoir (critical rate for both wells $\sim$ 19 m^3/day). Thus we see that when the actual rate is 210 m^3/day, the ratio of the breakthrough times is a factor of about 60 in favor of the horizontal well.

2.6 Conclusions

(i) Existing methods for calculating critical cresting rates for HWs are unreliable. The Efros method, which is the most pessimistic compared to the other methods, is accurate, but this only applies to a well at the top or bottom boundary.

(ii) Only Wheatley's method amongst the critical coning rate methods for VWs is accurate.

(iii) A new semi-analytical solution for estimating HW critical cresting rates has been developed whose predictions have been shown by simulation to give accurate results for a HW located at any level in the reservoir.

(iv) An *ad hoc* correction to the Papatzacos *et al* results gives useful estimates of breakthrough times for HWs flowing at supercritical rates.

(v) The time to breakthrough for a HW operated at a supercritical rate will usually be at least an order of magnitude greater than for a VW operated at a comparable rate.

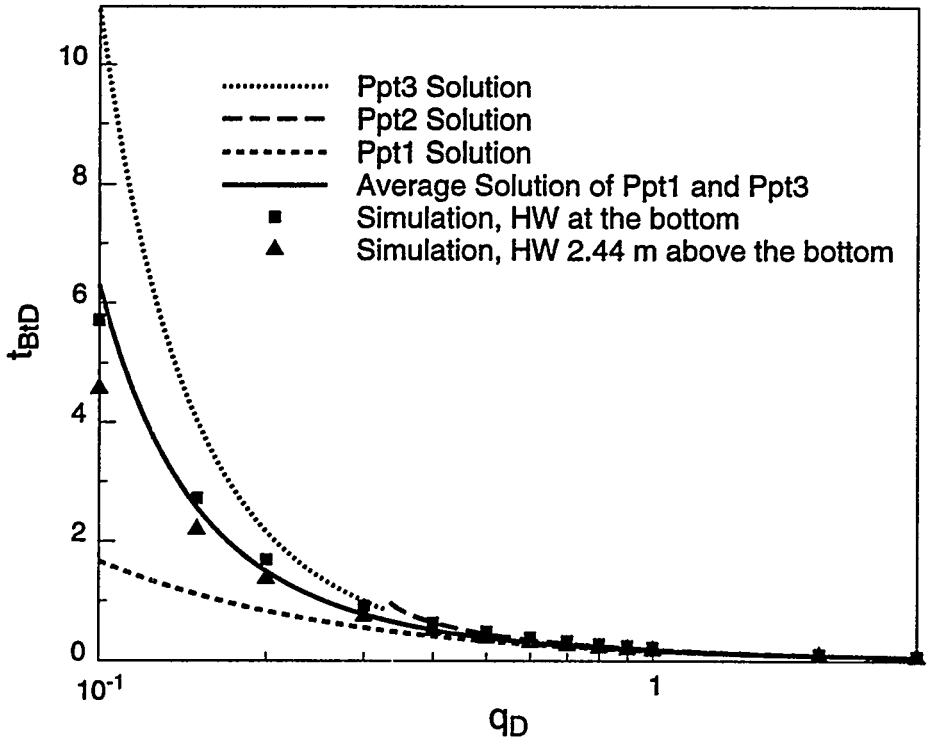

Figure 2.10: Comparison of breakthrough times between simulation and various analytical solutions

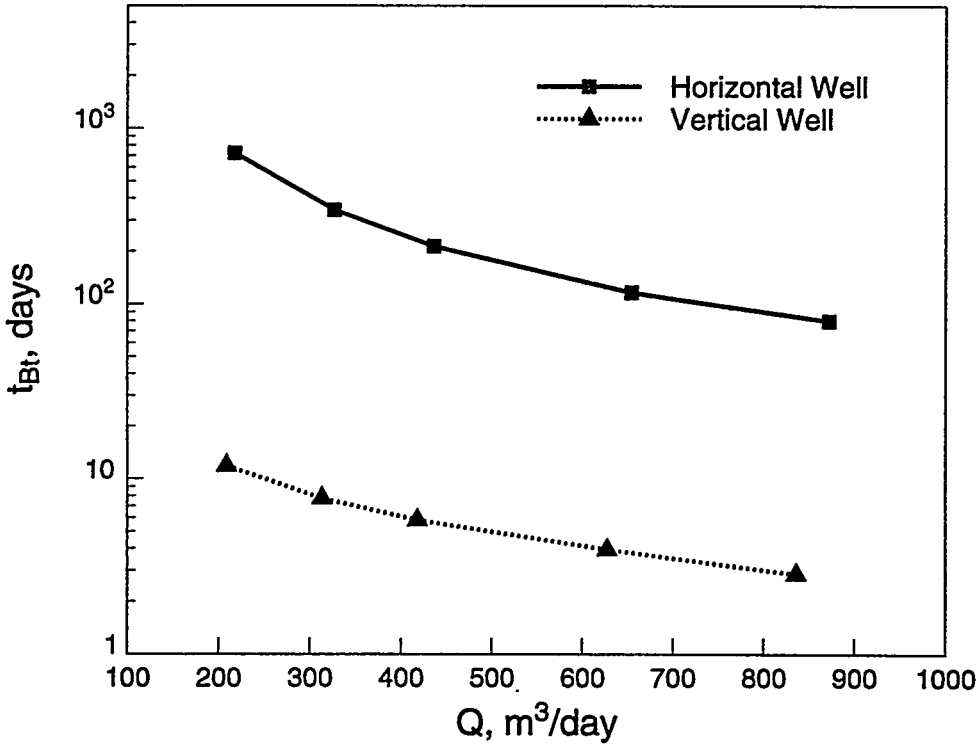

Figure 2.11: Comparison of breakthrough times for the horizontal and vertical wells at various supercritical rates from simulations

Nomenclature

a	line sink strength
b	line source strength
b_o	oil formation volume factor
g	gravitational acceleration
h	oil column thickness
h_w	location of horizontal well
k_h	horizontal permeability
k_v	vertical permeability
L	length of horizontal well
q	flow rate or line strength
q_D	dimensionless flow rate in Eq. (2.3)
q_c	critical rate or strength per unit length
Q_c	critical flow rate
Q_d	dimensionless flow rate in Eq. (2.18)
Q_{dc}	dimensionless critical flow rate
r_w	well radius
r_e	drainage radius of the vertical well
s_1	location of line sink
s_2	location of line source
S_g	gas saturation
t	time
t_{Bt}	breakthrough time
x_c	x position on fluid contact
x_e	half well spacing transverse to HW
x_m	x position for matching the shape of crest
y_c	y position on fluid contact
y_m	y position for matching the shape of crest
y_s	location of stagnation point
z	complex variable

Greek Letters

$\triangle\rho$	density difference
γ	complex potential
μ_o	oil viscosity
ω	base function
ϕ	porosity
Φ	potential function
Ψ	stream function

Subscript

a	average quantity
b	base or elementary functions
D,d	dimensionless parameter

Miscellaneous

upper case	dimensionless variable

References

[1] Fayers, F. J., Arbabi, S., and Aziz, K.: "Challenges in Reservoir Engineering from Prospects for Horizontal Wells," *Petroleum Geoscience*, (January 1995) **1**, No. 1, 13-23.

[2] Babu, D. K. and Odeh, A. S.: "Productivity of a Horizontal Well," *SPE Reservoir Engineering*, (November 1989) 417-421.

[3] Goode, P. A. and Kuchuk, F. J.: "Inflow Performance of Horizontal Wells," *SPE Reservoir Engineering*, (August 1991) 319-323.

[4] Haug, B. T.: "The Second Long-Term Horizontal Well Test in Troll: Successful Production From a 13-m Oil Column with the Well Partly Completed in the Water Zone," paper SPE 24943 presented at the 1992 SPE Annual Technical Conference and Exhibition, Washington D.C., October.

[5] Hoyland, L. A., Papatzacos, P. and Skjaeveland, S. M. : "Critical Rate for Water Coning: Correlation and Analytical Solution," *SPE Reservoir Engineering*, (Nov., 1989) 495-502.

[6] Wheatley, M. J.: "An Approximate Theory of Oil/Water Coning," SPE 14210 presented at the SPE 60th Annual Meeting, (Sept., 1985), Las Vegas.

[7] Papatzacos, P., Herring T. R., Martinsen R. and Skjaeveland, S. M.: "Cone Breakthrough Time for Horizontal Wells," *SPE Reservoir Engineering*, (Aug., 1991) 311-318.

[8] Efros, D. A.: "Study of Multiphase Flow in Porous Media," *Gastoptexizdat*, Leningrad, 1963 (in Russian) 351.

[9] Giger, F. M.: "Evaluation theorique de l'effet d'arete d'eau sur la production par horizontaux," *Revue de l'Institut Francais du Petrole*, (May-June 1983) **38** No. 3 (in French).

[10] Giger, F. M.: "Analytic 2-D Models of Water Cresting before Breakthrough for Horizontal Wells," *SPE Reservoir Engineering*, (November 1989) 409-416.

[11] Karcher, B. J., Giger, F. M., and Combe, J.: "Some Practical Formulas to Predict Horizontal Well Behavior," paper SPE 15430 presented at the SPE 61st Annual Technical Conference and Exhibition, New Orleans, Louisiana, October 5-8, 1986

[12] Joshi, S. D.: "Augmentation of Well Productivity with Slant and Horizontal Wells," *J. Pet. Tech.*, (June 1988) **40** 729-739.

[13] Joshi, S. D., *Horizontal Well Technology*, Pennwell books, Oklahoma (1991) 288-292.

[14] Chaperon, I.: "Theoretical Study of Coning Toward Horizontal and Vertical Wells in Anisotropic Formations: Subcritical and Critical Rates," paper SPE 15377 presented at the SPE 61st Annual Technical Conference and Exhibition, New Orleans, Louisiana, October 5-8, 1986.

[15] Guo, B. and Lee, R. L.: "An Exact Solution to Critical Oil Rate of Horizontal Wells with Water-Oil-Interface Cresting," Proceedings of the Lerkendal Petroleum Engineering Workshop, Trondheim, February 5-6 1992, 55-66.

[16] Muskat, M., *The Flow of Homogeneous Fluids through Porous Media*, McGraw-Hill, New York, (1937), 480-486.

[17] Meyer, H. L. and Garder A. O. : "Mechanics of Two Immiscible Fluids in Porous Media," *J. Applied Physics*, (Nov., 1954) **25** 11:1400-1406.

[18] Guo, B. and Lee, R. L.: "A Simple Approach to Optimization of Completion Interval in Oil/Water Coning Systems," *SPE Reservoir Engineering*, (Nov., 1993) 249-255.

[19] Piper, L. D. and Gonzalez Jr, F. M.: "Calculation of the Critical Oil Production Rate and Optimum Completion Interval," paper SPE 16206 presented at the SPE Production Operations Symposium, Oklahoma City, Oklahoma, March 8-10, 1987.

[20] Broyden, C. G., *Mathematics of Computation*, 1965, **19**, 577-593.

[21] Press, W. H., Teukolsky, S. A., Vetterling, W. T., and Flannery, B. P.: *Numerical Recipes in Fortran*, Cambridge University Press, Cambridge, 1992, 352-355.

Appendix: Semi-Analytical Solution for Critical Cresting Rate

The horizontal well is modeled as an infinite line sink, thus the 3D flow problem reduces to a 2D flow geometry in the Cartesian coordinates (x, y). The flow configuration for a water cresting problem (1/2 of the total domain) is depicted in Fig. 2.2. Complex potential $\gamma(z)$ is defined as

$$\gamma(z) = \Phi(x, y) + i\Psi(x, y) \tag{2.7}$$

in which Φ and Ψ are respectively the potential and stream functions, and $z = x + iy$. An appropriate functional form for γ for 2D flow problems involving sinks and sources is given by

$$\gamma(z) = \frac{q}{2\pi} \ln[\omega(z)] \tag{2.8}$$

Function $\omega(z) = f(x, y) + ig(x, y)$ is refered to as the "base function" which should be analytic, possess the correct periodicity, and the proper poles and zeros at sinks and sources for a given problem. Such a base function for our problem is provided by the function:

$$\omega(z) = \cot(\alpha z) \tag{2.9}$$

in which $\alpha = \pi/4x_e$, where x_e is the half well spacing transverse to the HW. The above function can be shown to yield the correct potential field for an infinite array of alternating sinks and sources with equal but opposite strengths q, needed to satisfy $\Phi = 0$ along $x = \pm x_e$. The base potential and stream functions are then given via the equations

$$\begin{aligned} \Phi &= \frac{1}{2} \ln(f^2 + g^2) \\ \Psi &= \arctan(g/f) \end{aligned} \tag{2.10}$$

resulting in

$$\Phi_b = -\frac{q}{4\pi} \ln \left[\frac{\sin^2 X - \cosh^2 Y}{\cos^2 X - \cosh^2 Y} \right] \tag{2.11}$$

$$\Psi_b = -\frac{q}{2\pi} \arctan \left[\frac{\sinh 2Y}{\sin 2X} \right] \tag{2.12}$$

where the dimensionless coordinates (X, Y) have the following definitions:

$$\begin{aligned} X &= \frac{\pi x}{4x_e} \\ Y &= \sqrt{\frac{k_h}{k_v}} \frac{\pi y}{4x_e} \end{aligned} \tag{2.13}$$

in which k_h and k_v are the horizontal and vertical permeabilities. The use of $\sqrt{k_h/k_v}$ rescales the $y-$coordinate for anisotropic conditions. Φ_b in Eq. (2.11) satisfies the requirement $\Phi_b \rightarrow (q/2\pi) \ln r$ when both X and Y are small (r is the distance to the well), and Ψ_b in Eq. (2.12) satisfies the requirement $\Psi_b \rightarrow -q/4$ along the axis $X = 0$ below the well.

We construct an approximate total potential function, Φ in the oil phase such that it satisfies Laplace's equation for steady state flow subject to all the boundary conditions of the problem. Our approximate potential is given by the well itself at depth H_w, an additional line sink of strength aq at depth S_1, and a line source of strength bq at S_2. The boundary conditions of the problem in terms of Φ and Ψ, in reference to Fig. 2.2, are:

(i) $\partial\Phi/\partial Y = 0$ and $\Psi = 0$ along the boundary BC. This constitutes BC as a no-flow boundary.

(ii) Constant potential, $\Phi = 0$, along the boundary CD.

(iii) $\partial\Phi/\partial X = 0$ along the boundary AB with $\Psi = 0$ above the HW and $\Psi = -q/2$ below the HW located at a distance H_w below the top boundary.

(iv) The boundary conditions on the OWC must satisfy $\Phi = -\triangle\rho \; g\frac{4x_e}{\pi}\sqrt{k_v/k_h}(H - Y)$ and $\Psi = \text{constant} = -q/2$.

The images of all three source/sink contributions have to be included in order to satisfy the no-flow boundary condition at the top of the reservoir.

The total potential and stream functions are then defined as

$$\Phi = A_1 + aA_2 + bA_3 \tag{2.14}$$

$$\Psi = B_1 + aB_2 + bB_3 \tag{2.15}$$

Functions A_1, A_2, and A_3 have the same forms as that of Φ_b in Eq. (2.11) with the only difference that they are now offset in the $Y-$direction by amounts H_w, S_1 and S_2 respectively, and also include their image terms. Similar comments apply to B_1 through B_3 in relation to Eq. (2.12).

Expressions for functions A_1 through A_3 in Eq. (2.14) are given by

$$\begin{aligned} A_1(X,Y) &= \Phi_b(X,Y-H_w)+\Phi_b(X,Y+H_w) \\ A_2(X,Y) &= \Phi_b(X,Y-S_1)+\Phi_b(X,Y+S_1) \\ A_3(X,Y) &= \Phi_b(X,Y-S_2)+\Phi_b(X,Y+S_2) \end{aligned} \tag{2.16}$$

and those for functions B_1 through B_3 in Eq. (2.15) are

$$\begin{aligned} B_1(X,Y) &= \Psi_b(X,Y-H_w)+\Psi_b(X,Y+H_w) \\ B_2(X,Y) &= \Psi_b(X,Y-S_1)+\Psi_b(X,Y+S_1) \\ B_3(X,Y) &= \Psi_b(X,Y-S_2)+\Psi_b(X,Y+S_2) \end{aligned} \tag{2.17}$$

The potential and stream functions defined in Eqs. (2.14) and (2.15) satisfy the Laplace's equation and the conditions on all the boundaries exactly, with the exception of the water/oil contact (condition (iv)). Our task is then to choose the four parameters of our potential function a, S_1, b, and S_2 to minimize the error on the contact.

Determination of Free Parameters

Four conditions are necessary to determine the four free parameters. Here we only present the conditions and the final resulting equations.

Condition 1: The stagnation point on the Y axis with coordinate Y_s is defined to be the point where

$$\partial\Phi/\partial Y|_{(X=0,Y=Y_s)} = 0. \tag{2.18}$$

This condition yields the following quadratic equation in $\cosh(4Y_s)$:

$$T_1\cosh^2(4Y_s)+T_2\cosh(4Y_s)+T_3=0. \tag{2.19}$$

in which

$$\begin{aligned} T_1 &= \cosh(2H_w)+a\cosh(2S_1)+b\cosh(2S_2) \\ T_2 &= -\cosh(2H_w)\cosh(4S_2)- \\ &\quad \cosh(4S_1)\cosh(2H_w)- \\ &\quad a\cosh(2S_1)\cosh(4S_2)- \\ &\quad a\cosh(2S_1)\cosh(4H_w)- \\ &\quad b\cosh(2S_2)\cosh(4S_1)- \\ &\quad b\cosh(2S_2)\cosh(4H_w) \\ T_3 &= \cosh(2H_w)\cosh(4S_1)\cosh(4S_2)+ \\ &\quad a\cosh(2S_1)\cosh(4H_w)\cosh(4S_2)+ \\ &\quad b\cosh(2S_2)\cosh(4H_w)\cosh(4S_1) \end{aligned} \tag{2.20}$$

Only one root of the above equation for Y_s satisfies the physical condition of $0 < Y_s < H$. The crest height is then fixed to be equal to Y_s, so that

$$\Psi(0, Y_s) = -q/2 \tag{2.21}$$

Condition 2: We fix the level of the stream function at the boundary point D by requiring that $\Psi(\pi/4, H) = -q/2$. This results in the following explicit equation for parameter a:

$$\begin{aligned} a \;=\; & [\pi - J(H - H_w) - J(H + H_w) - \\ & bJ(H - S_2) - bJ(H + S_2)] \,/ \\ & [J(H + S_1) + J(H - S_1)] \end{aligned} \tag{2.22}$$

in which $J(Y) = \arctan[\sinh 2Y]$.

In order to minimize the difference between the shapes of the potential function on the contact and the constant streamline, we use two conditions: (a) at a given X_m value, the interface from stream and potential functions cross each other, i.e., have the same height Y_m at a given X_m and (b) have the same slope at the crossing point (X_m, Y_m). Since it is more important to have a better match near the apex of the crest, a value of X_m close to $X = 0$ axis should be chosen.

Condition 3: The shape of interface from the potential function due to the boundary condition (iv) is given by

$$H + \frac{4\pi}{q} Q_d (A_1 + aA_2 + bA_3) - Y = 0. \tag{2.23}$$

Q_d is the dimensionless strength defined by

$$Q_d = \frac{q\sqrt{k_h/k_v}}{16 \triangle \rho g x_e} \tag{2.24}$$

The corresponding shape from the stream function is obtained from

$$B_1 + aB_2 + bB_3 + \frac{q}{2} = 0. \tag{2.25}$$

where A's and B's are given by Eqs. (2.16) and (2.17). We require that point (X_m, Y_m) simultaneously satisfies Eqs. (2.23) and (2.25).

Condition 4: We impose the condition that the shape of interface from potential and stream functions have the same slope at the crossing point $(X_m.Y_m)$. This condition implies the equation

$$dY/dX|_P - dY/dX|_S = 0 \tag{2.26}$$

Using the Cauchy-Riemann relations, the slope $dY/dX|_P$ from the potential function is given by

$$dY/dX|_P = \frac{\Psi_Y}{\Psi_X + \sqrt{k_v/k_h} \triangle \rho g 4 x_e/\pi} \tag{2.27}$$

in which $\Psi_Y = \partial\Psi/\partial Y$ and $\Psi_X = \partial\Psi/\partial X$. The slope from the stream function is given by

$$dY/dX|_S = -\frac{\Psi_X}{\Psi_Y} \tag{2.28}$$

Expressions for the partial derivatives of Ψ are analytically determined from Eq. (2.15).

Calculation of Critical Cresting Rates

An iterative procedure is used to determine the dimensionless critical rate Q_{dc}. A summary of the procedure is outlined below:

1. We start the iterative procedure by selecting *guess* values for Y_m, S_2, and b. A good value for X_m is 0.1.

2. S_1 is set to a value close to but smaller than S_2.

3. We solve for a from Eq. (2.22) and then for Y_s from Eq. (2.19).

4. Q_d is then calculated from Eq. (2.23) at point $(0, Y_s)$.

5. For a fixed Y_m, S_2, and b, S_1 is reduced and we repeat steps 3 and 4 until a maximum in Q_d, denoted by Q_{dc}, is obtained.

6. A new set of Y_m, S_2 and b is determined by simultaneously solving the three nonlinear Eqs. (2.23), (2.25), and (2.26). These equations are solved by the globally convergent Broyden's method [20] which is the counterpart of the secant method in multidimensions.

7. We repeat steps 2 through 6 until no further significant change ($< 10^{-8}$) in the parameters are made from one iteration to the next.

8. The shape of the interface from the stream and potential function is obtained respectively by solving for Y from Eqs. (2.23) and (2.25). This is accomplished by using the Brent's method [21] which is a combination of the bisection and inverse quadratic interpolation schemes.

To relate the critical reservoir well rate Q_c to Q_{dc}, we use Eq. (2.24) and thence

$$Q_c = \frac{1}{2}\frac{\sqrt{k_v k_h}}{\mu_o b_o} q_c \, L \tag{2.29}$$

3. Skin Factor Calculations for Vertical, Deviated, and Horizontal Wells (Task 2)

Research by Ph.D. student Raju Penmatcha
Advisors: Professors John Fayers and Khalid Aziz

3.1 Introduction

In order to calculate the productivity of a well we try to obtain a simultaneous solution between the reservoir and tubing calculations. While the tubing calculations is a whole different topic by itself, we try to concentrate on the completion calculations in this part of the study. Equations are given in Thomas et al. [1] that let us calculate the pressure drop induced in a reservoir due to the flow of fluids. While these equations are general and can be used for any completion, the skin factor in them varies from completion to completion. In this part of the work, a review is given on how to calculate this skin factor for various completions and how it can be used for reservoir pressure drop calculations for a vertical, deviated or a horizontal well. Equations are also presented for calculating non-Darcy flow effects and the effects of flow through a gravel pack. A computer code has been written in FORTRAN that can perform these calculations and the relative effects of various completions are compared using this code in the Appendix.

3.2 Radial Flow Equations

3.2.1 Vertical or Deviated Well

The following equations give the inflow relationship for pseudo-steady-state flow in vertical or deviated wells.

The equation for radial flow of oil from a reservoir where both the BHFP (bottom hole flowing pressure) and reservoir pressure are greater than the bubble point is [1],

$$q_O = J_O\left(\bar{p} - p_{wf}\right) \tag{3.1}$$

where

$$J_o = \frac{7.08 * 10^{-3} kh}{\left(B_o \mu_o \left\{ ln\frac{r_e}{r_w} - 0.75 - 0.5\, ln\frac{C_A}{31.62} + s \right\}\right)} \tag{3.2}$$

' r_e ' and ' r_w ' are the reservoir external radius and the wellbore radius respectively and ' $\bar{p}$ ' is the average reservoir pressure. ' C_A ' is the dimensionless shape factor. C_A=31.62 if the well is located at the center of a circular reservoir. More explanation is given on these shape factors by Dietz [2]. ' s ' is the skin factor. The calculation of ' s ' is described later.

For wells producing from an under-saturated reservoir with the BHFP less than the bubble point, the oil rate can be calculated as [3],

$$q_o = J_o\left(\bar{p}-p_b\right)+\left(\frac{J_o\bar{p}}{1.8}\right)\left[1-0.2\left(\frac{p_{wf}}{\bar{p}}\right)-0.8\left(\frac{p_{wf}}{\bar{p}}\right)^2\right] \tag{3.3}$$

where ' p_b ' is the bubble point pressure. The above equation is derived from the work of Vogel [4] and the details are given in [3].

For a gas reservoir, under pseudo-steady state conditions the gas flow rate is given as [3],

$$q_g = \frac{1.987*10^{-5}khT_{sc}\left[m(\bar{p})-m(p_{wf})\right]}{p_{sc}T\left[\ln\frac{r_e}{r_w}-0.75-0.5\left(\ln\frac{C_A}{31.62}\right)+s+Dq_g\right]} \tag{3.4}$$

where $m(p)=\int_{p_b}^{p}\frac{pdp}{\mu z}$ (3.5)

is the real gas pseudo pressure

' T_{sc} ' and ' p_{sc} ' are the temperature(60^0 F) and pressure (14.7 psia) at standard conditions. ' T ' is the reservoir temperature. ' D ' is the non-Darcy coefficient. Calculation of D is explained later. An explanation of all the terminology and the pertinent units is given in the Nomenclature.

For pressures below 1000 psi, Eq. (3.5) can be simplified as [3],

$$q_g = \frac{1.987*10^{-5}khT_{sc}\left[\bar{p}^2-p_{wf}^2\right]}{p_{sc}T\overline{z\mu_g}\left[\ln\frac{r_e}{r_w}-0.75-0.5\left(\ln\frac{C_A}{31.62}\right)+s+Dq_g\right]} \tag{3.6}$$

where $\bar{z}$ and $\overline{\mu_g}$ are calculated at the root mean square pressure given by $\left\{\frac{p^2+p_b^2}{2}\right\}^{0.5}$. This is because of the fact that $(\mu_g z)$ remains almost constant for pressures below 1000 psi.

For pressures above 5000 psi, it was observed [3] that $\left(\frac{p}{\mu_g z}\right)$ remains almost constant. Then for these pressures Eq. (3.5) simplifies to,

$$q_g = \frac{1.987 * 10^{-5} khT_{sc}(2p_i)\left[\bar{p} - p_{wf}\right]}{p_{sc}T\left(z\mu_g\right)_i\left[ln\frac{r_e}{r_w} - 0.75 - 0.5\left(ln\frac{C_A}{31.62}\right) + s + Dq_g\right]} \tag{3.7}$$

where p_i is the initial reservoir pressure.

Equations (3.1) - (3.7) can be used both for vertical and deviated wells. The difference between these two types of wells is captured by the skin due to well deviation. This skin remains zero for a vertical well while it becomes negative for a deviated well. Calculation of the skin due to well deviation is discussed later in section 3.3.5.

3.2.2 Horizontal Well

Equations (3.1) through (3.3) are applicable for pseudo-steady state in a horizontal well with the exception of the denominator for the PI in Eq. (3.2). The PI equation for single-phase oil flow where the wellbore pressure is greater than the bubble point pressure is given by [6]

$$J_o = \frac{7.08 * 10^{-3} kh}{B_o\mu_o\left(ln\frac{a_e + \left[a_e^2 - \left(\frac{L}{2}\right)^2\right]^{0.5}}{\left(\frac{L}{2}\right)} + \frac{\alpha h}{L} ln\frac{\left(\frac{\alpha h}{2}\right)^2 - (\alpha\delta)^2}{0.5\alpha h r_w} + s\right)} \tag{3.8}$$

where ' a_e ' is the major axis of the elliptical drainage area surrounding the well, ' α ' is $(k_H/k_V)^{0.5}$, and ' δ ' is the eccentricity or offset of the well from the center of the pay thickness.

3.3 Skin Factor

Figure 3.1 shows a typical well completion and illustrates perforation geometry, the damaged zone caused by drilling fluids, the crushed zone surrounding the perforation tunnel, casing pipe, and the cement behind the pipe. The skin factor used in the above equations can be calculated as follows. This skin which is referred to as laminar skin, occurs because of near-wellbore damage to the formation or limited entry and is constant for all flow rates.

Laminar skin $S = S_p + S_d + S_{cz} + S_{pp} + S_\theta$ (3.9)

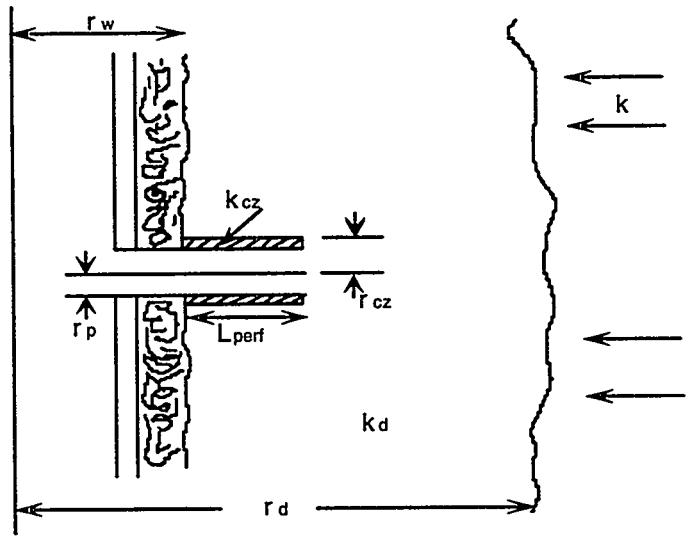

Figure 3.1: Perforation Geometry

with contributions from skins due to perforations (s_p), mud invasion(s_d), crushed zone(s_{cz}), partial penetration(s_{pp}), and well deviation(s_θ).

3.3.1 Calculation of Perforation Skin (s_p)

' s_p ' is the perforation skin. It is the skin caused due to the convergence of the flow lines into the perforations at the wellbore. Karakas and Tariq [7] have presented a semi-analytical expression for the calculation of the perforation skin, which they divide into components: the plane flow effect, s_H; the vertical converging effect, s_V; and the wellbore effect s_{wb}. Figure 3.2 illustrates some parameters in this model. Using a three-dimensional finite-element model, they formulated the dependency of perforation skin (s_p) on the angular perforation phasing (ϕ), the perforation length (L_{perf}) and the well radius (r_w).

The total perforation skin is given [8] as

$$s_p = s_H + s_V + s_{wb} \tag{3.10}$$

where

$$s_H = \ln \frac{r_w}{r_{wa}(\phi)} \tag{3.11}$$

' $r_{wa}(\phi)$ ' is the effective wellbore radius and is a function of the phasing angle 'ϕ ' . The skin due to the plane flow ' s_H ' is obtained using the ' effective well radius ' concept developed for vertical fractured wells by Prats [9].

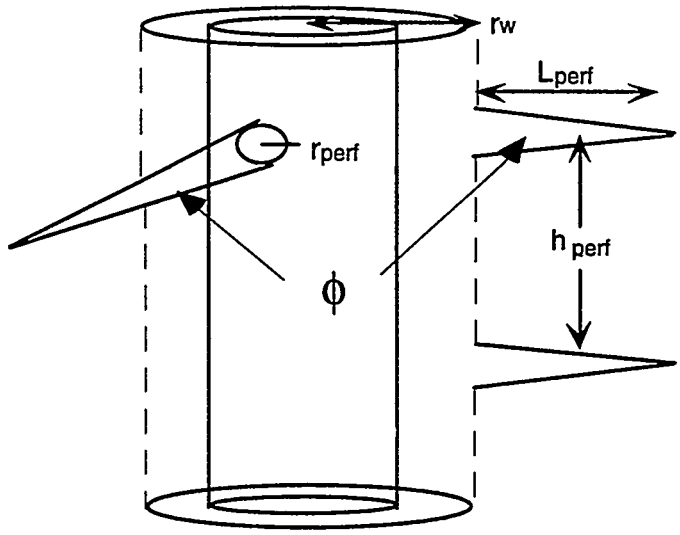

Figure 3.2: Perforation Skin Calculation

$$r_{wa}(\phi) = \frac{L_{perf}}{4} \quad \text{for} \quad \phi = 0$$

$$r_{wa}(\phi) = a_{\phi}\left(r_w + L_{perf}\right) \quad \text{for} \quad \phi \neq 0 \tag{3.12}$$

The constant ' a_{ϕ} ' depends on the perforation phasing and can be obtained from Table 3.1. The numerical values for ' a_{ϕ} ' were obtained by the authors [7] using finite-element simulations. This skin effect (s_H) is negative (except for $\phi = 0$), but its total contribution is usually small [8] (see example in Appendix).

and $$s_V = 10^{a} h_D^{b-1} r_D^{b} \tag{3.13}$$

where $$h_D = \frac{h_{perf}}{L_{perf}}\sqrt{\frac{k_H}{k_V}} \tag{3.14}$$

$$r_D = \frac{r_{perf}}{2h_{perf}}\left(1+\sqrt{\frac{k_V}{k_H}}\right) \tag{3.15}$$

$$a = a_1 \log r_D + a_2 \tag{3.16}$$

and $b = b_1 r_D + b_2$ (3.17)

a_1, a_2, b_1, b_2 are all functions of the perforation phasing and are given in Table 3.1. For large values of h_{perf} (less number of shots per foot), ' s_V ' can be large. ' s_V ' values can be minimized with deep penetrating perforators and/or high shot density perforating guns [8].

The skin due to the wellbore effect is given as [8],

$$s_{wb} = c_1 \exp(c_2 r_{wD}) \tag{3.18}$$

where $$r_{wD} = \frac{r_w}{L_{perf} + r_w} \tag{3.19}$$

The constants ' c_1 ' and ' c_2 ' are also given in Table 3.1. These constants are obtained from numerical simulations. This skin ' s_{wb} ' was found to be significantly larger for 0^o phasing than the multi-directional phasings.

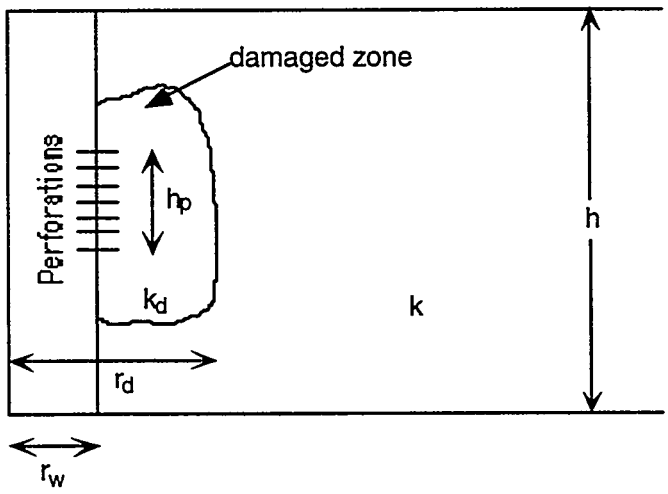

Figure 3.3: Partial Completion of a Well

3.3.2 Calculation of Damage Zone Skin (s_d)

Due to the flow of drilling mud into the formation, the permeability around the wellbore is reduced. Let ' k_d ' be the permeability and ' r_d ' the radius of this damaged zone. If the well is

completed along the entire length of the formation, then the Hawkin's formula [5] can be used to calculate the resulting skin.

$$s_d = \left(\frac{k}{k_d} - 1\right) \ln \frac{r_d}{r_w} \tag{3.20}$$

Now if the well is completed only partially as shown in Figure 3.3 then Jones et al. [10] suggested that Hawkin's formula can no longer be used since the flow into the well is no longer radial. Based upon the results from their numerical model they presented an adaptation of Hawkin's formula that can be used when the well is partially completed. It is as follows:

$$s_d = \frac{h}{h_p}\left[1 - 0.2\frac{(r_d - r_w)}{h_p}\right]\left(\frac{k}{k_d} - 1\right) \ln \frac{r_d}{r_w} \tag{3.21}$$

' h_p ' is the length of the perforated interval. This result theoretically applies only when ' h_p ' is small compared with ' h ' (total bed thickness) and when the perforated interval is in the center of the productive zone. But the authors suggested that for most cases of practical interest these restrictions can be ignored.

3.3.3 Calculation of Crushed Zone Skin (s_{cz})

The crushed zone around each perforation has a thickness of about 0.5 inches [11-13]. The permeability of this zone can be smaller or larger than the near-wellbore permeability, depending on whether compaction or collapse occurs. The equation for laminar skin through the crushed zone can be derived from the radial flow equations [11] and is given as

$$s_{cz} = \frac{h}{L_{perf}\, n_p}\left(\ln \frac{r_{cz}}{r_p}\right)\left(\frac{k}{k_{cz}} - \frac{k}{k_d}\right) \tag{3.22}$$

where 'r_p ' is the radius of the perforation. ' r_{cz} ' and ' k_{cz} ' are the radius and permeability of the crushed zone. When $k_{cz} = k_d$ then no additional damage was done due to the crushed particles and hence ' s_{cz} ' becomes zero.

3.3.4 Calculation of Partial Penetration Skin (s_{pp})

A positive skin results from a partially penetrating well. The necessary theoretical development is presented by Nisle [14] and in another paper by Brons et al. [15]. This skin is calculated from

$$s_{pp} = \frac{(1-b)}{b}\left[\ln\left(\frac{h\sqrt{\frac{k_H}{k_V}}}{r_w}\right) - G(b)\right] \tag{3.23}$$

where

$$G(b) = 2.948 - 7.363\,b + 11.45\,b^2 - 4.675\,b^3 \tag{3.24}$$

and ' b ' is the fractional penetration of the well. Equation (3.24) was determined numerically [16] by the same authors as in Ref [11].

3.3.5 Calculation of Well Deviation Skin (s_θ)

A deviated well gives negative skin. It is due to the increase in the producing-interval area exposed to flow. Cinco et al. [5] developed a pseudo skin factor which gives the difference between the dimensionless pressure created by a slanted well and that created by a vertical well. They suggested that standard well-test analysis methods are valid to analyze transient pressure data of a slanted well during the pseudo-radial flow period because the pressure-time relationship for this case is similar to that of a vertical well. However, the calculation of skin factor must be modified because of the difference between the pressure of a slanted well and the pressure of a vertical well. For slant angles from 0 to 75 degrees, and $\frac{h}{r_w} > 40$, the skin for a deviated well was evaluated as

$$s_\theta = -\left(\frac{\theta'}{41}\right)^{2.06} - \left(\frac{\theta'}{56}\right)^{1.865} \log_{10}\left(\frac{h_{wd}}{100}\right) \tag{3.25}$$

where

$$\theta' = \tan^{-1}\left(\sqrt{\frac{k_V}{k_H}}\tan\theta\right) \tag{3.26}$$

and

$$h_{wd} = \frac{h}{r_w}\sqrt{\frac{k_H}{k_V}} \tag{3.27}$$

3.4 Non-Darcy Flow

Non-Darcy flow occurs primarily in the near-wellbore region where fluid velocities are high. While this effect is usually negligible for single phase oil flow, it becomes important for gas flow at the wellbore. The equation for calculating the non-Darcy flow coefficient for gas flow comprises three components: crushed zone, damaged zone, and near-wellbore reservoir rock [17].

$$D = 2.22*10^{-15}\frac{kh\gamma_g}{\mu_g}\left\{\frac{\beta_{cz}}{n_p^2L_{perf}^2}\left(\frac{1}{r_p}-\frac{1}{r_{cz}}\right)+\frac{\beta_d}{h_p^2}\left(\frac{1}{r_w}-\frac{1}{r_d}\right)+\frac{\beta}{h^2}\left(\frac{1}{r_d}-\frac{1}{r_e}\right)\right\} \tag{3.28}$$

where

$$\beta = \frac{2.6*10^{10}}{k^{1.2}}$$

$$\beta_d = \frac{2.6*10^{10}}{k_d^{1.2}} \tag{3.29}$$

$$\beta_{cz} = \frac{2.6*10^{10}}{k_{cz}^{1.2}}$$

β is the turbulence factor.

3.5 Pressure Drop Due to the Gravel Pack

To prevent formation loss at the wellbore, wells are usually completed with gravel pack. This causes additional pressure drop to the flow of formation fluids. This pressure drop is a result of two components: gravel in the perforation tunnel and gravel between the liner and the casing.

For a gas well, the pressure loss through the gravel pack can be calculated [18,19] by,

$$p_{wf}^2 - p_{wperf}^2 = \frac{8.93zT\mu_g q_g L_{perf}}{k_{gr}A_p}+\frac{1.247*10^{-16}\beta_g zT\gamma_g L_{perf}q_g^2}{A_p^2} \tag{3.30}$$

where 'k_{gr}' is the gravel permeability in mD and $A_p = n_p\pi r_p^2$,

and

$$p_{wperf}^2 - p_{wliner}^2 = \frac{1424\,\mu_g z T q_g}{k_{gr} h}\left(\ln\frac{r_c}{r_L} - 0.5 + Dq_g\right) \tag{3.31}$$

where $$D = \frac{2.22*10^{-15}\beta\gamma_g k_g}{h_p \mu_g}\left(\frac{1}{r_L} - \frac{1}{r_c}\right) \tag{3.32}$$

Nomenclature

a_ϕ = constant

a_1 = constant

a_2 = constant

a_e = major axis of the elliptical drainage area for the horizontal well

A = area, ft^2

A_P = area of perforation, ft^2

b = fractional well penetration

b_1 = constant

b_2 = constant

B_g = gas FVF, ft^3/Mcf

B_o = oil FVF, RB/STB

c_1 = constant

c_2 = constant

C_A= shape factor, dimensionless (= 31.62 for a well at the center of a circular reservoir)

d = diameter, ft

D = non-Darcy flow coefficient, D/Mcf

G(b) = function of fractional well penetration 'b'

h = bed thickness, ft

h_D = dimensionless height

h_p = length of the perforated interval, ft

h_{perf} = height between perforations (= 1/np)

h_{wD} = dimensionless height w.r.t. wellbore (Eq. 3.27)

J_g = gas productivity index, Mcf/D/psi

J_o = oil productivity index, STB/D/psi

k = absolute permeability, mD

k_{cz} = crushed zone permeability, mD

k_d = damaged zone permeability, mD

k_{gr} = gravel pack permeability, mD

k_H = horizontal permeability, mD

k_r = relative permeability, fraction

k_V = vertical permeability, mD

L = horizontal well length, ft

L_{perf} = length of perforation tunnel, ft

$m(p)$ = real gas pseudo pressure, $psia^2/cp$

n_p = number of shots per foot

p = pressure, psia

$\bar{p}$ = average reservoir pressure, psia

p_b = bubble point pressure, psia

p_i = initial reservoir pressure, psia

p_{sc} = pressure at standard conditions, psia

p_{wf} = bottom hole flowing pressure, psia

p_{wperf} = perforation flowing pressure, psia

p_{wliner}= liner flowing pressure, psia

q_g = gas production rate, Mcf/D

q_o = oil production rate, STB/D

r_c = radius of casing, ft

r_{cz} = radius of the crushed zone, ft

r_d = radius of the damaged zone, ft

r_D = dimensionless perforation radius

r_e = reservoir external radius, ft

r_L = liner radius, ft

r_{perf} = radius of perforation, ft

r_w = wellbore radius, ft

r_{wa} = apparent (effective) wellbore radius

r_{wD} = dimensionless well radius

s = total laminar skin factor

s_{cz} = crushed zone skin factor

s_d = damaged zone skin factor

s_H = plane flow skin factor

s_p = perforation skin factor

s_{pp} = partial penetration skin factor

s_{wb} = wellbore skin factor

s_θ = well deviation skin factor

s_V = vertical flow skin factor

T = reservoir temperature, ^oR

T_{sc} = temperature at standard conditions, ^oR

z = gas compressibility factor

β = turbulence factor, 1/ft

γ_g = gas gravity (=1.0, for air)

α = aspect ratio $\left(\sqrt{\frac{k_H}{k_V}}\right)$

μ_g = gas viscosity, cp

μ_o = oil viscosity, cp

δ = eccentricity or offset of the well, ft

θ = well inclination angle, degrees

ϕ = perforation phasing angle, degrees

θ' = function of well deviation (Eq. 3.26)

Subscripts

b = bubble point

cz = crushed zone

d = damaged zone

D = dimensionless

e = external boundary, elliptic region

g = gas

gr = gravel pack

H = horizontal, plane flow

i = initial

L = liner

o = oil

p = perforation

perf = perforation

pp = partial penetration

sc = standard conditions

V = vertical

w = wellbore

wa = apparent wellbore

wb = wellbore

wf = well flowing

θ = well inclination

References

1. Thomas, L. K., Evans C. E., Plerson, R. G. and Scott, S. L.: "Well Performance Model," JPT (Feb. 1992) 220-29.

2. Dietz, D. N.: "Determination of Average Reservoir Pressure from Build-up Surveys," JPT (August 1965) 955-59.

3. Brown, K.E.: "The Technology of Artificial Lift Methods, Volume 4," PennWell Books (1984) 5-70.

4. Vogel, J.V.: "Inflow Performance Relationships for Solution Gas Drive Wells," JPT (Jan. 1968) 83-93.

5. Cinco-L., H., Miller, F. G., and Ramey, H. J. Jr.: "Unsteady-State Pressure Distribution Crested by a Directionally Drilled Well," JPT (Nov. 1975) 1392-1400; Trans., AIME, 259.

6. Joshi, S. D.: "Augmentation of Well Productivity Using Slant and Horizontal Wells," JPT (June 1988) 729-39; Trans., AIME, 285.

7. Karakas, M. and Tariq, S.: "Semi-analytical Productivity Models for Perforated Completions," SPE 18247.

8. Economides et al. "Petroleum Production Systems", PTR Prentice Hall (1994) 83-117.

9. Prats, M.: "The Effect of Vertical Fractures on Reservoir Behavior-Incompressible Fluid Case," SPEJ (June 1961) 105-117.

10. Jones, L. G. and Watts, J. W.: "Estimating Skin Effects in a Partially Completed Damaged Well," JPT (Feb. 1971) 249-52; Trans., AIME, 251.

11. McLeod, H. D. Jr.: "The Effect of Perforating Conditions on Well Performance," JPT (Jan. 1983) 31-39.

12. Klotz, J. A., Krueger, R. F. and Pye, D. S.: "Effect of Perforation Damage on Well Productivity," JPT (Nov. 1974) 1303-14; Trans., AIME, 257.

13. Saucier, R. J. and Lands, J. F. Jr.: "A Laboratory Study of Perforations in Stressed Formation Rocks," JPT (Sept. 1978) 1347-53.

14. Nisle, R. G.: "The Effect of Partial Penetration on Pressure Build-up in Oil Wells," Trans., AIME (1958) 213, 85.

15. Brons, F. and Marting, V. E.: "The Effect of Restricted Fluid Entry on Well Productivity," Preprint of paper 1322-G presented at 34th Annual Fall Meeting at SPE (Oct. 4-7, 1959) in Dallas.

16. Brons, F. and Marting, V. E.: "The Effect of Restricted Fluid Entry on Well Productivity," JPT (Feb. 1961) 172-74; Trans., AIME, 222.

17. Firoozabadi, A. and Katz, D. L.: "Analysis of High-Velocity Gas Flow Through Porous Media," JPT (Feb. 1979) 211-16.

18. Jones, L.G. and Blount, E.M.: "Use of Short-Term Multiple Rate Flow Tests To Predict Performance of Wells Having Turbulence," paper SPE 6133 presented at the 1976 SPE Annual Technical Conference and Exhibition, New Orleans, Oct. 3-6.

19. Saucier, R.J.: "Considerations in Gravel Pack Design," JPT (Feb. 1974) 205-12; Trans., AIME, 257.

Appendix: An Example Problem

Consider a well completed in a reservoir with the following properties:

Pay zone thickness h = 30 ft
Perforation thickness h_p = 10 ft
Wellbore radius r_w = 0.4 ft
Damaged zone radius r_d = 1.4 ft
Perforation radius r_p = 0.19 ft
Compacted zone radius r_{cz} = 0.19+0.5=0.69 ft
Absolute permeability of the pay zone k = 200 mD
Absolute permeability of the damaged zone k_d = 50 mD
Absolute permeability of the compacted zone k_{cz} = 5 mD
Absolute horizontal permeability k_H = k = 200 mD
Absolute vertical permeability k_v = 20 mD
Length of the perforation L_{perf} = 0.75 ft
Number of perforations per foot n_p = 52
Fractional penetration of the well b = 0.2
Well slant angle θ = 15°

Skin due to the Perforations (s_p)

The computer code is run for the cases given in Economides et al. [8] and the results in example 5-4 and Table 5-4 of that reference were exactly reproduced. From these examples, it was understood that s_V was the major contributor to s_p. In example 5-4, s_V=4.3, while s_H=-0.4 and s_{wb}=0.1. We next consider the sensitivities of these skins by using the values given above.

S_V (the vertical converging effect)

SPF	*k_V/k_H = 10*	*k_V/k_H = 5*	*k_V/k_H = 1*
0.5	21	15.6	7.6
1	10.1	7.5	3.6
2	4.7	3.5	1.6
4	2.1	1.5	0.7
8	0.8	0.6	0.2
20	0.2	0.1	0.03
40	0.03	0.02	0.002

The above Table shows that 's_V' becomes a small number for perforation densities higher than 4.

S_H(the plane flow effect)

Phasing Angle	*r_w=0.2*	*r_w=0.4*	*r_w=0.8*
0 (360)	0.07	0.8	1.5
180	-0.9	-0.4	0.03
120	-1.1	-0.6	-0.2
90	-1.2	-0.7	-0.3
60	-1.35	-0.85	-0.45
45	-1.4	-0.91	-0.51

So this skin is generally small and almost always negative.

S_{wb}(the wellbore effect)

r_w	*L_{perf} = 0.25*	*L_{perf} = 0.75*	*L_{perf} = 2.0*
0.2	0.5	0.3	0.2
0.4	0.8	0.4	0.25
0.8	1.2	0.6	0.3

This skin is also small for all these cases and the reduction is not much as the perforation length is increased. Also this skin increases as the wellbore radius is increased, because it is the skin caused due to the presence of the wellbore.

Skin due to the Damaged Zone (s_d)

The values given in the paper by Jones et al. [10] are reproduced by the computer code.

The skin caused by the damaged zone can be calculated from Eq. (3.21) as

$$s_d = \frac{h}{h_p}\left[1 - 0.2\frac{(r_d - r_w)}{h_p}\right]\left(\frac{k}{k_d} - 1\right)\ln\frac{r_d}{r_w}$$

$$= \frac{30.0}{10.0}\left[1.0 - 0.2\frac{(1.4 - 0.4)}{10.0}\right]\left(\frac{200}{50} - 1\right)\ln\frac{1.4}{0.4}$$

$$= 11.05$$

Now if k_d = 5 mD, then s_d = 143.65 (an increase of 13 times)

So, permeability reduction (k_d) has a larger effect on the skin than the penetration of damage (r_d). The penetration of damage 'r_d' is in the logarithmic factor and hence its effect is less pronounced.

Skin due to the Crushed Zone (s_{cz})

The example given in the appendix of Mcleod's paper was reproduced by the computer code.

The skin caused by the crushed zone can be calculated from Eq. (3.22) as

$$s_{cz} = \frac{h}{L_{perf}\, n_p}\left(\ln\frac{r_{cz}}{r_p}\right)\left(\frac{k}{k_{cz}} - \frac{k}{k_d}\right)$$

$$= \frac{30}{(0.75)(52)}\left(\ln\frac{0.69}{0.19}\right)\left(\frac{200}{5} - \frac{200}{50}\right)$$

$$= 35.71$$

If the crushed zone permeability is same as the damaged zone permeability (i.e., $k_{dp}=k_d$) then s_{dp} becomes zero, which is not very surprising.

Skin due to Well Deviation (s_θ)

The skin caused due to the deviation of the well can be calculated from Eqs. (3.25)-(3.27) as

$$\theta' = \tan^{-1}\left[\sqrt{\frac{k_V}{k_H}}\tan\theta\right]$$

$$= \tan^{-1}\left[\sqrt{\frac{20}{200}}\tan(15^o)\right] = 4.843$$

$$h_d = \frac{h}{r_w}\sqrt{\frac{k_H}{k_V}} = \frac{30}{0.4}\sqrt{\frac{200}{20}} = 237.17$$

$$s_\theta = -\left(\frac{\theta'}{41}\right)^{2.06} - \left(\frac{\theta'}{56}\right)^{1.865}\log_{10}\left(\frac{h_D}{100}\right)$$

$$= -\left(\frac{4.843}{41}\right)^{2.06} - \left(\frac{4.843}{56}\right)^{1.865} \log_{10}\left(\frac{237.17}{100}\right)$$
$$= -0.016$$

while s_θ is small when $\theta = 15^0$, $s_\theta = -1.79$ when $\theta = 65.9^0$ (example in Thomas et al.'s [1] paper).

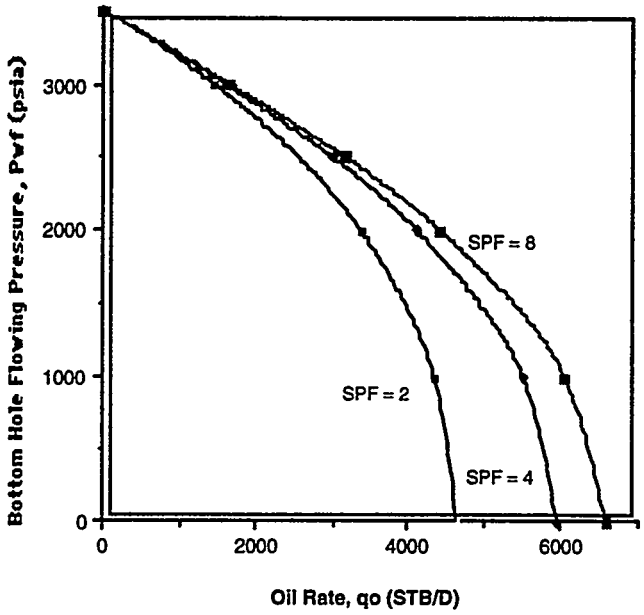

Figure 3.4: Well Flowing Pressure vs. Oil Rate

Calculation of J_o

Figure 2 in Thomas et al. [1] is exactly reproduced by the computer code. The results are shown in Figure 3.4

Numerical Comparison of Various Skin Factors

$s_H = 0.76$
$s_V = 0$
$s_{wb} = 0.41$
$s_p = 1.16$
$s_d = 11.05$
$s_{cz} = 35.7$
$s_{pp} = 14.3$
$sq = -0.02$

$s(total) = s_p + s_d + s_{cz} + s_{pp} + sq$
$= 62.20$

Table 3.1: Constants For Perforation Skin Effect Calculation

Perforation-Phasing Angle	a_ϕ	a_1	a_2	b_1	b_2	c_1	c_2
0 (360)	0.250	-2.091	0.0453	5.1313	1.8672	1.6E-1	2.675
180	0.500	-2.025	0.0943	3.0373	1.8115	2.6E-2	4.532
120	0.648	-2.018	0.0634	1.6136	1.7770	6.6E-3	5.320
90	0.726	-1.905	0.1038	1.5674	1.6935	1.9E-3	6.155
60	0.813	-1.898	0.1023	1.3654	1.6490	3.0E-4	7.509
45	0.860	-1.788	0.2398	1.1915	1.6392	4.6E-5	8.791

4. A Dissipation-Based Coarse Grid System and its Application to the Scale-up of Two Phase Problems (Tasks 2 and 4)

Research work by Ph.D student Tomomi Yamada
Advisors: Professors Thomas Hewett and John Fayers.

4.1 Introduction

A horizontal well is one of the prospective choices to develop low permeability reservoirs. However, predicting their production performance is a difficult problem if the low permeability is the result of heterogeneous sand-shale sequences. This will be one of the situations where a stochastic approach plays an important role in accessing uncertainties in the production forecast.

Advances in geostatistical techniques enable engineers to produce an unlimited number of equiprobable reservoir images on the basis of all the available information that includes well logs, seismic response, geological setting, and so on. These images are typically generated with 10^4 cells for two dimensional and 10^6 cells for three dimensional models. Furthermore, one has to simulate the flow of hydrocarbons on hundreds of these equiprobable stochastic realizations to get some sense of uncertainty. Therefore, it is necessary to reduce the computation time for each simulation even if a very fast supercomputer is available.

There are mainly two types of approaches to accomplish this, scaling up and streamtube mapping methods. Scaling up is an attempt to represent fine scale heterogeneities with coarser grids for a finite difference formulation. Streamtube mapping is the mapping of one-dimensional saturation profiles along streamlines derived from the full-field Laplace solution. It is commonly recognized that existing scaling up techniques tend to suffer from inaccuracy problems while streamtube methods are inherently limited in their applicability.

The inaccuracy for existing upscaling techniques is most pronounced if they are applied to solving fluid flow in the vicinity of wells or in extremely heterogeneous reservoirs. However, an upscaling approach could be more widely applicable than streamtube mapping if its accuracy is drastically improved.

The purpose of this work is to develop a new method to calculate coarse grid transmissibilities and effective relative permeabilities for the scaling up of two phase problems, that can be used for characterizing reservoirs with extremely heterogeneous variations of permeability, where flow is driven by realistic boundary conditions.

4.2 Existing Methods Based on Isolated Elements

Fig. 4.1 is a cross section of a sand shale sequence generated with a sequential indicator simulation technique [2]. Sand (white cells) permeability is 100 mD and shale permeability (black cells) is 0.1 mD. The volumetric fraction of shale is 0.434 of the total rock volume.

Figure 4.1: Sand/Shale Sequence for Scale-up

Water Rel-Perm	$k_{rw} = S_w^2$
Oil Rel-Perm	$k_{ro} = S_o^2$
Water Viscosity	1.0 cp
Oil Viscosity	1.0 cp
Capillary Pressure	Neglected
Gravity Effect	Neglected

Table 4.1: Two Phase Sample Problem

The reservoir is dipping to the right at about 12 degrees to the horizontal plane. This geological structure is represented with fine cells of 140 in the horizontal and 58 in the vertical directions.

As a starting point, existing upscaling methods are tested to see how they behave for this sample problem. The single phase and two phase fine-scale flow response is approximated with 11 by 11 coarser grids shown by the thicker lines in Figure 4.4. In both cases, the well(s) are modeled by the actual PI calculated from the full field Laplace solution.

A single well problem is modeled for the single phase sample problem. A horizontal well is located at the center and is producing oil under constant pressure (5002.20 psi) outer boundary conditions. The well is represented as four fine grids at the center with a large permeability. A full permeability tensor for each isolated coarse grid is calculated under periodic boundary conditions [4] and the pressure field is solved on the coarse grid system. One of the advantages of this method is the fact that the derived permeability tensor is guaranteed to be symmetric and positive definite. However, the result shows a significant difference between the coarse grid pressure solution (Fig. 4.2) and the fine grid reference solution sampled at coarse grid nodes (Fig. 4.3). The coarse grid well pressure is 4219.2 psi, 123% greater in the total draw down than the corresponding fine grid result (4648.8 psi). The pressure contours also fail to capture the dipping feature that is reflected in the fine grid isobars.

In contrast to single phase problems, there are few methods developed for two phase scaling up. Kyte and Berry's method [6] is tested here since it is commercially available and is commonly used in the industry. The standard use of this method is to 'pseudoize' vertical heterogeneity to a coarser grid for a typical cross section, using pseudo relative permeability functions. Sometimes the intention is to reduce a three-dimensional problem to a two-dimensional one, assuming the cross section is representative of the entire reservoir. The technique is applied to isolated coarse grids here for scaling up a two-phase displacement process. Absolute permeabilities (K_x and K_y) are calculated using a Laplace solver ([3]). For this sample problem, a constant rate of water is injected from a horizontal well at the lower left and the same reservoir volume of total liquid is produced from the producer at the upper right (see Fig. 4.4). The external boundary is no flow. Two phase properties are given in Table 4.1. Gravity is neglected for simplicity.

Fig. 4.5 shows the resultant well performances from the coarse grid simulation, plotted along with the reference fine grid result. Well pressures of both the injector and the producer from the coarse grid simulation are far from the fine grid result. A convergence problem that

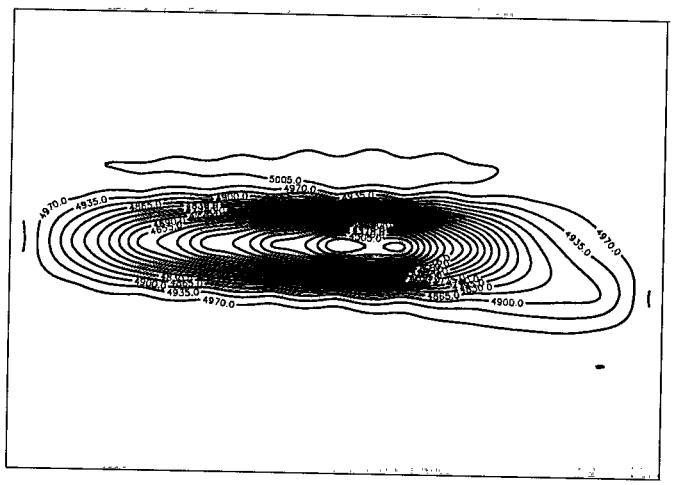

Figure 4.2: Isobar from Coarse Grid Simulation Using K_{tensor}

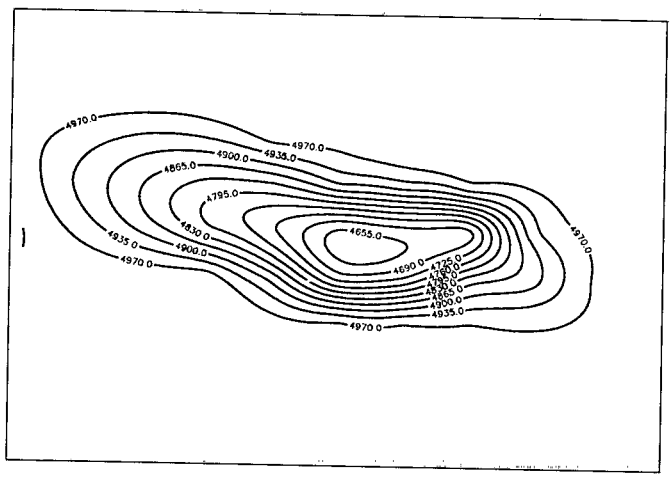

Figure 4.3: Fine Grid Pressure 'Sampled' at Coarse Grid Nodes

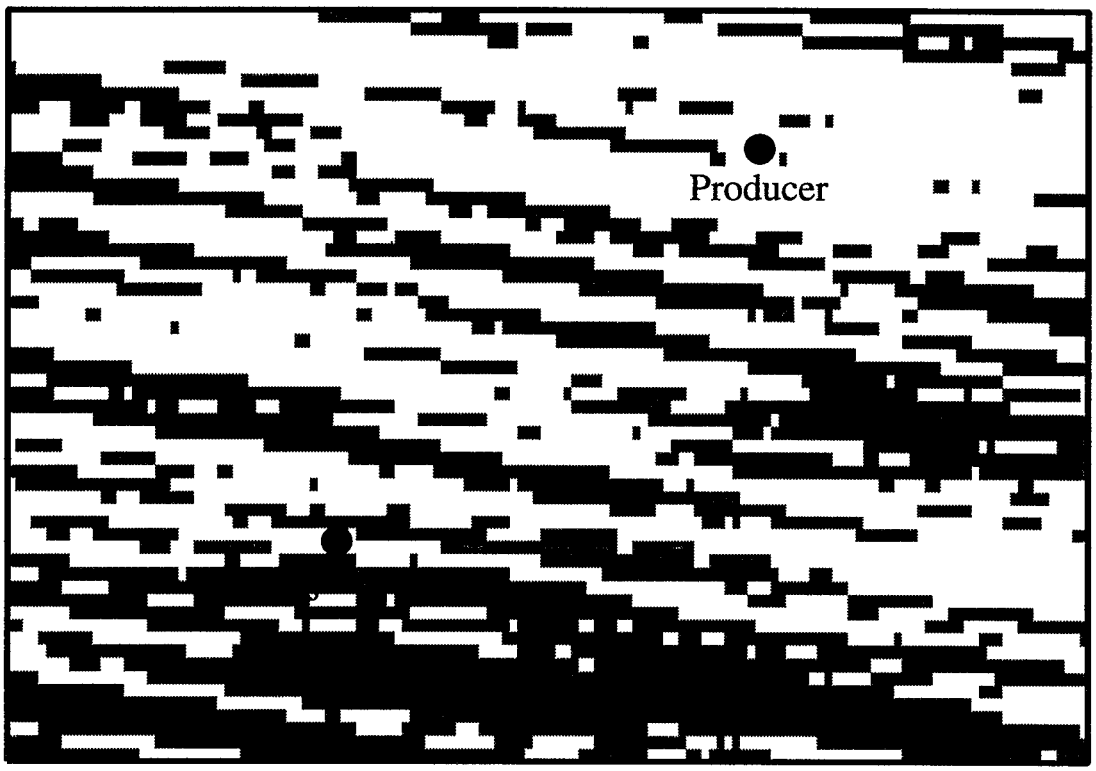

Figure 4.4: Two Phase Sample Problem

occurred around $0.48PV$ injection terminates the coarse grid run, but there had been no water production in the coarse grid case up to that time.

An inherent problem for scaling-up techniques based on isolated elements is that there is no way to know the actual flow geometry within a coarse grid when it is embedded in full field models. As Yamada and Hewett [9] pointed out, effective flow properties are strongly dependent on the boundary conditions for extremely heterogeneous media. The use of periodic boundary conditions is a sophisticated approach to generalize real boundary conditions; however, the results tell us that it is not sufficient for this kind of problem.

The inaccuracy for the two phase problem comes from the implicit assumption that flow is parallel to the grid orientation, which is not appropriate for a problem with extremely tortuous flow paths. Scaling up of two phase flow needs to be done on a grid system that correctly captures the flow geometry so that the grid orientation effect is minimized.

Using the full field Laplace solution under real boundary condition is the way to settle these problems. Here all the flow properties are calculated specific to the imposed global boundary conditions. Once these outer boundary conditions are applied, there is no need to worry about applying special pressure gradients on internal boundaries. Scalar expressions of permeability or transmissibility and relative permeabilities across an interface are sufficient when the exact internal boundary conditions are imposed. Of course, they may need to be updated as the outer boundary conditions change. The advantage of this concept will be judged on the basis of a comparison of computation time and accuracy for these sample problems.

4.3 Dissipation–Based Coarse Grid System

The essential task of scaling up is to find a way to satisfy the physics on both fine and coarse scales at the same time. As pressure and flux are the primary concern in single phase problems, the material balance is the one to be preserved. That can be done by defining coarse grid transmissibilities as,

$$T_{ij} = \frac{Q_{ij}}{\Delta P_{ij}} \tag{4.1}$$

Where,

$$Q_{ij} = \sum_k q_{ij}^k \tag{4.2}$$

The q_{ij}'s are fluxes from fine grid simulations. Their sum along any coarse grid interface also satisfies the material balance in an incompressible single phase system, i.e.

$$\textbf{(flux in)} = \textbf{(flux out)} \tag{4.3}$$

Therefore, once the coarse grid system is defined by transmissibilities derived from Q_{ij}'s, it reproduces fine grid pressure distributions as a solution of the coarse grid Laplace equations.

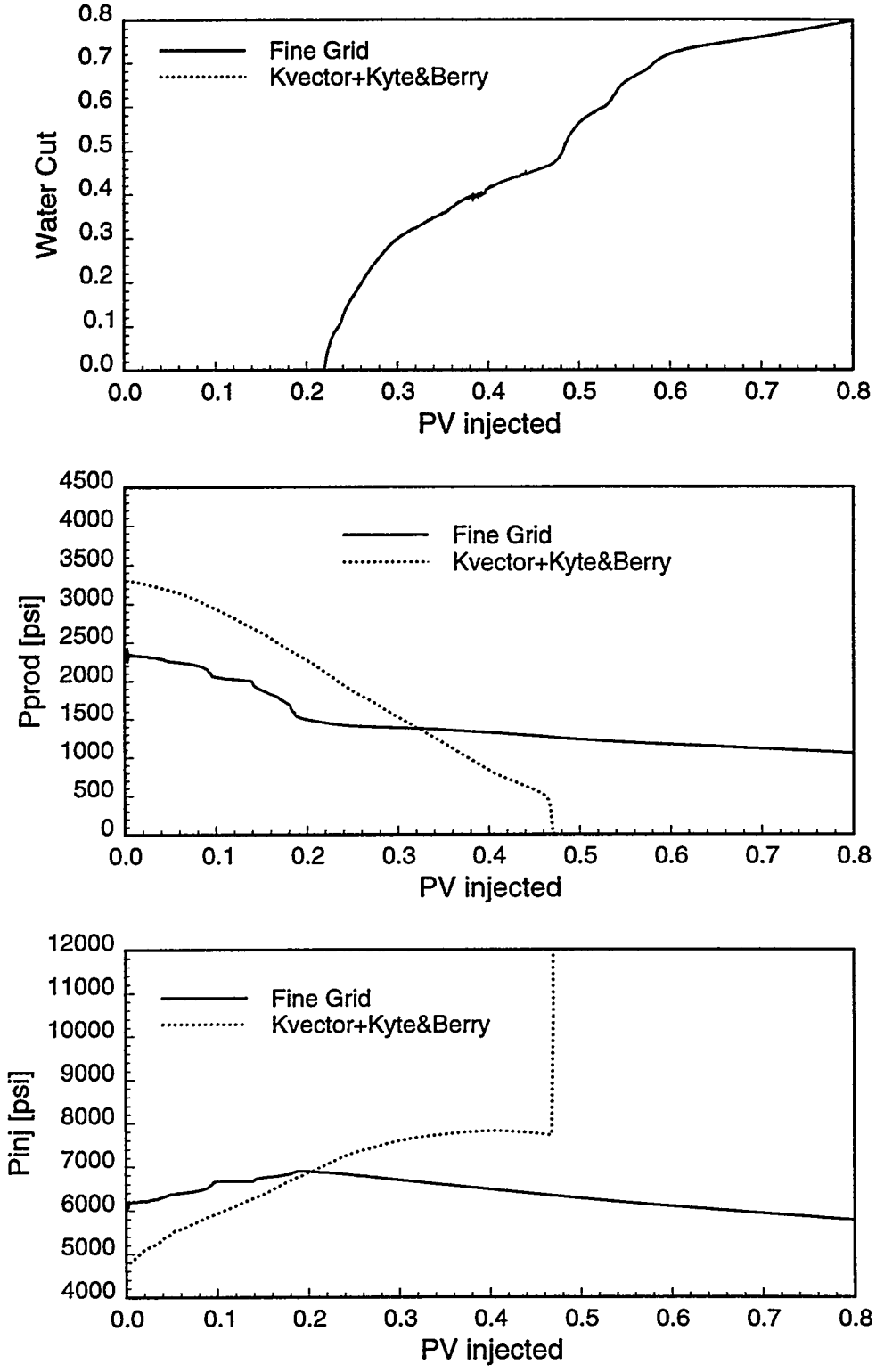

Figure 4.5: Coarse Grid Solution from Kyte & Berry's Method

However, if this approach is applied, some of the transmissibilities turn out to be negative (marked by gray circles in Fig. 4.6), which means fluid is flowing against the apparent pressure gradient. Although the pressure field could be solved in spite of these negative transmissibilities by a direct solver, the computation may not converge if an iterative solver is used. Generally, use of negative transmissibilities would lead to difficulties in reservoir simulation. This is related to a physical instability of the coarse grid system. The concept is clearly illustrated by looking at dissipation of energy due to flow in a porous medium. Dissipation is defined in a finite difference form as,

$$\dot{S} = \sum_i \sum_j \left\{ -q_{xi,j}(P_{i+1,j} - P_{i,j}) - q_{y_{i,j}}(P_{i,j+1} - P_{i,j}) \right\} \tag{4.4}$$

where

$$q_{xi,j} = -T_{xi,j}(P_{i+1,j} - P_{i,j}) \tag{4.5}$$

If this is differentiated with respect to the grid pressures,

$$\begin{aligned} &\frac{1}{2}\frac{\partial \dot{S}}{\partial P_{i,j}} = \\ &\quad +T_{xi-1,j}(P_{i,j} - P_{i-1,j}) + T_{y_{i,j-1}}(P_{i,j} - P_{i,j-1}) \\ &\quad -T_{xi,j}(P_{i+1,j} - P_{i,j}) - T_{y_{i,j}}(P_{i,j+1} - P_{i,j}) = \\ &\quad -Q_{xi-1,j} - Q_{y_{i,j-1}} + Q_{xi,j} + Q_{y_{i,j}} \end{aligned} \tag{4.6}$$

This is a material balance equation if the right hand side is equated to zero. The second derivative of dissipation is,

$$\frac{1}{2}\frac{\partial^2 \dot{S}}{\partial P_{i,j}^2} = T_{xi-1,j} + T_{y_{i,j-1}} + T_{xi,j} + T_{y_{i,j}} \tag{4.7}$$

Which is the sum of transmissibilities for all interfaces of each coarse cell.

Usually, one is solving the material balance equation to find a stationary point of dissipation. If all of the second derivatives are positive, the material balance relation minimizes dissipation, which is more commonly called 'Entropy Production' ([1]). This fact is relevant to the second law of thermodynamics which states that entropy is minimized at equilibrium. However, if part of the second derivative is negative, the material balance solution may be at the saddle point, instead of the minimum. Such a state is physically unstable. The state of the system is easily destroyed even by a small physical or numerical pressure perturbation.

Two important requirements have been presented here for deriving coarse grid transmissibilities. First, they must be calculated from fluxes of fine grid full field Laplace solutions under the real boundary conditions, which ensures the coarse scale material balance. Second, they need to be nonnegative, which guarantees the coarse grid system to be physically stable. The only possible approach that satisfies both requirements is to modify the coarse grid boundaries. Remember that Eq. 4.1 can be applied regardless of coarse grid shapes. However, as modifying one interface may affect the surrounding transmissibilities, it must be done systematically so that all transmissibilities are nonnegative at the same time.

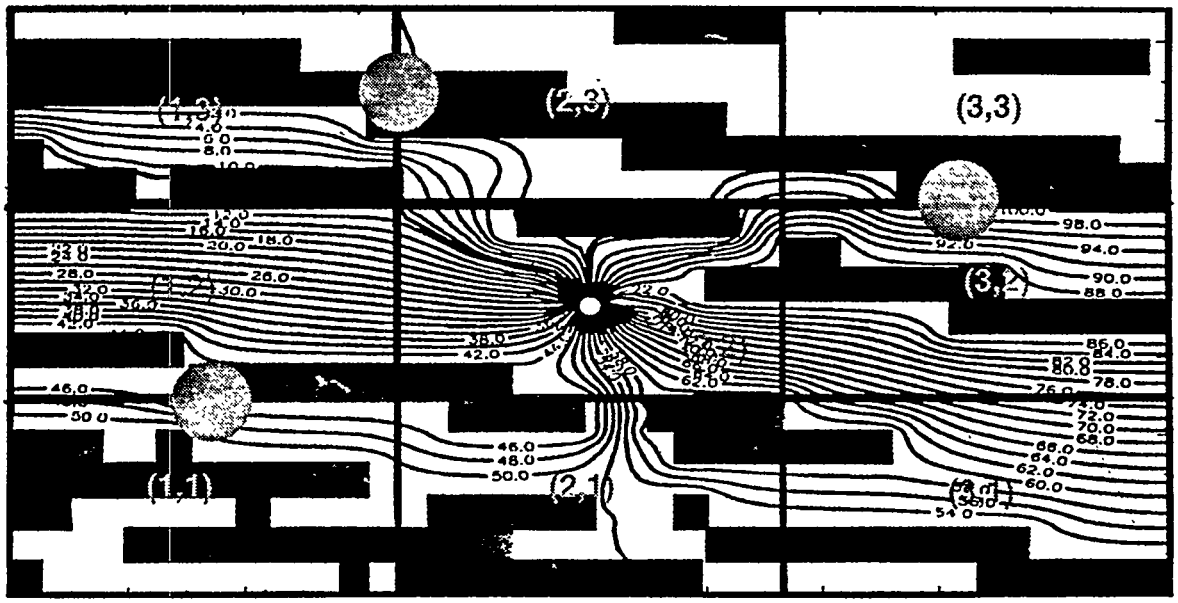

Figure 4.6: Simplified Up-Scaling Problem for Illustration of the Method

This can be done by working in a transformed space with potential function (Φ) and stream function (Ψ) as coordinates. Fig. 4.7 is the transformation of Fig. 4.6, in which any horizontal line is a streamline and any vertical line is an isobar, vertical edges are flux boundaries and horizontal edges are no flow boundaries, the height is the total flux and the width is the total pressure drop, and any area is dissipation. The nine coarse grids occupy strange shaped areas. Grid (2,2) extends over the total flow rate because it includes the well while all other grids are squeezed into the right of the Φ-Ψ plane. These grid areas collapse to vertical line segments whatever their original shapes are as they are assigned single pressures on the coarse scale.

Accordingly, dissipation in the coarse grid system has a rectangular area in transformed space as it is expressed as,

$$\dot{S} = q \cdot \Delta P = \Delta\Psi \cdot \Delta\Phi \tag{4.8}$$

Consider that energy dissipates when fluid goes between cell centers, across cell interfaces. The dissipation due to flow across an interface is a rectangle bounded by its pressure drop and flow rate. Fig.4.8 is the Φ-Ψ plane filled with dissipation areas due to all interfaces. The entire plane must be filled but there can be some overlaps of these areas. In fact, there are three overlaps in this case because of the complicated flow geometry. When there is an overlap, there must be a negative area that cancels the duplicate, which results in a negative transmissibility.

If the $\Phi - \Psi$ plane is refilled without any overlaps by modifying grid boundaries, all dissipation areas will be positive and there will be no negative transmissibilities. This can be done graphically. In order to do this, the boundaries of the original coarse grid blocks are reshaped systematically to conform to a requirement for positive dissipations. In achieving this, it becomes necessary to allow for diagonal connections.

The inversion of the new dissipation boundaries in (Φ, Ψ) space to generate the deformed coarse grids in the physical space is shown in the upper part of Fig. 4.9. The node

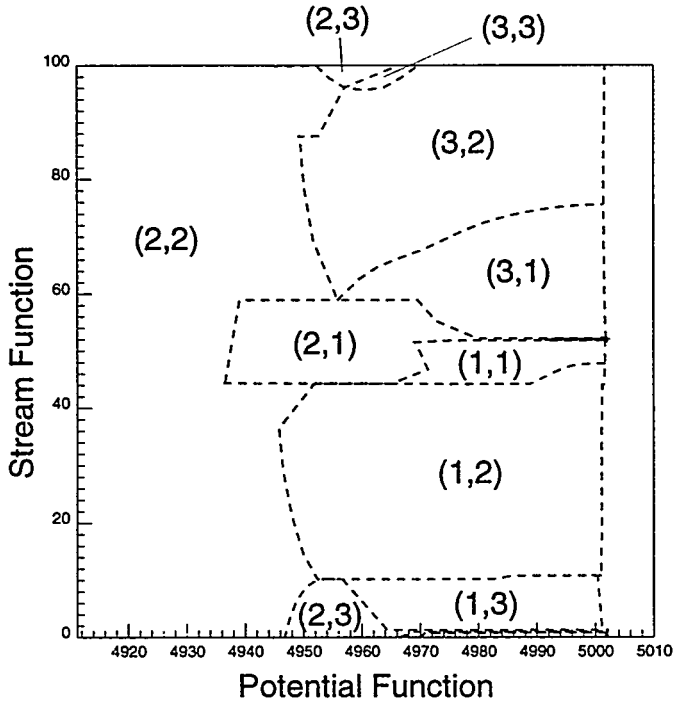

Figure 4.7: Transformed Coarse Grids in $\Phi - \Psi$ Space

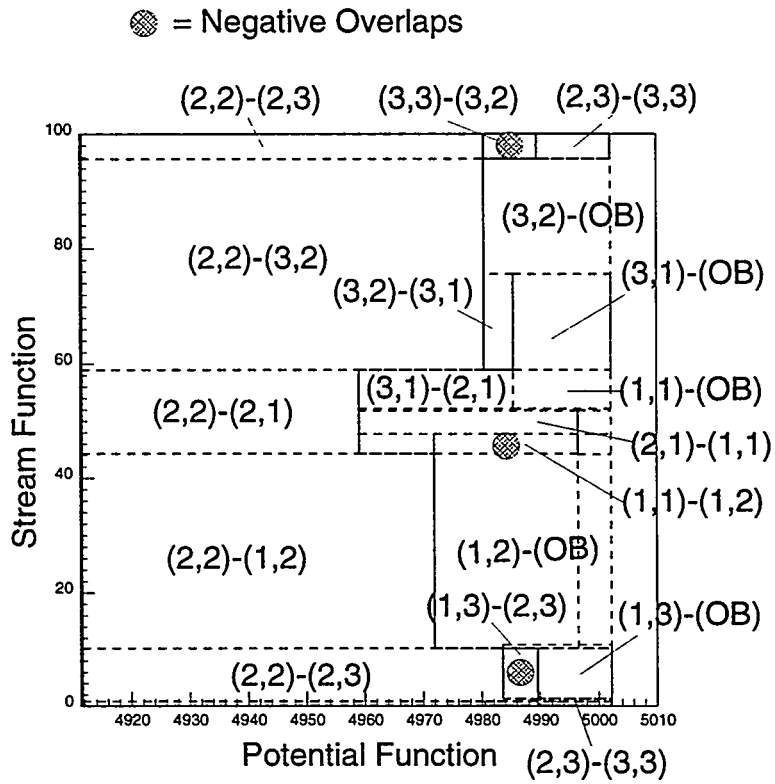

Figure 4.8: Rectangular Dissipation Areas Due to Grid Interfaces

centers for the deformed coarse gid are retained at their previous regular positions.

Finally, transmissibility for each connection is calculated as,

$$T = \frac{\sum_k \dot{S}}{\Delta\Phi^2} \tag{4.9}$$

where the summation is taken over all the streamtubes which cross the modified interfaces. For validation, these transmissibilities are input in the ECLIPSE simulator and the resulting single phase incompressible problem is solved on the coarse grid. The dissipation-based transmissibilities are explicitly specified to the simulator. Non-neighbor connections are used to deal with the added diagonal connections.

The result is shown in Fig. 4.9. The fine grid pressure solution is almost exactly reproduced. The well pressure from the coarse grid simulation is 4911.63psi, only 0.01psi different from the reference solution.

4.4 Derivation of Pseudo-Relative Permeabilities

In order to complete the two phase coarse grid system, a relative permeability function for each interface needs to be constructed.

We recall that a reshaped coarse grid is a cluster of rectangular dissipation areas in the $\Phi - \Psi$ space. Its inversion to the physical space is a bundle of streamtubes, which is one of the advantages of this method. The dissipation-based reshaped coarse grid system makes it possible to bring a streamtube approach into the finite difference formulation.

Upscaled relative permeability can be defined by superposing the saturation, the fractional flow and the mobility of streamtubes that constitute a reshaped coarse grid. There are three steps to do that. First, establish the relationship between displacement front locations of streamtubes. Second, define the representative values of each streamtube. Finally, find appropriate averaging criteria to derive grid effective values from these streamtube values.

The first step can be solved by using the same concept as Dykstra and Parsons approach [5] for a two layer displacement model. The two layers are replaced by an arbitrary pair of streamtubes and the method is extended to non-piston like displacement. Information from the Laplace solution, including flow rate, pressure profile, and local volume along streamtubes are used.

Starting with Darcy's law and using the concept of linear scaling, an equation can be derived which links front positions in pairs of streamtubes. This can be expressed in the form:

$$F(x_{f_d}^{\,l}) = R_{k,l} F(x_{f_d}^{\,k}) \tag{4.10}$$

where $R_{k,l}$ is a relative dimensionless speed ratio for tubes l and k and F is a characteristic dimensionless energy for each tube as a function of x_{fd}. x_{fd} is the dimensionless displacement front location, and is specific to each streamtube. Equation (4.10) is derived from the fact that the product of the flow resistivity and the flux, which is the total pressure drop along a streamtube, is always equal among streamtubes that share common boundaries.

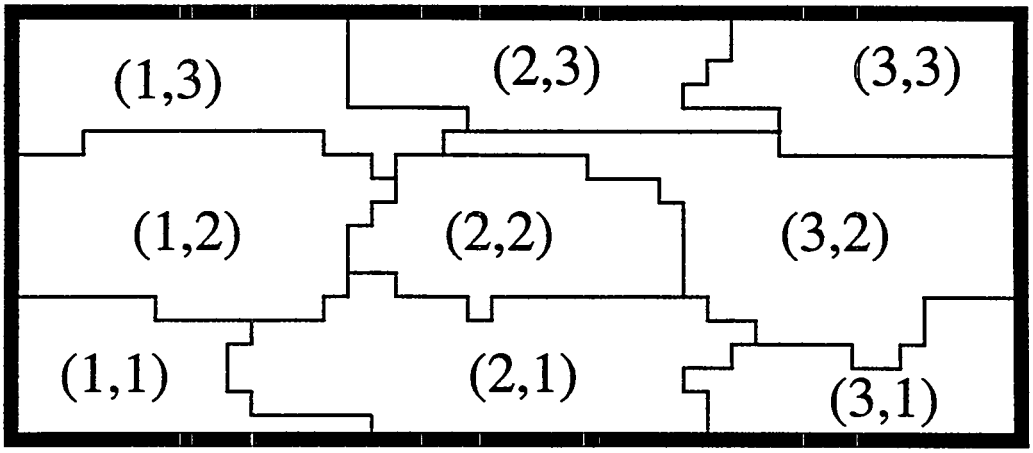

(A) Reshaped Coarse Grids

Fine: 4983.59 Coarse:4983.46	Fine: 4989.59 Coarse:4989.56	Fine : 5002.12 Coarse:5002.09
Fine : 4971.94 Coarse:4971.91	See Pwf	Fine : 4980.53 Coarse:4980.50
Fine: 4996.57 Coarse:4996.54	Fine: 4959.09 Coarse:4959.05	Fine: 4985.53 Coarse:4985.49

(B) Pressure Solution

Figure 4.9: Reshaped Coarse Grid System and Pressure Solution for Nine point Scheme:$Pwf(Fine) = 4911.63psi, Pwf(Coarse) = 4911.62psi$

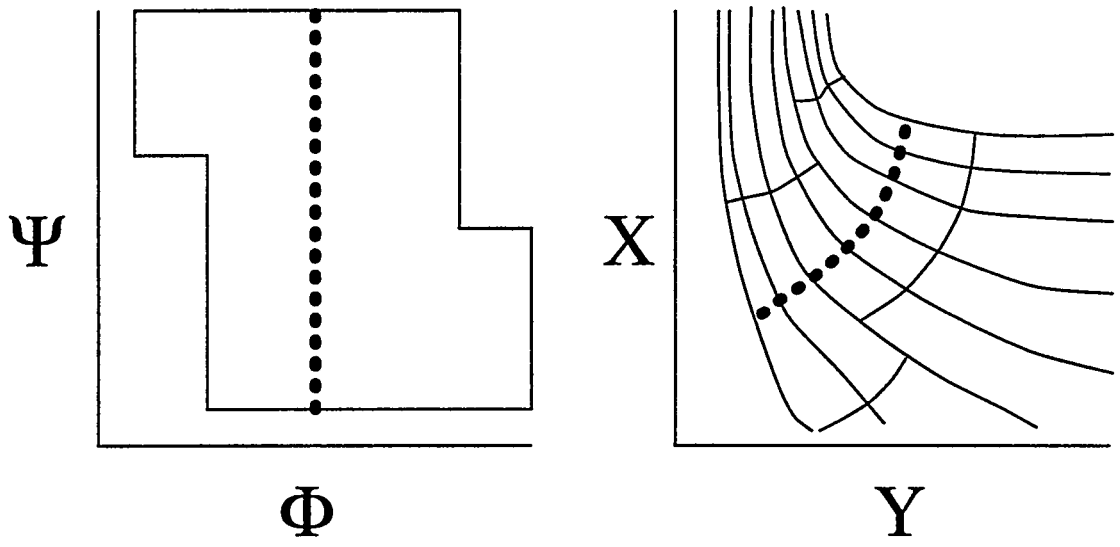

Figure 4.10: Reshaped Coarse Grid in $\Phi - \Psi$ Space and Physical Space

The scaling factor, R is defined from the streamtube volumes, V_{end}, and initial fluxes of the pair:

$$R_{k,l} = \left[\frac{q_0^l V_{end}^k}{q_0^k V_{end}^l}\right] \tag{4.11}$$

Notice that these equations are independent from other streamtubes. There is no need for time marching to get the relation for relative positions of displacement fronts. Once the functions $F(x_{f_d})$ are calculated for all streamtubes, the front of a streamtube can be established from that of any other tube.

The next step is to find the two phase flow properties for each streamtube. The one dimensional Buckley-Leverett profile is input and scaled with respect to the front locations. The water saturation is integrated over each streamtube segment. Relative mobility and fractional flow are defined at the inlet interface of each coarse grid because of upstream weighting.

Finally, these are averaged over streamtube volumes contained with a deformed grid block to get effective values. The grid saturation is the volume-weighted average of streamtube saturations.

$$\bar{S}_w(t) = \frac{\sum_{l=1}^{n^G} \Delta V S_w^l}{\sum_{l=1}^{n^G} \Delta V} \tag{4.12}$$

The effective relative mobility is defined as a property of the interface and is derived from the relation of total flux to pressure drop. Its final form is an initial-flux-weighted sum of streamtube relative mobilities.

$$\bar{\lambda}_t(t) = \sum_{l=1}^{n^I} \left(\frac{q_0^l}{Q_0}\right) \lambda_t^l(t) \tag{4.13}$$

The effective fractional flow is also specific at the interface and comes from the phase

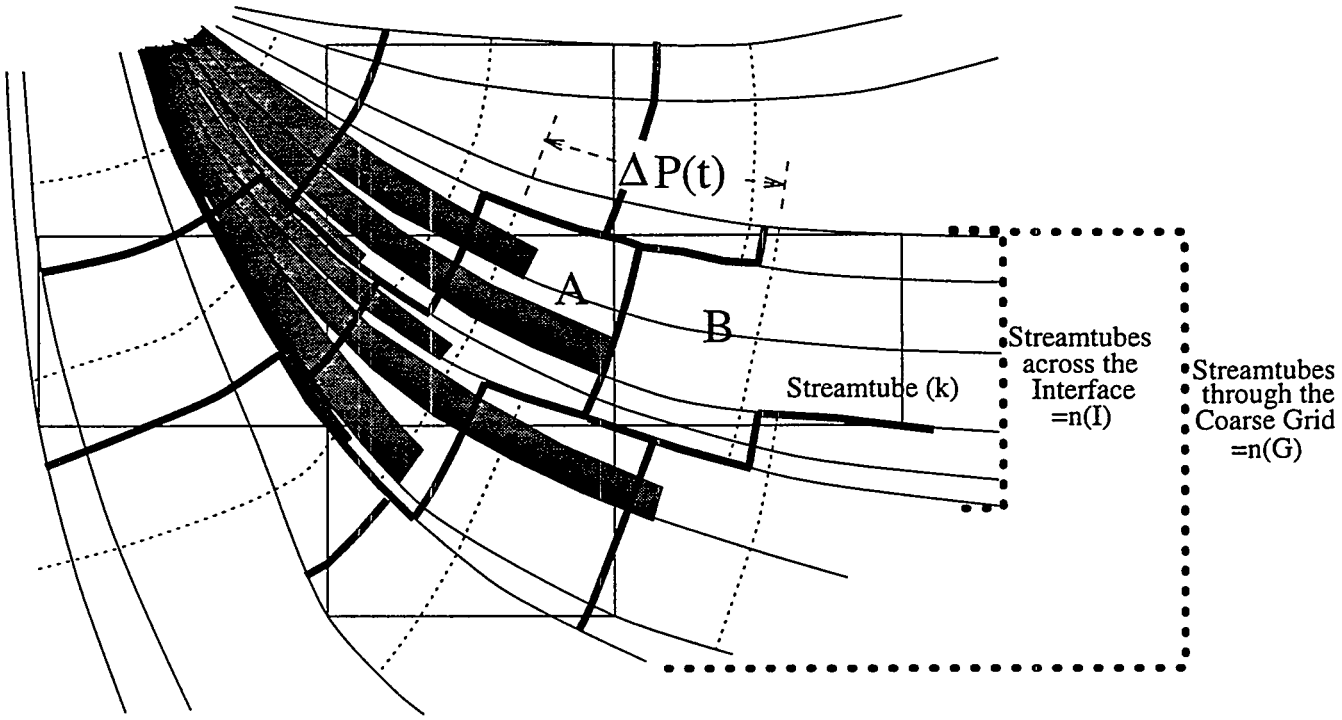

Figure 4.11: Superposition of Streamtube Flow Properties

flux and pressure drop. It is a mobility-normalized initial flux-weighted sum of streamtube fractional flows.

$$\bar{f}_w(t) = \sum_{l=1}^{n^I} \left(\frac{q_0^l}{Q_0}\right) \left(\frac{\lambda_t^l(t)}{\bar{\lambda}_t(t)}\right) f_w^l(t) \tag{4.14}$$

The effective relative permeabilities of an interface are calculated as,

$$\bar{k}_{rw}(t) = \bar{f}_w(t)\bar{\lambda}_t(t)\mu_w \tag{4.15}$$

$$\bar{k}_{ro}(t) = (1.0 - \bar{f}_w(t))\bar{\lambda}_t(t)\mu_o \tag{4.16}$$

Since both the saturations and relative permeabilities are known as functions of time, they can be evaluated simultaneously to calculate the relative permeabilities as functions of saturation.

The above semi-analytical procedure for solving Buckley-Leverett problems along streamtubes completely eliminates the need for a fine grid numerical solution of the two-phase flow problem to generate coarse grid pseduo-functions.

4.5 Applications

The method is validated by applying it to the two phase problem presented in Fig. 4.4. In the original coarse grid system, 28 out of a total of 220 interfaces had negative transmissibilities. After the modification of coarse grid boundaries, 180 positive transmissibilities and 75 non neighbor connections were defined. Effective relative permeabilities were specified for all of the 255 interfaces and the producing well.

Some typical effective relative permeabilities for the water phase are presented in Fig. 4.12 along with the rock curves. They do not necessarily preserve the features of the rock curves. The calculated transmissibilities and relative permeabilities were explicitly specified to a commercial simulator (ECLIPSE).

The well performance from the fine grid, coarse grid with new transmissibilities and relative permeabilities (W/ RPERM), and coarse grid with the new transmissibilities but with the original rock relative permeabilities (W/O RPERM) are compared in Fig. 4.13. The fine grid solution is closely tracked by "W/ RPERM" while "W/O RPERM" results in a significant delay in water breakthrough. We also show in Fig. 4.13 the results which would be obtained by using standard procedures, in which $\bar{k}_x$ and $\bar{k}_y$ are computed for each coarse grid using a Laplace solver, and the pseudo relative permeabilities are evaluated from the Kyte and Berry method. The last results are very unsatisfactory.

Fig. 4.14 shows the water saturation distribution from the fine grid simulation immediately after water breakthrough (0.24 PV Injection). We have averaged the fine grid results over reshaped coarse grids for comparison purposes. Solution from "W/O RPERM" and "W/ RPERM" cases at the same time are presented in Fig. 4.15 and 4.16, respectively. Preferential flow paths observed in the fine grid result is clearly reproduced for the "W/ RPERM" case while the "W/O RPERM" case misses preferential paths.

Two other cases were tested to see the effect of changing mobility ratio. These were end point mobility ratios of 0.2 and 5.0. The same rock k_r functions were used but the viscosity ratio of water and oil was changed. The results are presented in Fig. 4.17 as plots of recovery against pore volume injection. Water cut of the three cases presented at the end of the simulation is around 80%, usually regarded as watered-out.

There is a good agreement between the fine grid and the coarse grid results. The difference is within a few percent of recovery, except for the end part of $M_{end\ point} = 0.2$, which is discussed later.

The total computation time for these particular problems is a few hundred seconds CPU, including solving Laplace equations, calculating dissipation based transmissibilities, deriving effective relative permeabilities, and the coarse grid simulation, while the fine grid simulation takes several hundred thousand second CPU. About 1/1,000 of computation time is required to approximate the fine grid result.

4.6 Advantage over Streamtube Mapping Methods

So far the discussion has been based on a comparison with existing single phase and two phase upscaling techniques. However, recent advances in streamtube mapping methods provide quite accurate, numerical-dispersion-free solutions for heterogeneous reservoirs [8] and they are a potential substitute for upscaling methods in many aspects in production forecasting. Although dissipation-based scaling up has been shown to dramatically improve the accuracy in forecasting well performance and displacement processes, it remains to be seen if this method is also advantageous over streamtube methods.

Of course, one of the definite advantages of the proposed method is the fact that all the existing facilities in the ECLIPSE simulator can be used through the finite difference formulation. Besides that, the new method is widely applicable to problems with different

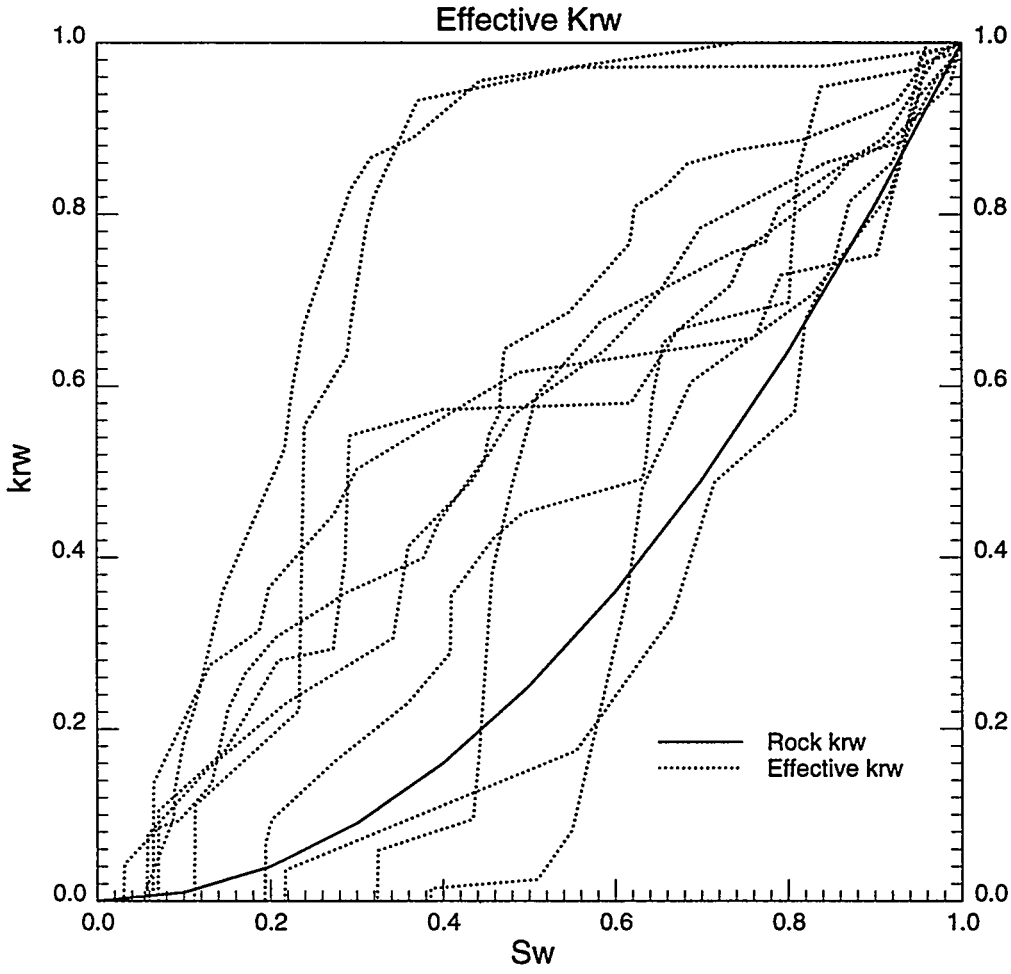

Figure 4.12: Typical Effective k_{rw}'s for $k_{rw} = S_w^2$, $\mu_o/\mu_w = 1.0$

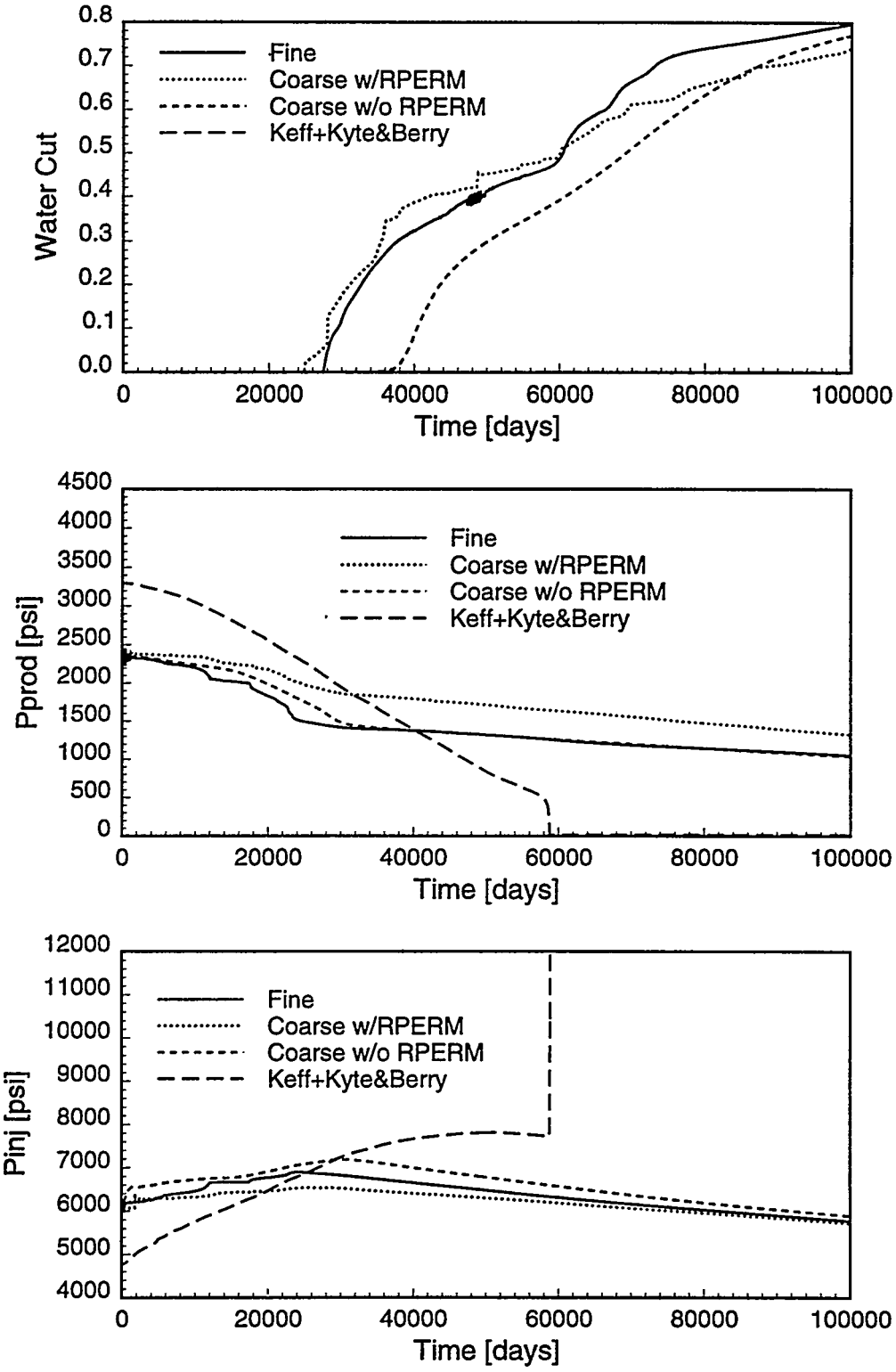

Figure 4.13: Well Performance, k_{rw}'s for $k_{rw} = S_w^2$, $\mu_o/\mu_w = 1.0$

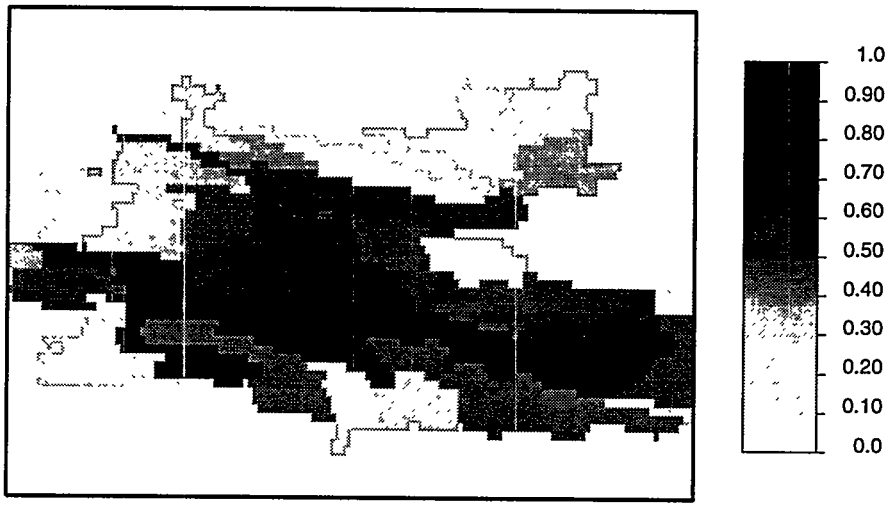

Figure 4.14: Water Saturation at 0.24 PV Injection, Fine Grid Solution for $k_{rp} = S_p^2 \quad \mu_o/\mu_w = 1.0$

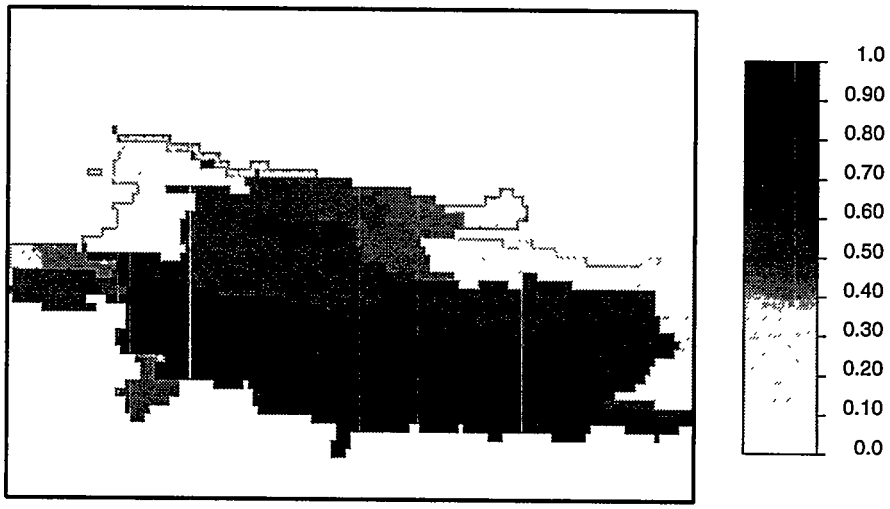

Figure 4.15: Water Saturation at 0.24 PV Injection, Coarse Grid with Rock k_r's, $k_{rp} = S_p^2 \quad \mu_o/\mu_w = 1.0$

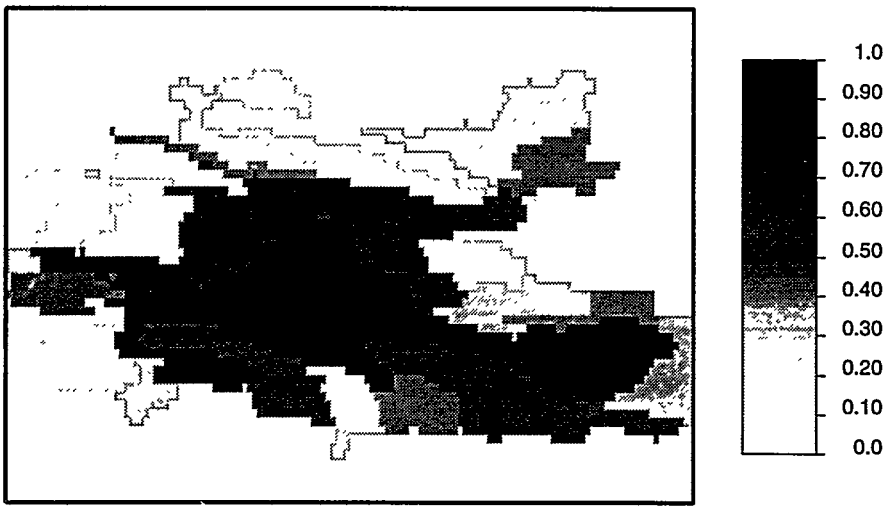

Figure 4.16: Water Saturation at 0.24 PV Injection, Coarse Grid with Derived Effective k_{rp}'s, for rock $k_{rp} = S_p^2 \quad \mu_o/\mu_w = 1.0$

features. As is commonly known, streamtube approaches assume that the fluids and the formation are incompressible and the initial water saturation must be uniform. However, there are certain situations where these assumptions do not hold. The following examples demonstrate the applicability of the new method to problems for which streamtube methods cannot readily be used.

4.6.1 Pressure Transient Problem

One of the situations where fluid and formation compressibilities are important is the transient pressure problem where formation fluid is driven to a well by compressive forces until boundary effects dominate. In this example, the drawdown pressure of the producer in Fig. 4.4 right after the beginning of production is calculated. The injector starts water injection at the same time as the production commences. Thus, this is a two phase pressure drawdown problem in a waterflooding situation. The compressibilities assumed for oil, water, and rock for this case are $1.5 \times 10^{-5}[psi^{-1}]$, $3.0 \times 10^{-6}[psi^{-1}]$, and $3.0 \times 10^{-6}[psi^{-1}]$, respectively. These are typical values in real problems.

Fig. 4.18 is the log-log plot of ΔP and the pressure derivative simulated by both fine grid and coarse models. The agreement between the two simulations is extremely good except for the very beginning of the production, which is usually masked by wellbore storage and skin effects in field cases and typically is neglected. Although the new method is based on incompressible flow mechanisms, it also gives a good approximation for compressible problems of this kind.

4.6.2 Infill Well Problem

An infill well project is one of the cases where a non-uniform initial water saturation distribution is involved. The equivalent involving horizontal wells is as follows.

The 'Injector' in Fig. 4.19 displaces oil toward 'Producer 1' which is completed at the same height. After the water-out of 'Producer 1', its interval is abandoned and 'Producer 2',

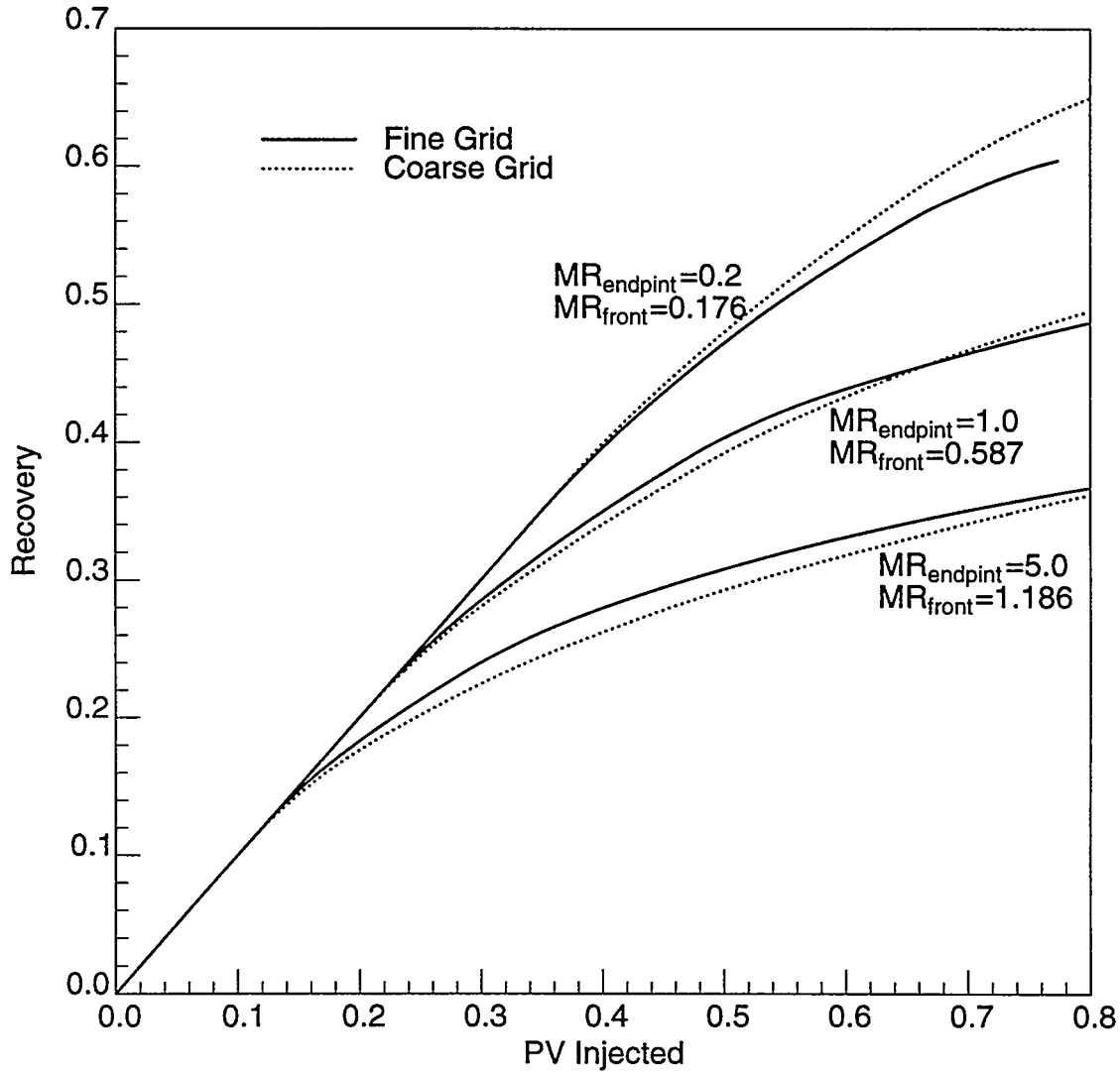

Figure 4.17: Recovery vs PV Injected

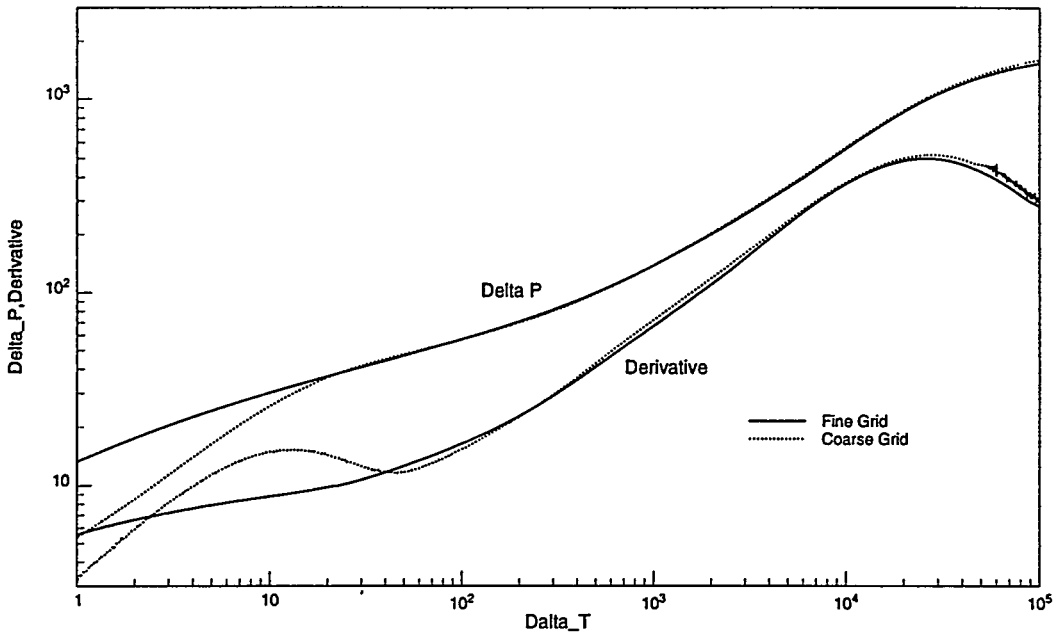

Figure 4.18: Pressure Transient under Waterflooding

is recompleted by side track above the previous one and put into production immediately. Now 'Producer 2' has to start production from a nonuniform initial water saturation as is shown in Fig. 4.20.

Transmissibilities and relative permeabilities for the coarse grid simulation are recalculated for a restart run as the inner boundary condition (well) has been changed. Herein, a single phase Laplace solution is used again. The saturation at the end of the initial run is re-averaged over the new coarse grids for the restart run.

The recovery from the coarse grid simulation is shown along with the fine grid result in Fig. 4.21. The producer is switched at about $0.24PV$ of water injection when the water cut is around 80%. There is a few percent of difference in the recovery, which mainly comes from the first producer, partly because there are only three coarse grids between the 'Injector' and 'Producer1' grids. However, the overall approximation will be acceptable for practical use.

This result indicates that the derived effective k_r's are capable of approximating the advance of displacement fronts in a formation with non-uniform initial water saturation distribution, although they are based on the Buckley-Leverett approach that assumes uniform initial water saturation.

4.7 Future Development

Although the new method improves the accuracy of scaling up and is more widely applicable than streamtube mapping techniques, there is a potential for further improvement in both accuracy and applicability.

Figure 4.19: Side Track Completion to Recover Unswept Oil

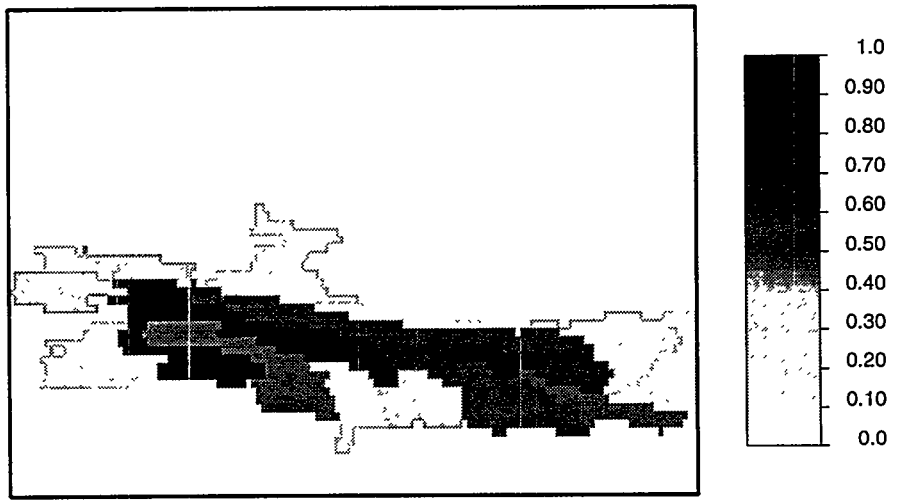

Figure 4.20: Initial Water Saturation for the Side Track Interval

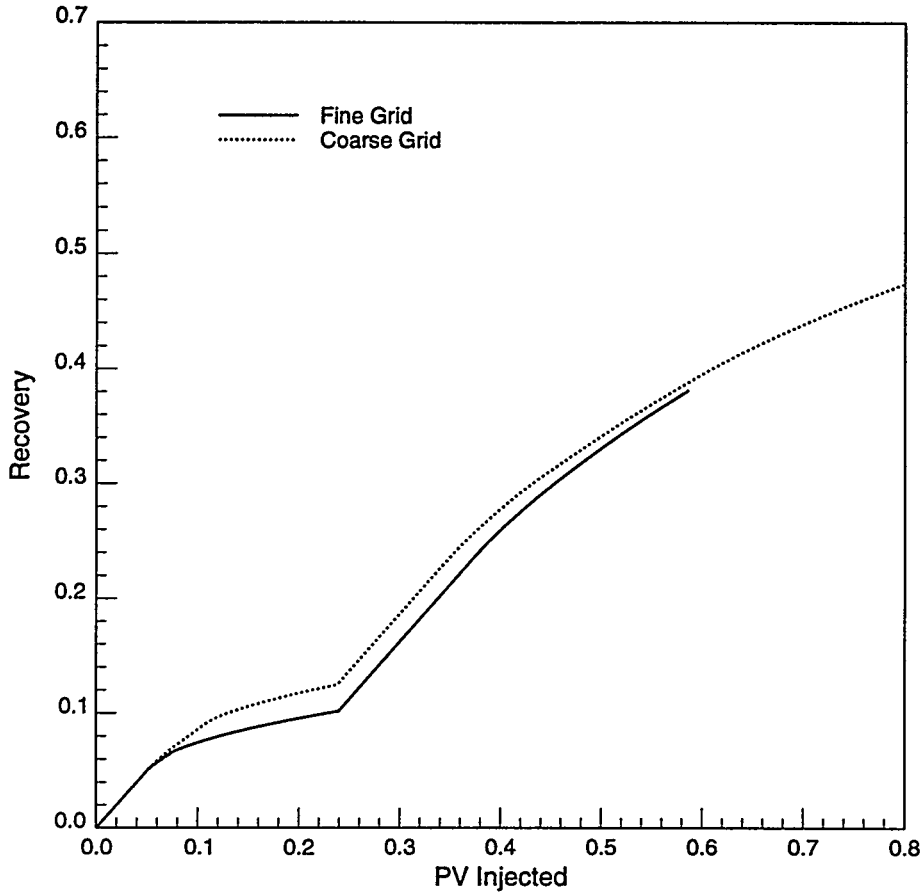

Figure 4.21: Comparison between Fine Grid and Coarse Grid Result, Side Track Problem

- In this work, the streamtube geometry is assumed to be fixed at the initial (single phase) state and only the change in flux with the advancement of the displacement front is considered. Neglect of streamtube deformation at the displacement front is related to the error in the coarse grid solution for cases with favorable end point mobility ratios. As discussed in a previous work [7], the mobility contrast at the front controls the deformation of the flow geometry. As a recent work on the streamtube method showed, a few updatings of streamtubes cures the problem [8]. Updating of transmissibilities and relative permeabilities should also solve the problem for this method. To achieve upscaling, an inhomogeneous Laplace equation needs to be solved as the mobility distributions change. The computation cost remains much less than for a fine grid simulation.

- The $\Phi - \Psi$ transformation requires that the streamfunction at each fine grid node be uniquely defined. The current version uses numerical integration from an origin to get Ψ values. This method causes the same value of Ψ to be assigned to more than one streamline, if there are more than a pair of injector/producer within the domain, due to discontinuities of Ψ around wells (this is not a problem if the wells are at the boundary grids). This problem can be solved if some other methods, like streamline tracking, are used for the stream function calculation.

- In general, a displacement phenomenon consists of more than one physical process and may include viscous, gravity, capillary, and diffusivity processes. However, only the viscous displacement is modeled here and the others are neglected for simplicity. Studies on applying streamline methods to problems with gravity are being pursued.

- The program is coded for two dimensional problems. As is common in model development, the next step will be three dimensional problems. Although the same concept will work, the stream functions are replaced by bistream functions($\Psi 1$ and $\Psi 2$), the $\Phi - \Psi$ plane by $\Phi - \Psi 1 - \Psi 2$ space, the dissipation area by dissipation volume, and so on. The maximum number of connections for a grid is 8 for 2-D, but it will be 26 in 3-D. The computational capacity will also be a critical problem for scaling-up calculations in 3-D.

- The minimum resolution of the method is given by the size of the fine grid. The volume of a streamtube is expressed in terms of the number of fine grid nodes it involves. Thus, some streamtubes get only a single fine grid volume or, even zero volume. This will be part of the reason for the difference from a fine grid solution. Improvement of the volumetric resolution of streamtubes will remedy that.

- As the Buckley-Leverett saturation profile is required as an input, the current application is limited to problems with a single set of rock k_r-functions. This seems to be the most difficult problem to be settled under the framework of the proposed method. The effect of different rock k_r on one dimensional displacements may need to be studied.

4.8 Conclusions

- Scaling up techniques, for either single or two phase flow, based on isolated elements tend to induce significant physical error due to the inevitable simplification of boundary conditions applied to calculate effective flow properties. This is more pronounced if they are applied to flow problems around a well, where the flow geometry is unpredictable. A successful scaling up technique must account for the flux and pressure profiles at coarse grid boundaries under the global boundary conditions for each particular problem. Use of the Laplace solution under the real boundary conditions is a solution. Although it requires the solution of the full field Laplace equation, the computational cost still is much smaller compared with fine grid simulation.

- There are two rules to be observed to calculate coarse grid transmissibilities. One is to satisfy the coarse scale material balance and the other is to secure physical stability of the coarse grid system. They can be achieved by deriving coarse scale transmissibilities from fine grid fluxes while constraining them to be nonnegative. The only way to satisfy both of these two requirements is to modify coarse grid interfaces. This can be systematically done in a transformed space based on the positive dissipation theorem. The resulting reshaped coarse grids are streamtube bundles in the physical space. This gives a background to bring streamtube approaches into scaling up techniques.

- The Dykstra and Parson's approach is extended to non piston-like displacements to derive relations between front locations of a pair of streamtubes. The effective relative permeabilities are calculated by superposing the saturation, the fractional flow, and the total mobility of streamtubes that constitute each coarse grid.

- Combinations of dissipation based transmissibilities and streamtube based relative permeabilities build a two phase coarse grid system. Coarse grid simulations using that system approximate displacement processes and well performance within acceptable differences from the corresponding fine grid simulations. The differences in pressure, saturation, and water cut are within ten percent where the computation time that includes solving the Laplace equation, deriving transmissibilities and relative permeability functions, and simulating the coarse scale problem is on order of 1/1,000 of a fine grid simulation.

- Although being based on fixed streamtube geometry and uniform initial water saturation, the applicability of this method is widened beyond these assumptions through the finite difference formulation. Applications to some compressible problems and nonuniform initial water saturation problems has given acceptable results.

- The new method is coded for two dimensional problems without gravity, capillary, and diffusivity effects. It assumes a fixed streamtube geometry. It can treat only single rock k_r functions. It solves problems with up to two wells in the domain. The minimum volumetric resolution is the size of a fine grid. Further development will be needed to lift these constraints.

Nomenclature

f_w	=	Fractional Flow of Water
F	=	A specified Function
k_r	=	Relative Permeability
n^g	=	Number of Streamtubes Go through a Reshaped Coarse Grid
n^i	=	Number of Streamtubes Go across a Coarse Grid Interface
P	=	Coarse Grid Nodal Pressure, psi
P_{wf}	=	Flowing Bottomhole Pressure, psi
ΔP	=	Pressure Difference between Coarse Grid Nodes, psi
P_0	=	Pressure Along Streamtube, Single Phase Unit Viscosity, psi
P_d	=	Dimensionless Pressure Along Streamtube, psi
q	=	Fine Scale Flux, bbl/d
q_0	=	Flow Rate of Streamtube, Single Phase Unit Viscosity, bbl/d
Q	=	Coarse Scale Flux, bbl/d
$\dot{S}$	=	Energy Dissipation (Entropy Production) $(bbl/d) \times psi$
R	=	A specified Factor
S	=	Phase Saturation
S_w	=	Water Saturation
S_{wi}	=	Initial Water Saturation
T	=	Coarse Scale Transmissibility, $bbl/d/psi$
t	=	Time, d
V	=	Local Pore Volume of Streamtube bbl
V_d	=	Dimensionless Local Pore Volume of Streamtube
ΔV	=	Volume of Streamtube Segment within a Reshaped Coarse Grid
x	=	Distance on Streamtube Coordinate, ft
x_d	=	Dimensionless Distance on Streamtube Coordinate

Greek Letters

Φ	=	Potential Function, psi
ϕ	=	Porosity
λ	=	Mobility, cp^{-1}
λ_t	=	Total Mobility, cp^{-1}
λ_0	=	Mobility of Single Phase of Unit Viscosity, cp^{-1}
μ	=	Viscosity cp
Ψ	=	Stream Function, bbl/d

Subscripts

0	=	Single Phase with Unit Viscosity
i, j	=	Integer Indices for Grids
o	=	Oil Phase
p	=	Phase, Oil or Water
t	=	Total of Oil and Water Phase
w	=	Water Phase
x, y	=	Principle Coordinates

Superscripts

k, l, m	=	Integer Indices for Streamtubes

References

[1] J. Bear. *Flow through porous media.* New York, Academic Press, New York, 1969.

[2] C. Deutsch and A. Journel. *GSLIB: Geostatistical Software Library and User's Guide.* Oxford University Press, New York, 1992.

[3] C. V. Deutsch. A probabilistic approach to estimate effective absolute permeability. Master's thesis, Stanford University, Stanford, CA, 1987.

[4] L. J. Durlofsky. Numerical calculation of equivalent grid block permeability tensors for heterogeneous porous media. *Water Resources Research, vol.27, no.5*, pages 699–708, 1991.

[5] H. Dykstra and R. L. Parsons. The prediction of oil recovery by waterflood. *Secondary Recovery of Oil inthe United States, API*, pages 160–174, 1950.

[6] J. R. Kyte and D. W. Berry. New pseudo functions to control numerical dispersion. *SPE Journal*, pages 269–276, August 1975.

[7] J. C. Martin and R. E. Wegner. Numerical solution of multiphase, two-dimensional incompressible flow using stream-tube relationships. *SPE Journal*, pages 313–323, October 1979.

[8] M. R. Thiele, M. J. Blunt, and F. M. Orr. A new technique for predicting flow in heterogeneous systems using streamtubes. In *SPE/DOE Ninth Symposium on Improved Oil Recovery, Tulsa, OK*, number 27834, pages 571–582, Richardson, TX, April 1994. Society of Petroleum Engineers.

[9] T. Yamada and T. A. Hewett. Production-based effective vertical permeability for a horizontal well in the presence of a stochastic distribution of shales. In *SPE Annual Conference and Exhibition v Omega 1994, New Orleans, LA*, number 28446, pages 853–865, Richardson, TX, September 1994. Society of Petroleum Engineers.

5. Analyses of Experiments at Marathon Oil Company (Task 3)

Research undertaken by Dr. Sepehr Arbabi and Don Schroeder (Marathon)
Advisor: Professor John Fayers

This chapter provides the experimental data and their analyses for all the experiments performed so far. Figure 5.1 shows a simple sketch of the Marathon Wellbore Model. The wellbore is essentially a transparent acrylic pipe with an average ID of 6.2 inches. The layout consists of 20 ft of blank acrylic, followed by 20 ft of smooth perforations, followed by 15 ft of sharp perforations. Liquid or gas inflow can be supplied by the connected manifold to the next 40 ft of smooth edged perforations. The remaining 5 ft of the model is a blank section of acrylic casing. There are small variations in the diameter of the wellbore which have been measured by mechanical and ultrasonic techniques. Figure 5.2 displays these variations as a function of position along the wellbore model.

Four types of experiments have been performed in the wellbore model which are listed below:

1. Single phase flow of water or oil in the axial flow with no inflow through perforations
2. Single phase flow of water or oil in the axial flow plus inflow of water or oil through perforations
3. Two-phase flow of oil and nitrogen in the core flow with no inflow through perforations
4. Single phase flow of water or oil in the axial flow with inflow of air or nitrogen through perforations

The oil flow rate has been varied between 100-410 gpm (3429-14057 STB/day) in the experiments while the nitrogen gas flow rate has been supplied at the fixed maximum rate of about 0.45 MMscfd. Differential pressure drops per 10 ft have been measured along the wellbore by two methods. In the first method, liquid manometers are used and in the second method the differential pressure drops are recorded electronically using Rosemount pressure transducers which have a relative accuracy of $\pm 0.2\%$. The Rosemount data are recorded about every 0.25 seconds and the experiments are run long enough so that steady conditions have been achieved.

5.1 Single Phase Flow Experiments

The single phase axial flow experiments, listed as item (1) above, are performed in order to characterize the wellbore model in terms of roughness and also to have a base case experiment. Figure 5.3 shows data and calculated results for a sample of single phase experiments with an oil rate of 408 gallons per minute (gpm). Both Rosemount and manometer measurements are shown which are in close agreement with each other. Calculations are

done with two values of roughness namely $e = 8 \times 10^{-5}$ and $e = 2.5 \times 10^{-4}$ ft. The variations of the diameter of the wellbore are taken into account in the computations. It can be seen that both values of roughness give reasonable matches with the data, but the higher value of $e = 2.5 \times 10^{-4}$ ft provides the best overall fit to the seven data points and thus is the preferred choice for the roughness of the wellbore model. It is important to note that there is no apparent effect of different types of perforations on pressure drops when there is no inflow through them. A record of differential pressures with time from the Rosemount gauge for the 45-55 ft section for this experiment is shown in Fig. 5.4. A very stable and constant reading is observed for this single-phase flow experiment. The magnitudes of the occasional fluctuations (± 0.002 psi) from the central 0.049 value can be regarded as a measure of the accuracy of the Rosemount pressure transducers.

The effect of flow through perforations is studied in the second type of experiments. Figure 5.5 shows the case where 408 gpm of oil flows in the core but an additional 85 gpm of oil also enters radially through perforations. The influx is uniformly distributed over the inflow length of 40 ft along the wellbore (see Fig. 5.1). Computations with the base roughness of 2.5×10^{-4} nearly match the pressure drop data in the entrance section of the wellbore but it underestimates the values in the radial inflow section. On the other hand, calculated results based on $e = 0.001$ ft show a closer match with the data in the radial inflow region. A higher roughness in this experiment indicates that radial inflow of oil in a single phase flow experiment increases the apparent effective roughness of the wellbore. Keeping the radial influx rate at about 85 gpm, we have also conducted experiments with variable axial flow rates. Figure 5.6 shows the data for a case where the axial flow rate is reduced by 25% to 306 gpm. Lowering the axial flow rate while keeping the radial influx constant is equivalent to increasing the contribution of the inflow to the pressure drop, Figure 5.6 also shows that data points in the inflow section (5-45 ft section) have started to move toward and above the calculated line with the high roughness value of 2.5×10^{-4} ft, signifying a larger effect of the fluid entering radially on the pressure drop in the wellbore. This fact becomes even more evident for still lower influx rates of 203 and 102 gpm whose results are depicted in Figs. 5.7 and 5.8. Data in Figure 5.8 lie well above the calculated line with $e = 2.5 \times 10^{-4}$ ft. It might be possible to derive a correlation for apparent effective roughness based on the relative Reynolds numbers for perforation and core flows, R_{ep}/R_{ec}, but as the pressure drops are all very small, there would not be much practical importance for the range of flow rates investigated so far.

5.2 Two-Phase Flow Experiments

The third type of experiments listed above involves two-phase core flows along the entire length of the wellbore, with no inflow through the perforations. Figure 5.9 illustrates the data for an oil rate of 403 gpm and a gas rate of 0.441 MMscfd where larger pressure drops than those in the single phase experiments are observed. The two data points at the 80-90 and 60-70 ft locations show much smaller pressure drops which are due to the entrance effects. Calculations are performed with the ASA Software [1] using the Beggs and Brill model [2], the Dukler *et al.* model [3] and the newly developed Stanford Mechanistic model, all with the base roughness value of $e = 2.5 \times 10^{-4}$. The Stanford Mechanistic model is

currently under development and testing and hence the present model predictions should be regarded as preliminary. However, Fig. 5.9 indicates good agreement between all three models for this experiment. Figure 5.10 displays a record of the measured pressure drops with time from the Rosemount pressure gauge for the 45-55 ft section. This record shows a substantial variation in pressure drop as a liquid slug passes by the measuring device. These large fluctuations in the pressure drop are inherent to the two-phase flow and particularly slug flow regime which in turn make the modeling of the two-phase flow more difficult. The data in Fig. 5.9 and all the other subsequent two-phase flow experiments represent average values obtained by simple averaging of all the Rosemount or manometer data. Figure 5.11 displays the results for the same type of experiment but with lower oil rate of 306 gpm (gas rate of 0.466 MMscfd is almost the same as in the experiment in Fig. 5.9). For this case the Stanford Mechanistic model predicts differently, and is only in agreement with the two data points with high pressure drops. Keeping the gas flow rate almost unchanged, the experiments have been repeated with lower oil rates of 204 and 102 gpm. Data and the predictions are illustrated in Figs. 5.12 and 5.13. The Beggs and Brill and the Dukler *et al.* models overpredict the data for the last case where the ratio of the oil to gas flow rates has been reduced by a factor of 4 of the experiment shown in Fig. 5.9.

In the last type of experiment, two-phase flow is established only along the inflow section of the wellbore by supplying gas radially through perforations. Figure 5.14 presents the data and the calculated predictions with an oil rate of 408 gpm and a gas rate of 0.425 MMscfd. It is clear that predictions with the base roughness value of $e = 2.5 \times 10^{-4}$ ft underestimate the data in the two-phase region. The results with the higher $e = 0.002$ ft show better agreement with the two-phase data as depicted in Fig. 5.15. The results in Figs. 5.14 and 5.15 demonstrate that radial influx of gas through perforations increases the pressure drop in comparison with uniform two-phase core flow, and therefore a higher apparent effective roughness is required to model the experiments. In a manner similar to the single phase inflow experiments, we have increased the contribution of the flow through perforations by reducing the axial oil flow rate. Figure 5.16 displays the data and the model predictions for the case where the oil flow rate has been lowered to 306 gpm. Lower pressure drops are observed as expected but the same effect of perforation flow as in Fig. 5.15 can be seen. Further decrease in the axial oil rate brings down the pressure drop as shown in Fig. 5.17 for oil rate of 199 gpm. With this liquid rate, a shift in flow regime occurs for the *current* Stanford Mechanistic model which leads to substantial underprediction. The data for the lowest oil rate of 102 gpm in Fig. 5.18 shows a reasonable match with the Dukler *et al.* method, but the Beggs and Brill method overpredicts and some tendency to underpredict is seen for the Mechanistic model.

5.3 Liquid Holdup Measurements

In addition to the pressure drop measurements, liquid holdups (*in-situ* liquid volume fractions) have been measured by a capacitance holdup meter stationed downstream at the 12-ft mark of the wellbore. Figure 5.19 shows the % liquid holdup versus time for the two phase core flow experiment where the oil flow rate is 204 gpm and the gas flow rate is 0.448 MMscfd. The average holdup is estimated to be respectively 29.5% and 44% from the Beggs

and Brill and the Stanford Mechanistic model while the experimental average holdup is about 23%. Figure 5.20 displays an equivalent case in terms of both oil and gas flow rates with the difference that gas is now entered radially through perforations. The experimental holdup data with an average value of 36.3% are now larger than the previous case with no gas inflow. The predictions of the Beggs and Brill and the current Stanford Model remain unchanged as they are not equipped to model the perforation flow. The effect of inflow of gas on liquid holdup is more clearly shown in Fig. 5.21 where the two previous cases have been superimposed. The cyclic jumps observed in the Figure are the result of liquid slugs rapidly passing by the meter. The data clearly shows that radial influx of gas increases the liquid holdup.

The results of the Stanford Mechanistic model presented in this chapter are based on unadjusted and unimproved available correlations used in the model and should only be regarded as preliminary. The tuning and improvement of the model is currently underway and is the subject of the next chapter.

References

[1] ASA Multiphase Flow Software Systems User Guide: Aziz, Spencer & Associates Inc. (1993).

[2] Beggs, H. D. and J. P. Brill : "A Study of Two Phase Flow in Inclined Pipes," *J. Pet. Tech.*, (May 1973) 25:607-617.

[3] Dukler, A. E., Wicks M., and R. G. Cleveland: "Frictional Pressure Drop in Two-Phase Flow: An Approach Through Similarity Analysis," *AIChE.J.*, (January 1964) 10: 44-51.

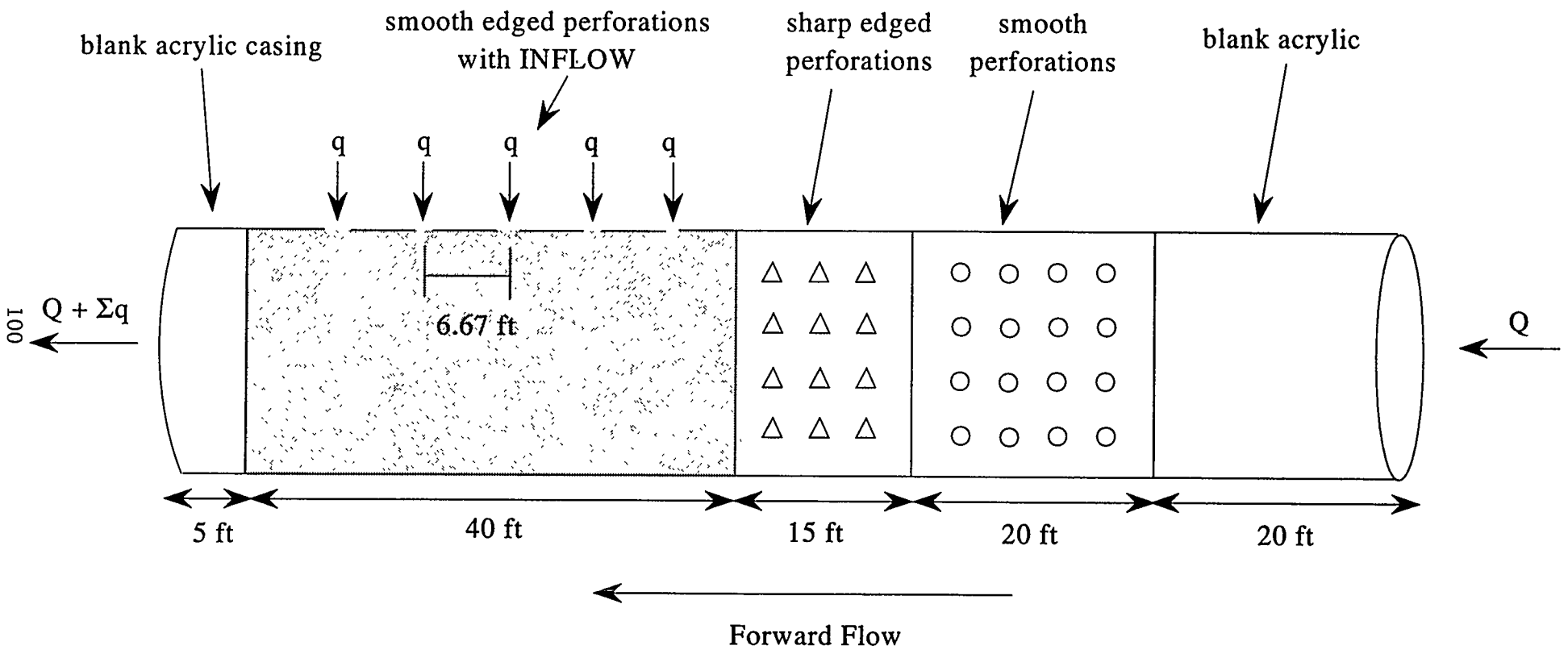

Figure 5.1: Layout of Marathon Wellbore Model

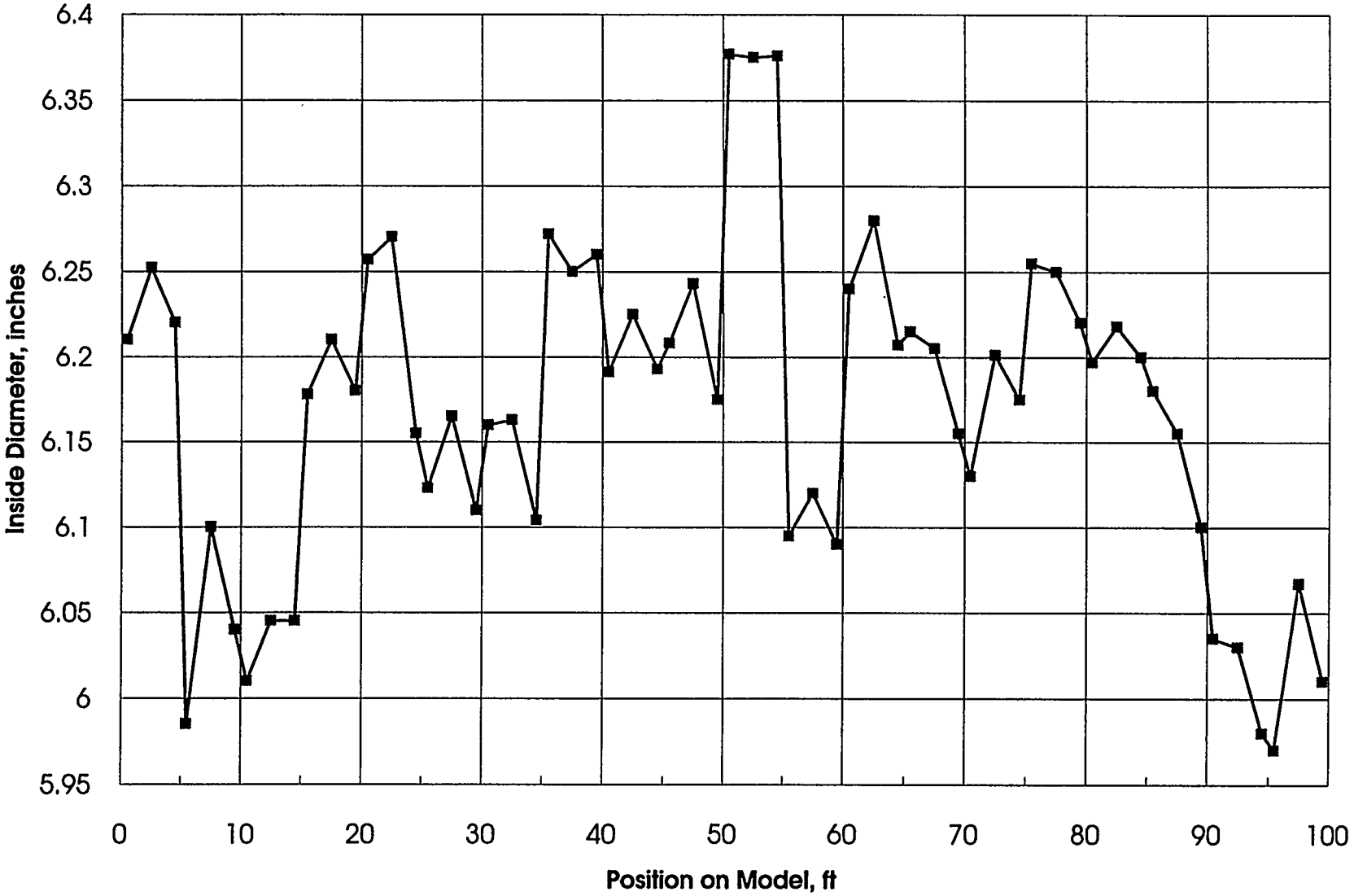

Figure 5.2: Variation of the Wellbore Inside Diameter Based on Ultrasonic and Circumference Measurements

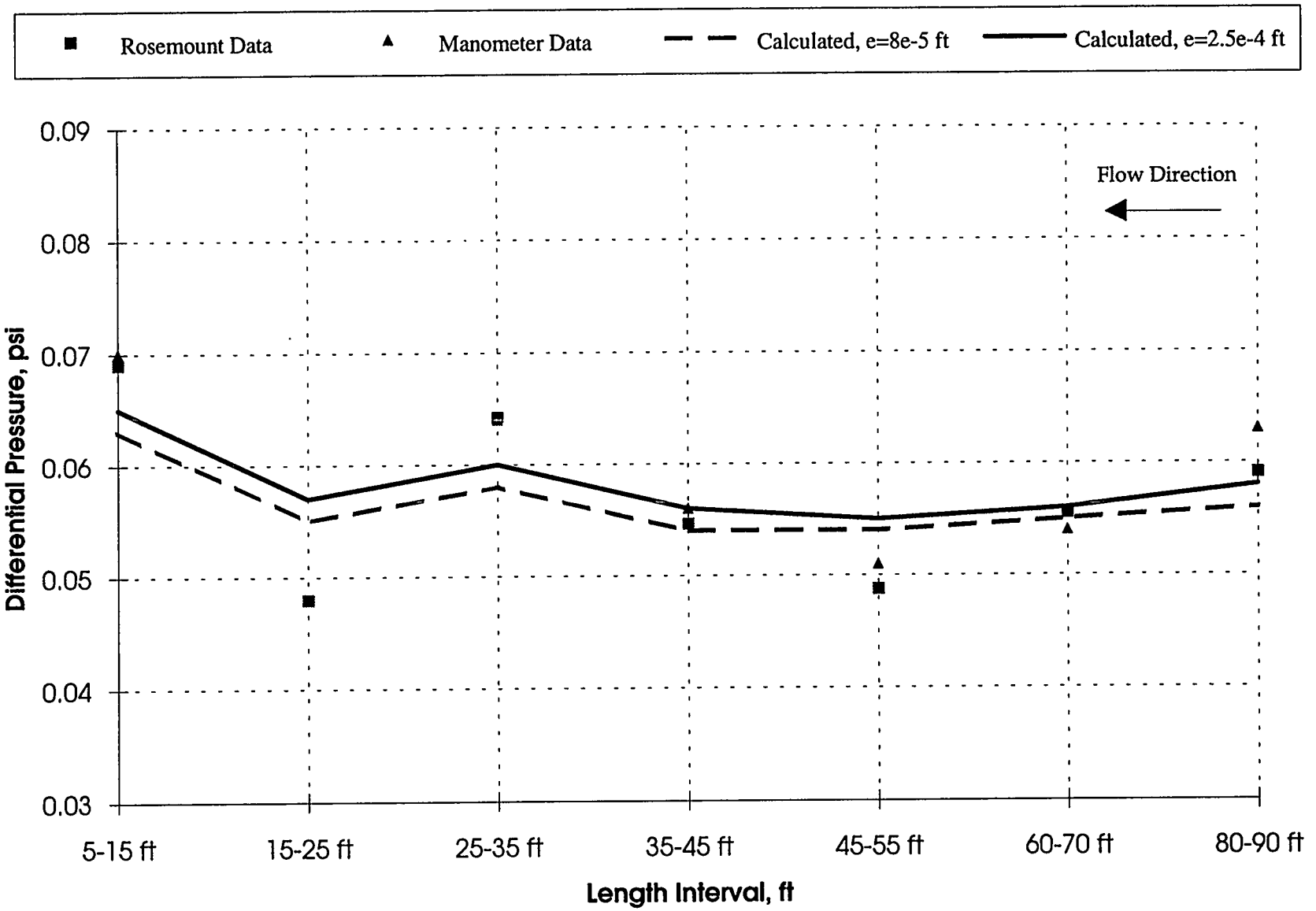

Figure 5.3: Single Phase with Oil (408 gpm) Axial Flow and no Inflow (Oil Viscosity=9.17 cP)

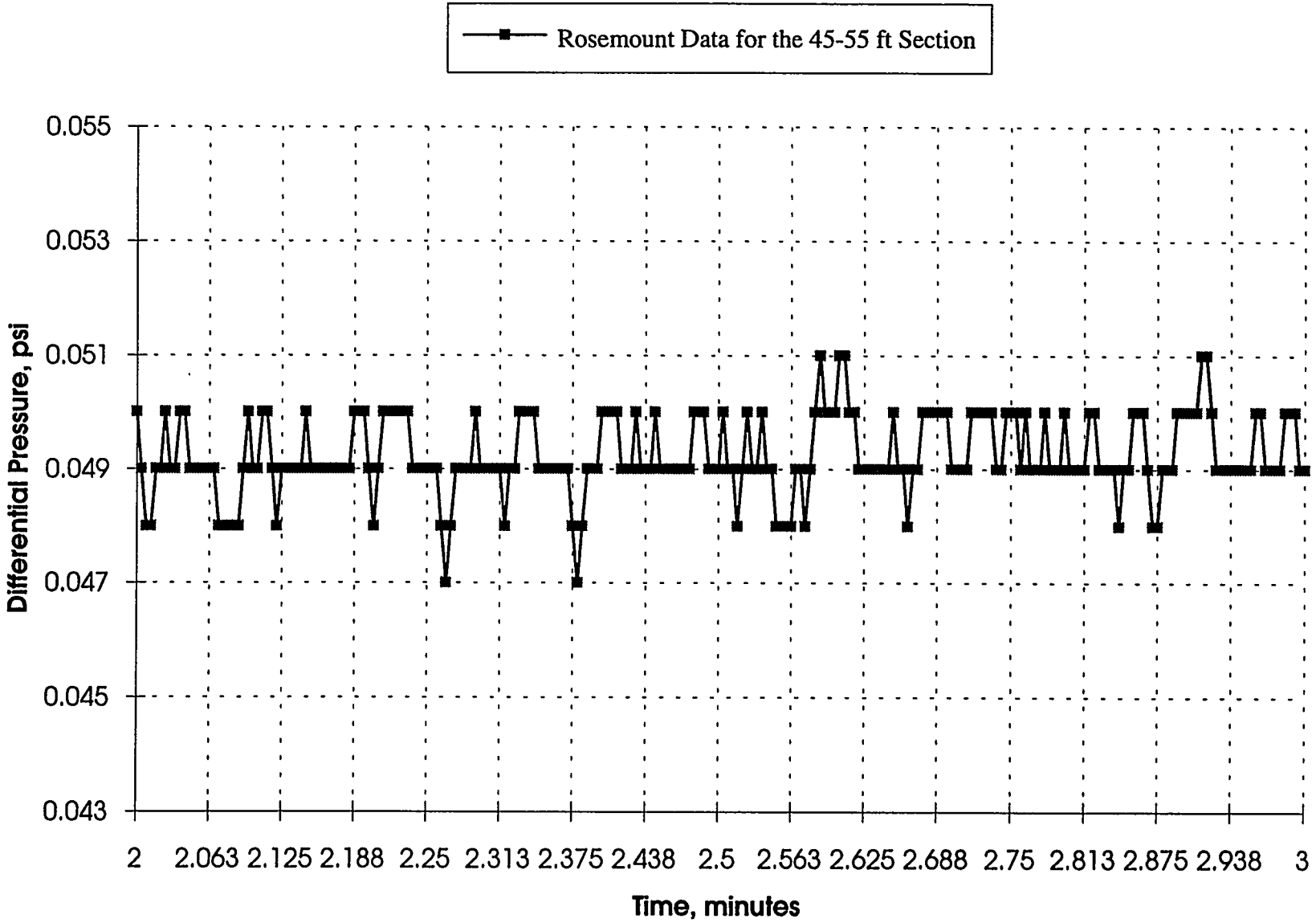

Figure 5.4: A Record of Differential Pressures Measured by the Rosemount Gauge for the Experiment in Figure 5.3

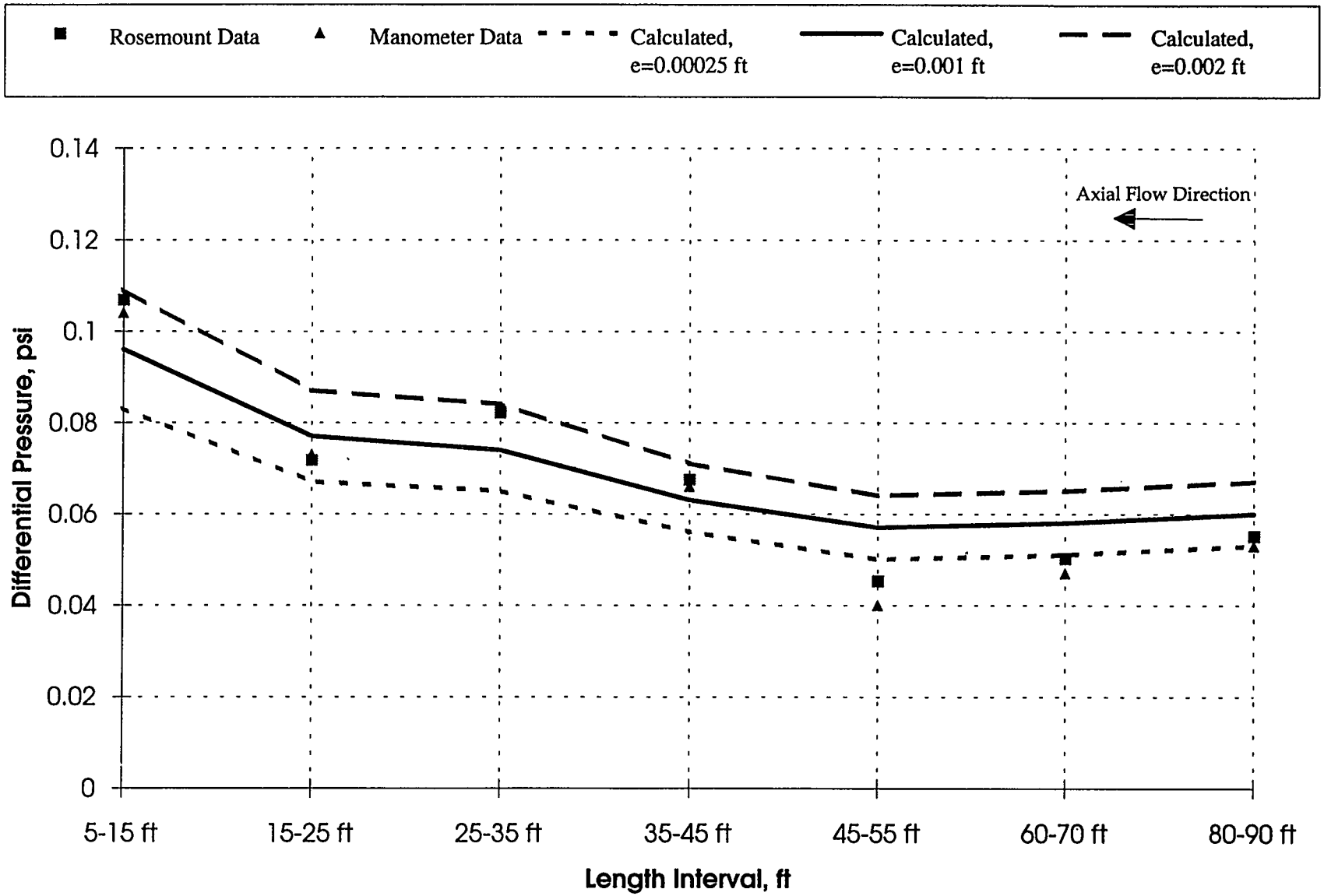

Figure 5.5: Single Phase with Oil (408 gpm) Axial Flow and Oil (85 gpm) Inflow

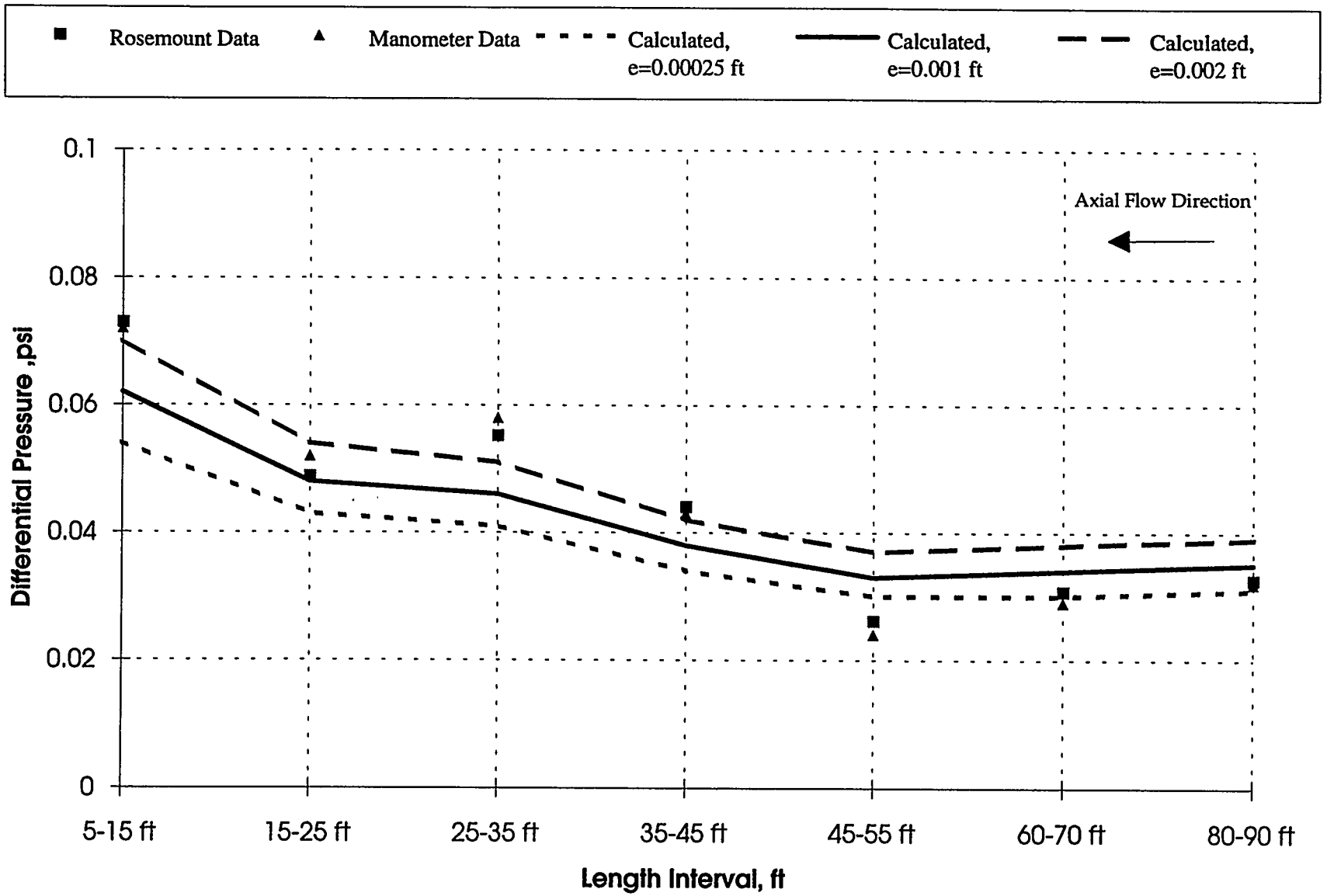

Figure 5.6: Single Phase with Oil (306 gpm) Axial Flow and Oil (85 gpm) Inflow

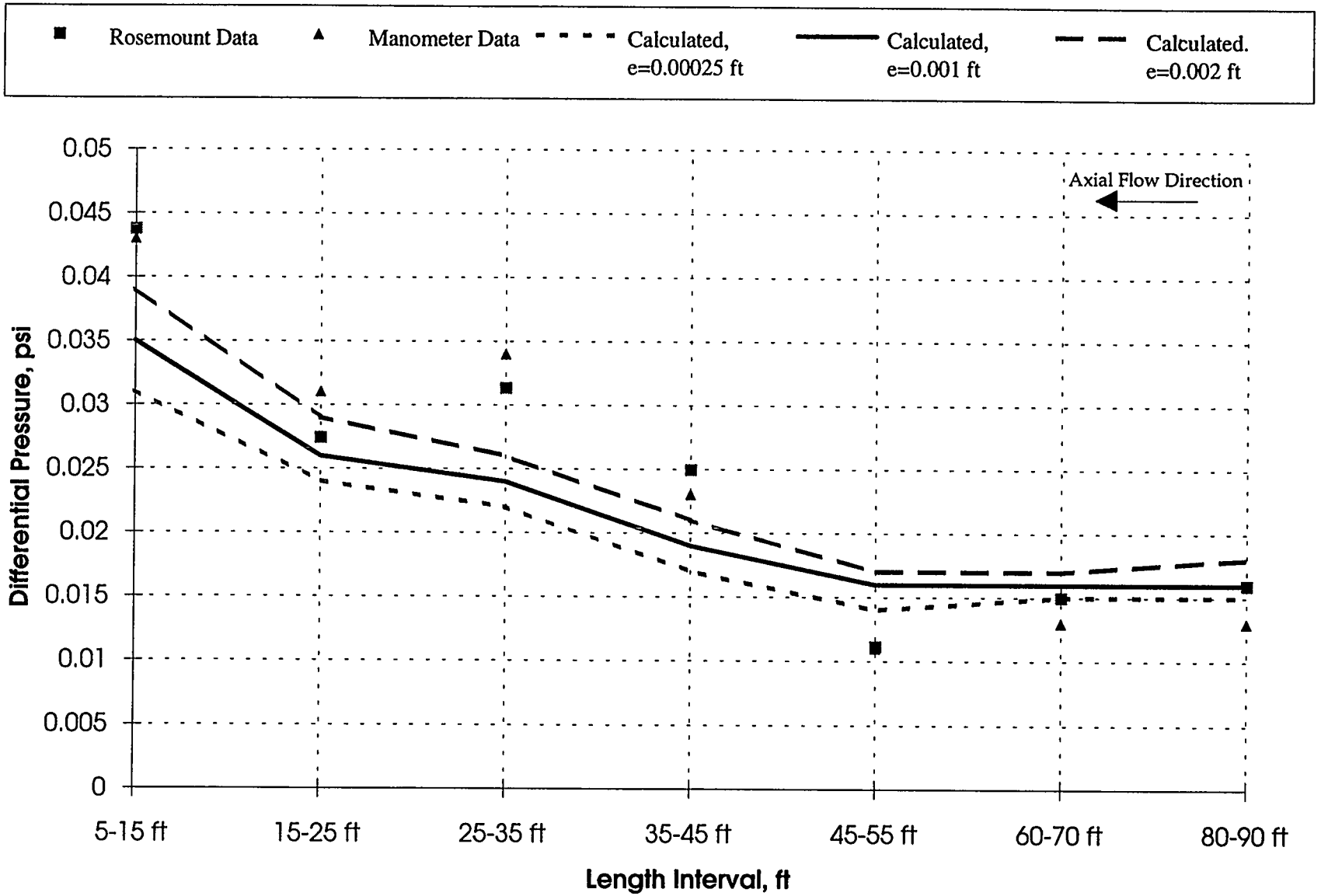

Figure 5.7: Single Phase Oil (203 gpm) Axial Flow and Oil (85 gpm) Inflow

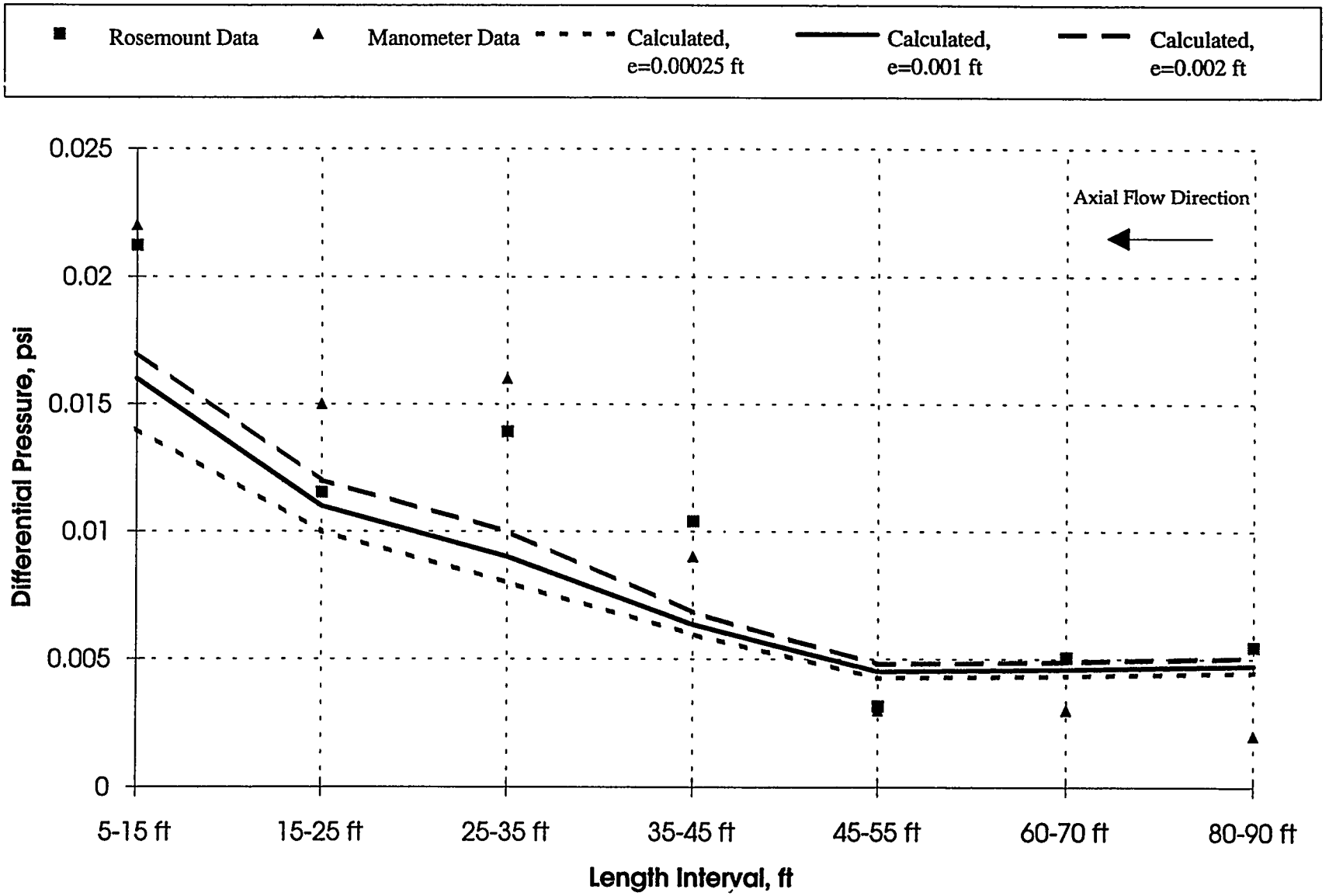

Figure 5.8: Single Phase with Oil (102 gpm) Axial Flow with Oil (84 gpm) Inflow

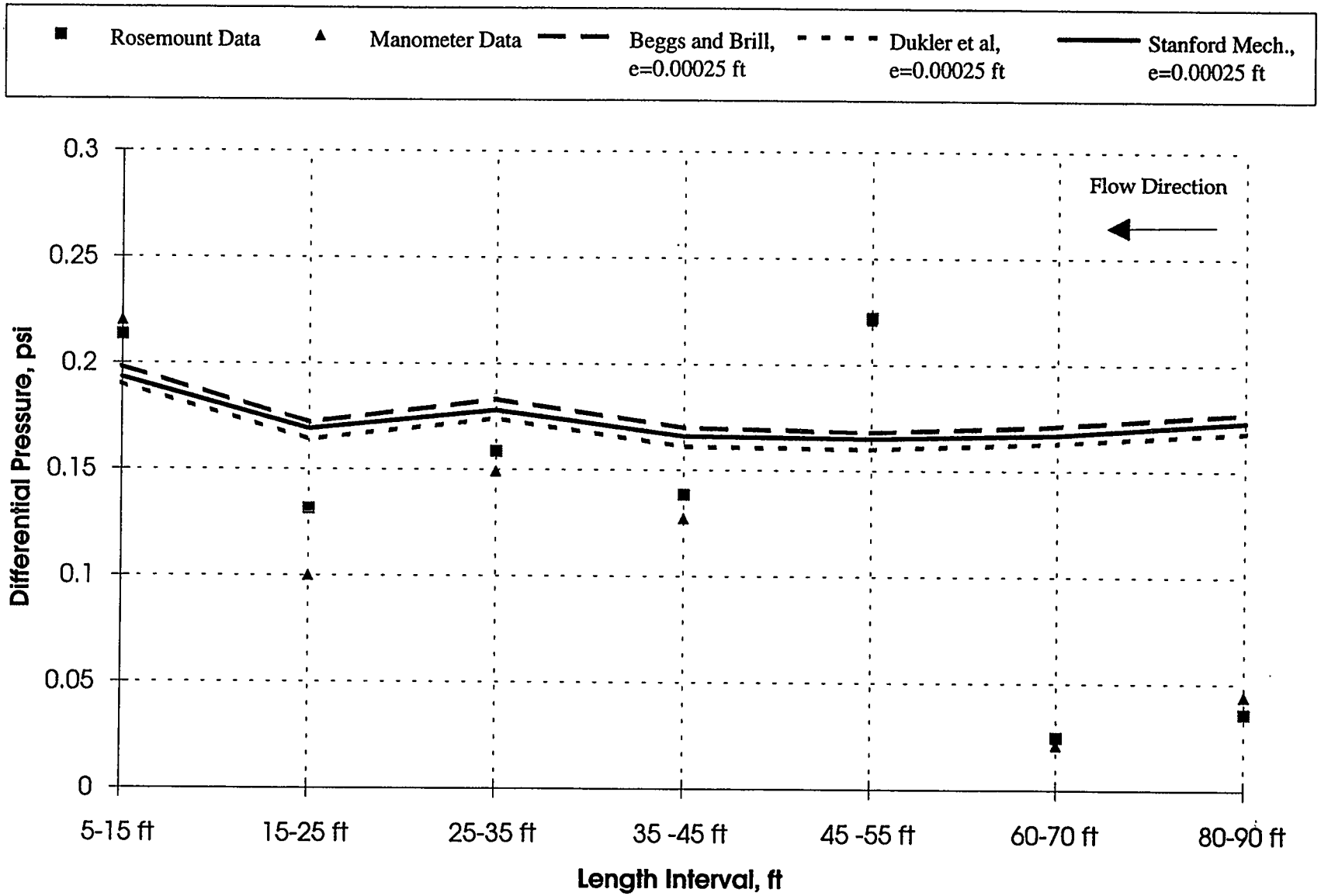

Figure 5.9: Two-Phase with Oil (403 gpm) and N2 (0.441 MMscfd) in Axial Flow with no Inflow

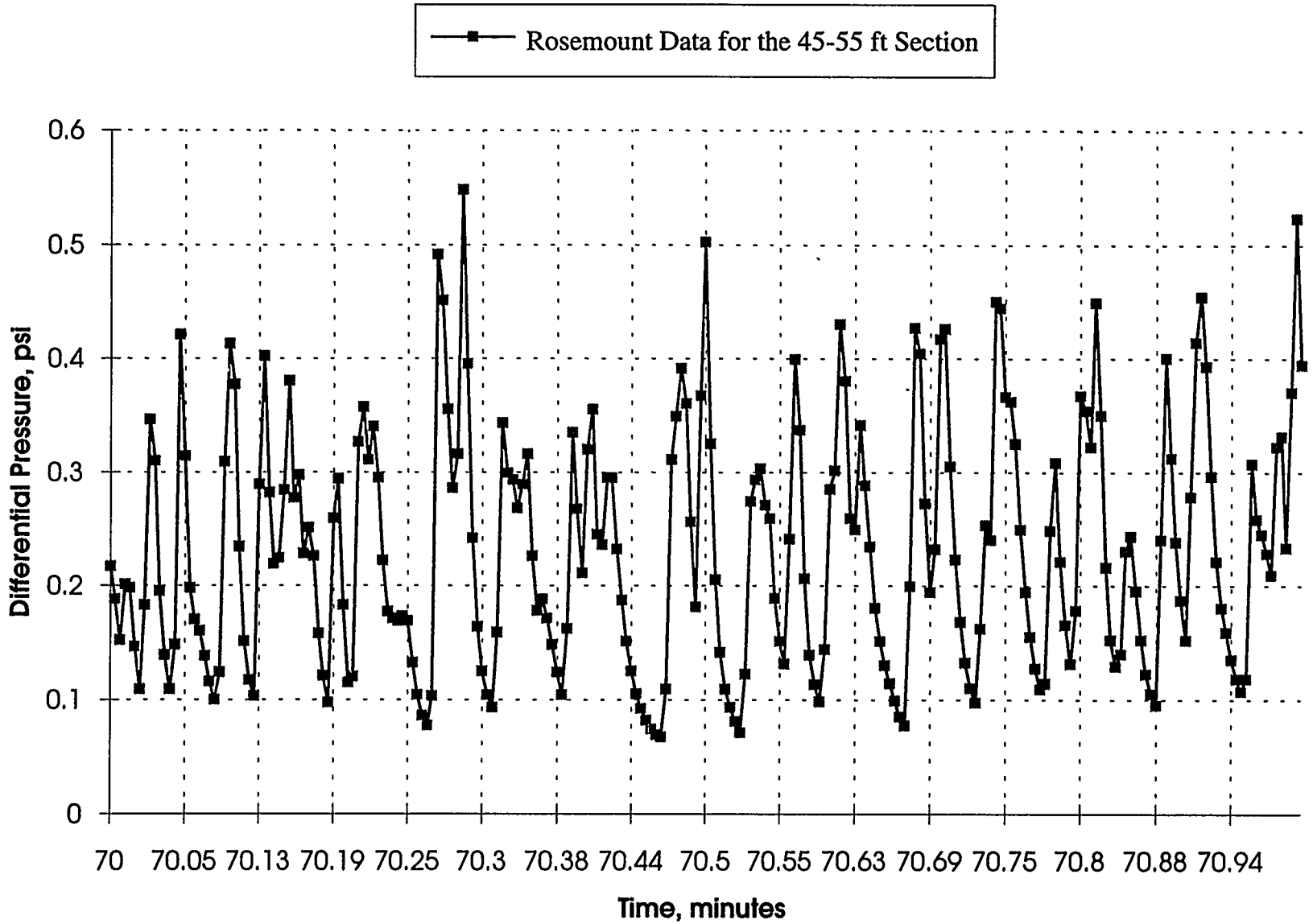

Figure 5.10: A Record of Differential Pressures Measured by the Rosemount Gauge for the Experiment in Figure 5.9

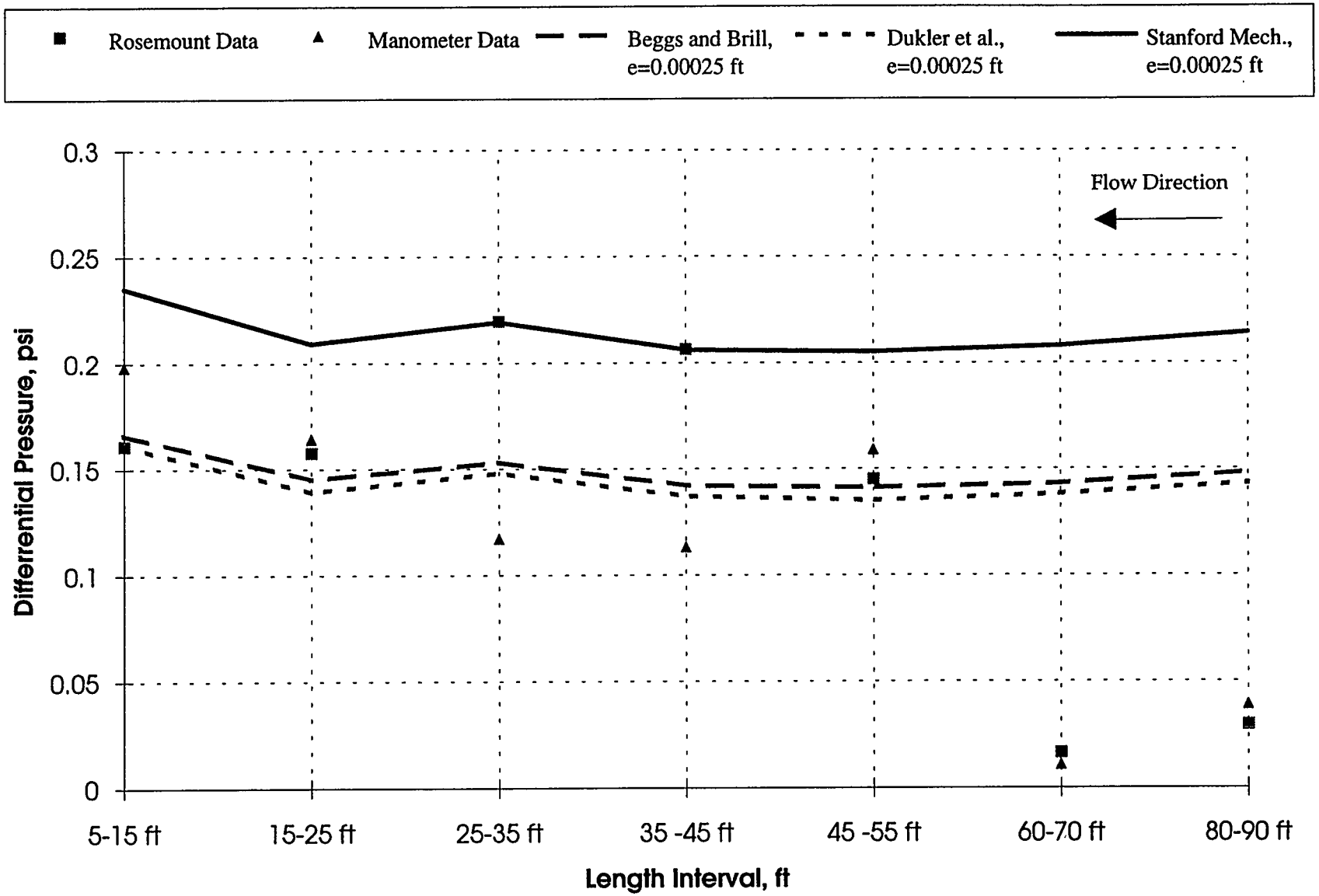

Figure 5.11: Two-Phase with Oil (306 gpm) and N2 (0.466 MMscfd) in Axial Flow with no Inflow

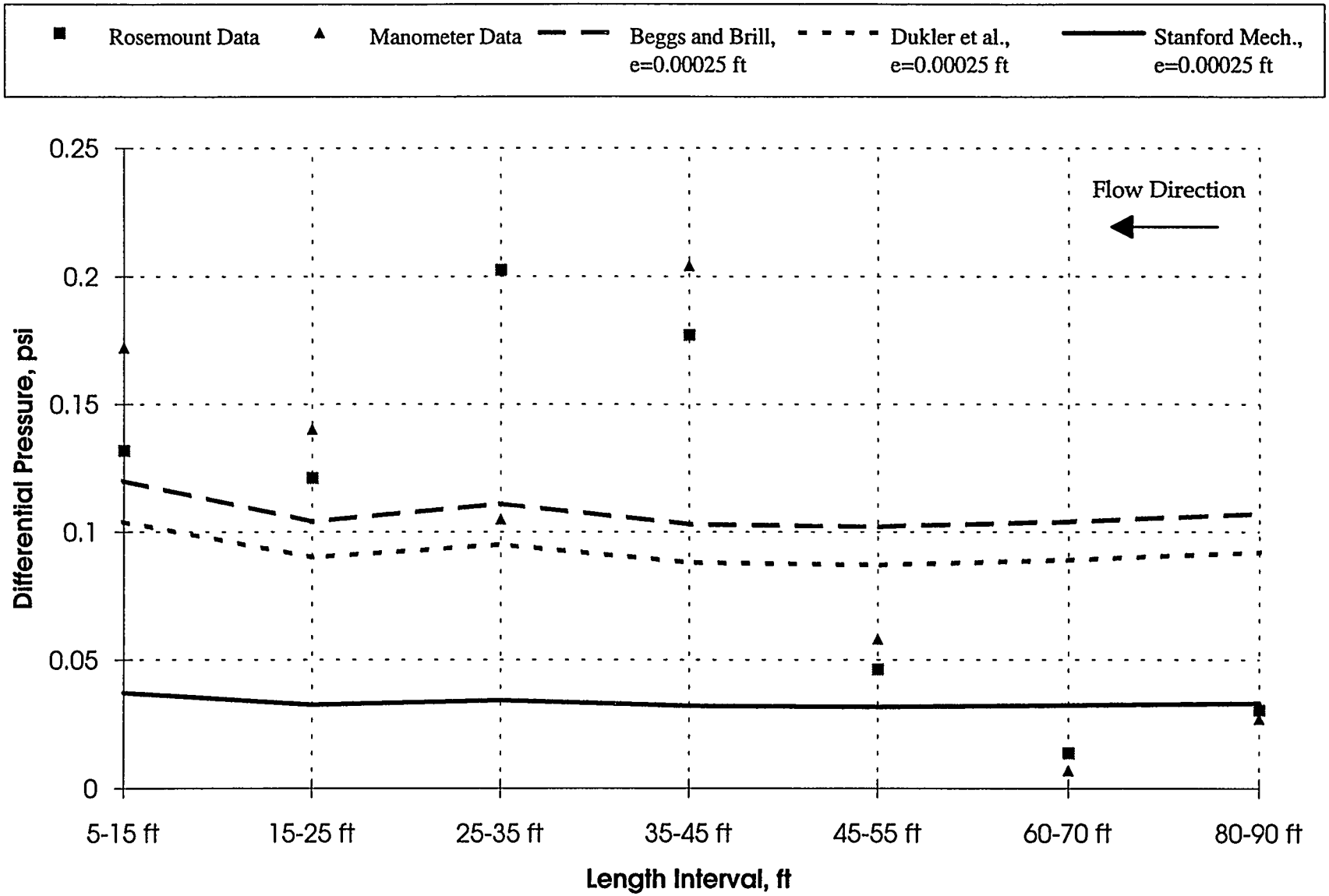

Figure 5.12: Two-Phase with Oil (204 gpm) and N2 (0.448 MMscfd) in Axial Flow with no Inflow

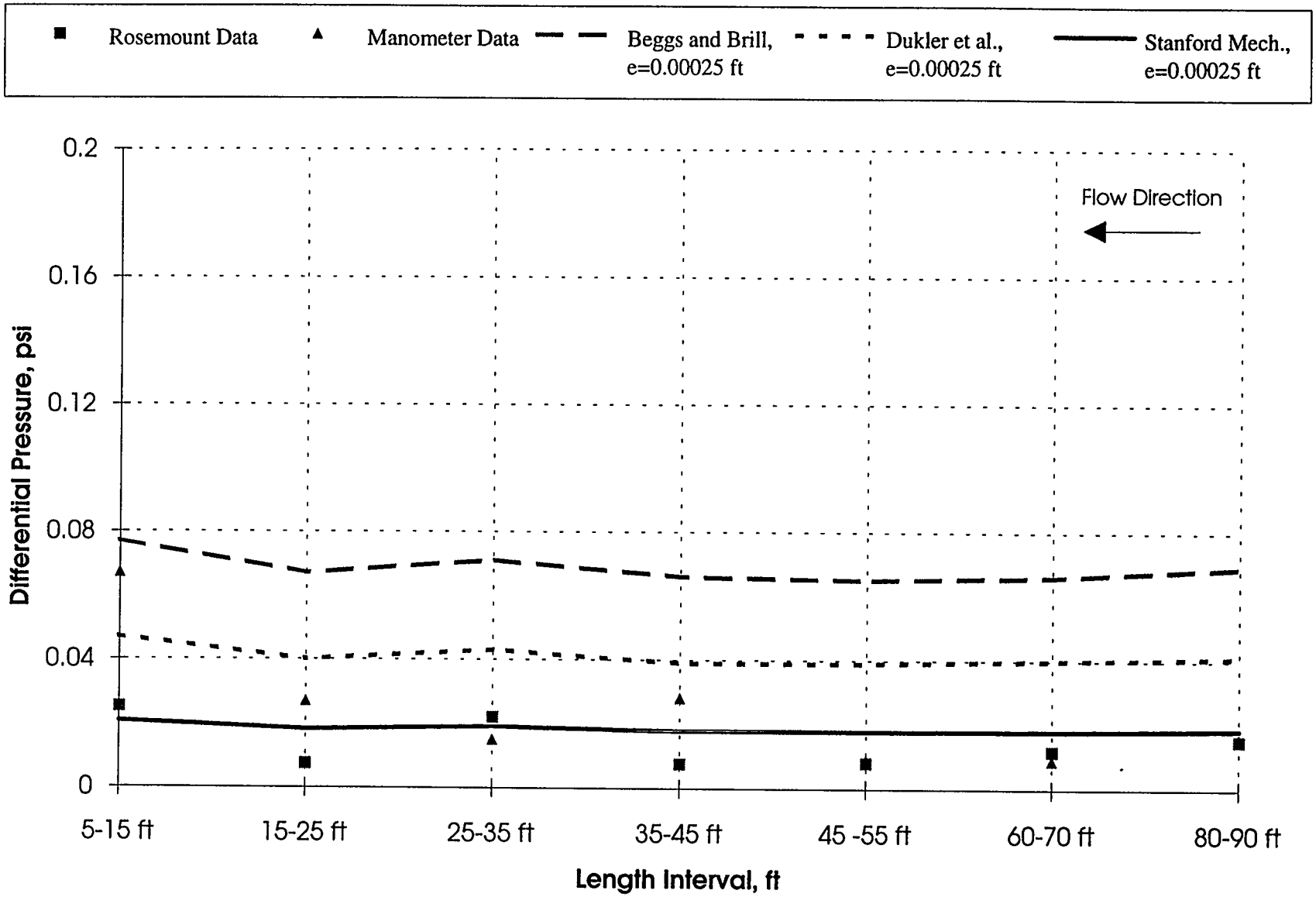

Figure 5.13: Two-Phase with Oil (102 gpm) and N2 (0.472 MMscfd) in Axial Flow and no Inflow

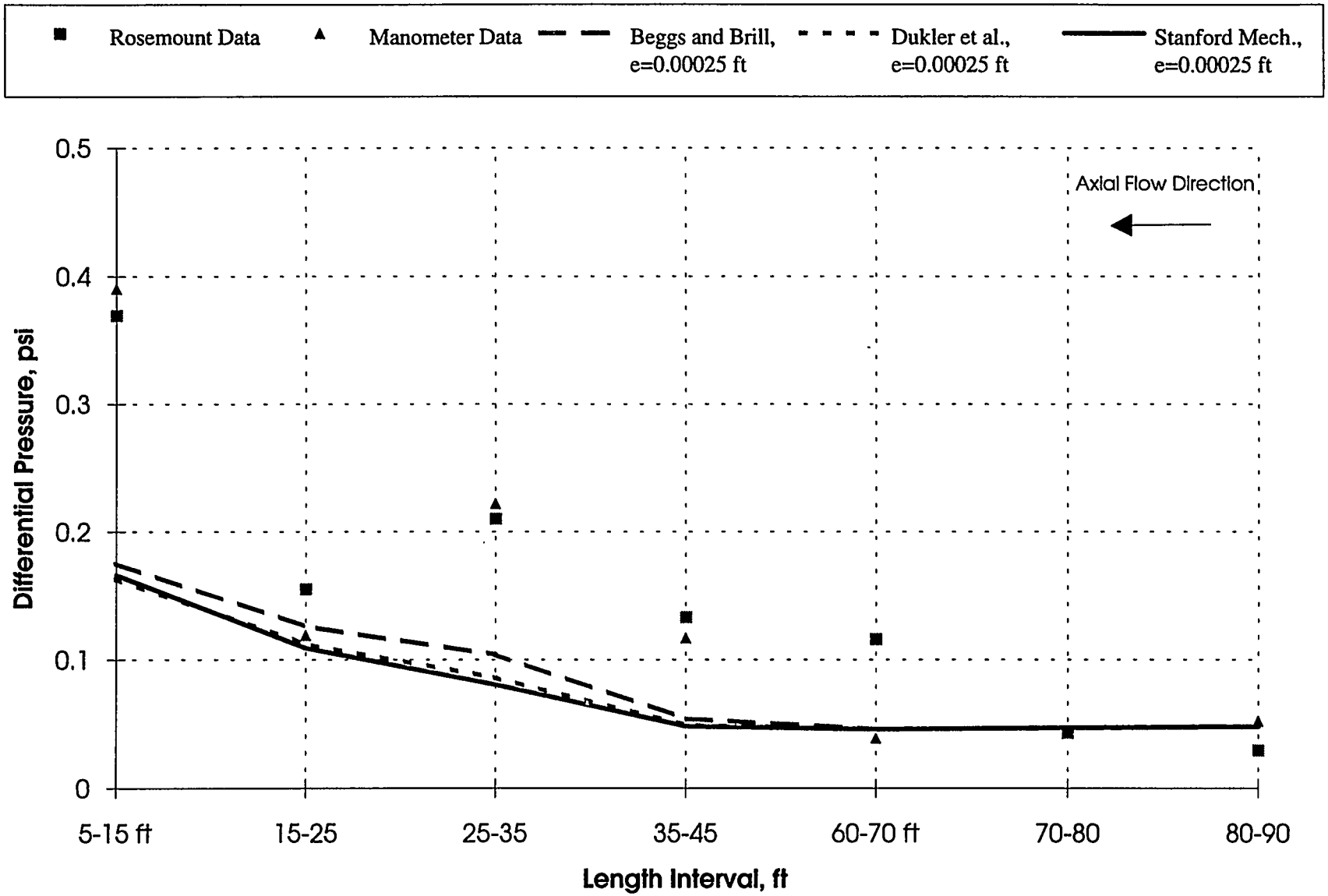

Figure 5.14: Two-Phase with Oil (408 gpm) Axial Flow and N2 (0.425 MMscfd) Inflow with e=0.00025 ft

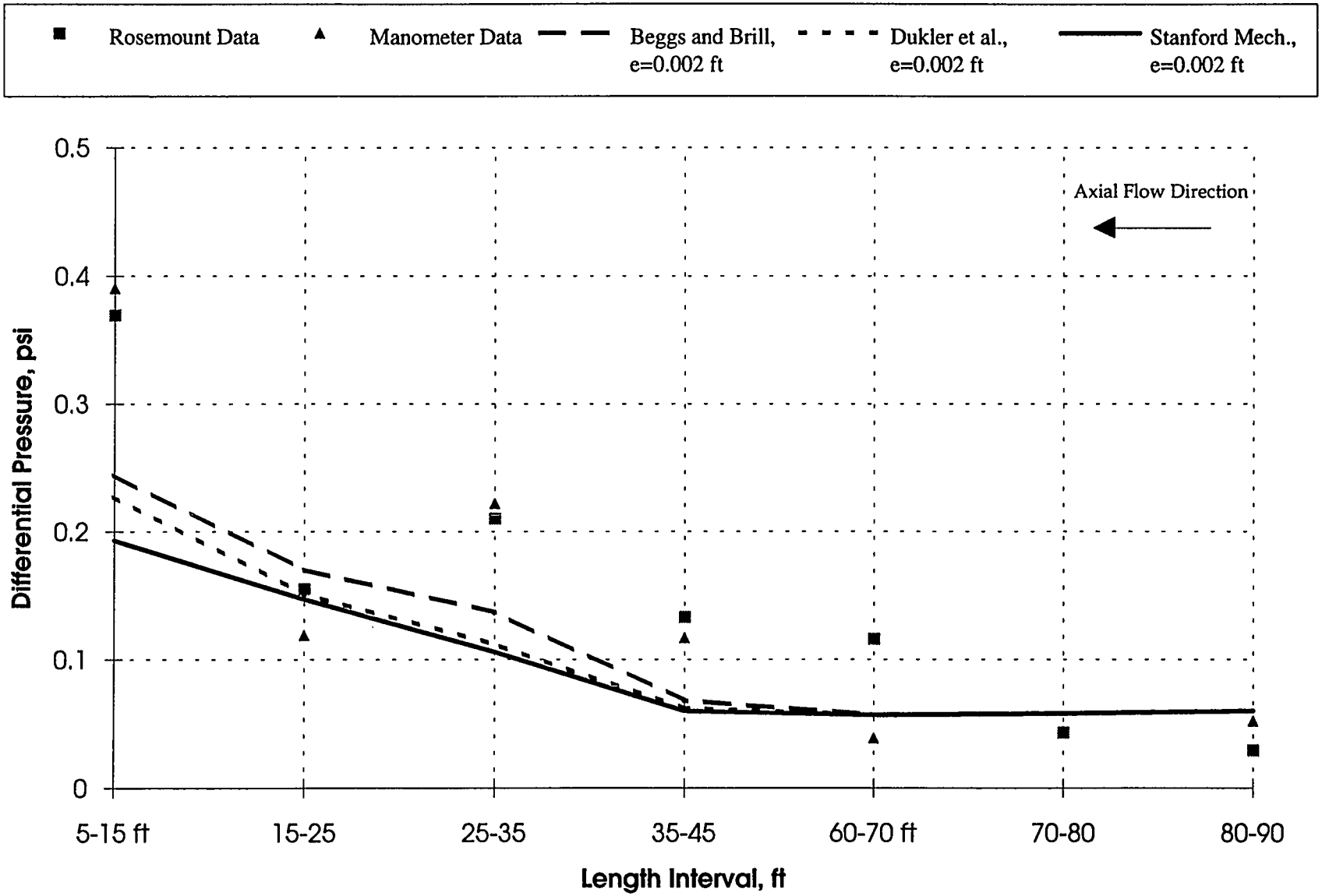

Figure 5.15: Two-Phase with Oil (408 gpm) Axial Flow and N2 (0.425 MMscfd) Inflow with e=0.002 ft

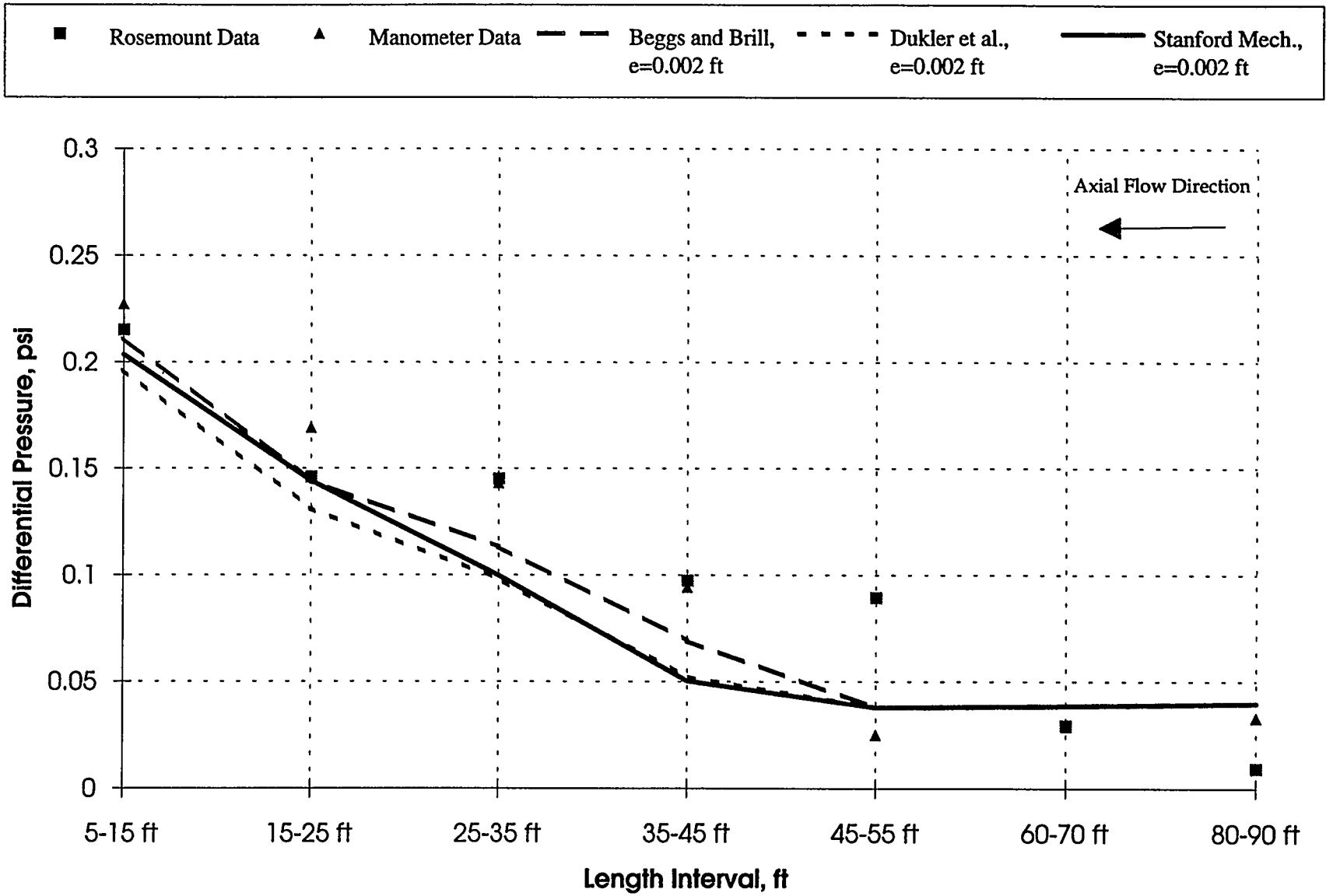

Figure 5.16: Two-Phase with Oil (306 gpm) Axial Flow and N2 (0.426 MMscfd) Inflow

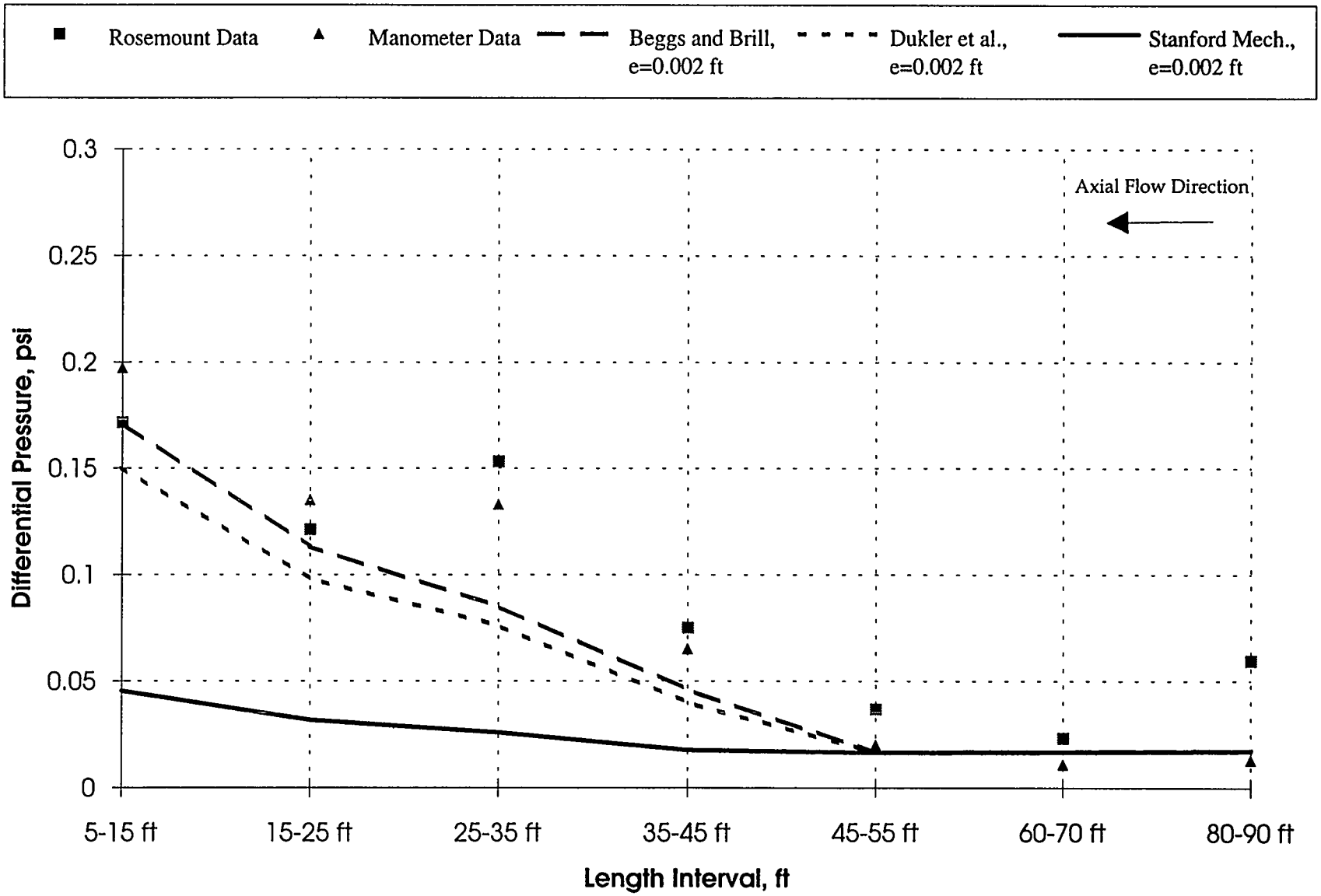

Figure 5.17: Two-Phase with Oil (199 gpm) Axial Flow and N2 (0.432 MMscfd) Inflow

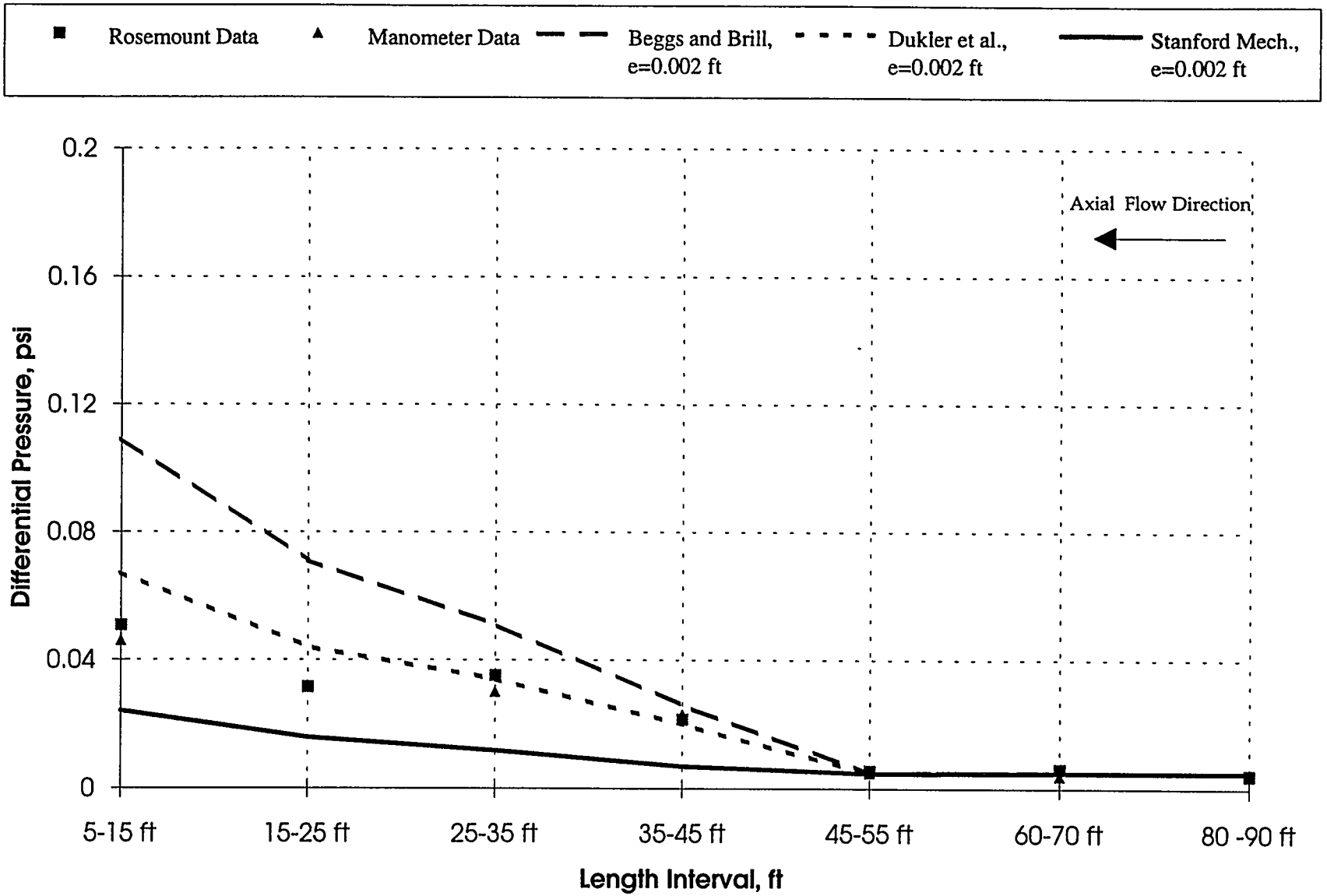

Figure 5.18: Two-Phase with Oil (102 gpm) Axial Flow and N2 (0.450 MMscfd) Inflow

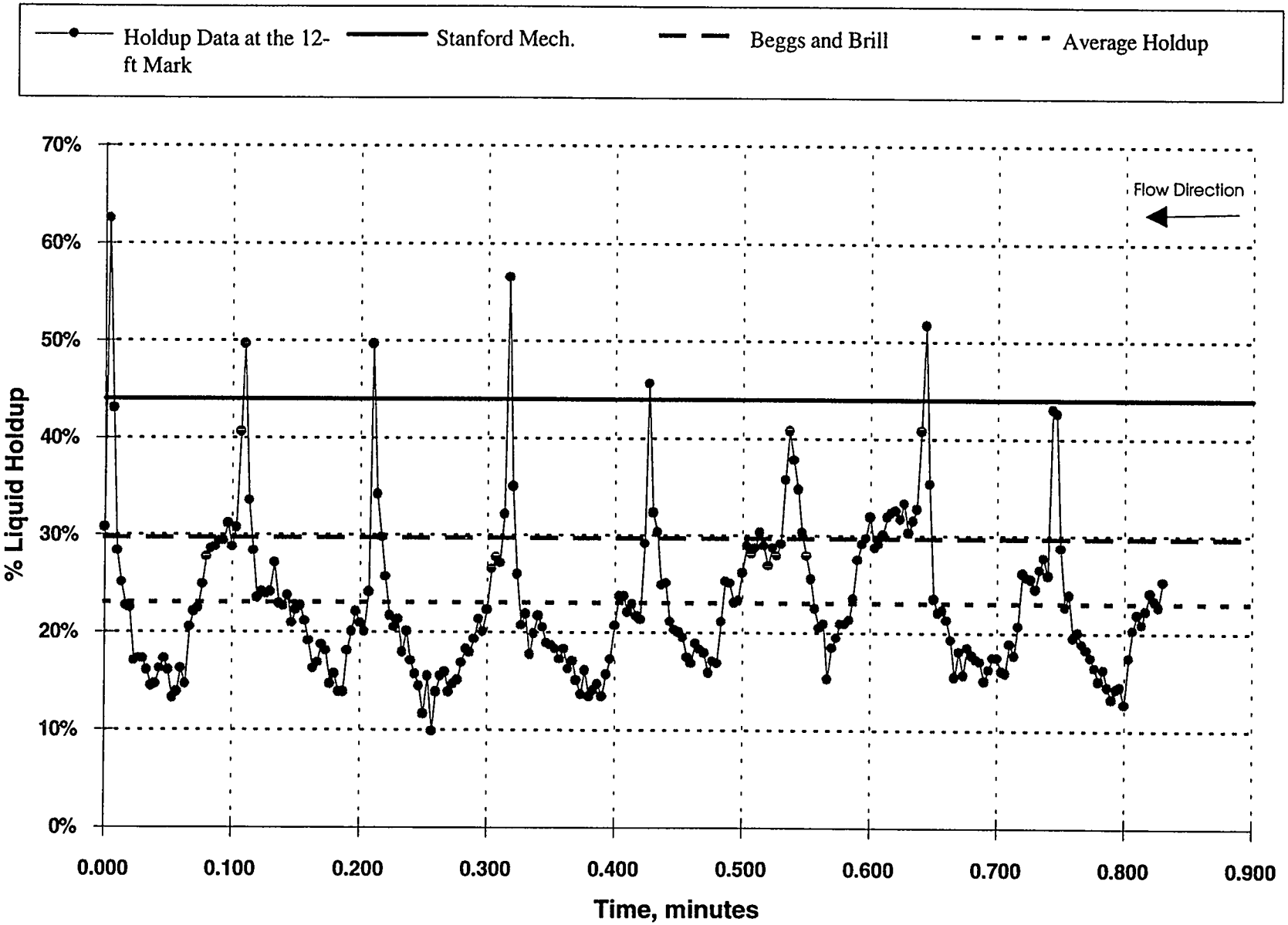

Figure 5.19: Liquid Holdup with Oil (204 gpm) and N2 (0.448 MMscfd) in Axial Flow with no Inflow

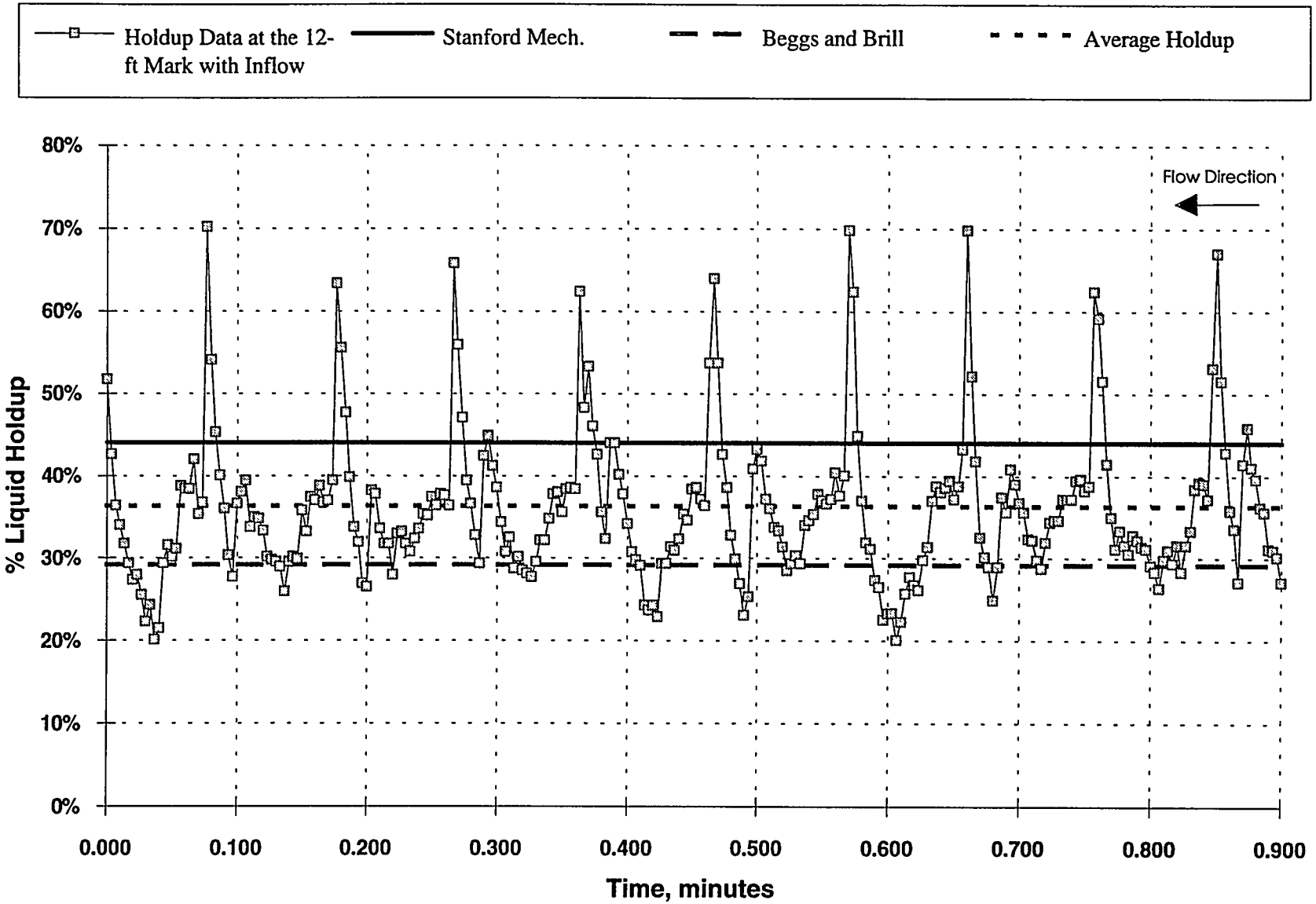

Figure 5.20: Liquid Holdup with Oil (199 gpm) Axial Flow and N2 (0.432 MMscfd) Inflow

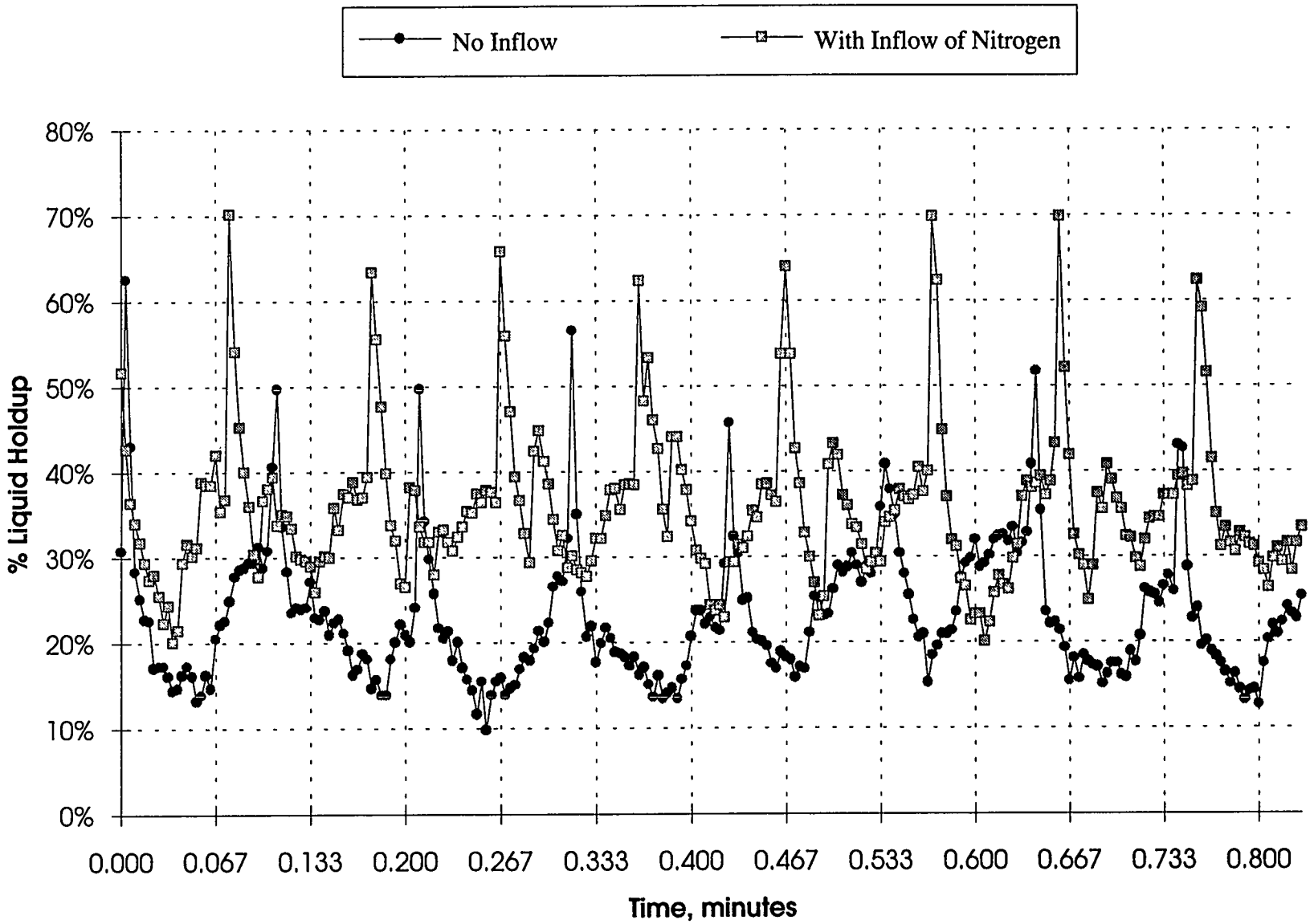

Figure 5.21: Direct Comparison of Liquid Holdups Based on the Data in Figs. 5.19 and 5.20

6. Development of Mechanistic Model for Multiphase Flow in Horizontal Wells (Task 3)

Research undertaken by Nick Petalas and Ph.D. student Liang-Biao Ouyang
Advisor: Professor Khalid Aziz

6.1 Introduction

The development of a mechanistic model for the analysis of multiphase flow in pipes has progressed to the point where it is being tested against experimental data. This has led to the development of a database program for managing all the experimental data that are available to us and for providing data retrieval in formats that are useful for analysis.

Since, even with a mechanistic multiphase flow model, it is required that certain empirical correlations be used, it is important to evaluate the validity of the selected correlations against experimental data. Our studies of the stratified flow and the annular-mist flow regimes have shown that none of the existing empirical correlations yield satisfactory results. For this reason, we have found it necessary to develop new correlations that provide for a better fit of the experimental data with the new model.

6.2 Stanford Multiphase Flow Database

The development of the Stanford Multiphase Flow Database (SMFD) was initiated in June 1994 in an effort to collect, in a usable format as much of the available multiphase flow experimental data as possible. It has been developed using the Microsoft Access relational database engine (version 2.0) which features an easy-to-use graphical user interface as well as sophisticated programming capabilities.

The main design characteristics of the database include:

- A versatile, easily maintainable data structure.
- The ability to select specific data types for output such as would be suitable for testing empirical correlations as well as general design procedures (i.e. experimental data as well as field data are available).
- Support for a variety of output formats, specific to the type of data requested.

The current version of the SMFD includes data from the following sources:

1. The University of Calgary's Multiphase Flow Databank which includes 203 data sets consisting of 20,271 measurements.
2. The University of Tulsa's Well Flow Databank which includes 1,775 data sets of actual well data. Some of these data sets also include pressure and temperature profiles, gas injection, and PVT characteristics.

A mechanism for selecting records from the database is provided and the selection criteria can include any, or all of the following:

- Specification of a pipe internal diameter range
- Specification of an angle of inclination range
- Specification of gas and/or liquid viscosity ranges
- Specification of gas and/or liquid density ranges
- Specification of gas and/or liquid flow rate ranges
- Only records which include flow pattern observations
- Only records which include liquid holdup measurements
- Only records which include pressure gradient measurements
- Only records which include inclination angle specifications
- Only records for rough-pipes or for smooth pipes
- Specific types of fluids for gas and/or liquid phase

Thus it is possible, for example, to extract all stratified smooth flow data which include measurements of liquid holdup and pressure gradient. These can be output in a printable report format, an Excel spreadsheet format, or in a format suitable for reading from a FORTRAN program.

The use of the SMFD has proven crucial to the analysis of the mechanistic model and has simplified the process of extracting data and ensuring their consistency and accuracy.

6.3 Stratified Flow Model

The Stratified flow pattern is one of the most basic flow patterns in the analysis of multiphase flow in pipes. A good model for this flow pattern is particularly important for building general purpose mechanistic models. All such models start with the assumption that the flow is stratified. After testing for the stability of the stratified flow pattern, other transitions are investigated, if stratified flow is found to be unstable.

The SMFD contains over 900 measurements from different sources for stratified flow holdup and pressure drop. Prior to using these experimental data it is important to test their consistency. This can be done by using the momentum balance equations for the gas and liquid phases and comparing the interfacial shears calculated from both equations. If the model is realistic, the interfacial friction shear stresses obtained from both equations should be equal. Our tests, however, showed that the average absolute relative deviation between the two interfacial friction shear amounted to more than 50

The large errors encountered in the check of consistency suggest two possibilities: a) the deviations are a result of errors associated with the experimental measurements, or,

b) the model used is inappropriate. Based on an examination of the experimental data, it was shown that measurement errors have only a marginal influence on the data consistency checks. Therefore, the stratified flow model needed to be reconsidered.

The most likely component of the stratified flow model which can give rise to these errors lies in the determination of the shear stress due to wall friction. The Colebrook-White equation or Blasius-type equations are usually used to compute the wall friction factors for both the gas and the liquid phases in stratified flow models. All of these equations are based on single phase flow. Direct measurements of wall friction shear reported in the literature have verified that the determination of this quantity (i.e., the wall friction factor) for the gas phase is more reliable than that for the liquid phase. Hence it seems likely that a new correlation is required in order to calculate the liquid/wall friction factor and one such correlation has been developed and is currently being tested.

An empirical correlation is also required for the gas/liquid interfacial friction factor in order to complete the stratified flow model. The shear stress due to interfacial friction is an intrinsic characteristic of gas-liquid two-phase flow and it has a profound influence on the properties and the nature of the flow processes. A number of the existing correlations that have been reported in the literature were reviewed and used to determine pressure drop and liquid holdup using the mechanistic model. For most of these correlations, large deviations were found between the measured and the predicted values. A new correlation therefore is also being developed for the calculation of the interfacial friction factor during stratified flow.

6.4 Annular Mist Flow Model

Annular-Mist flow is characterized by a liquid "film" flowing around a "core" of gas with (possibly) entrained liquid droplets. The momentum balance equations for the annular-mist region can be solved for the dimensionless liquid film height which is then used to determine the volume fractions of the flowing phases. In order to do this, two other quantities need to be calculated: the fraction of liquid entrained in the gas core, FE, and the gas/liquid interfacial friction factor, f_i. Both of these must be determined empirically.

Although numerous correlations for f_i and FE have been presented in the literature they are not suitable for use in the present model. The problem stems from the fact that these quantities are not measured experimentally, they are calculated from experimental measurements such as pressure gradient and liquid holdup. Thus, the resulting "experimental" values of f_i and FE, and hence the correlations developed from them, depend on the model used to calculate them. Furthermore, since the two quantities are related, they cannot be treated as independent variables and the correlations for each quantity must be developed concurrently. It is inappropriate to use a correlation developed by one researcher with one developed by another unless the modeling assumptions used by each are consistent.

The approach used in developing correlations for f_i and FE for the mechanistic model involves using the Newton-Raphson method for multiple variables to determine the values of f_i and FE that are required in order that the pressure gradient and liquid holdup as predicted by the mechanistic model match the experimental results. Correlations are then developed based on the converged values of these quantities.

For the annular-mist flow regime the total number of measurements contained in the SMFD amount to 1007 valid measurements. These data include changes in pipe diameter, fluid properties and pipe inclination (upward and downward inclinations are represented).

6.5 Conclusion and Future Work

The development of a mechanistic model for the analysis of multiphase flow in pipes has reached the stage where it is being tested using experimental data. The approach used involves the refining of existing correlations and, in certain cases, the development of entirely new correlations for each of the flow patterns concerned. To date, these include the stratified and the annular-mist flow regimes. The process of testing the model and of developing new correlations has been greatly facilitated as a result of the development of a database program for multiphase flow data.

Future work includes the investigation of the remaining flow patterns with the ensuing development of new correlations, as required. The model will then be refined such that transitions between flow regimes are smooth and discontinuities are eliminated. The model will then be implemented in pipeline and well analysis programs so as to be tested using actual field data.

Once a model is available for predicting pressure drop and holdup in long pipes where the flow is stabilized (i.e., far from the entrance sections), we will then turn our attention to developing models for horizontal wells with influx along the pipe. Such models will be tested with data obtained from the Marathon facility.

7. Sensitivity Studies of Wellbore Friction and Inflow for a Horizontal Well (Task 8)

This study has been conducted by Lillian Berge, a Visiting Scholar from Norsk-Hydro. Advisors: Professors Khalid Aziz and John Fayers

7.1 Introduction

7.1.1 Background

Over the last decade the application of horizontal wells has increased tremendously, and is now a well established technology. The reasons for preferring horizontal wells to vertical wells may be to limit gas and/or water coning, to increase well productivity, to connect blocks in a vertically fractured reservoir, to increase pre breakthrough recovery by having a maximum distance to the unwanted fluid, or to access flank oil or other unswept fluid pockets. Horizontal wells are usually able to drain larger areas than vertical wells, and thus reduce the total number of wells required. Although horizontal wells are more expensive to drill and complete, they can be more attractive due to increased recovery per well.

The modeling of horizontal wells poses additional requirements to the simulation tools. One example is the modeling of frictional pressure drop in the wellbore. Inflow to a horizontal well is distributed over a large section relative to that for a vertical well. Flow conditions in the wellbore can change significantly over this length, which will affect the inflow profile and drainage along the well.

7.1.2 Literature

The importance of modeling frictional pressure drop in horizontal wells has been discussed in the literature[1]–[8]. A few practical examples are reported [2, 3, 4] and [7] where the inclusion of wellbore friction was found to be essential for the prediction of well performance. Common to all these cases are a high permeability (lowest k_h is 1000 mD and lowest k_v is 100 mD). More general results on the effect of frictional pressure drop are given by Dikken[2] and Novy[1]. Dikken presented his results obtained by a simple analytical reservoir / well model, in dimensionless form, which can be useful for quick estimates of optimum well lengths, for given reservoir, fluid and well data. Using a similar but improved analytical model, Novy derived simple guidelines indicating when frictional pressure drop can be neglected. Conservative values were calculated for the well length where friction reduces production rate (or: productivity) by 10 % relative to the rate without friction. These lengths were plotted against production rate of liquid or gas for different wellbore diameters for rough and smooth pipe. Comparison with field data suggests that for many oil wells and most of the gas wells investigated, frictional pressure drop will reduce production rate by less than 10 %, and thus (single phase) friction can be regarded as not significant[1].

7.1.3 Pressure Drop and Inflow

Frictional pressure drop in the perforated section of the well will influence well performance if this pressure drop is significant relative to pressure drawdown at the heel. (Novy[1] suggests 10–15 % of drawdown as a significance limit.) The available pressure drawdown is the driving force for inflow to the well. Friction acts against the flow direction and is a resistance which the incoming fluid must overcome to be able to flow in the wellbore. Pressure drawdown is largest at the heel and smallest at the toe of a horizontal well, the difference being equal to the frictional pressure drop over the perforated well length, (when there is no elevation changes in the well path and provided the reservoir pressure is uniform). If the frictional pressure drop at some distance from the heel becomes as large as the available drawdown at the heel, then no inflow is possible past this point. On the other hand, if the total frictional pressure drop is small compared to the maximum drawdown, then drawdown will not show much variation along the well, and inflow will be fairly uniform, given that the productivity does not change along the well.

The permeability level of the reservoir can to a large extent determine whether wellbore friction will be important or not. For high permeability reservoirs pressure drawdowns for horizontal wells are usually low, because the production rate must be constrained due to process or pipeline requirements or to reduce coning and cusping. Wells will have high productivities and can deliver a high rate at a small pressure drawdown. Under such conditions the frictional pressure drop in the wellbore is likely to be important. Also, for small diameter wells, long perforated sections and high rates the effects of wellbore friction may be significant.

7.1.4 Frictional Pressure Drop in the Simulator

Some kind of frictional pressure drop calculations in the wellbore are available in several of the commercial reservoir simulators. The Eclipse simulator which is used in this study, has a simple single phase frictional pressure drop calculations[6]:

$$\Delta P_f = \frac{2f\rho v^2 L}{D} = \frac{32f\rho Q^2 L}{\pi^2 D^5} \tag{7.1}$$

where f is the Fanning friction factor,
D is the inner diameter of the wellbore,
L is the length of the perforated section,
ρ is the fluid density,
v is the fluid velocity,
Q is the local volumetric flow rate .

The Fanning friction factor is a function of the Reynolds number both for laminar and turbulent flow[6]. For turbulent flow the friction factor also depends on the relative pipe roughness, (ε/D). The friction factor correlations used are developed for pipe flow, and the effect of radial inflow through the perforations is not taken into account. In the case of multiphase flow in the well, it is assumed that the phases are completely mixed giving a homogeneous fluid with average density and viscosity. The average density is calculated as the mass flow rate divided by the total volumetric flowrate at reservoir conditions, and the

mixture viscosity is the volumetric flow weighted average of the phase viscosities[6]. When no slip between the phases is assumed, the in situ volume fractions (holdup) are equal to the input volume fractions. In other words, the mixture property (density or viscosity) is the sum of the products of phase property and phase input volume fraction, for all phases. Well pressure and fluid inflow rates along the well are solved for simultaneously, which is required for numerical stability as the inflow and pressure profiles are dependent on each other[6, 3].

7.1.5 Radial Inflow

The effect of radial inflow on the frictional pressure drop has been regarded as largely unknown[6]. Recognizing that the traditional friction factors used are valid only for stabilized flow (i.e. velocity profile does not change), Joshi[8] argues that the effect of inflow through the perforations can be neglected for turbulent flow, but may give 3–4 times larger frictional pressure drops for laminar flow than calculated by the traditional friction factors. However, experimental and theoretical work done by Asheim et al [5] shows that even small inflow rates can be significant for the total pressure loss in the pipe. Based on the assumption that the acceleration of incoming fluid dominates relative to the disturbance of the boundary layer, they derived a flow resistance model that accounts for radial inflow along the pipe. Total effective friction factor can be estimated as:

$$f = f^{o} + 4D(\frac{Q_L}{Q}) \tag{7.2}$$

where f^{o} is the wall friction factor (Fanning),
D is the inner diameter of the wellbore,
Q_L is the inflow rate per unit length,
Q is the local volumetric flow rate.

These experiments are done with water in a small diameter pipe (1.7 inches) of length 1.4 meters, and for Reynolds numbers in the range 14000–84000.

7.1.6 This Study

To gain more understanding about wellbore friction, how it interacts with inflow to the well, and the sensitivity to different well and reservoir parameters, a series of reservoir simulations have been done based on a field example where wellbore friction is expected to play a dominant role. The frictional pressure drops calculated by Eclipse are compared to the frictional pressure drops obtained by a multiphase pipe flow program (ASAPIPE), for a few selected flow conditions.

7.2 Case Description

7.2.1 Reservoir properties and well characteristics

The case under study is a horizontal well of length 500 meters producing from a thin oil zone in a high permeability reservoir, which has a large gas cap and bottom aquifer. The

reservoir is a poorly consolidated, layered sandstone, with mostly high porosities (30–35% in the clean sands) and anisotropic permeabilities, with ratios $k_x/k_y = 1/3$ and $k_z/k_y = 1/10$ in the model. A heterogeneous distribution of sand properties was used similar to that set up by the operating oil company. Permeabilities and porosities are constant within each layer, but with some variation from layer to layer. The maximum horizontal permeabilities (k_y) are in the order of 2000–20000 mD, in a direction normal to the well. Most of the large bottom aquifer has been given low vertical permeabilities (1–2 mD), as a result of averaging permeabilities over a sequence with some tight zones in between. The upper part of the aquifer has a 20 meter residual oil zone, which gives reduced water mobility. One set of rock relative permeability curves is used for the entire hydrocarbon zone, while for the aquifer (below residual oil zone) the relative permeability to water is assumed to vary linearly with water saturation, with a maximum relperm of 1.0. Some fluid and rock properties are given in Table 7.1.

Table 7.1: Rock and Fluid Properties Used.

Initial pressure at GOC	158 bara
Oil viscosity	1.3–1.5 cP
Gas viscosity	0.016–0.020 cP
Oil formation volume factor, at initial pressure	1.17 Rm^3/Sm^3
Gas formation volume factor, at initial pressure	0.0065 Rm^3/Sm^3
Solution gas-oil ratio, at initial pressure	69.0 Sm^3/Sm^3
Rock compressibility, at initial pressure	1.74 bar^{-1}
Connate water saturation	7%
Critical gas saturation	10%
Residual oil saturation to water	25%
Residual oil saturation to gas	7%
Max. relperm to water in presence of residual oil	0.28
Capillary pressure	none

In this single well model the reservoir is horizontal, and permeabilities are constant within each layer. The horizontal well section is also modeled as being perfectly horizontal, to be able to easily isolate the effects of wellbore friction. The well is completed in the lower part of the 20 meter thick oil zone, 4 meters above the oil-water contact, and experiences both gas and water coning. To limit sand production, the horizontal section is completed using a prepacked screen, which has a 6 inch inner diameter and the absolute roughness is estimated to be 1 mm.

The original dataset has been simplified for the purpose of studying wellbore friction. In addition to straightening out the well path to remove any hydrostatic head in the wellbore, the geology has been modified to give uniform conditions (constant productivity) along the well. Local calcite strings, cutting through the well path at high angle, are excluded. These were originally modeled as permeability reductions at the gridblock boundaries, and gave some restriction to vertical flow and flow along the well direction.

7.2.2 Simulation Grid

The simulation grid used has a very good vertical resolution, with 0.5–2.0 meter thick layers through the entire oil column, using a total of 23 layers from the gas-oil contact to the water-oil contact. In the Y-direction (normal to the well), the grid spacing is gradually increased by a factor 2–3 outwards from the well, starting with a 5 meter wide wellblock. Along the well (in X-direction) a constant grid interval of 50 meters is used from 200 meters past the toe until 200 meters past the heel, and is then coarsening upwards by a factor 2–3 for the more distant parts of the drainage volume. The simulation grid is shown in Figures 7.1 and 7.2.

7.2.3 Production Schedule

A production period of 7 years is simulated, with a target oil rate of 2500 Sm^3/D, and a maximum gas rate of 2E+06 Sm^3/D. The minimum bottomhole pressure is set to 150 bars (ca. 10 bars lower than initial pressure at the well). At the top of the reservoir 70% of the produced gas is reinjected, by a single block gas injector (point source) in the middle of the top layer.

Initially, the target oil rate will limit production. Later when gas breaks through, the well will be constrained by the specified maximum gas offtake, and at the end the available pressure drawdown is the limiting factor. This schedule is made to go through these typical phases of a well's expected production history within a relatively short period, and still have appropriate production rates. The maximum rates are chosen for this study, and no optimization is done with respect to oil recovery. (It is realized that the 2E+06 Sm^3/D gas rate may be on the high side, and the minimum bottomhole pressure of 150 bars may be on the low side.) For the purpose of this study, it is considered appropriate to apply the pressure limit downhole, rather than as a minimum surface pressure.

7.3 Simulations

It was discovered that the grid used in the original dataset had some unfortunate effects on the simulation results, and therefore some grid sensitivity studies were done to find a more suitable simulation grid. Then the effect of wellbore friction could be studied for various reservoir and well conditions.

7.3.1 Grid Sensitivities

To reduce the CPU-time per simulation, the grid sensitivities are undertaken with a smaller simulation model, made by peeling off the outer bands of grid blocks in the X- and Y-direction and removing 2 layers at the top and 4 at the bottom of the original model. Almost 2000 grid blocks are removed. In the new mini-model most of the gas cap and aquifer is removed and the oil volume is 3.5 times smaller. Porevolumes in the new bottom layer is increased and transmissibility to the layer above is reduced significantly to resemble the original aquifer. Gas and water are injected through line sources parallel to the producer at top and bottom of the mini-model, and injection rates of gas and water are tuned to get a similar well behavior for the horizontal producer as in the original model.

A series of simulations are run with slightly different grids, the total number of gridblocks varying from originally about 4000 and up to almost 19000. Some experimenting is done with different rates of coarsening up the grid away from the well in the Y-direction, and with how far past the well in the X-direction (along the well) relatively fine blocks should be used. Different grid block lengths in the X-direction have been tried at the ends of the well. The original grid was very detailed in the Z-direction, but a few experiments are done with even finer layering. Only a period of 3 years is simulated, which includes the gas breakthrough and the following gas rate increase. Figures 7.3–7.6 show some of the grids used for these sensitivities.

7.3.2 Parameter Variations

A total of 19 sensitivities are simulated, varying one parameter at a time. A summary of all the cases investigated is given in Table 7.2. All sensitivities (cases 3–19) include frictional pressure drop calculations.

Key parameters like the friction factor (roughness) and pipe inner diameter have been changed, and one run has been made with a longer horizontal well. Also, the skin factor along the wellbore has been manipulated. Lower levels of permeability are investigated, along with a few attempts to "homogenize" the reservoir, using constant average values for k_h and k_v for the entire reservoir. Liquid rates vary when changing the permeability, and two different maximum gas rates are compared. A lower target oil rate is tried, to see the influence of friction for low liquid rates. The effect of the residual oil zone and the low aquifer permeability is also briefly looked at.

The inner diameter of the liner is changed without changing the well diameter. (The liner diameter is used in frictional pressure drop calculations, and the well diameter is used to calculate the well productivity index.) To change the well diameter by the same ratio as the liner diameter is changed would only have a small effect on well productivity, and here productivity is kept constant. It is believed that frictional pressure drops can be much larger for multiphase flow than for single phase (depending on the flow regime), and for one case an arbitrary and artificially high effective roughness is used during free gas production to mimic this. To simulate a longer production well, the grid was adjusted to have the same gridblock sizes along the well length as for the shorter well.

7.3.3 Comparison with ASAPIPE

For a few selected flow conditions, the inflow distribution along the well as calculated by Eclipse, is fed into a multiphase pipe flow program (ASAPIPE) [9] to get an alternative calculation of the frictional pressure drop in the perforated section of the well. The multiphase flow program employs empirical correlations to calculate liquid holdup and pressure drop in the pipe. Different correlations are available. For this study two different approaches are used; the composite method of Mandhane, Gregory and Aziz (MGA), and the popular

*Based on layers 2–24, (oil zone permeabilities more dominating).
†Based on layers 1–36 (all layers).
‡For layers 35–36.

Table 7.2: List of the Sensitivity Cases Considered

Case no.	Description
1	Reference case, including friction, $\varepsilon = 1$ mm (prepacked screen)
2	Reference case, without friction
3	Smooth pipe, $\varepsilon = 0.05$ mm (new liner)
4	Synthetic high roughness, $\varepsilon = 10$ mm, during free gas production
5	Smaller inner diameter, $ID = 5$ inches
6	Larger inner diameter, $ID = 7$ inches
7	Longer well, $L = 1000$ meters
8	Skin factor $S = 3$, constant along the well
9	Variable skin, $S = 5$–1, largest at heel
10	Skin factor $S = 10$, constant along the well
11	Local flow barriers (stochastical calcite (shale) realization)
12	Permeabilities reduced by a factor 10 ($k_y = 200$–2000 mD)
13	Permeabilities reduced by a factor 100 ($k_y = 20$–200 mD)
14	"Homogeneous" case, avg. $k_h = 7000$ mD, avg. $k_v = 1400$ mD *
15	"Homogeneous" case, avg. $k_h = 1500$ mD, avg. $k_v = 300$ mD †
16	No residual oil zone in the aquifer, (increased water mobility)
17	Vertical aquifer permeability incr. by a factor 100 ‡
18	Maximum gas rate 1E+06 Sm^3/D
19	Low oil rate, 1000 Sm^3/D

Beggs and Brill method. With the former approach the flow pattern is predicted by a correlation developed by Mandhane, Gregory and Aziz, and the flow pattern is then used to choose an appropriate correlation for the prediction of liquid holdup and pressure drop according to the MGA-method. The Beggs and Brill method also calculates liquid holdup and pressure drop based on flow pattern, but their flow patterns are different from the most commonly recognized terms. The Beggs and Brill pressure drop correlation for rough pipe is used.

Starting from the upstream end of the well, one run with the ASAPIPE program has to be made for every pipe segment corresponding to the distance from the midpoint of a wellblock to the midpoint of its downstream neighbor. Over each segment the flow rates are constant, and the pressure at the inlet end is updated according to the previous calculation. As far as possible the fluid properties are kept similar as in the reservoir simulator. (Gas viscosity, solution gas-oil ratio, oil formation volume factor and liquid viscosity are tabulated against pressure (for saturated fluid). Oil viscosity values are used as liquid viscosity, and gas formation volume factors could not be entered, as the program estimates gas compressibility from correlations based on specific gas gravity. A liquid-gas interfacial tension of 20 mN/m is used.)

Table 7.3: Flow Conditions Selected for Frictional Pressure Drop Calculations.

Calc. no.	Flow condition taken from	Oil rate (Sm^3/D)	Water rate (Sm^3/D)	Gas rate (Sm^3/D)
1	Case 1, at 1095 days (3 yr)	2143	1616	2000000
2	Case 1, at 1460 days (4 yr)	1844	1416	955078
3	Case 12, at 365 days (1 yr)	819	383	2000000
4	Case 12, at 1095 days (3 yr)	515	333	2000000
5	Case 14, at 365 days (1 yr)	1451	4900	2000000
6	Case 5, at 730 days (2 yr)	2190	1445	2000000

7.4 Results

7.4.1 Coning of gas and water

Typically, water breaks through immediately because of the proximity to the water zone. The water production rate increases constantly, but stabilizes when the maximum gas rate is reached. (Consequently, the time to gas breakthrough can influence the maximum liquid rates for this case.)

The shape of the developing gas cone depends on how drawdown varies along the well, which is determined by the pressure profile within the wellbore (i.e. the frictional pressure drop along the well). Hence, the time to gas breakthrough shows a large variation as drawdown along the well is changed. With no friction in the wellbore, free gas breaks through over a large section at the middle of the well. This is also the situation when permeability is reduced to a level where pressure drawdown becomes much larger than the frictional pressure drop. For all other cases investigated, the gas breakthrough occurs at the heel, where the maximum drawdown occurs. The well length over which the free gas enters may change with the drawdown / inflow distribution for each case, and is here usually limited to the first 100–200 meters closest to the heel. The different shape of the gas cone with and without wellbore friction is illustrated by Figures 7.7–7.8 and 7.9–7.10. (In some of these contour plots th e line of 0% gas saturation may show a strange behavior, but this has no physical meaning.) The reservoir pressure gradients in the well area, with and without wellbore friction, can be seen in Figures 7.11 and 7.12.

The gas cone gradually widens (and elongates) and gas rate increases rapidly to a specified maximum which marks the end of the oil rate plateau (see Fig. 18). On bottomhole pressure control, available drawdown is reduced and as a result the gas cone withdraws from the well, and oil rate then declines rapidly. How fast this gravity segregation occurs depends on the maximum pressure drawdown. For larger pressure drawdowns gravity is less dominating, and the gas cone moves more slowly away from the well.

The tips of the gas cone and water cone will meet in the wellbore. The gas cone, being much deeper and wider than the water cone, is pushing some oil into the water zone at each side of the well.

7.4.2 Flow in the near well area

Fluid flow in the near well area is studied by dividing the reservoir model into 10 regions, a top slab (reg. 1), a bottom slab (reg. 10) and a thin slab of 3 layers around the well (reg. 2-9), which is further subdivided as shown in Fig. 13. A rectangular cylinder of 3×3 gridblocks along the well is isolated (reg. 3+6) to better illustrate flow into the near well area.

Vertical and horizontal flow of oil into the well region is of the same magnitude when friction is included (Case 1), but without friction the horizontal oil inflow is larger (Fig. 14). The effect of wellbore friction is to slightly increase the vertical inflow of oil and reduce horizontal inflow from the time free gas is being produced. This may be because with friction gas breaks through over a small section of the well, leaving a higher mobility to oil and larger hydrostatic head for the rest of the well, than is the case without friction.

The flow of oil in the reservoir parallel to the well is very small. (This can intuitively be seen from the pressure contour plots in Figures 7.11 and 7.12.) With friction in the wellbore there is initially a small flow towards the heel (from regions 2,3 and 4 to regions 5,6 and 7), increasing with the frictional pressure drop, as illustrated by Figure 7.15. Later when the well is on bottomhole pressure control, the flow goes the other way, towards midwell or toe region. When the well is controlled by bottomhole pressure, drawdown is reduced a lot more at the heel than at the toe, the difference in drawdown along the well disappears, and more of the inflow is from the toe end. (A more uniform inflow promotes larger frictional pressure drop, which is not possible when the bottomhole pressure is fixed, so this redistribution of inflow amplifies the decline in oil rate at this stage.) Without wellbore friction flow along the well is always towards the middle of the well.

In this model the well penetrates only a small fraction of the drainage volume (ca. 1/5), and there is a large flow of oil out of the regions past the ends of the well (regions 8 and 9). This flow is almost 50 % as large as the total horizontal inflow of oil to the well. Especially when free gas has broken into the well, a large part of the oil inflow takes place at the ends of the well, supported by the flow out of regions 8 and 9.

7.4.3 Frictional Pressure Drop

Frictional pressure drop follows the variations in fluid rates, and is largest when the well produces at its maximum gas rate (highest fluid velocities) as shown in Fig. 19. When the frictional pressure drop in the wellbore changes, so does the inflow distribution along the well, and vice versa. The pressure profile in the wellbore and the inflow distribution are interdependent, and show a highly nonlinear variation over the well length, as illustrated by Figs. 20 and 21. For instance, the frictional pressure drop over the last half wellblock at the heel (25 m) may be of the same order of magnitude as the pressure drop over the whole upstream well length (almost 500 meters).

Frictional pressure drop is calculated as the difference between the first connection pressure (wellbore pressure) at the toe and the bottomhole pressure, which is here the wellbore pressure at the very downstream end of the perforation interval. Pressure drawdown is calculated as the difference between the most distant reservoir pressure (at the drainage boundary) and the well pressure. For drawdown at the heel, the bottomhole pressure is used. The reservoir pressure is taken as the pressure of a grid block on the edge of the model (past

the toe of the well) at the same depth as the horizontal well. (The average pressure for the hydrocarbon porevolume could not be used, because the well is close to the bottom of the hydrocarbon volume, and the average pressure is representative for the reservoir pressure at some shallower depth (the gravity center).)

7.4.4 Grid

Inflow rate and well pressure are assumed constant over the length of each grid block. The shape of the wellbore pressure profile therefore indicates that ideally, gridblock lengths should be gradually smaller closer to the heel to get the most accurate inflow and pressure distribution in the well. In practice, use of too small gridblocks has to be avoided because of numerical problems and large CPU-times. The result is smoothed inflow and pressure profiles, which at the last few meters from the heel look more uniform than they should be.

In the Eclipse simulator inflow to the well is treated as entering at the midpoint of the perforated interval in each wellblock (which in this example is at the middle of the wellblocks). At the heel of the well the inflow is high and very non-linear with well length. With larger grid intervals (Δx) at the heel, some of the fluid will enter the wellbore too far upstream. Especially for the last half wellblock at the heel the pressure drop in the well may be too high, and bottomhole pressure too low. Simulation results with two different gridblock lengths at the heel are compared in Figures 7.18–7.21.

Due to the 3-dimensional shape of the gas cone, relatively fine grid blocks should be used along the well length, and also past the heel and toe in the well direction. The pressure and saturation gradients can be large near the ends (see Figs. 7.7–7.12). A too coarse grid will distort the shape of the cone, and can give wrong breakthrough times.

Grid sensitivities have discovered that for this problem and with the available resources, it is not possible to simulate with as fine a grid as needed and still achieve acceptable CPU-times. Finer grid gives later gas breakthrough, but some refinements are too expensive (Fig. 16 and 17). It is necessary to find a compromise, and get as good a solution as possible for a tolerable CPU-time. Based on the grid sensitivities with the mini-model, the friction sensitivities are simulated using $25 \times 13 \times 36 = 11700$ grid blocks, (based on Grid 9). A few sensitivities are also repeated with more blocks along the well ($30 \times 13 \times 36 = 14040$, based on Grid 4, which has $\Delta x = 25$m at the heel end), to get a more detailed inflow and pressure profile (cf. Figs. 18–21). For these simulations the CPU-time is approximately 2 times larger than with the base case grid, (21 hours vs. 10 hours, when the simulations are run on a Dec-Alpha work station).

7.4.5 CPU-time

The size of the smallest grid block will control the time step and hence have a strong influence on the CPU-time. For a coning problem the smallest grid blocks are typically the wellblocks, where the largest flow velocities occur. Flow through a wellblock can be very large. (For example, with the finest grid used here (Grid 2), the minimum porevolume is 9 m^3, and at one point in time, inflow to this wellblock was found to be 500 times the porevolume per day.) At the surface of the cone, saturation can change rapidly, and numerical problems may occur. The simulator has large difficulties during the period of increasing gas rates

following the breakthrough, and most of the CPU-time is spent on this period.

With practically no limitation on the maximum time step, the next timestep will increase by a specified factor and the number of Newton iterations increase until convergence cannot be reached within the maximum number of iterations. Then the time step is chopped by a specified factor and repeated, and the cycle starts again. By fixing the time step to a value just below the time step size where chopping usually occurs, it is possible to save CPU-time, as less iterations are done. For this example, a maximum time step of 1 day is used during the period where most numerical problems are expected. Before and after this period the maximum time step is 10 days.

The CPU-time could also be reduced by loosening the convergence tolerances. For instance, 50 times larger tolerances than default for the residuals for linear and nonlinear equations, gave essentially the same gas breakthrough and oil recovery, for significantly less CPU-time. Changing the convergence tolerances is generally not recommended and should be done with care.

7.4.6 Effect of Changing the Parameters

The results of the sensitivity simulations are summarized in Table 7.4. (See Table 7.3 for a description of the cases simulated.)

Pipe roughness and friction factor are uncertain parameters, and they may change with time. Even the high "effective roughness" used to account for non-homogeneous multi-phase flow of free gas and liquid, does not seem to be very detrimental to the oil production. In this case the frictional pressure drop is up to 85 % of the available drawdown at the downstream end. The production performance of the well with different levels of wellbore friction (roughness) is presented in Figures 7.22–7.27. The most important difference is the shift in gas breakthrough time and position, and the principally different drainage along the well when friction is eliminated.

Skin damage actually has a small positive effect on oil production, giving slightly more uniform inflow along the well, which can be explained by the increased drawdown making frictional effects less important. A larger skin at the heel due to formation damage during drilling is reasonable, because of longer exposure time to drilling mud. This makes the inflow profile more uniform, but nonetheless the effect of wellbore friction dominates for this high permeability case. Results for different skin factors are shown in Figures 7.28–7.30, where it is also illustrated that frictional pressure drop increases when more fluid travels from the distant parts of the well.

The frictional pressure drop is very sensitive to the pipe diameter, as can be seen directly from Eq. (7.1). The time to gas breakthrough and length of oil plateau show a large variation (up to 50 %) when the pipe diameter is changed by 1 inch, as illustrated by Figure 7.31. To increase the inner diameter by 1 inch (from 6 to 7 inches) has about the same effect on production performance as to reduce the pipe roughness by a factor 20 (from 1 mm to 0.05 mm) for this example. Both frictional pressure drop and drawdown change a lot with the diameter (Figs. 7.32 and 7.33). When frictional pressure drop can be a problem, it should be considered to use a larger wellbore diameter. As Figures 7.34 and 7.35show, inflow is more uniform with larger wellbores and free gas inflow is distributed over a larger section. In particular, it is detrimental to use a smaller pipe diameter than 0.152 meters (6

inches) in this case.

Table 7.4: Summary of Simulation Results. (Absolute times and volumes are given only for case 1. For the other cases the differences relative to case 1 are shown. Frictional pressure drop is reported at max. gas rate, and all results are with the basic grid ($25 \times 13 \times 36$).)

Case no.	Time to gas breakthrough (days)	Oil rate plateau (days)	Time to min. BHP (days)	Cum. oil production (10^6 Sm^3)	Frictional pressure drop (bars)
1	465	730	1299	4.6	2.0–1.8
2	+365	+146	+321	+0.1	0.0
3	+170	+117	+143	+0.1	1.2–1.1
4	+0	-206	-265	-0.1	3.9–3.4
5	-234	-240	-340	-0.2	4.0–3.5
6	+207	+132	+161	+0.1	1.1–1.0
7	+442	—	+425	+1.2	>2.3
8	+117	+43	-50	+0.1	2.3–2.1
9	+202	+117	-55	+0.3	2.6–2.3
10	+208	+79	-184	+0.3	2.9–2.6
11	+16	+0	-46	+0.0	2.2–1.9
12	-445	-669	-134	-3.1	3.5–1.7
13	—	—	-1299	-3.9	>0.7
14	-363	-588	-664	-2.6	4.0–3.3
15	-431	-679	-378	-3.4	3.5–2.4
16	-222	-310	-560	-1.5	3.5–3.1
17	-91	-119	-174	-0.6	2.4–2.2
18	+0	-103	+490	+0.2	1.3–1.0
19	—	—	—	-2.4	0.1–0.2 [§]

Lower permeabilities give earlier gas breakthrough due to a larger drawdown being necessary to obtain the specified rate. When permeability is reduced by a factor 10 (k_y in the range 200–2000 mD), the shape of the gas cone is less influenced by friction and free gas enters the well over most of the horizontal section. For very low permeabilities (k_y in the range 20–200 mD), the specified rates cannot be obtained, the well is controlled by bottomhole pressure all the time, and friction effects are not significant. Rather, well productivity is the limiting factor for production. With very low permeabilities, the viscous forces are so large that gravity segregation does not occur, (except maybe a small decrease in GOR at late time). When the maximum gas rate is reached, oil rate declines more sharply, giving very high GOR-values. The simulations are much faster and have less numerical problems for lower permeabilities. Production profiles are very different for the three permeability levels, as shown in Figure 7.36. Figure 7.37 and 7.38 demonstrate how the inflow profile changes with the ratio of frictional pressure drop to drawdown at the heel ($\Delta P_f / \Delta P_d$).

[§]Max. gas rate not reached.

With uniform horizontal and vertical permeabilities throughout the reservoir (case 14 and 15), the production rate of water increases dramatically compared to the reference case. Then larger pressure drawdowns are needed to obtain the target oil rate, and very early gas break through occurs. Due to the high liquid rates, frictional pressure drops are large. For the lower permeability level (k_h=1500 mD and k_v=300 mD), less liquid is produced and inflow is more uniform. In the reference case water influx is strongly limited by very low vertical permeabilities in the aquifer and by the residual oil zone. The water cut does not increase above 45 %, while wateriest of 80 % are obtained with uniform permeabilities.

The original vertical permeability in the aquifer is very low, and only a large increase in k_v will have any effect on production performance. As can be seen from Table 7.4, the residual oil zone has a very positive effect on the oil recovery. When the vertical aquifer permeability is increased to be in the order of 100–200 mD (Case 17), the maximum liquid rate increases from 4200 (Case 1) to 4900 Sm^3/D, and when the residual oil zone is removed (Case 16) the liquid rate increases up to 6500 Sm^3/D. Fluid inflow along the well is already very non-uniform and the distribution does not change much as the liquid rate goes up. For these high liquid rates it seems that the frictional pressure drop increases almost linearly by 0.6 bars per 1000 Sm^3/D of liquid rate. (This is to be expected for single phase laminar flow, as can be seen if we substitute the expression for the laminar friction factor into Eq. (7.1).)

The effect of local flow barriers (calcites) is studied with the original simulation grid, for which a stochastical calcite realization was available. The gas breakthrough comes a few days later, and the first GOR-increase is slower, due to a more tortuous path for the gas flow down to the well. The frictional pressure drop and drawdown increase slightly, as the inflow is a little more uniform than without these local flow restrictions. In a way the calcites can have a similar effect as wellbore skin, namely to increase drawdown. Furthermore, a higher density of calcites at the heel than along rest of the well also contributes to more uniform inflow. Almost no effect can be seen on the total oil recovery.

By lowering the maximum gas rate from 2E+06 Sm^3/D to 1E+06 Sm^3/D, the frictional pressure drop in the well is significantly reduced. At a liquid rate of 4000 Sm^3/D, the frictional pressure drop is 2.0 barsa with a gas flow of 2E+06 Sm^3/D, and 1.3 barsa with 1E+06 Sm^3/D of gas, i.e. 35 % reduction. Relative to pressure drawdown at the heel, the frictional pressure drop is less important for the lower gas rate, but the ratio $\Delta P_f/\Delta P_d$ is still 50–60% and the inflow is dominated by the effect of friction.

For a target oil rate of 1000 Sm^3/D there is no gas breakthrough within the 7 year period simulated. Only a small gas cone, several meters above the well has developed. This gas cone is almost of the same depth along the entire well, being only a couple of meters deeper at the last half near the heel. The liquid rate stabilizes at 1500–1600 Sm^3/D. The frictional pressure drop is less than 0.2 bars, which is about 30 % of pressure drawdown at the heel, and the inflow profile is not much affected by friction.

In this model a 1000 meter long well (Case 7) performs a lot better than a 500 meter horizontal well. The frictional pressure drop eventually increases up to 75 % of drawdown at the downstream end as the gas rate increases, but with the fluid inflow distributed over a much larger area, the gas rate increases more slowly. Oil recovery is larger, due to a much later gas break through. However, on a field scale the drainage volume of one well will typically be much smaller than in this single well model, which covers an area of 2600 × 2800 m^2 and contains 46 mill. Sm^3 of oil. The effect of drilling longer wells will then be

more modest.

7.4.7 Comparison with ASAPIPE

A comparison of frictional pressure drops calculated by the reservoir simulator (Eclipse) and by the multiphase pipeflow program (ASAPIPE) is shown in Table 7.5. The MGA-method predicts frictional pressure drops of the same magnitude as Eclipse, while the Beggs and Brill method gives much larger pressure drops for the flow conditions investigated. The relative difference in pressure drops is apparently depending on the flow regime.

Table 7.5: Frictional Pressure Drops in the Horizontal Well, Calculated by Eclipse and by ASAPIPE Using the Method of Mandhane, Gregory and Aziz (MGA) and the Beggs and Brill Method (BB), for the Flow Conditions in Table 7.3.2. (Flow Regimes Predicted by the Beggs and Brill Method are Not Available.)

Calc. no.	Flow regime [¶] in the well from toe [‖]	Frictional Pressure Drop (bars)		
	ASAPIPE	ASAPIPE		Eclipse
	MGA-method	MGA	BB	
1	450m EBF, 25m SLG	1.7	2.6	1.9
2	475m EBF	1.0	1.3	1.0
3	50m STF, 250m EBF, 175m SLG	2.0	3.0	1.9
4	50m STF, 250m EBF, 175m SLG	1.8	2.6	1.6
5	450m EBF, 25m SLG	3.3	5.1	3.7
6	450m EBF, 25m SLG	3.3	5.3	3.7

For this example, the frictional pressure drops calculated by the MGA-method range from 11 % below the Eclipse calculated values to 13 % above. For elongated bubble flow, also termed plug flow, the pressure drops are almost similar with the MGA-method and with the homogeneous mixture calculation in Eclipse. When the transition from elongated bubble flow to slug flow occurs in a region where wellbore pressure is changing slowly and most of the pressure drop is within the slug flow regime, the MGA-method predicts larger frictional pressure drops than Eclipse. However, when the transition to slug flow is very close to the heel where wellbore pressure changes rapidly and both upstream and downstream pressure drops are large, the MGA-method gives a smaller total frictional pressure drop than Eclipse, the deviation being mainly within the short slug flow part of the well. In one of the calculations a small discontinuity in pressure drop at the transition between the two flow regimes (EBF and SLG) is evident. This pressure discontinuity is probably larger for flow conditions where pressure drops are larger, and that may be the reason why the MGA-method predicts smaller total frictional pressure drops than Eclipse for some cases.

The Beggs and Brill method predicts 30–60 % larger frictional pressure drops than Eclipse, for the flow conditions selected. The largest deviations occur for Calculations 3 and 4

[¶]STF=Stratified Flow, EBF=Elongated Bubble Flow, SLG=Slug Flow.

[‖]Total effective perforated length is 475 m, as the first inflow is 25 m from the toe (at the block midpoint).

(cf. Table 7.5), where the MGA-method predicts the largest interval of slug flow. Compared to the MGA-method, the Beggs and Brill rough pipe correlation estimates 60–120 % larger pressure drops for the pipe segments where slug flow is predicted. For the pipe segments where the MGA-method predicts elongated bubble flow, the Beggs and Brill method comes up with almost identical pressure drops as the MGA-method when the GOR is very low (close to solution gas-oil ratio), but the Beggs and Brill method has up to 45 % larger values for larger GOR-values (when gas cap gas enters the pipe) in the same flow regime. For stratified flow it seems like the Beggs and Brill method gives lower pressure drops than the MGA-method, but this has no effect on the total pressure drop, as the frictional pressure drops are very small in this flow regime. Previous studies [10] have also reported larger frictional pressure drops with the Beggs and Brill method than by the MGA-method.

A major drawback with this comparison is that the inflow profile calculated by Eclipse is forced into the pipeflow program. Then some of the actual difference between these different methods of pressure drop calculation is removed. In reality, when the mutliphase pipe flow program calculates a slightly different pressure drop over a pipe segment than Eclipse does, the inflow along the pipe should be redistributed in the pipe flow program, due to the dependency between wellbore pressure and inflow profiles. To do a correct comparison between different methods for frictional pressure drop calculation, the multiphase calculations should be integrated in the reservoir simulator.

7.5 Observations and Conclusions

Based on these simulation results for a reservoir with large permeabilities, it appears that frictional pressure drop in the wellbore only has a small influence on the cumulative oil produced. (For the cases where oil recovery is significantly reduced (Table 7.4), major changes have been made to the geology and these cases represent reservoirs with less favorable properties.) Frictional pressure drop needs to be modeled properly to accurately predict the time to gas break through and how fast the gas rate will increase. Frictional pressure drop will dominate inflow to the wellbore when this pressure drop is significant compared to pressure drawdown. Here, frictional pressure drop is more than 50 % of the available drawdown at the heel end for most of the cases studied. For the more complex cases when conditions like permeability, distance to barriers, etc. varies along the well, the relative importance of wellbore friction may be different for each case. The position and extent of the gas breakthrough along the well is sensitive to wellbore pressure drop, and this could have implications for a recompletion policy to reduce gas production. For high permeability reservoirs, like that studied here, wellbore friction cannot be neglected.

An interesting and unexpected result is that increasing skin damage seems to be favorable for this highly productive well, and the reason is that increasing pressure drawdown here makes the inflow profile less dominated by the frictional pressure drop. The sensitivity simulations done suggest that the influence of friction can be reduced by controlling the inflow or by careful well design. For further investigations it could be useful to be able to vary inner diameter and effective roughness along the pipe in the reservoir simulator.

Somewhat surprisingly, it was found that the frictional pressure drops obtained by the MGA-method could deviate by about 10 % on either side of the values from Eclipse, for

certain flow conditions. The Beggs and Brill method predicted significantly larger frictional pressure drops than the MGA-method, and other multiphase pressure drop correlations would probably not agree with either the MGA-method or the Beggs and Brill method. Multiphase flow correlations would normally be expected to give larger frictional pressure drops than the homogeneous / single phase calculations in Eclipse. It is nor clear, however, which method gives the most reliable results for different flow conditions.

Analytical methods for evaluating the effect of frictional pressure drop, as presented by Novy[1] and Dikken[2], may be useful for understanding the phenomena and for screening purposes, but will be too simplified to be applied for detailed studies of real wells. It may be required to do reservoir simulations, but even the simulators have a very simplified approach to frictional pressure drop calculations in the wellbore. More accurate solutions could be obtained by incorporating better procedures for calculating pressure drops in non-homogeneous multiphase flow, and by developing friction factor correlations more appropriate for flow in perforated pipes, that accounts for variable perforation density and the effect of radial inflow through the perforations. Some results are published[5] on the effect of radial inflow for single phase flow of water, and these need to be verified for multiphase liquid-gas flow.

References

[1] Novy,R.A.: "Pressure Drops in Horizontal Wells: When Can They Be Ignored?", paper SPE 24941 presented at the 1992 SPE Annual Technical Conference, Washington, DC, OCT. 4–7.

[2] Dikken, B.: "Pressure Drop in Horizontal Wells and Its Effect on Production Performance", JPT (Nov. 1990) 1426–33.

[3] Seines, K. et al: "Considering Wellbore Friction Effects in Planning Horizontal Wells", JPT (Oct. 1993) 994–1000.

[4] Collins, D. et al: "Simulation of Horizontal Well Performance in Heterogeneous Reservoirs", preprint prepared for 1991 CIM/CANMET Conference, Regina, Oct. 7–9.

[5] Asheim, H. et al: "A Flow Resistance Correlation for Completed Wellbore", Jornal of Petroleum Science and Engineering, 8 (1992) 97–104.

[6] Eclipse 92A User's Manual, Appendix: "Wellbore Friction Option", Intera Information Technologies Limited.

[7] Marett, B.P. and Landman, M.J.: "Optimal Perforation Design for Horizontal Wells with Boundaries", paper SPE 25366 presented at 1993 SPE Asia Pacific Oil & Gas Conference & Exhibition, Singapore, Feb. 8–10.

[8] Joshi, S.D.: "Horizontal Well Technology", Pennwell Publishing Company, Tulsa, Oklahoma (1991).

[9] "ASAPIPE & ASAPROP, User Guide and Reference, Version 2.01", Aziz, Spencer & Associates Inc. (1993).

[10] Fayers, J. et al: "Opportunities for Horizontal Wells and Problems in Predicting Their Performance", preprint prepared for 1994 SPE/CIM/CANMET Conference, Calgary, March 20–24.

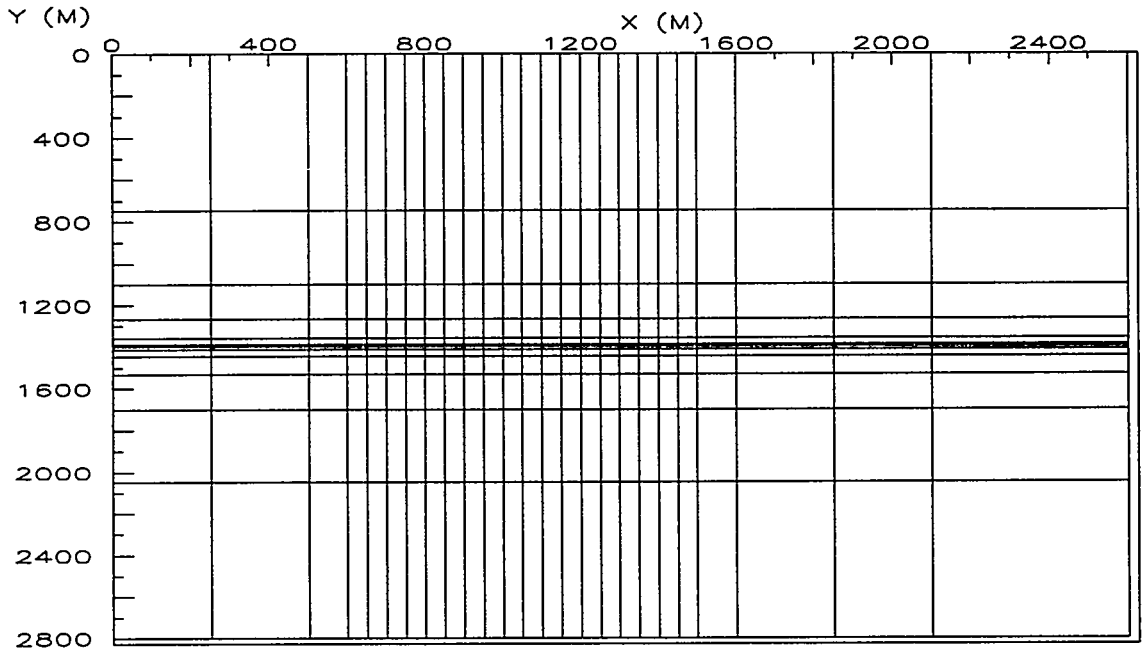

Figure 7.1: Areal simulation grid

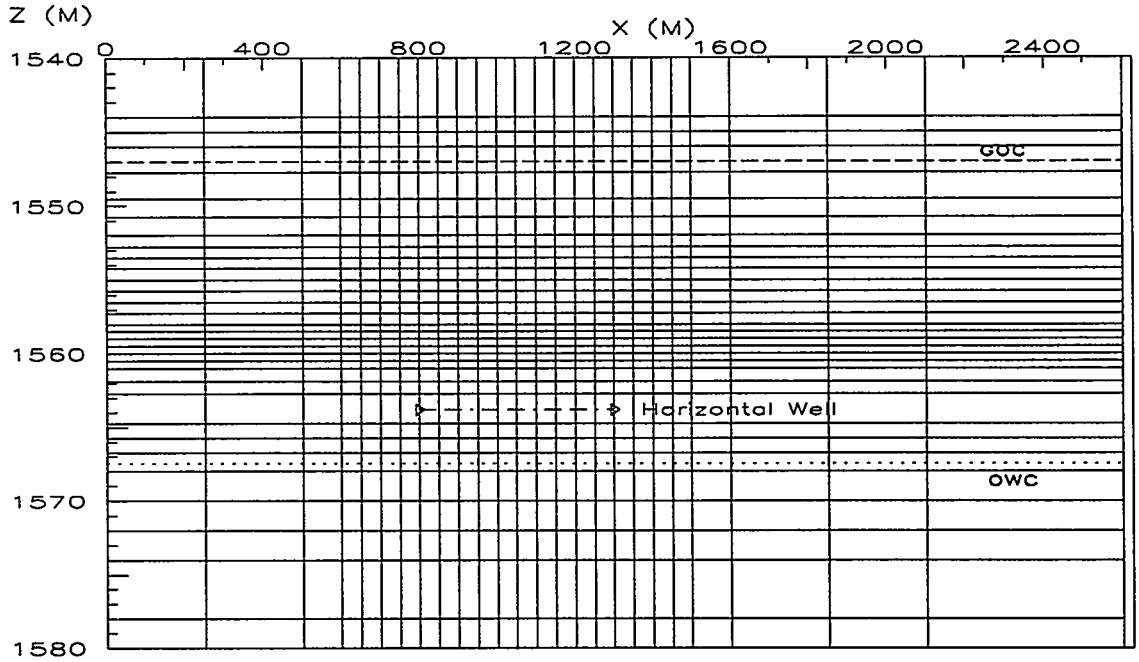

Figure 7.2: Cross section along the horizontal well

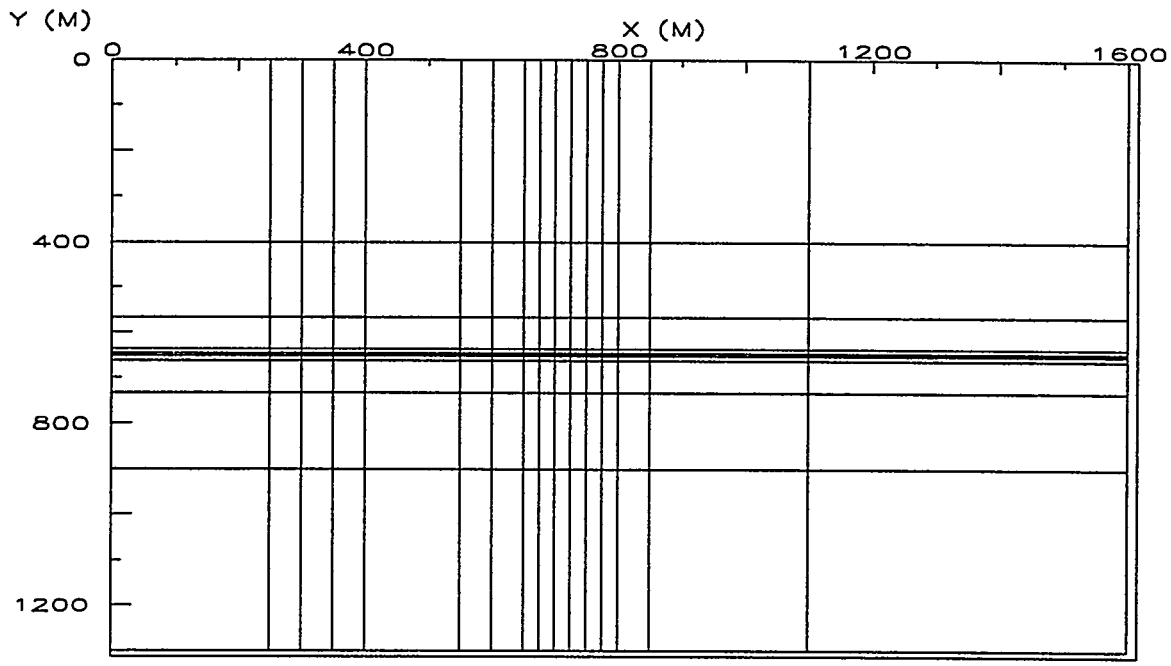

Figure 7.3: Grid 1, XY-plane (Mini-model)

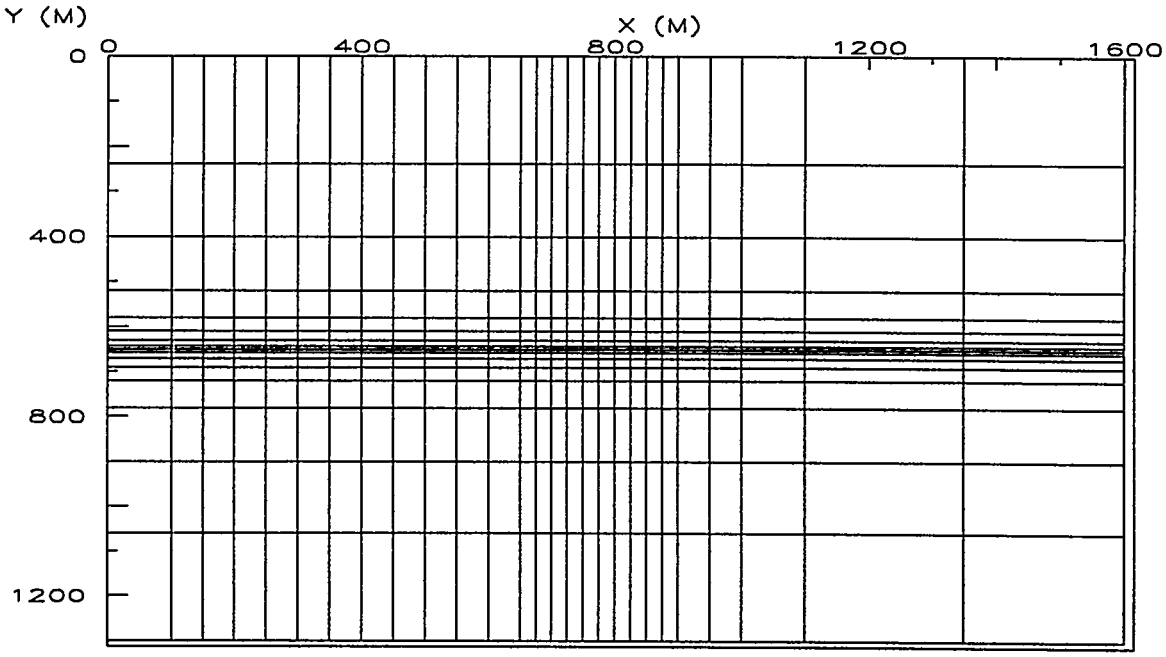

Figure 7.4: Grid 2, XY-plane (Mini-model)

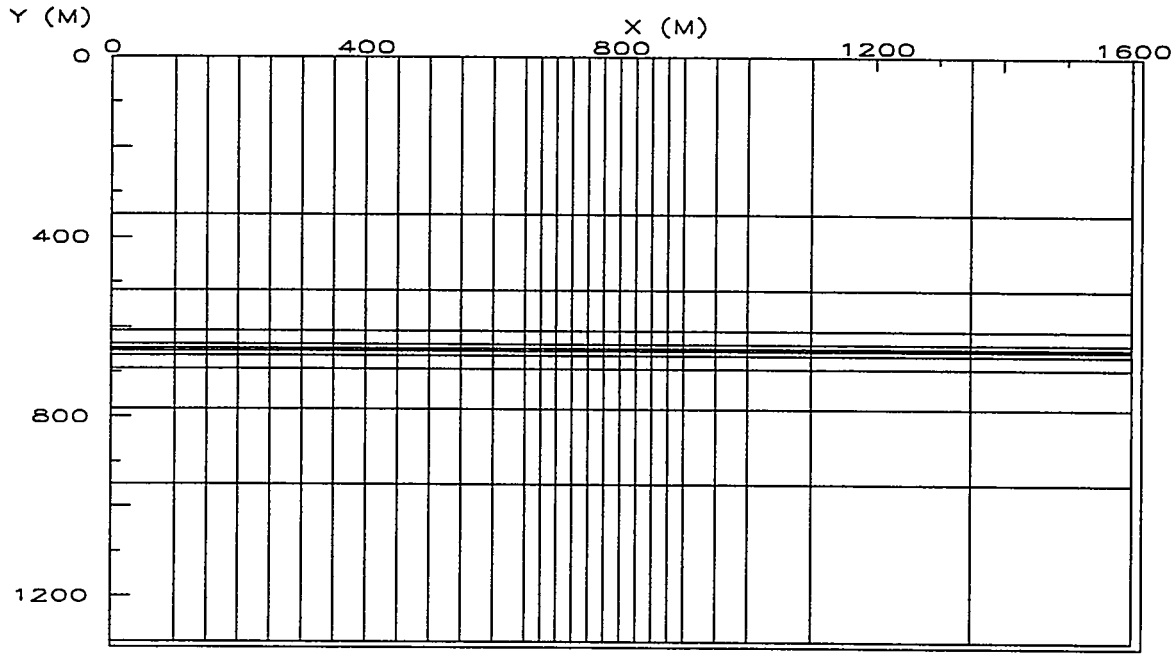

Figure 7.5: Grid 4, XY-plane (Mini-model)

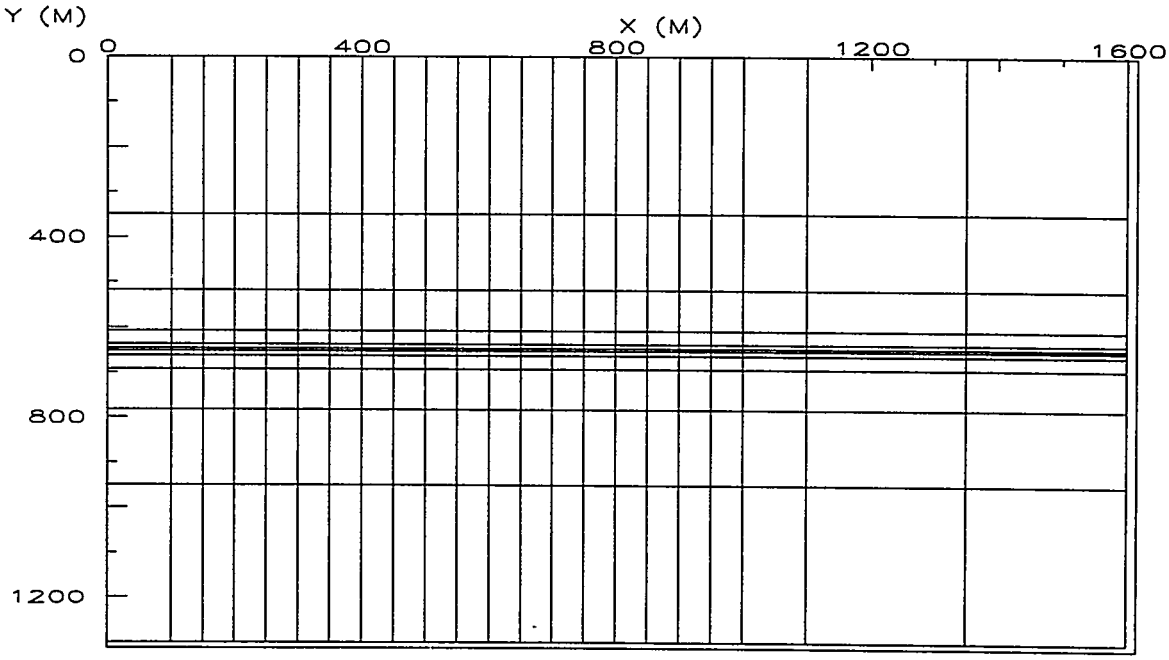

Figure 7.6: Grid 9, XY-plane (Mini-model)

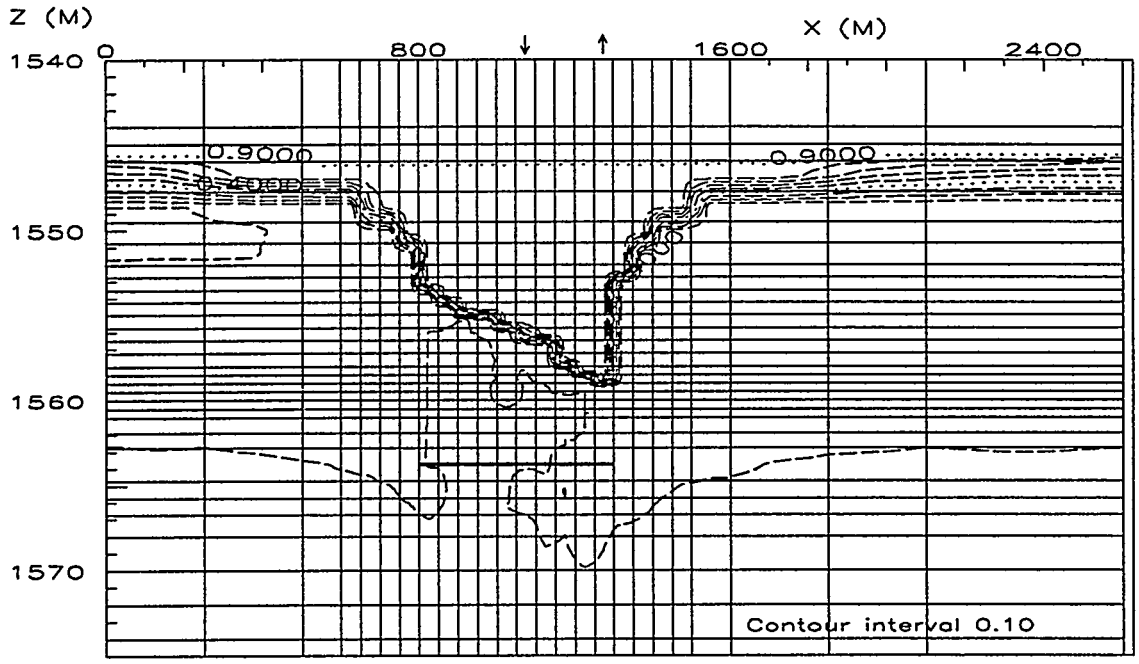

Figure 7.7: Gas cone at 365 days, with friction

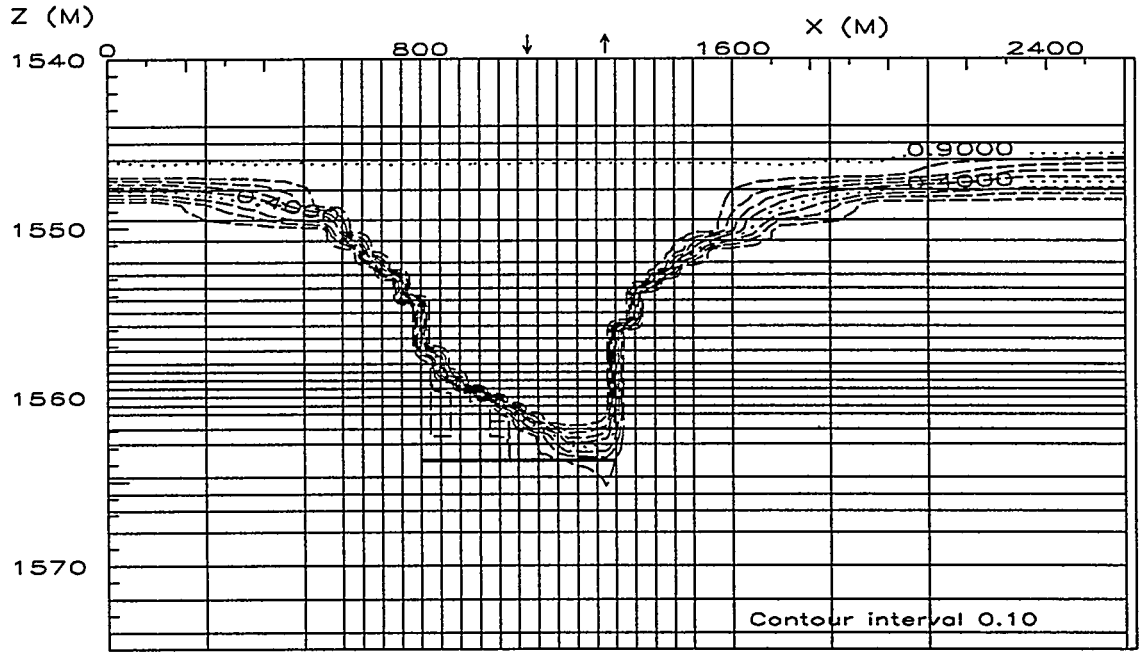

Figure 7.8: Gas cone at 1095 days, with friction

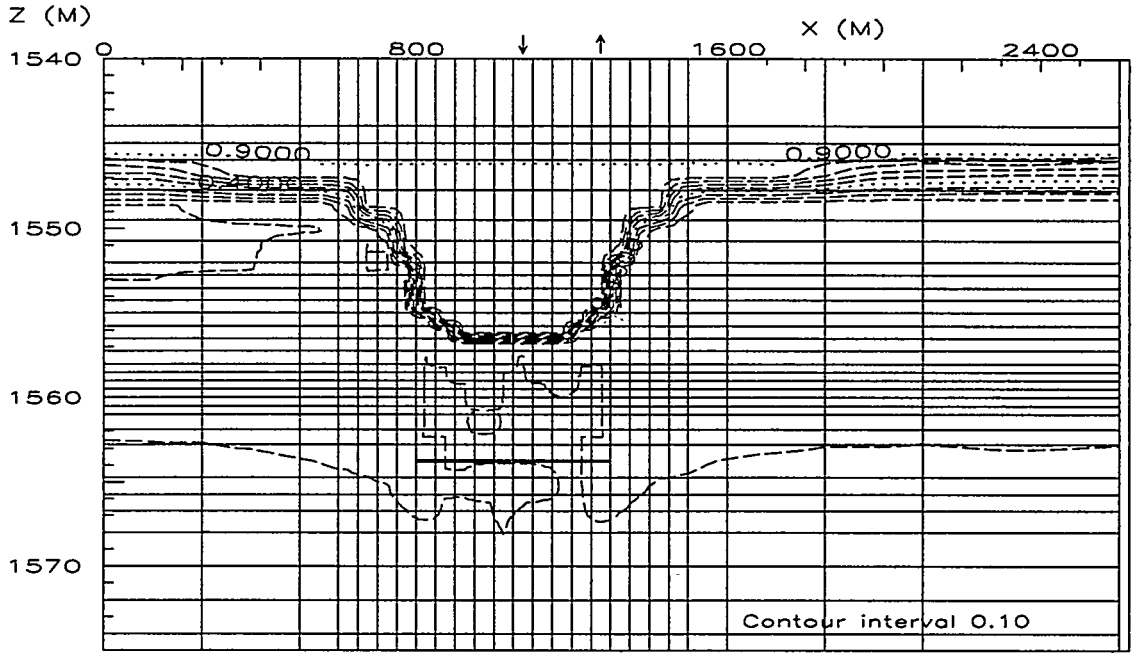

Figure 7.9: Gas cone at 365 days, without friction

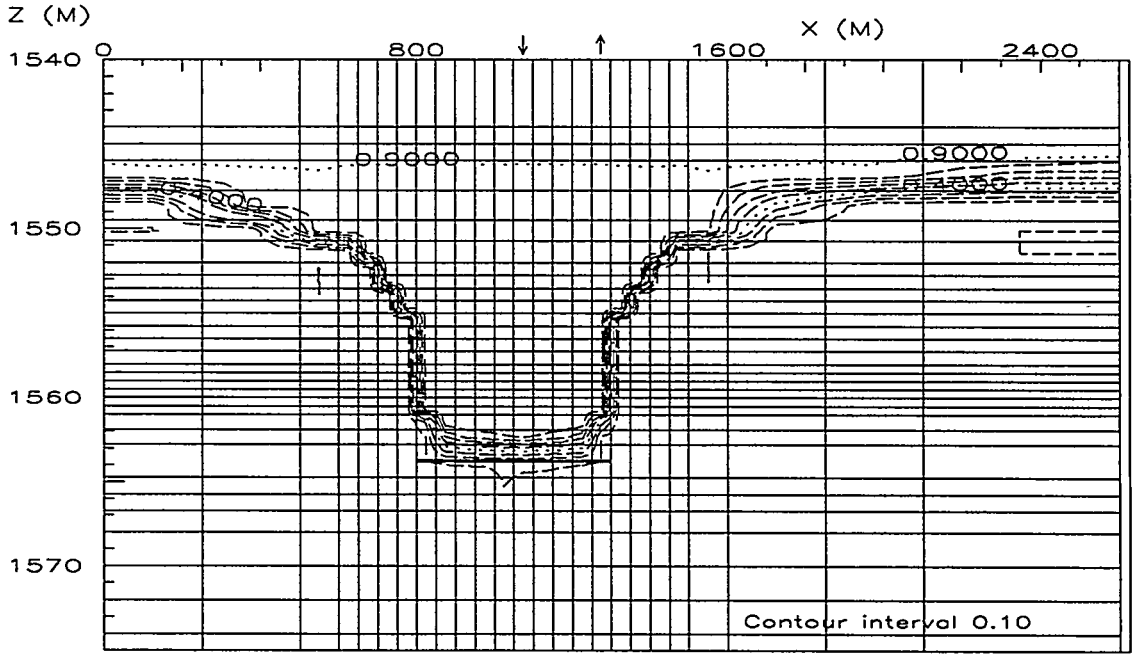

Figure 7.10: Gas cone at 1095 days, without friction

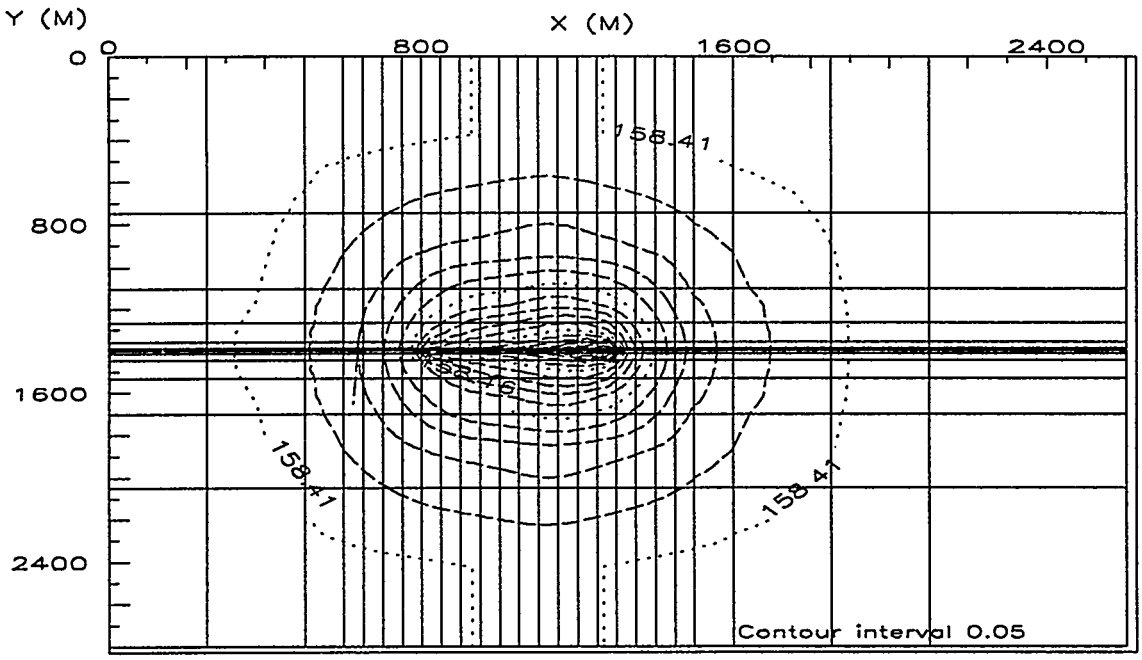

Figure 7.11: Reservoir pressure at 365 days, with friction

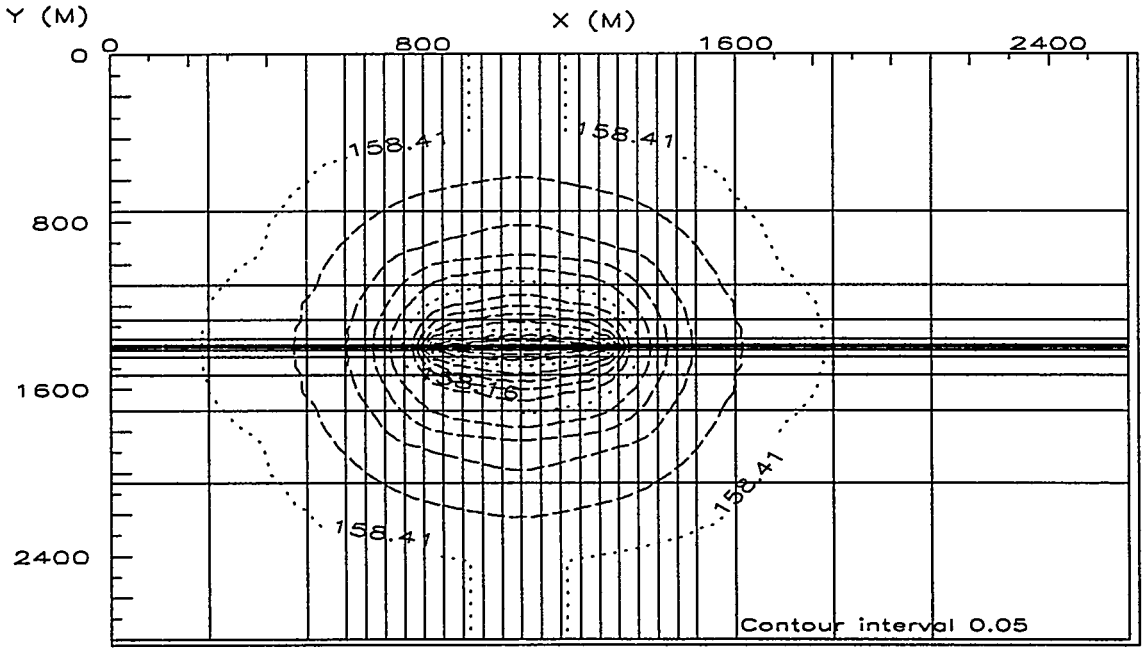

Figure 7.12: Reservoir pressure at 365 days, without friction

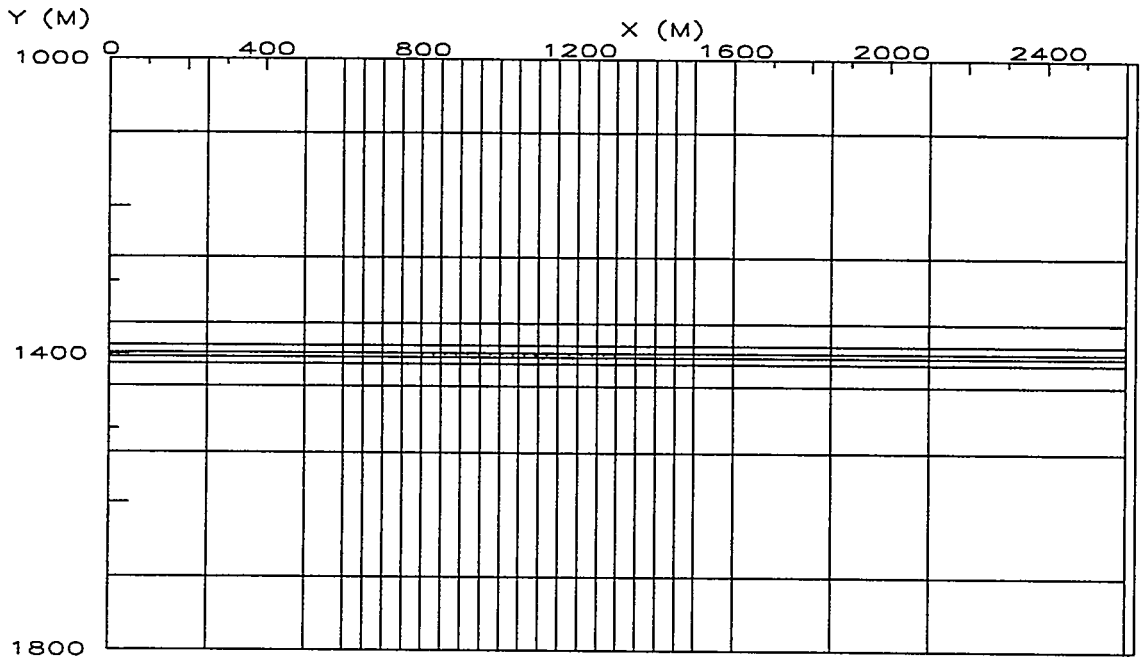

Figure 7.13: Fluid flow regions

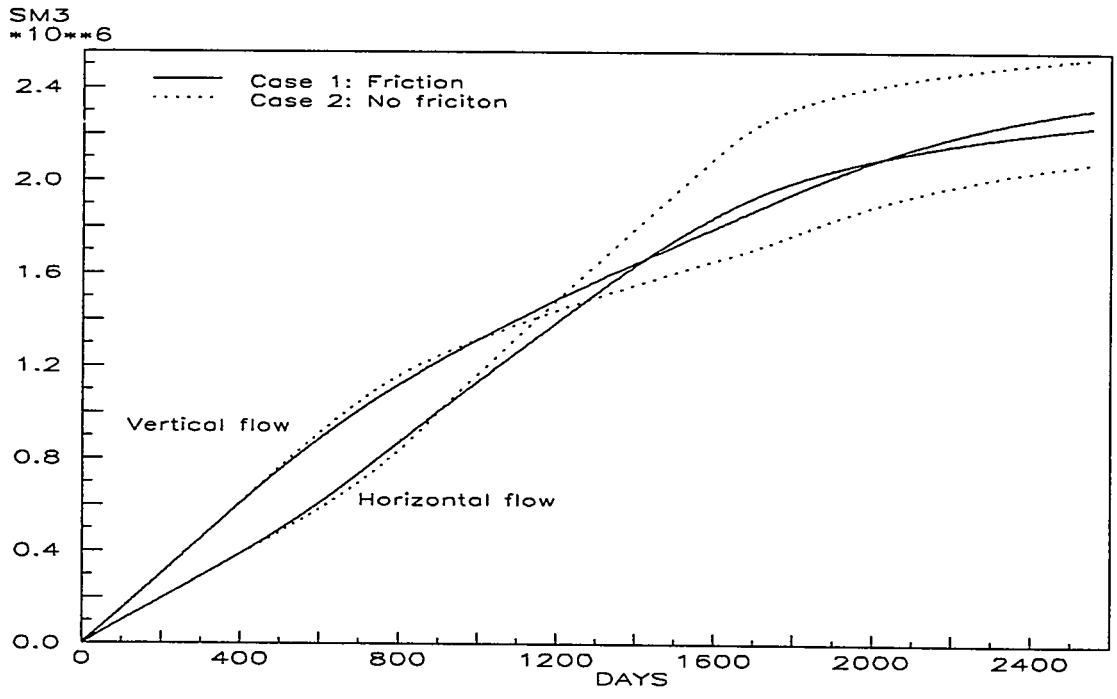

Figure 7.14: Vertical and horizontal inflow of oil to the well region

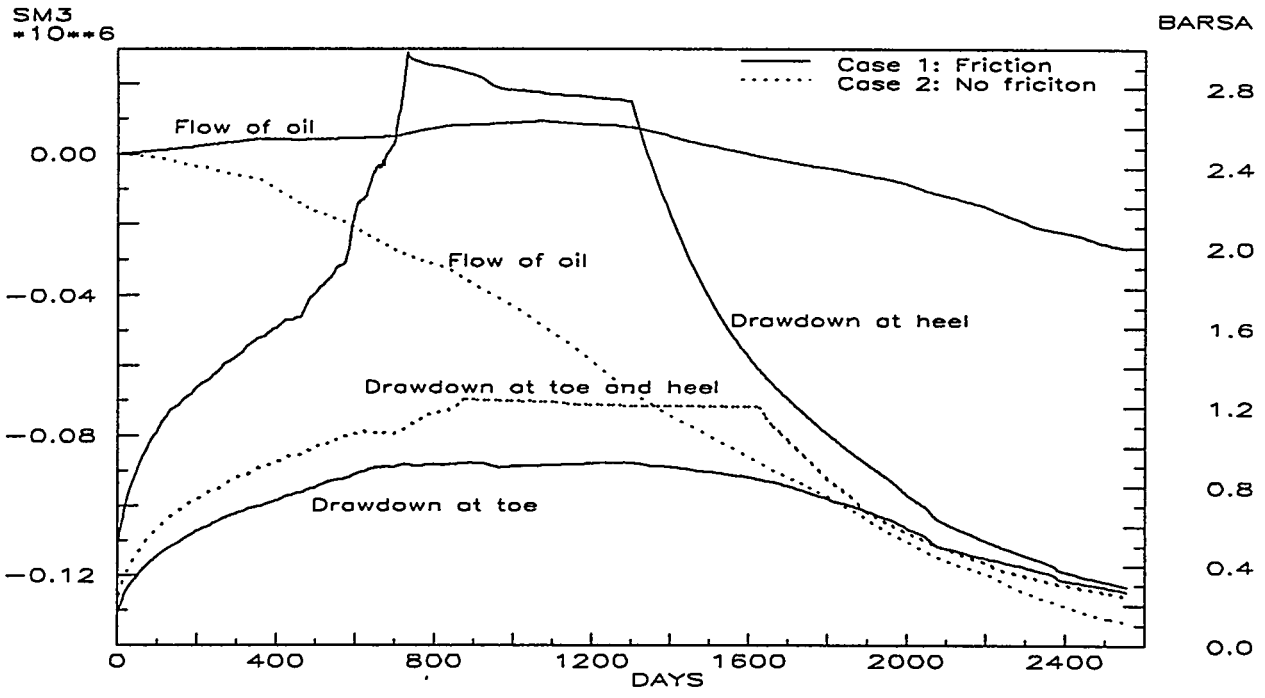

Figure 7.15: Pressure drawdown at toe and heel, and flow of oil in the reservoir parallel to the well (positive towards heel, from Regions 2,3 and 4 to Regions 5,6 and 7)

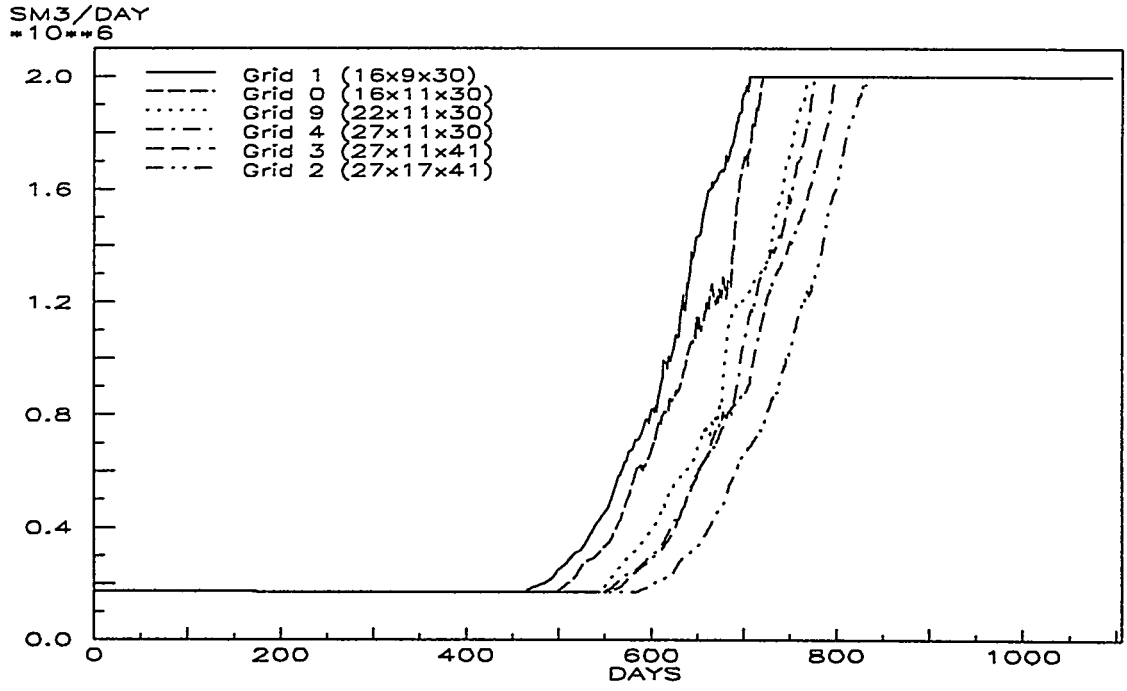

Figure 7.16: Gas rates with different grids (Mini-model)

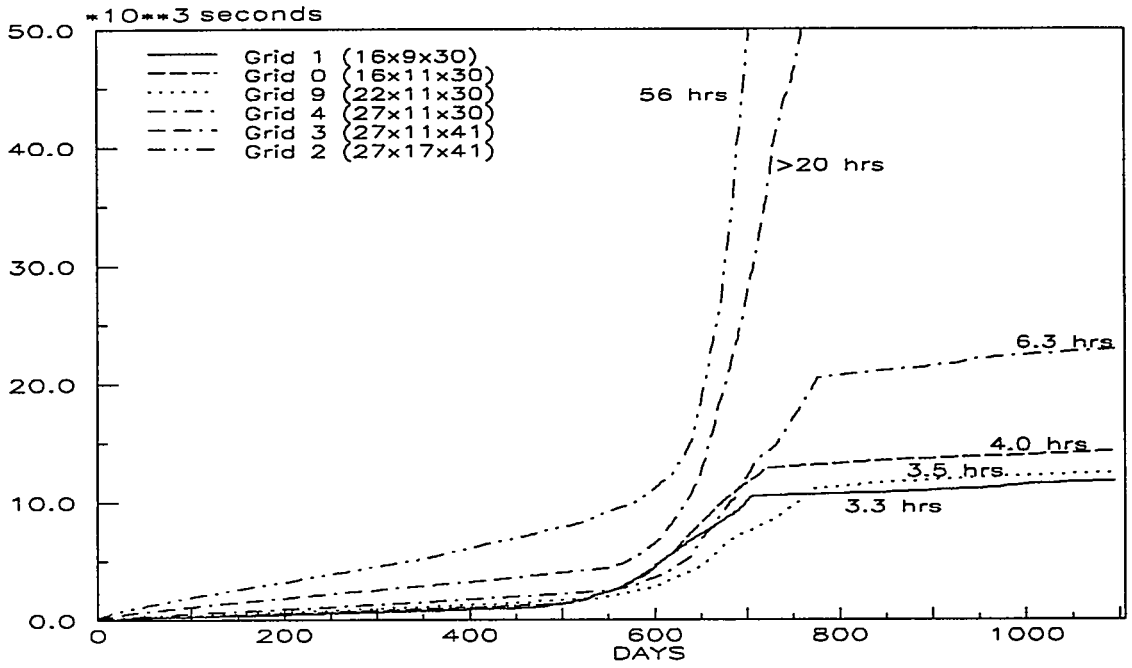

Figure 7.17: CPU-times with different grids (Mini-model)

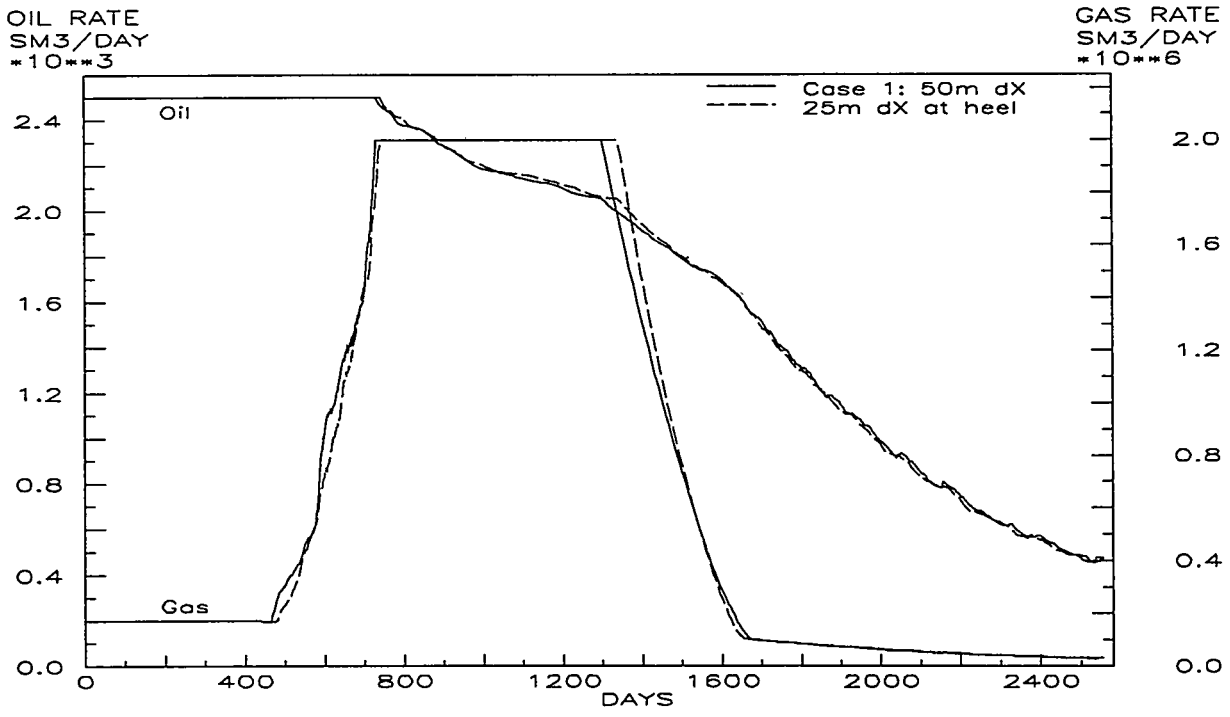

Figure 7.18: Oil and gas production rates with different grids

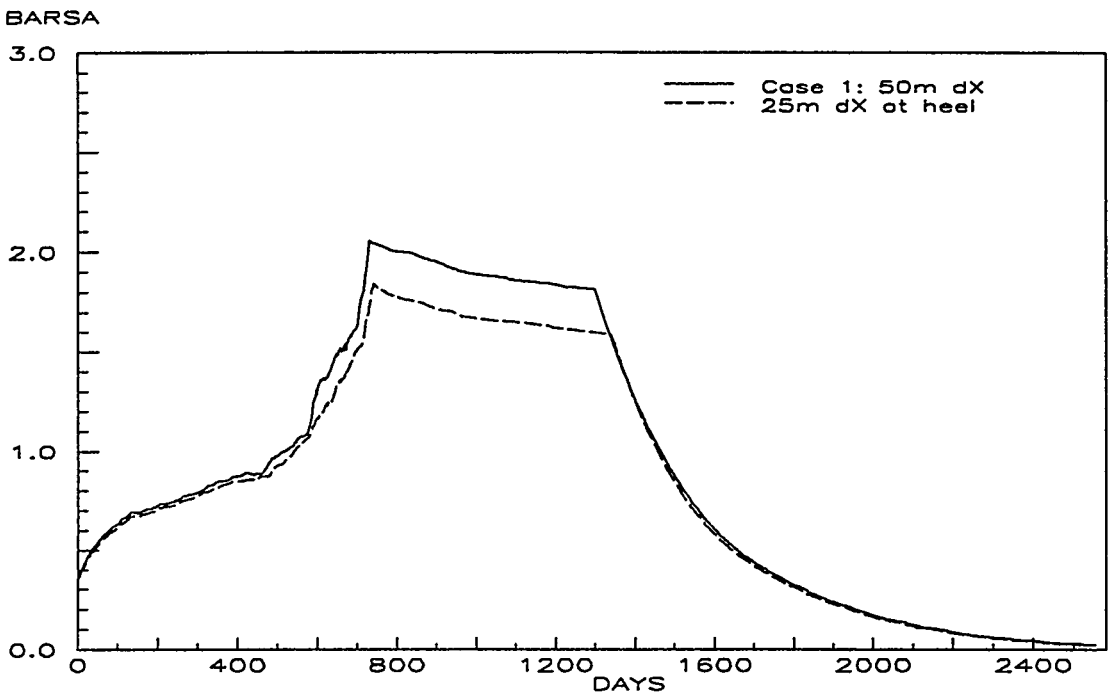

Figure 7.19: Frictional pressure drop in the well (Calculated as the difference between well pressure at the toe and bottomhole pressure)

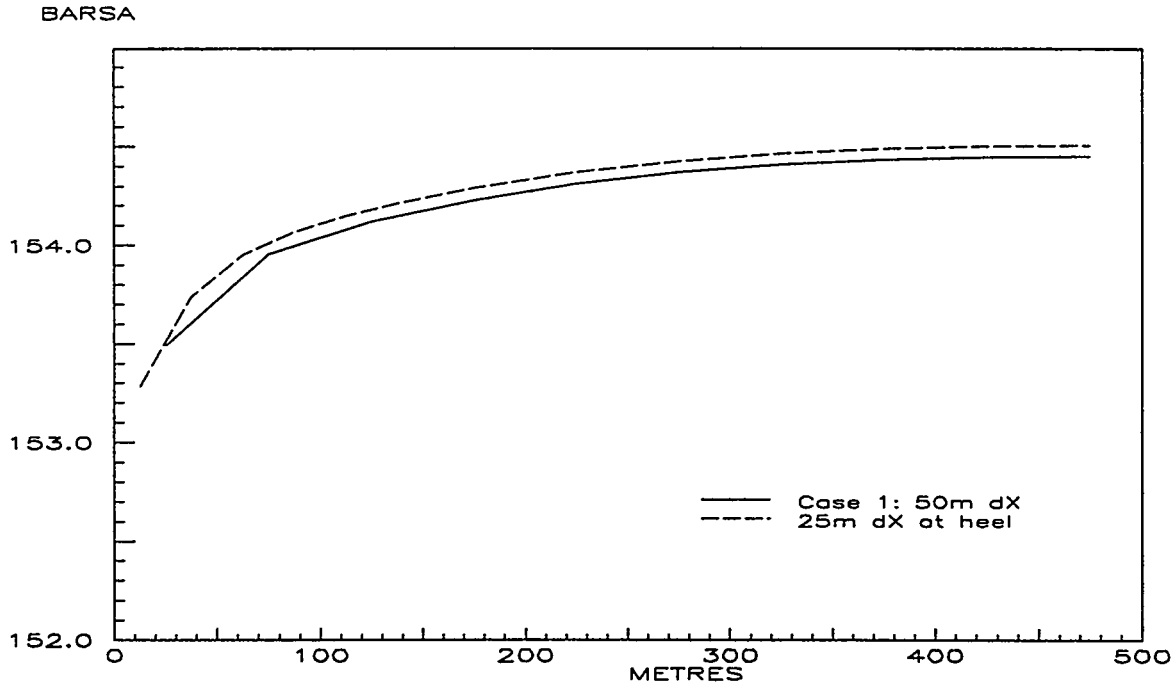

Figure 7.20: Pressure profile in the well, at 911 days (2.5 years) when liquid and gas rates are high

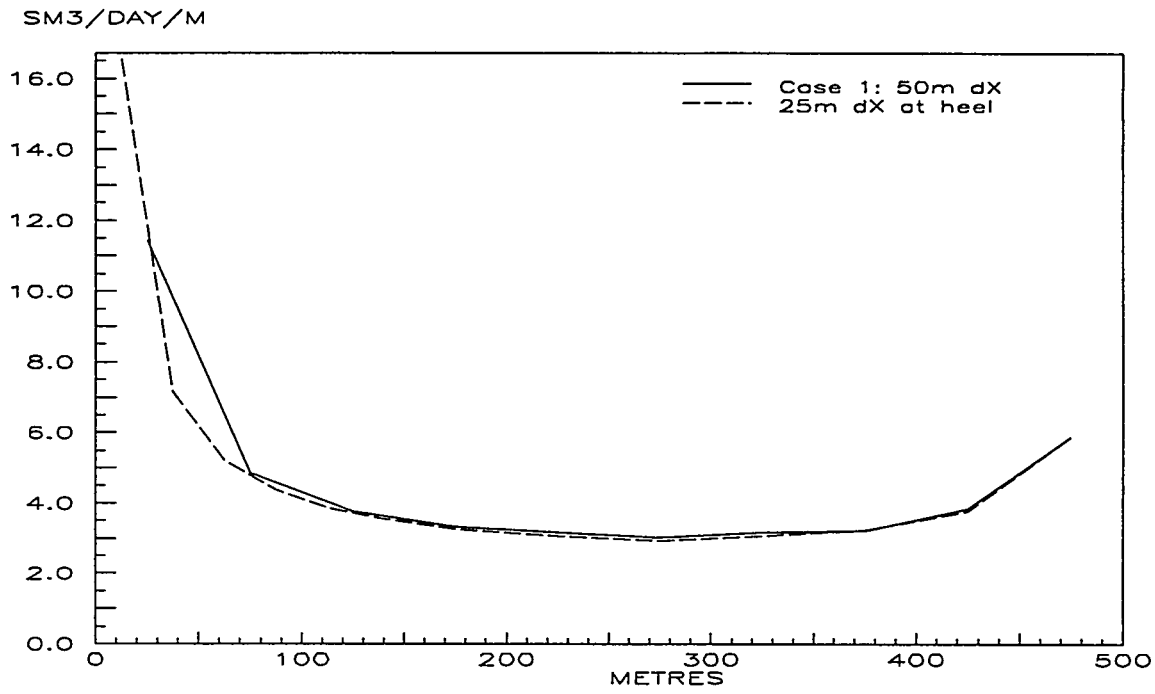

Figure 7.21: Inflow of oil along the well, at 911 days (2.5 years) when liquid and gas rates arre high

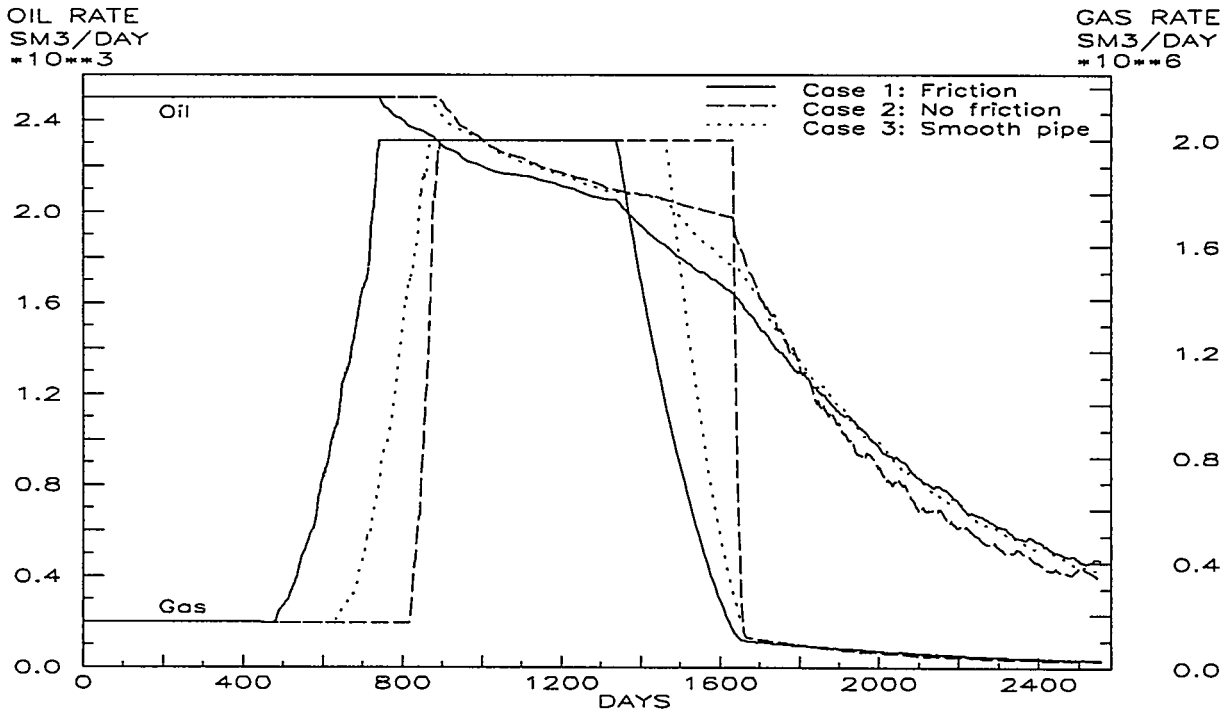

Figure 7.22: Oil and gas production rates with different levels of wellbore friction

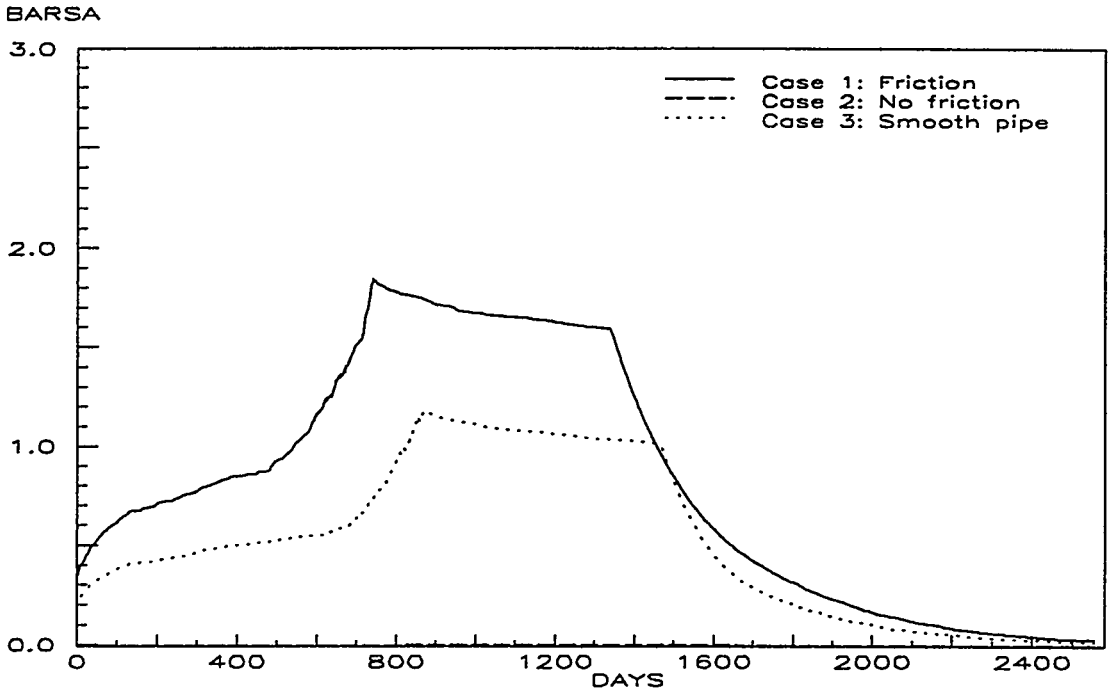

Figure 7.23: Frictional pressure drop in the well (Calculated as the difference between well pressure at the toe and bottomhole pressure)

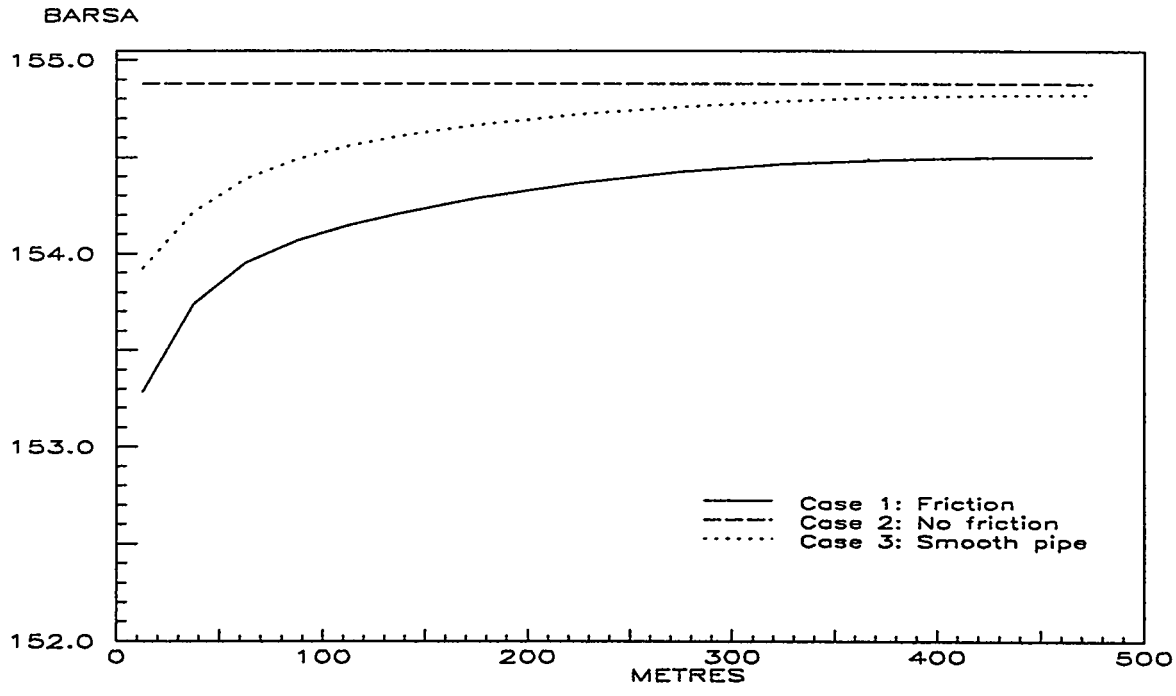

Figure 7.24: Pressure profile in the well, at 911 days (2.5 years) when liquid and gas rates are high

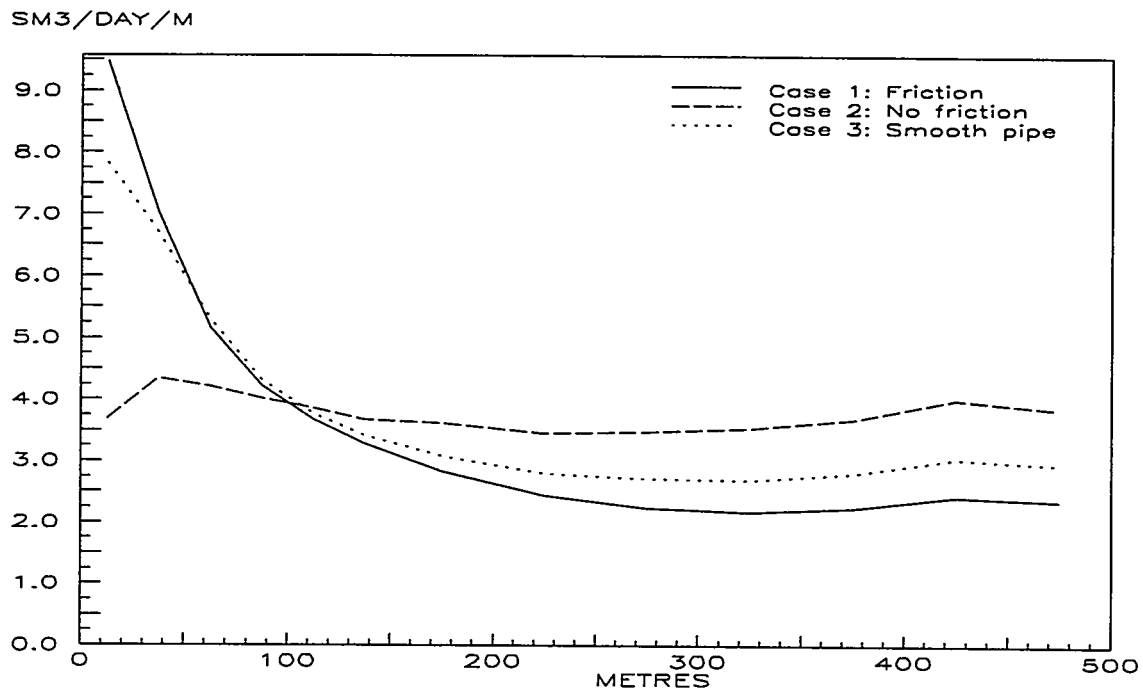

Figure 7.25: Inflow of water along the well, at 911 days (2.5 years)

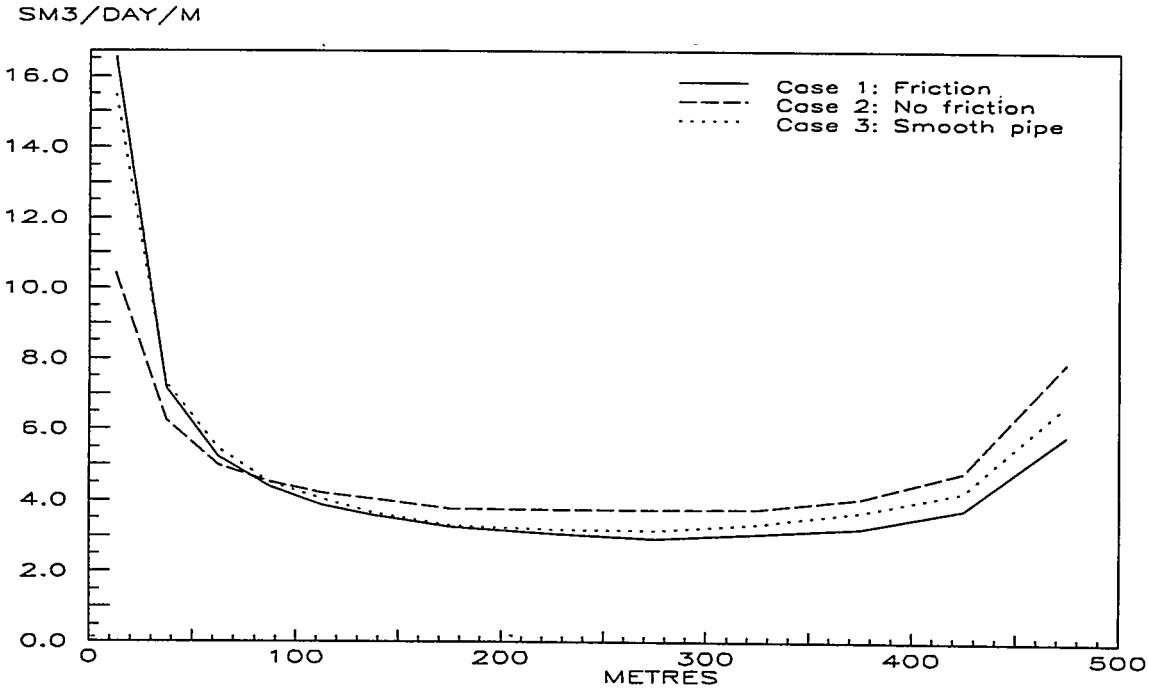

Figure 7.26: Inflow of oil along the well, at 911 days (2.5 years)

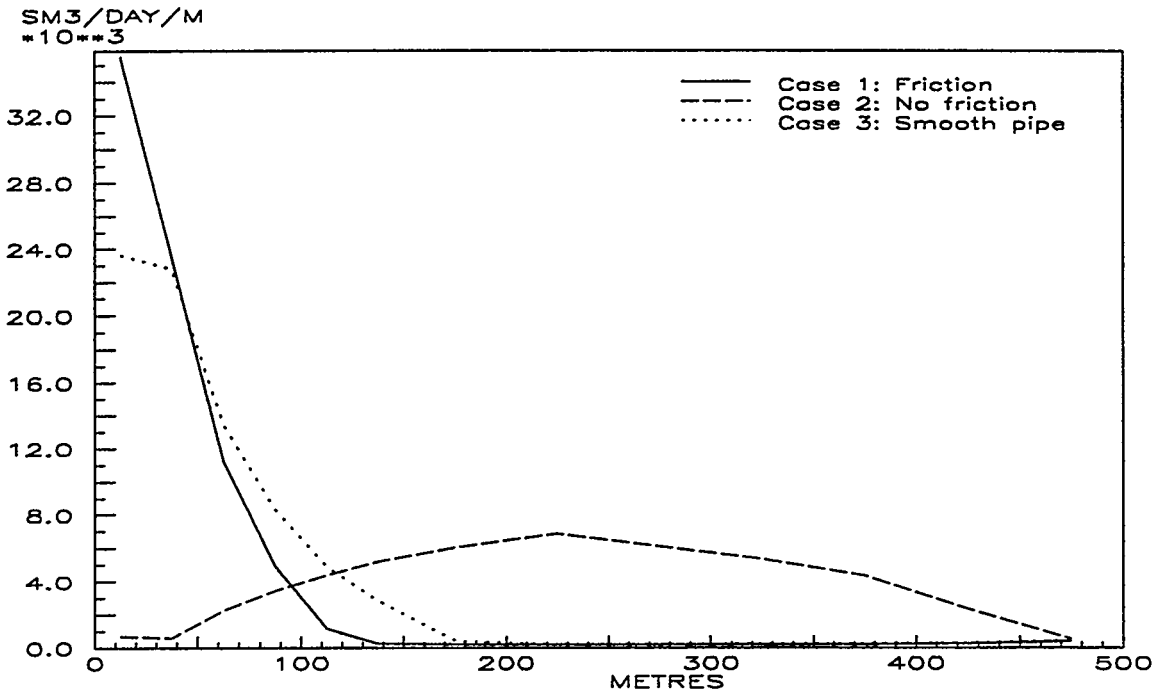

Figure 7.27: Inflow of gas along the well, at 911 days (2.5 years)

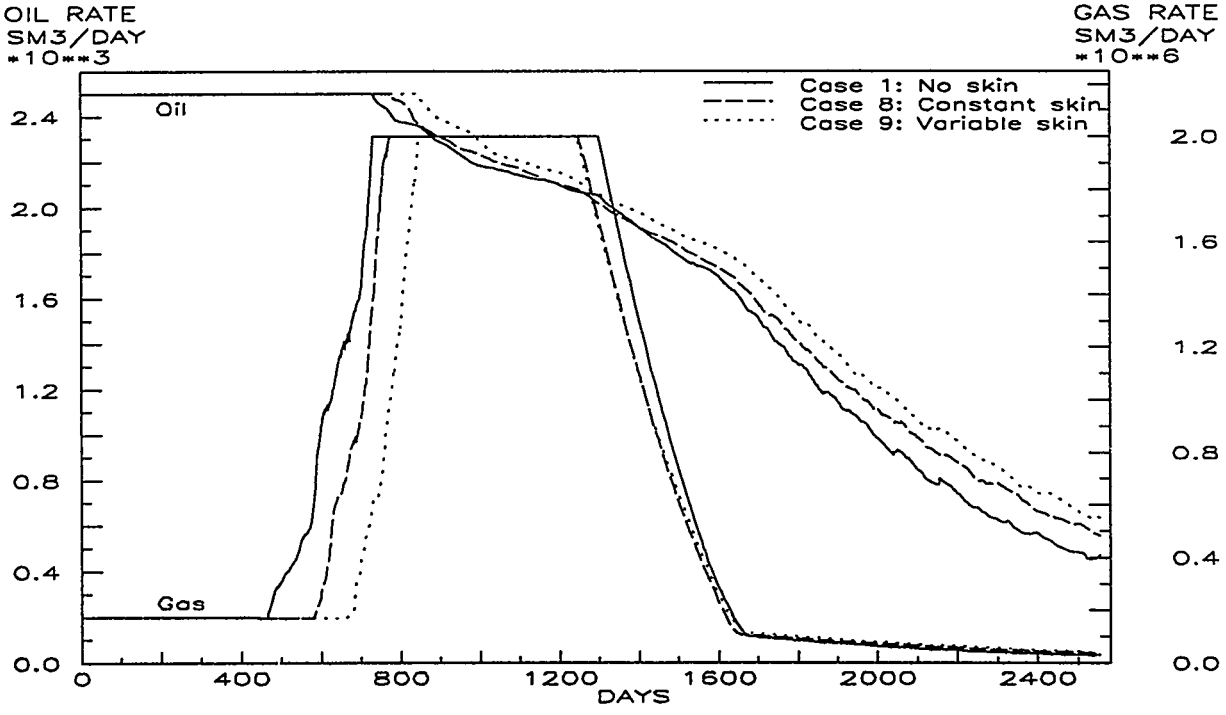

Figure 7.28: Oil and gas production rates with different skin damage

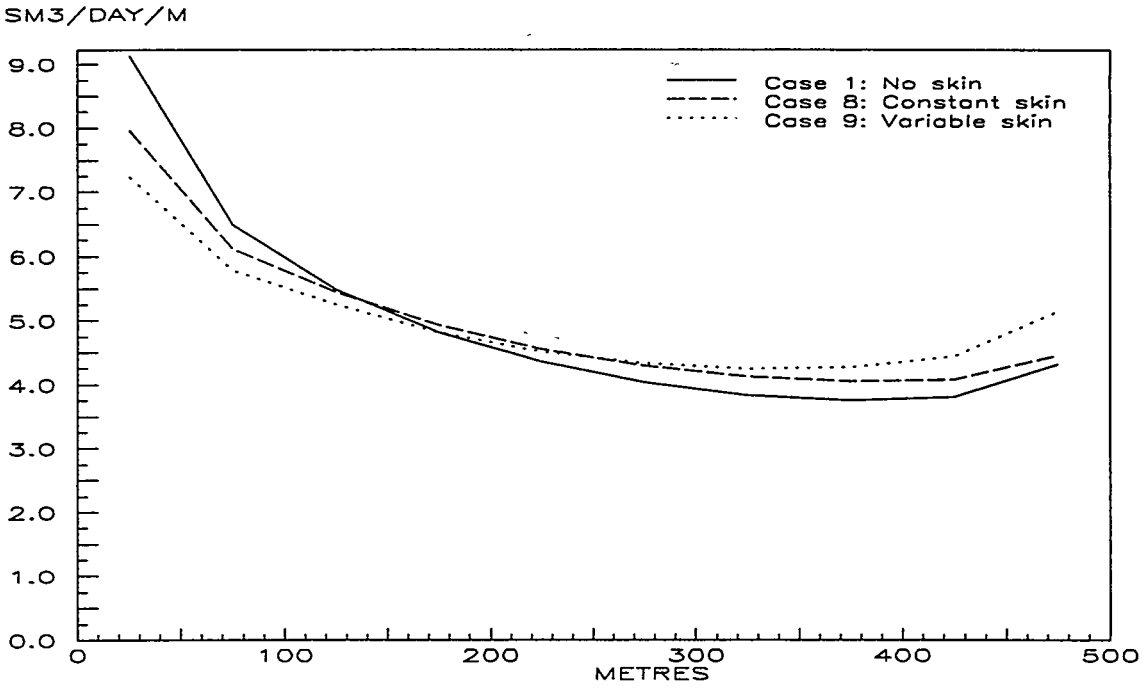

Figure 7.29: Inflow of oil along the well, at 30 days, before gas breakthrough

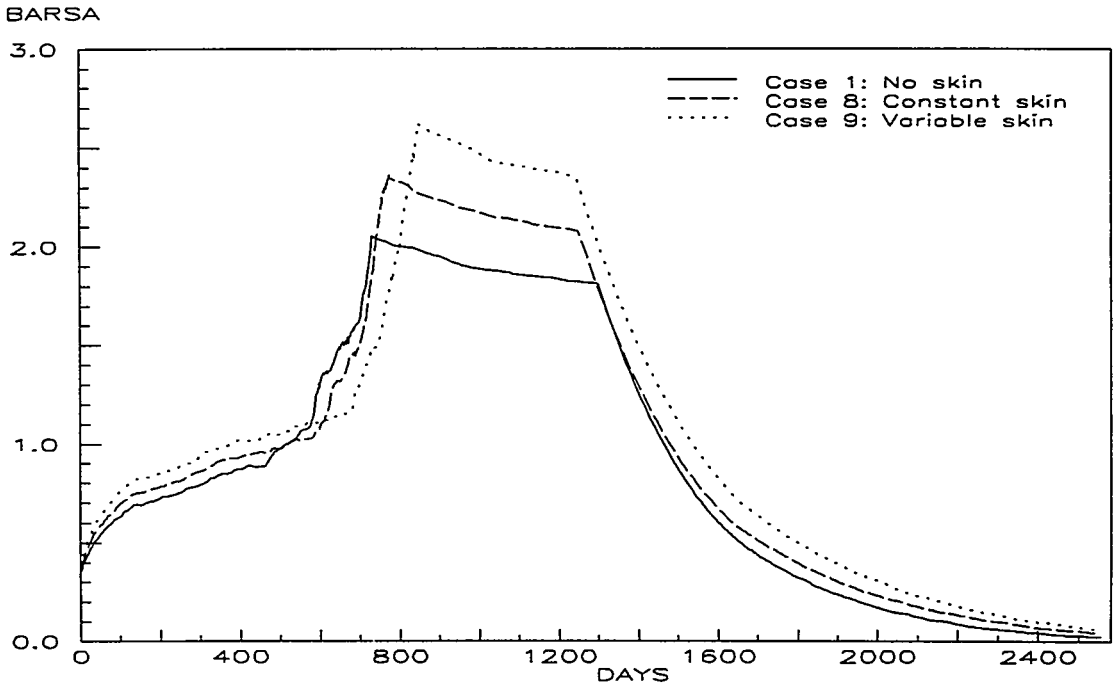

Figure 7.30: Frictional pressure drop in the well (Calculated as the difference between well pressure at the toe and bottomhole presssure)

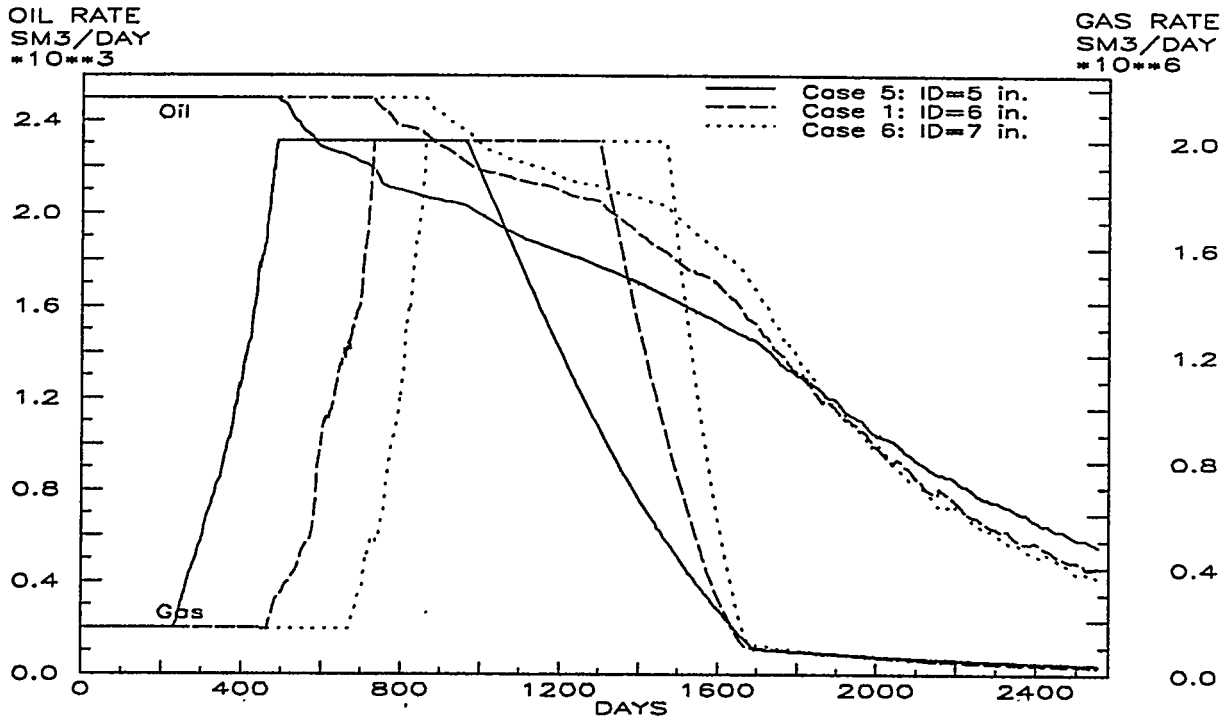

Figure 7.31: Oil and gas production rates with different wellbore diameters

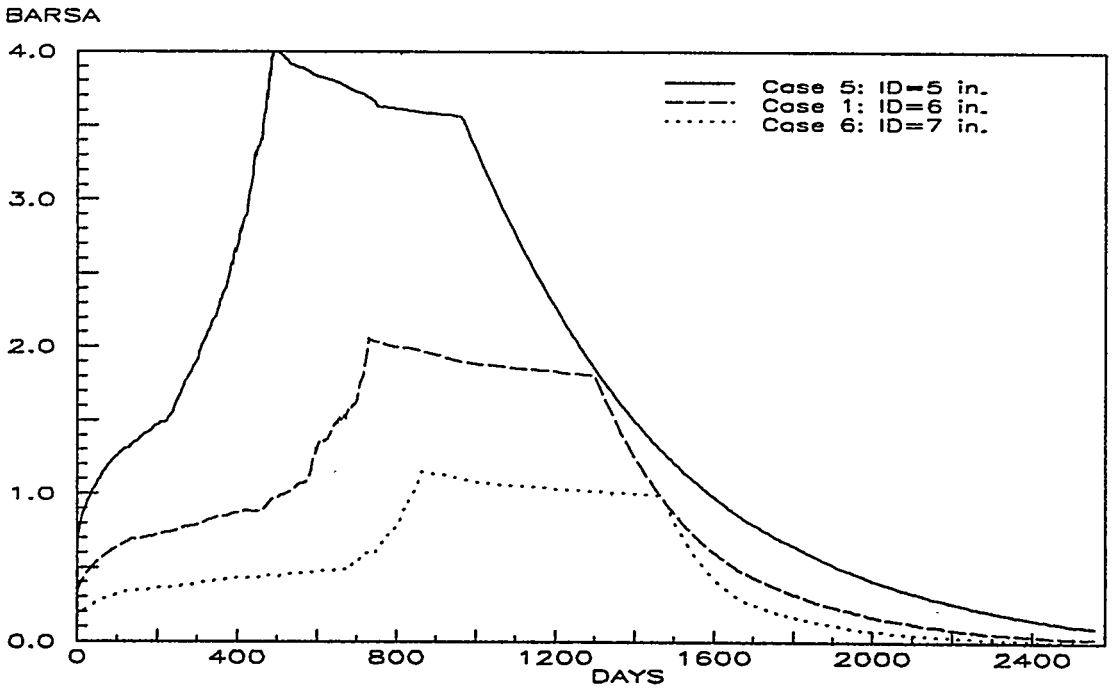

Figure 7.32: Frictional pressure drop in the well

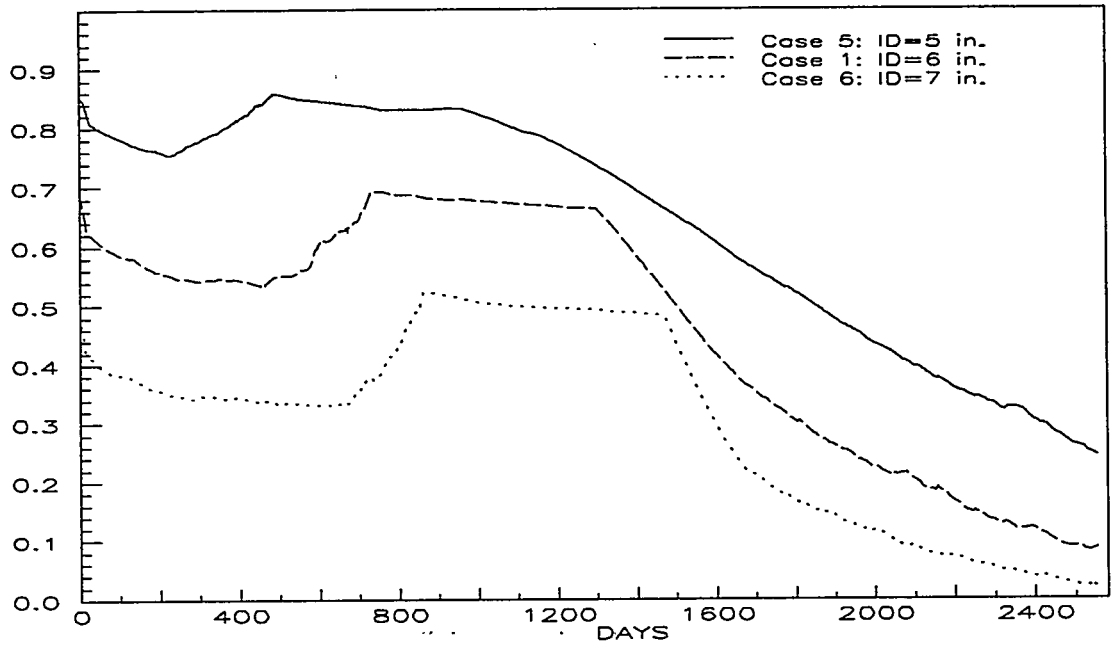

Figure 7.33: Ratio of frictional pressure drop to drawdown at heel

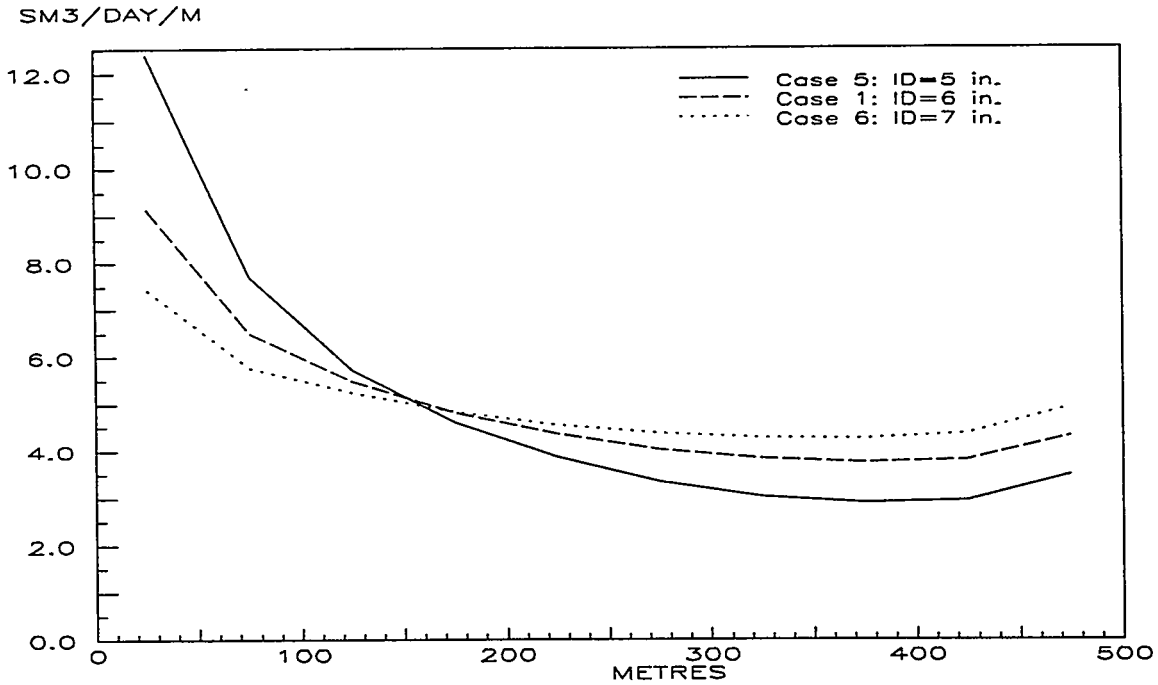

Figure 7.34: Inflow of oil along the well, at 30 days

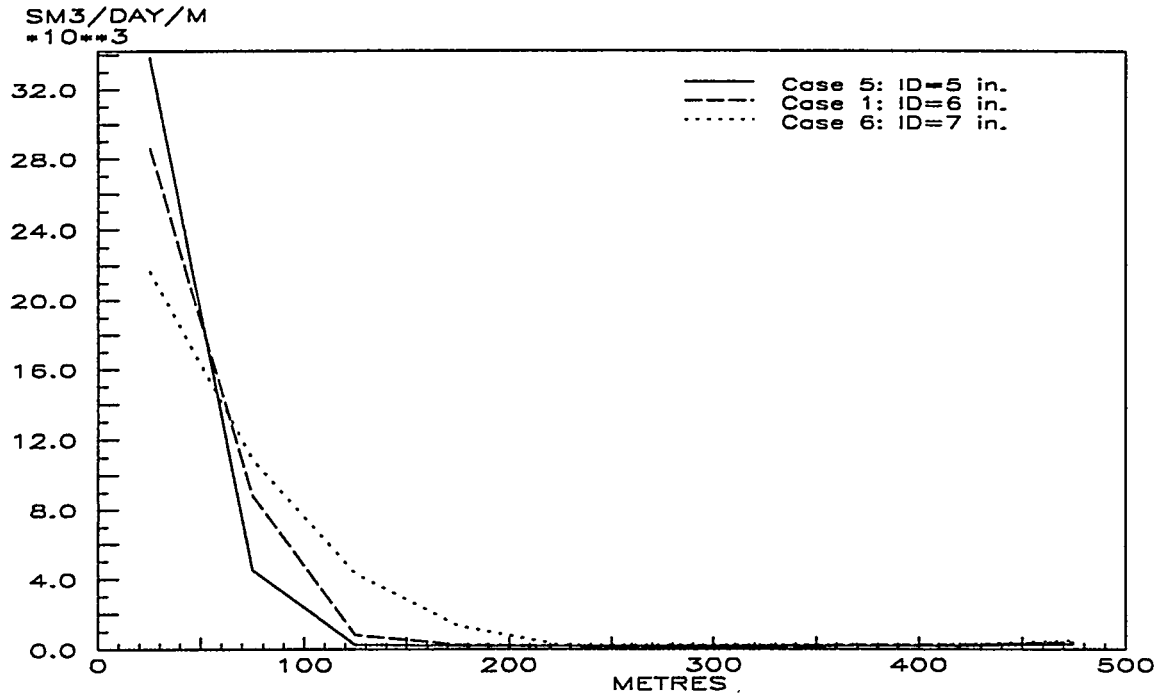

Figure 7.35: Inflow of gas along the well, at 911 days (2.5 years)

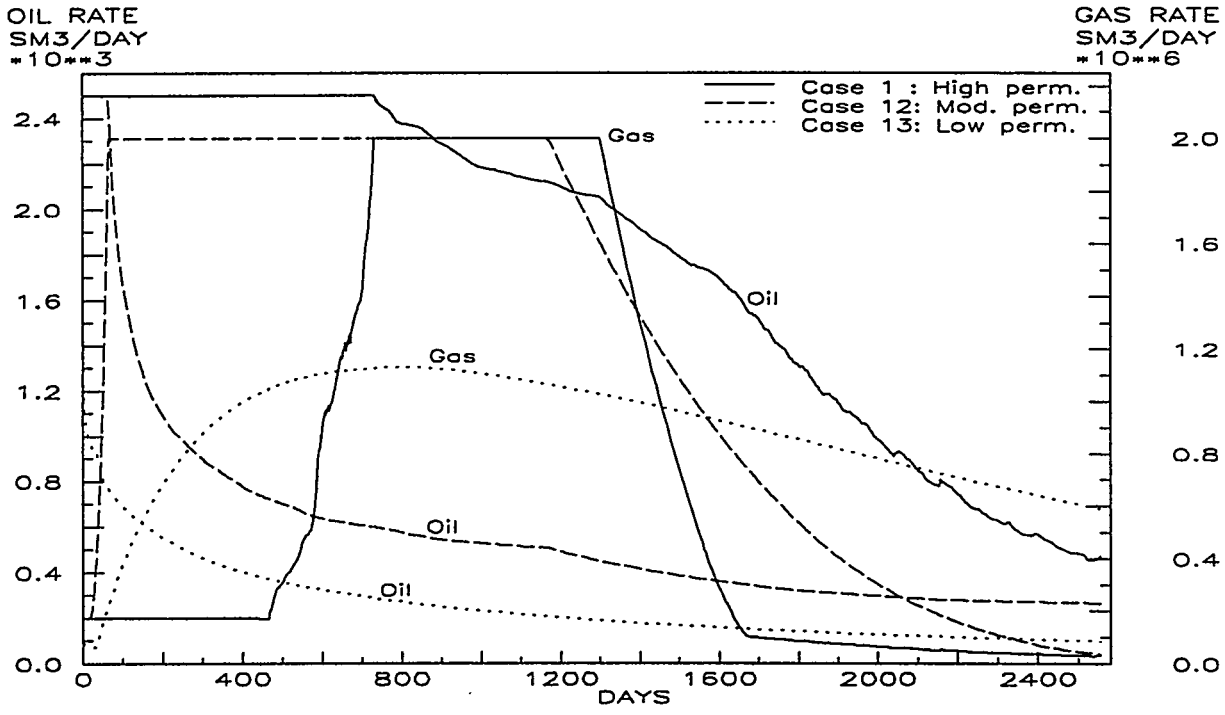

Figure 7.36: Oil and gas production rates with different levels of permeability

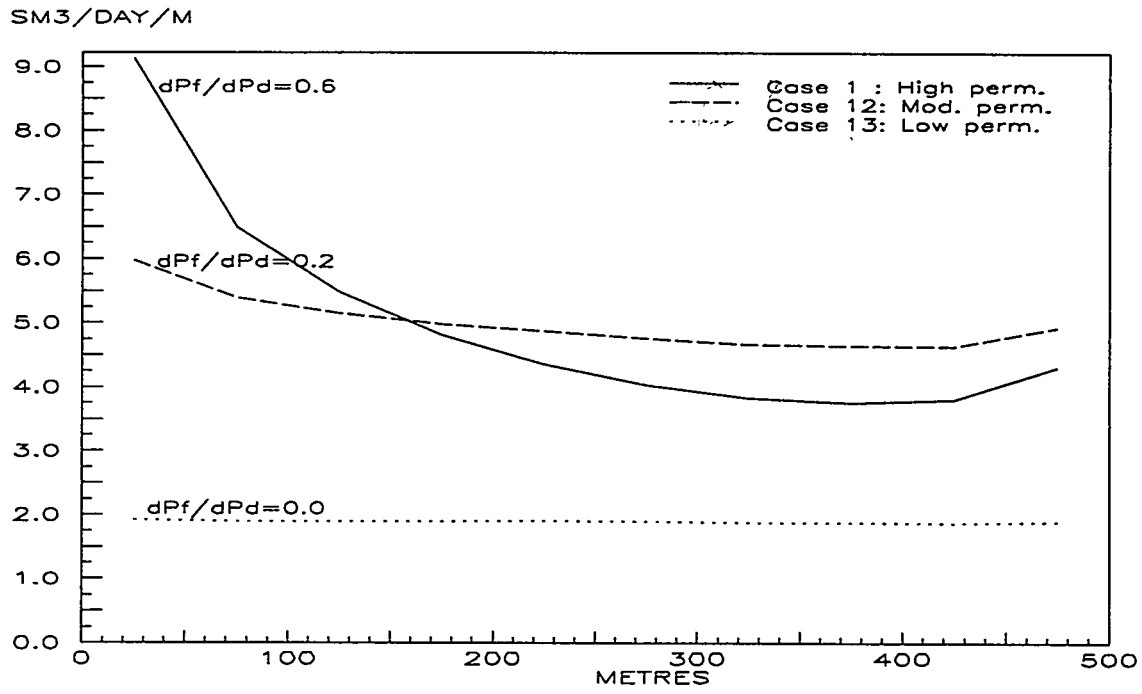

Figure 7.37: Inflow of oil along the well, at 30 days

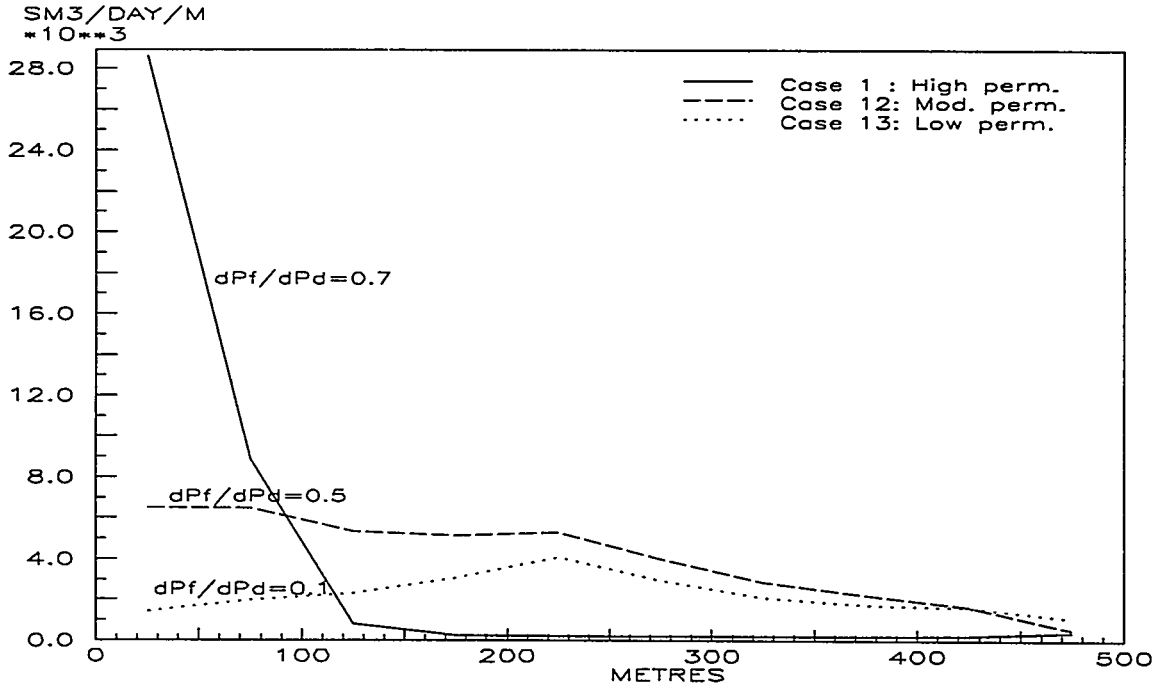

Figure 7.38: Inflow of gas along the well, at 911 days (2.5 years)

☆U.S. GOVERNMENT PRINTING OFFICE: 1995 - 660-029/20049